# NAMBE & QME 2023 Program Key

| | |
|---|---|
| **GD** | MBE-Grown Devices |
| **NM** | Novel Materials |
| **QME** | Workshop on Quantum Materials Epitaxy |
| **ST** | Science and Technology of MBE |

## Key to Session/Paper Numbers

Sessions are labeled with acronyms (e.g. **QME, NM, etc.**), then a dash followed by the first two characters of the day of the week: **Sa**turday, **Su**nday, **Mo**nday, **Tu**esday, **We**dnesday, then a single letter for **M**orning, **A**fternoon, **P**oster, and finally a number indicating the starting time slot for the paper.
Example: GD-MoA1-1 (Photonic Devices Session, Monday Afternoon, 1:30 pm).

# NAMBE & QME 2023 Program Overview

| Room /Time | BALLROOM A | HALL OF IDEAS E-J |
|---|---|---|
| SaM | QME-SaM1: Oxides I<br>QME-SaM2: Topological and Magnetic Materials I | |
| SaA | QME-SaA1: 2D and Heteroepitaxial Integration<br>QME-SaA2: Poster Highlights | |
| SaP | QME POSTER SESSION | |
| SuM | QME-SuM1: Oxides II<br>QME-SuM2: Topological and Magnetic Materials II | |
| MoM | NM-MoM1: Oxide Semiconductors<br>NM-MoM2: Nitrides | |
| MoA | GD-MoA1: Photonic Devices<br>NM-MoA2: Strong Spin-Orbit Oxides | |
| MoP | | NAMBE POSTER SESSIONS |
| TuM | NM-TuM1: Novel Materials, Optoelectronics<br>NM-TuM2: Thin Film Membranes | |
| TuA | GD-TuA1: Solar Cell and Quantum Computing<br>NM-TuA2: Novel Oxides and Superconductors | |
| WeM | ST-WeM1: Advancement in MBE Growth Approaches<br>ST-WeM2: Fundamentals of MBE Growth | |
| WeA | NM-WeA: Low Dimensional and Topological Materials | |

# Saturday Morning, September 16, 2023

| | Room Ballroom A | |
|---|---|---|
| 8:00am | **INVITED: QME-SaM1-2** Hunting for New Oxide Superconductors using MBE, ***Darrell Schlom,*** Cornell University | **Workshop on Quantum Materials Epitaxy**<br>**Session QME-SaM1**<br>**Oxides I**<br>**Moderator:**<br>**Bharat Jalan**, University of Minnesota |
| 8:15am | | |
| 8:30am | **INVITED: QME-SaM1-4** Advanced Epitaxial Growth of Quantum Materials Using Thermal Laser Epitaxy, ***Jochen Mannhart,*** Max Planck Institute for Solid State Research, Germany | |
| 8:45am | | |
| 9:00am | **INVITED: QME-SaM1-6** Superconductivity at Interfaces of $KTaO_3$ and its Possible Origins, ***Anand Bhattacharya,*** Argonne National Laboratory | |
| 9:15am | | |
| 9:30am | **INVITED: QME-SaM1-8** Synthesis of Electronic-Grade Quantum Heterostructures by Hybrid PLD, ***Chang-Beom Eom,*** University of Wisconsin-Madison | |
| 9:45am | | |
| 10:00am | **BREAK** | |
| 10:15am | | |
| 10:30am | **INVITED: QME-SaM2-12** Invited Paper, ***Stuart Parkin,*** Max Planck Institute of Microstructural Physics, Germany | **Workshop on Quantum Materials Epitaxy**<br>**Session QME-SaM2**<br>**Topological and Magnetic Materials I**<br>**Moderator:**<br>**Nitin Samarth**, Pennsylvania State University |
| 10:45am | | |
| 11:00am | **INVITED: QME-SaM2-14** The Art and Science of Molecular Beam Epitaxy —— from Topological Materials to Interfacial Superconductivity, ***Cui-Zu Chang,*** Pennsylvania State University | |
| 11:15am | | |
| 11:30am | **INVITED: QME-SaM2-16** Epitaxial Control of Topological Semimetals, ***Kirstin Alberi,*** National Renewable Energy Laboratory | |
| 11:45am | | |
| 12:00pm | **INVITED: QME-SaM2-18** Growth and Investigations of Topological and Quantum Phenomena in Epitaxial Semimetallic Thin Films, ***Chris Palmstrøm,*** University of California, Santa Barbara | |
| 12:15pm | | |

# Saturday Afternoon, September 16, 2023

| | Room Ballroom A | |
|---|---|---|
| 2:00pm | **INVITED: QME-SaA1-1** Invited Paper, ***Grace Xing***, Cornell University | **Workshop on Quantum Materials Epitaxy**<br>**Session QME-SaA1**<br>**2D and Heteroepitaxial Integration**<br>**Moderator:**<br>**Roman Engel-Herbert**, Paul Drude Institute, Germany |
| 2:15pm | | |
| 2:30pm | **INVITED: QME-SaA1-3** Growth of Topological Materials by Molecular Beam Epitaxy, ***Stephanie Law***, Pennsylvania State University | |
| 2:45pm | | |
| 3:00pm | **INVITED: QME-SaA1-5** Big Flat Quantum Crystals: Wafer-Scale Growth of 2D Materials by Metalorganic Chemical Vapour Deposition, ***James A. Gupta***, University of Ottawa, Canada | |
| 3:15pm | | |
| 3:30pm | **INVITED: QME-SaA1-7** Advanced Heterogeneous Integration Enabled by Remote Epitaxy, ***Jeehwan Kim***, Massachusetts Institute of Technology | |
| 3:45pm | | |
| 4:00pm | **BREAK** | |
| 4:15pm | | |
| 4:30pm | **QME-SaA2-11** Poster Highlights Session - 3-Minute Oral Presentations from Poster Presenters, | **Workshop on Quantum Materials Epitaxy**<br>**Session QME-SaA2**<br>**Poster Highlights**<br>**Moderator:**<br>**Jason Kawasaki**, University of Wisconsin - Madison |
| 4:45pm | | |
| 5:00pm | | |
| 5:15pm | | |

## Workshop on Quantum Materials Epitaxy
## Room Ballroom A - Session QME-SaP
## Workshop on Quantum Materials Epitaxy Poster Session
## 5:30 – 7:00 pm

**QME-SaP-1** Optimization of Hybridized InAsSb/InGaSb Semiconductor Topological Materials, ***Heather Haugan***, Air Force Research Laboratory; *D. Das, L. Ram-Mohan,* Worcester Polytechnic Institute; *J. Corbett, K. Mahalingam, R. Bedford, K. Eyink,* Air Force Research Laboratory

**QME-SaP-2** Doping the Undopable: Hybrid Molecular Beam Epitaxy Growth, n-type Doping, and Field-Effect Transistor using $CaSnO_3$, ***Fengdeng Liu***, University of Minnesota, USA; *P. Golani,* University of Minnesota; *T. Truttmann,* University of Minnesota, USA; *I. Evangelista,* University of Delaware; *M. Smeaton,* Cornell University; *D. Bugallo,* Drexel University; *J. Wen,* University of Minnesota; *A. Kamath Manjeshwar,* University of Minnesota, USA; *S. May,* Drexel University; *L. Kourkoutis,* Cornell University; *A. Janotti,* University of Delaware; *S. Koester,* University of Minnesota; *B. Jalan,* University of Minnesota, USA

**QME-SaP-3** Solid Source Metal-Organic Molecular Beam Epitaxy for Epitaxial $SrRuO_3$ Films, ***Anusha Kamath Manjeshwar***, *S. Nair, A. Rajapitamahuni, R. James, B. Jalan,* University of Minnesota

**QME-SaP-4** Growth Mechanism of $SrTiO_3$ on a Graphene-covered Substrate using Hybrid MBE0, ***Sooho Choo***, *H. Yoon,* University of Minnesota, USA, Republic of Korea; *B. Matthews,* Pacific Northwest National Laboratory; *S. Sharma,* University of Minnesota, USA; *S. Spurgeon, S. Chambers,* Pacific Northwest National Laboratory; *R. James, B. Jalan,* University of Minnesota, USA

**QME-SaP-5** Growing Clean Crystals from "Dirty" Precursors in MBE, ***Rashmi Choudhary***, University of Minnesota, USA; *Z. Liu, J. Cai, X. Xu, J. Chu,* University of Washington; *B. Jalan,* University of Minnesota, USA

**QME-SaP-6** Growth of $EuIn_2As_2$ Thin Films by MBE: Towards Investigating the Topological Properties of a Candidate Axion Insulator, ***Muhsin Abdul Karim***, University of Notre Dame, Ghana; *J. Wang,* University of Notre Dame, China; *K. Yoshimura,* University of Notre Dame, Japan; *S. Bac,* University of Notre Dame, Korea (Democratic People's Republic of); *X. Liu,* University of Notre Dame, China; *B. Assaf,* University of Notre Dame

**QME-SaP-7** Synthesis of Free-Standing Membranes Using a Sacrificial Layer Method Grown by Hybrid MBE, ***Shivasheesh Varshney***, *S. Choo, Z. Yang, J. Wen, S. Koester, B. Jalan,* University of Minnesota, USA

**QME-SaP-8** Epitaxial Growth of Precursor Phases of Novel Cuprate Superconductors Using Oxide MBE, ***Jinkwon Kim***, *C. Kim, D. Schlom,* Cornell University

**QME-SaP-9** MBE of $Ba_2BiTaO_6$, a Candidate *p*-type Oxide Semiconductor, ***Anna Park***, *Y. Birkhölzer, M. Barone, D. Schlom,* Cornell University

**QME-SaP-10** Flexomagnetism and Strain Induced Superconductivity in Rippled GdAuGe Heusler Membranes, ***Tamalika Samanta***, *Z. LaDuca, D. Du, T. Jung, S. Manzo, K. Su, M. Arnold, J. Kawasaki,* University of Wisconsin - Madison

**QME-SaP-11** Engineering Metal Oxidation Towards Epitaxial Growth of Complex Iridates using Molecular Beam Epitaxy, ***Sreejith Nair***, *Z. Yang, D. Lee, S. Guo,* University of Minnesota, USA; *J. Sadowski,* Brookhaven National Laboratory; *S. Johnson,* Auburn University; *A. Saboor,* University of Delaware; *Y. Li, H. Zhou,* Argonne National Laboratory, USA; *R. Comes, W. Jin,* Auburn University; *K. Mkhoyan,* University of Minnesota, USA; *A. Janotti,* University of Delaware; *B. Jalan,* University of Minnesota, USA

**QME-SaP-12** Improved Epitaxy of Unconventional Metals for Quantum Applications, ***Stefania Isceri***, *M. Giparakis, R. Svagera, M. Waas,* Technische Universität Wien, Austria; *V. Butera, E. Kolibalova, O. Man,* Central European Institute of Technology, Czechia; *L. Fischer, H. Detz, W. Schrenk, G. Strasser, S. Buehler-Paschen, A. Andrews,* Technische Universität Wien, Austria

**QME-SaP-13** Growth and Angle-Resolved Photoemission of Strain-and Thickness-Tuned α-Sn Films, ***Aaron Engel***, *C. Dempsey, H. Inbar, S. Nishihaya, Y. Chang,* University of California, Santa Barbara; *A. Fedorov,* Advanced Light Source, Lawrence Berkeley National Laboratory; *M. Hashimoto, D. Lu,* SLAC National Accelerator Laboratory; *P. Taylor, P. Folkes,* US Army Research Laboratory; *C. Palmstrøm,* University of California, Santa Barbara

**QME-SaP-14** Electrostatic Gating of $SrSnO_3$ Thin Films with Improved Mobilities, ***Zhifei Yang***, *F. Liu, T. Truttmann, B. Jalan,* University of Minnesota, USA

**QME-SaP-15** Epitaxial Growth and Transport Properties of Square-Net Rare Earth Telluride Thin Films, ***Adrian Llanos***, *J. Falson,* California Institute of Technology

**QME-SaP-16** Improving MBE $(Bi,Sb)_2(Te,Se)_3$ Topological Materials Via Resonant and Magnetic Dopants, ***Patrick Taylor***, Army Research Laboratory

**QME-SaP-17** Growth of $Cd_3As_2$ on GaAs(001), GaAs(110), and Si(001) Substrates, ***Anthony Rice***, *I. Leahy, A. Norman, K. Alberi,* National Renewable Energy Laboratory

**QME-SaP-18** Molecular Beam Epitaxy of Superconducting ZrN Thin Films on GaN Substrates, ***Kevin D. Vallejo***, *D. Hurley, K. Gofryk, B. May,* Idaho National Laboratory

**QME-SaP-19** Quasi Van Der Waals Epitaxy of Magnetic Topological Insulators on a Gaas (111) Substrate, ***Yuxing Ren***, University of California at Los Angeles; *L. Tai,* 404 Westwood Plaza, Engineering VI, 310; *K. Pan, S. Srivastava, Y. Xie, M. Goorsky, K. Wang,* University of California at Los Angeles

**QME-SaP-20** Transforming Rotating RHEED Data for Post-Growth Characterization Using Automated Machine Learning, ***Chris Price***, Atomic Data Sciences

# Sunday Morning, September 17, 2023

| | Room Ballroom A | |
|---|---|---|
| 8:30am | **INVITED: QME-SuM1-3** Design of Quantum Oxide Heterostructures, ***Nini Pryds,*** Technical University of Denmark | **Workshop on Quantum Materials Epitaxy**<br>**Session QME-SuM1**<br>**Oxides II**<br>**Moderator:**<br>**Julia Mundy**, Harvard University |
| 8:45am | | |
| 9:00am | **INVITED: QME-SuM1-5** Interfacial Phenomena in 4d and 5d Transition Metal Oxides Grown by Metal-organic MBE, ***Ryan Comes,*** Auburn University | |
| 9:15am | | |
| 9:30am | **INVITED: QME-SuM1-7** Investigating the Electronic Structure of Coupled Electric Fields at the Surface and Buried Interface of an Epitaxial Complex Oxide/Group IV Semiconductor Heterostructure, ***Scott Chambers,*** Pacific Northwest National Laboratory; *J. Ngai,* University of Texas at Arlington; *P. Sushko,* Pacific Northwest National Laboratory; *E. Ramirez,* University of Texas at Arlington; *T. Lee, D. Biswas,* Diamond Light Source, UK | |
| 9:45am | | |
| 10:00am | **BREAK** | |
| 10:15am | | |
| 10:30am | **INVITED: QME-SuM2-11** Molecular Beam Epitaxy of Topological Semimetal Heterostructures, ***Nitin Samarth,*** Penn State University | **Workshop on Quantum Materials Epitaxy**<br>**Session QME-SuM2**<br>**Topological and Magnetic Materials II**<br>**Moderator:**<br>**Chris Palmstrøm**, University of California, Santa Barbara |
| 10:45am | | |
| 11:00am | **INVITED: QME-SuM2-13** Controlling Magnetism in Layered Quantum Materials Through Designer Defects, ***Matthew Brahlek,*** Oak Ridge National Laboratory | |
| 11:15am | | |
| 11:30am | **INVITED: QME-SuM2-15** Epitaxy of Rare Earth Compounds on Atomically Flat Surfaces, ***Joseph Falson,*** Caltech | |
| 11:45am | | |
| 12:00pm | **INVITED: QME-SuM2-17** Reactive Force Field Simulations as Versatile Tool to Explore the Growth Kinetics in Molecular Beam Epitaxy of Quantum Materials at the Atomic Scale, ***Roman Engel-Herbert,*** Paul Drude Institute, Germany | |
| 12:15pm | | |

# Monday Morning, September 18, 2023

| | Room Ballroom A | |
|---|---|---|
| 7:45am | **Welcome and Sponsor Thank Yous** | **Novel Materials**<br>**Session NM-MoM1**<br>**Oxide Semiconductors**<br>**Moderator:**<br>**Bharat Jalan**, University of Minnesota |
| 8:00am | **INVITED: NM-MoM1-2** Art Gossard MBE Innovator Awardee Talk: Setting a New Quality Standard for Both Holes and Electrons in GaAs Ultra-High Mobility Quantum Wells, ***Loren N. Pfeiffer,*** Princeton University | |
| 8:15am | | |
| 8:30am | **NM-MoM1-4** Silicon-doped $\beta$-$Ga_2O_3$ Films Grown at 1 µm/h by Suboxide Molecular-Beam Epitaxy, ***Kathy Azizie****, F. Hensling, C. Gorsak,* Cornell University*; Y. Kim,* Air Force Research Laboratory*; N. Pieczulewski,* Cornell University*; D. Dryden,* Air Force Research Laboratory*; M. Senevirathna, S. Coye,* Clark Atlanta University*; S. Shang,* Penn State University*; J. Steele, P. Vogt, N. Parker, Y. Birkhölzer,* Cornell University*; Z. Liu,* Penn State University*; M. Williams,* Clark Atlanta University*; K. Chabak,* Air Force Research Laboratory*; D. Muller,* Cornell University*; A. Neal, S. Mou,* Air Force Research Laboratory*; D. Schlom,* Cornell University | |
| 8:45am | **NM-MoM1-5** Improving Si Dopant Control in n-type $\beta$-Gallium Oxide, ***Brenton Noesges****, Y. Kim, A. Neal, S. Mou, T. Asel,* Air Force Research Laboratory, Materials and Manufacturing Directorate, USA | |
| 9:00am | **NM-MoM1-6** The Effect of Gallium Beam Flux on Electron Transoport in $\beta$-$Ga_2O_3$ Grown via Plasma Assisted Molecular Beam Epitaxy, ***Thaddeus Asel****, B. Noesges, Y. Kim, A. Neal, S. Mou,* Air Force Research Laboratory, Materials and Manufacturing Directorate | |
| 9:15am | **NM-MoM1-7** Growth of $\alpha$-$(Al_xGa_{1-x})_2O_3$ by Suboxide Molecular-Beam Epitaxy, ***Jacob Steele****, K. Azizie, N. Pieczulewski, J. McCandless,* Cornell University*; I. Matara Kankanamge, M. D. Williams,* Clark Atlanta University*; H. Xing, D. Jena, D. Muller,* Cornell University*; T. Onuma,* Kogakuin University, Japan*; D. Schlom,* Cornell University (USA) and Leibniz-Institut für Kristallzüchtung (Germany) | |
| 9:30am | **NM-MoM1-8** Electrostatic Gating of $SrSnO_3$ Thin Films with Improved Mobilities, ***Zhifei Yang****, F. Liu, T. Truttmann, B. Jalan,* University of Minnesota, USA | |
| 9:45am | **BREAK & EXHIBITS** | |
| 10:00am | | |
| 10:15am | **NM-MoM2-11** Molecular Beam Epitaxy of Binary and Ternary Manganese and Chromium Nitrides, *K. Vallejo, K. Gofryk,* Idaho National Laboratory*; S. Gutierrez-Ojeda,* Universidad Nacional Autónoma de México*; G. Cocoletzi,* Benemérita Universidad Autónoma de Puebla, Mexico*;* ***Brelon May****,* Idaho National Laboratory | **Novel Materials**<br>**Session NM-MoM2**<br>**Nitrides**<br>**Moderator:**<br>**Lutz Geelhaar**, Paul-Drude-Institut für Festkörperelektronik Leibniz-Institut im Forschungsverbund Berlin, Germany |
| 10:30am | **NM-MoM2-12** Achieving Atomically Ordered GaN/AlN Quantum Heterostructures: The Role of Surface Polarity, ***Yuanpeng Wu****, P. Zhou, Y. Xiao, K. Sun, D. Wang, P. Wang, Z. Mi,* University of Michigan, Ann Arbor | |
| 10:45am | **NM-MoM2-13** Epitaxial Cubic Boron Nitride Grown by Ion Beam-Assisted Molecular-Beam Epitaxy on Diamond, ***David Storm****, S. Maximenko, A. Lang, N. Nepal, T. Feygelson, B. Pate, D. Meyer,* US Naval Research Laboratory | |
| 11:00am | **NM-MoM2-14** Optical Properties of ScN Layers Grown on Sapphire Using Plasma-Assisted Molecular Beam Epitaxy, ***Duc V. Dinh****,* Paul-Drude-Institut für Festkörperelektronik, Leibniz-Institut im Forschungsverbund Berlin e.V., Germany*; F. Peiris,* Kenyon College*; J. Lähnemann, O. Brandt,* Paul-Drude-Institut für Festkörperelektronik, Leibniz-Institut im Forschungsverbund Berlin e.V., Germany | |
| 11:15am | **NM-MoM2-15** Epitaxial Growth of High ScN Fraction ScAlN on NbN and SiC, ***Matthew Hardy****, A. Lang, E. Jin, N. Nepal, B. Downey, V. Gokhale, S. Katzer, V. Wheeler,* U.S. Naval Research Laboratory | |
| 11:30am | **NM-MoM2-16** High Efficiency Micrometer Scale Green and Red Light Emitting Diodes, ***Yixin Xiao****, R. Maddaka, Y. Wu, Y. Malholtra, Y. Guo, S. Yang, J. Liu, K. Sun, A. Pandey, J. Min, Z. Mi,* University of Michigan | |
| 11:45am | **NM-MoM2-17** AlN/AlGaN Short Period Superlattices With Sub 2 nm Layers Grown by MME, ***Alexander Chaney****,* Azimuth Corporation*; C. Bowers, K. Mahalingam,* UES INC*; S. Mou, K. Averett, T. Asel,* Air Force Research Laboratory, Materials and Manufacturing Directorate, USA | |

# Monday Afternoon, September 18, 2023

| | Room Ballroom A | |
|---|---|---|
| 1:30pm | **GD-MoA1-1** Separate Absorption, Charge, and Multiplication Avalanche Photodiodes With InGaAs/GaAsSb Type-II Superlattices Grown by Molecular Beam Epitaxy, ***Hyemin Jung***, *S. Lee,* The Ohio State University; *X. Jin, Y. Liu,* University of Sheffield, UK; *T. Ronningen,* The ohio state university; *C. Grein,* University of Illinois at Chicago; *J. David,* University of Sheffield, UK; *S. Krishna,* The Ohio State University | **MBE-Grown Devices**<br>**Session GD-MoA1**<br>**Photonic Devices**<br>**Moderator:**<br>**Minjoo Larry Lee**, University of Illinois Urbana-Champaign |
| 1:45pm | **GD-MoA1-2** Growth of MWIR ICLEDs on Silicon using Molecular Beam Epitaxy, ***Mega Frost***, *T. Rotter, F. Ince, G. Balakrishnan,* University of New Mexico; *M. McCartney, D. Smith,* Arizona State University; *C. Canedy, W. Bewley, S. Tomasulo, C. Kim,* U.S. Naval Research Laboratory; *M. Kim,* Jacobs Corporation; *I. Vurgaftman, J. Meyer,* U.S. Naval Research Laboratory | |
| 2:00pm | **GD-MoA1-3** Monlithic Integration of InAs Quantum Dot Lasers with Silicon Photonic Waveguides, ***Alec Skipper***, *K. Feng,* University of California Santa Barbara; *G. Leake, J. Herman,* SUNY POLY, Albany; *C. Shang, R. Koscica,* University of California Santa Barbara; *D. Harame,* SUNY POLY, Albany; *J. Bowers,* University of California Santa Barbara | |
| 2:15pm | **GD-MoA1-4** Reducing Threading Dislocation Density of Pocket-Grown InAs Quantum Dot Lasers on Patterned $SiO_2$/Si, ***Rosalyn Koscica***, *C. Shang, K. Feng, J. Bowers,* University of California Santa Barbara | |
| 2:30pm | **GD-MoA1-5** MBE Growth of Near-Infrared Heterojunction Phototransistors and Visible LEDs for Night Vision Applications, ***David Montealegre***, University of Illinois at Urbana Champaign; *Y. Song,* Yale University; *S. Lee,* University of Washington; *B. Kim, M. Kim,* University of Illinois at Urbana Champaign; *F. Xia,* Yale University; *M. Li, A. Majumdar,* University of Washington; *M. Lee,* University of Illinois at Urbana Champaign | |
| 2:45pm | **GD-MoA1-6** Optically-Addressed Monolithically-Integrated Multi-band Photodetectors Using Type-II Superlattice Materials, ***Zheng Ju***, *X. Qi, A. McMinn, Y. Zhang,* Arizona State University | |
| 3:00pm | **BREAK & EXHIBITS** | |
| 3:15pm | | |
| 3:30pm | **NM-MoA2-9** Atomic Scale Modeling of the Hybrid Molecular Beam Epitaxy Growth Process Using Reactive Force Field Simulations, *B. Yalcin, D. Yilmaz, A. van Duin,* Pennsylvania State University; ***Roman Engel-Herbert***, Pennsylvania State University, USA, Paul-Drude-Institute for Solid State Electronics, Berlin, Germany | **Novel Materials**<br>**Session NM-MoA2**<br>**Strong Spin-Orbit Oxides**<br>**Moderator:**<br>**Ryan Comes**, Auburn University |
| 3:45pm | **NM-MoA2-10** Engineering Metal Oxidation Towards Epitaxial Growth of Complex Iridates using Molecular Beam Epitaxy, ***Sreejith Nair***, *Z. Yang, D. Lee, S. Guo,* University of Minnesota, USA; *J. Sadowski,* Brookhaven National Laboratory; *S. Johnson,* Auburn University; *A. Saboor,* University of Delaware; *Y. Li, H. Zhou,* Argonne National Laboratory; *R. Comes, W. Jin,* Auburn University; *K. Mkhoyan,* University of Minnesota, USA; *A. Janotti,* University of Delaware; *B. Jalan,* University of Minnesota, USA | |
| 4:00pm | **NM-MoA2-11** Solid Source Metal-Organic Molecular Beam Epitaxy for Epitaxial $SrRuO_3$ Films, ***Anusha Kamath Manjeshwar***, *S. Nair, A. Rajapitamahuni, R. James, B. Jalan,* University of Minnesota | |
| 4:15pm | **NM-MoA2-12** Growth of Ruddlesden-Popper Ruthenates via Thermal Laser Epitaxy, ***Brendan D. Faeth***, *F. Hensling, V. Harbola, L. Majer,* Max Planck Institute for Solid State Research, Germany; *H. Boschker,* Epiray GMBH, Germany; *W. Braun, J. Mannhart,* Max Planck Institute for Solid State Research, Germany | |
| 4:30pm | **NM-MoA2-13** Growing Clean Crystals from "Dirty" Precursors in MBE, ***Rashmi Choudhary***, University of Minnesota, USA; *Z. Liu, J. Cai, X. Xu, J. Chu,* University of Washington; *B. Jalan,* University of Minnesota, USA | |
| 4:45pm | **NM-MoA2-14** MBE Growth of $BaCo_2Ru_4O_{11}$: A Metallic Ferromagnetic Hexaferrite, ***Yilin Evan Li***, Department of Materials Science and Engineering, Cornell University; *M. Brützam,* Leibniz-Institut für Kristallzüchtung, Germany; *R. Cava,* Department of Chemistry, Princeton University; *C. Guguschev,* Leibniz-Institut für Kristallzüchtung, Germany; *D. Schlom,* Department of Materials Science and Engineering, Cornell University | |
| 5:00pm | **NM-MoA2-15** Hybrid Molecular Beam Epitaxy of $SrIrO_3$ Films and Heterostructures, ***Gaurab Rimal***, *T. Tasnim, J. Ahammad,* Auburn University; *G. Sterbinsky,* Argonne National Lab; *J. Sadowski,* Brookhaven National Laboratory; *M. Boebinger,* Oak Ridge National Laboratory; *R. Comes,* Auburn University | |

## MBE-Grown Devices
## Room Hall of Ideas E-J - Session GD-MoP
## MBE-Grown Devices Poster Session
## 5:15 – 7:00 pm

**GD-MoP-2** Parity-Time Symmetry Single-Mode Double-Microdisk InGaAs Quantum Dot Lasers, *K. Lin, C. Xu,* ***Tsong-Sheng Lay,*** National Chung Hsing University, Taiwan

**GD-MoP-3** Impact Ionization Coefficients of AlxGa1-xAsSb ($x$=0 – 1) Lattice Matched to InP Substrates, ***Seunghyun Lee,*** The Ohio State University*; X. Jin,* University of Sheffield, UK*; H. Jung,* The Ohio State University*; J. David,* University of Sheffield, UK*; S. Krishna,* The Ohio State University

**GD-MoP-4** Superconducting Germanium for Scalable Qubit Architectures, ***Patrick Strohbeen,*** *A. Brook, J. Shabani,* Center for Quantum Information Physics, New York University

**GD-MoP-5** Epitaxial Growth of High-Quality Aluminum Thin Films via Mbe for the Experimental Realization of Majorana Bound States, *A. Elbaroudy, B. Khromets, E. Bergeron, T. Blaikie, Y. Shi, A. Tam, S. Sadeghi, F. Sfigakis,* ***Zbig Wasilewski,*** *J. Baugh,* University of Waterloo, Canada

**GD-MoP-6** Submicron-Scale Light Emitting Diode with Efficient and Robust Red Emission, ***Yixin Xiao,*** *R. Maddakka,* University of Michigan, Ann Arbor

**GD-MoP-7** Impact of Built-in Electric Field Direction on Performance of GaN-Based Laser Diodes, ***Henryk Turski,*** Institute of High Pressure Physics PAS, Poland*; L. van Deurzen,* Cornell University*; M. Hajdel, M. Chlipala, M. Zak, G. Muziol, C. Skierbiszewski,* Institute of High Pressure Physics PAS, Poland

**GD-MoP-8** Demonstration of a 4.32 µm Cutoff InAsSbBi nBn Photodetector, a Lattice-matched Random Alloy III-V Solution for Mid-wave Infrared Sensing, ***Preston T. Webster,*** *J. Logan, L. Helms, P. Grant, C. Hains, R. Carrasco, A. Newell,* Air Force Research Laboratory, Space Vehicles Directorate*; M. Milosavljevic, S. Johnson,* Arizona State University*; G. Balakrishnan,* University of New Mexico*; D. Maestas, C. Morath,* Air Force Research Laboratory, Space Vehicles Directorate

**GD-MoP-11** Zeeman Field-Induced Two-Dimensional Weyl Semimetal Phase in Cadmium Arsenide Thin Films, ***Binghao Guo,*** *W. Miao, V. Huang, A. Lygo,* University of California, Santa Barbara*; X. Dai,* University of Science and Technology, Hong Kong, China*; S. Stemmer,* University of California, Santa Barbara

**GD-MoP-12** MBE Grown InAs/GaAs Quantum Dot Columns as a Buffer Layer for Spatial and Spectral Homogeneity, ***Nazifa Tasnim Arony,*** *L. McCabe, J. Zide,* University of Delaware

## Novel Materials
## Room Hall of Ideas E-J - Session NM-MoP
## Novel Materials Poster Session
## 5:15 – 7:00 pm

**NM-MoP-1** A Study of the Effect of Substrate Misorientation on the Strain Relaxation of InSb Grown on GaAs (001), ***Trevor Blaikie,*** *M. Tam, Y. Shi,* University of Waterloo, Canada*; A. Rahemtulla, N. Appathurai, B. Moreno,* Canadian Light Source, Inc., Canada*; Z. Wasilewski,* University of Waterloo, Canada

**NM-MoP-2** 2DEG Transport at the Interface of $SrNbO_3/BaSnO_3$, ***Brian Opatosky,*** *S. Thapa, T. Tasnim, G. Rimal, P. Gemperline,* Auburn University*; S. Mahatara,* New Mexico State University*; H. Paik,* University of Oklahoma*; R. Vukelich, M. Giri, D. Hilton,* Baylor University*; B. Kiefer,* New Mexico State University*; R. Comes,* Auburn University

**NM-MoP-3** $SrIrO_3$ Films and Heterostructures Grown by Hybrid Molecular Beam Epitaxy, ***Tanzila Tasnim,*** Auburn University, Bangladesh*; G. Rimal, B. Opatosky,* Auburn University*; G. Sterbinsky,* Argonne National Laboratory*; M. Boebinger,* Oak Ridge Natinal Laboratory*; R. Comes,* Auburn University

**NM-MoP-4** Characterization of MBE Grown $Fe_{0.75}Co_{0.25}$ in Composite Multiferroics, ***Katherine Robinson,*** Ohio State University*; M. Newburger, M. Page,* Air Force Research Laboratory*; R. Kawakami,* Ohio State University

**NM-MoP-5** Multicolor Micrometer Scale Light Emitting Diodes Monolithically Grown on the Same Chip, ***Yifu Guo,*** *Y. Xiao, Y. Malholtra, Y. Wu, S. Yang, J. Liu, A. Pandey, Z. Mi,* University of Michigan

**NM-MoP-6** Bismuth Surfactant Enhancement of Surface Morphology and Film Quality of Low-Temperature Grown GasB, ***Pan Menasuta,*** *K. Grossklaus, J. McElearney, T. Vandervelde,* Tufts University

**NM-MoP-7** Study the Temperature Effect on the Stability and Performance of III-Nitride HEMT Based Magnetic Fields Sensors , ***Satish Shetty,*** Institute for Nanoscience and Engineering, University of Arkansas*; A. Kuchuk,* 1Institute for Nanoscience and Engineering, University of Arkansas*; H. Mantooth,* Department of Electrical Engineering, University of Arkansas*; G. Salamo,* Institute for Nanoscience and Engineering, University of Arkansas

**NM-MoP-8** Optimization of Heteroepitaxial $ZnGeN_2$/GaN Quantum Wells for Green LEDs, *M. Miller,* Colorado School of Mines*; A. Rice,* National Renewable Energy Laboratory*; D. Diercks,* Colorado School of Mines*; A. Tamboli,* ***Brooks Tellekamp,*** National Renewable Energy Laboratory

**NM-MoP-9** Machine Learning Analysis and Predictions of PAMBE III–Nitride Growth, ***Andrew Messecar,*** *S. Durbin, R. Makin,* Western Michigan University

**NM-MoP-10** Tuning the Emission Wavelength by Varying the Sb Composition in InGaAs/GaAsSb W-quantum Wells Grown on GaAs(001) Substrates, *. Zon, S. Voranthamrong,* Department of Electrical Engineering, National Chung Hsing University, Taichung, Taiwan*; C. Cheng,* Department of Physics, National Central University, Chung-Li, Taiwan*; Z. Lee, T. Lo, C. Liu,* Department of Electrical Engineering, National Chung Hsing University, Taichung, Taiwan*; C. Chiang, L. Hung, M. Hsu,* Epileds Co., Ltd., Tainan, Taiwan*; W. Liu,* Department of Electrical Engineering, Yuan Ze University, Chung-Li, Taiwan*; J. Chyi,* Department of Electrical Engineering, National Central University, Chung-Li, Taiwan*;* ***Charles Tu,*** Department of Electrical Engineering, National Chung Hsing University, Taichung, Taiwan

**NM-MoP-11** Strong Correlation in Two-Dimensional 1T- $NbSe_2$, ***Joy Hsu,*** *R. Birchmier, M. Altvater, V. Madhavan,* University of Illinois at Urbana-Champaign

**NM-MoP-12** Growth of Cobalt-containing Compounds for Back-End-of-Line Interconnects, ***Yansong Li,*** *G. Zhou, C. Hinkle,* University of Notre Dame

**NM-MoP-13** Development of $Al_xGa_{1-x}as_{1-y}Bi_y$ for the Next Generation of APDs, ***Matthew Carr,*** *N. Bailey,* University of Sheffield, UK*; M. Sharpe, J. England,* University of Surrey, UK*; R. Richards, J. David,* University of Sheffield, UK

**NM-MoP-15** Epitaxial Growth of *a*-plane $Mn_3Sn$ on *c*-plane $Al_2O_3$ using Molecular Beam Epitaxy, ***Sneha Upadhyay,*** *T. Erickson,* Ohio University*; J. Moreno,* Universidad Autonoma de Puebla, Mexico*; H. Hall,* Ohio University*; K. Sun,* University of Michigan, Ann Arbor*; G. Cocoletzi,* Universidad Autonoma de Puebla, Instituto de fisica, Mexico*; N. Takeuchi,* Centro de Nanociencias y Nanotecnología, Universidad Nacional Autonoma de México*; A. Smith,* Ohio University

**NM-MoP-16** Surfactant Effect of Mn on AlN MBE Growth, ***Jesús Fernando Fabian Jocobi,*** *R. Trejo Hernández, A. Martínez López,* Nanoscience and Nanotechnology Program, Center for Research and Advanced Studies of the National Polytechnic Institute (CINVESTAV), Mexico*; Y. Casallas Moreno,* CONACYT-Interdisciplinary Professional Unit in Engineering and Advanced Technologies, National Polytechnic Institute, Mexico*; I. Koudriavysev,* Electrical Engineering Department, Solid State Electronic Section, Center for Research and Advanced Studies of the National Polytechnic Institute (CINVESTAV), Mexico*; D. Olguin Melo,* Center for Research and Advanced Studies of the National Polytechnic Institute Querétaro Unit, Mexico*; S. Gallardo Hernández, M. López López,* Physics Department, Center for Research and Advanced Studies of the National Polytechnic Institute (CINVESTAV), Mexico

**NM-MoP-17** Growth and Scattering Mechanisms of Metamorphic $In_{0.81}Ga_{0.19}As$ Quantum Wells, ***Jason Dong,*** University of California at Santa Barbara*; Y. Gul,* University College London, UK*; A. Engel, C. Dempsey, S. Chatterjee,* University of California at Santa Barbara*; M. Pepper,* University College London, UK*; C. Palmstrøm,* University of California at Santa Barbara

**NM-MoP-19** Light-enhanced Gating Effect at Conducting Interface of Laser MBE Grown EuO-$KTO_3$, ***Manish Dumen,*** *S. Chakraverty,* Institute of Nano Science and Technology, India

**NM-MoP-20** 4.3 µm InAs/AlSb Quantum Cascade Detector Strain-Balanced to a GaSb Substrate, ***Stefania Isceri,*** *M. Giparakis, W. Schrenk, B. Schwarz, G. Strasser, A. Andrews,* Technische Universität Wien, Austria

**NM-MoP-21** Growth and Surface Investigation of Antiferromagnetic $D0_{19}$ – $Mn_3Ga$ Thin Films on GaN (0001), ***Ashok Shrestha,*** *A. Abbas, D. Ingram, A. Smith,* Ohio University

**NM-MoP-22** Guided Anisotropic Oxygen Transport in Vacancy Ordered Oxides, ***Jeffrey Dhas,*** *Y. Du,* Pacific Northwest National Laboratory

**NM-MoP-23** Impact of Unintentional Sb in the Tensile Electron Well of Type-II InAs/InAsSb Superlattices Grown on GaSb by Molecular Beam Epitaxy, ***Marko Milosavljevic,*** Arizona State University*; P. Webster,* Air Force Research Laboratory*; S. Johnson,* Arizona State University

**NM-MoP-24** Local Droplet Etching and Filling Behavior of Nanoholes in $In_{0.52}Al_{0.48}As$ Layers, ***Dennis Deutsch,*** *V. Zolatanosha, C. Buchholz, K. Jöns, D. Reuter,* Paderborn University, Germany

**NM-MoP-25** Heteroepitaxial growth of (111)-oriented $SrTiO_3$ on ScAlN/GaN, *E. Jin, A. Lang, B. Downey, V. Gokhale,* ***Matthew Hardy,*** *N. Nepal, S. Katzer, V. Wheeler,* Naval Research Laboratory

**NM-MoP-26** Strain-Mediated Sn Incorporation and Segregation in Compositionally Graded $Ge_{1-x}Sn_x$ Epilayers Grown by MBE at Different Temperature, ***Nirosh M Eldose****, H. Stanchu, S. Das, S. Shetty, C. Li, Y. I Mazur, S. Yu, G. J. Salamo,* University of Arkansas

**NM-MoP-27** Growth and Characterization of GaAs (111) on 4H-SiC for Infrared Sensor, ***Subhashis Das****, N. M Eldose, H. Stanchu, F. Maia de Oliveira, C. Li, M. Benamara, Y. I. Mazur, G. Salamo,* University of Arkansas

**NM-MoP-28** Growth and Conductivity Control of AlN by Plasma Assisted MBE, ***Neeraj Nepal****, M. Hardy, B. Downey, A. Lang, D. Katzer, E. Jin, D. Storm, V. Gokhale, T. Growden, D. Meyer, V. Wheeler,* U.S. Naval Research Laboratory

**NM-MoP-29** Molecular Beam Epitaxy Grown Group-IV Alloys for Infrared Photodetector and Quantum Transport Applications, ***Tyler McCarthy****,* Arizona State University*; R. Basnet,* University of Arkansas*; Z. Ju, X. Qi, A. McMinn,* Arizona State University*; J. Hu, S. Yu,* University of Arkansas*; Y. Zhang,* Arizona State University

**NM-MoP-30** Transport of Rare-Earth Nitrides Deposited via Molecular Beam Epitaxy, ***Kevin Vallejo****, Z. Hua, Y. Zhang, K. Gofryk, B. May,* Idaho National Laboratory

**NM-MoP-31** High Al-Content AlGaN Grown on TaC Virtual Substrates with Metallic Conductivity, ***M. Brooks Tellekamp****, D. Roberts,* National Renewable Energy Laboratory*; M. Miller,* Colorado School of Mines*; A. Rice,* National Renewable Energy Laboratory*; J. Hachtel,* Oak Ridge National Laboratory*; N. Haegel,* National Renewable Energy Laboratory

**NM-MoP-32** Grafted AlGaAs/GeSn p-i-n Heterojunction for GeSn MIR Electrically Pumped Laser Application, ***Yang Liu****, J. Zhou, D. Vincent, J. Gong, S. Haessly, Y. Li, Q. Zhang,* University of Wisconsin - Madison*; S. Yu,* University of Arkansas*; Z. Ma,* University of Wisconsin - Madison

**NM-MoP-34** Molecular Beam Epitaxy of Kagome-Structured Antiferromagnetic FeSn Grown on $LaAlO_3$ (111), ***Tyler Erickson****, S. Upadhyay, H. Hall, D. Ingram, S. Kaya, A. Smith,* Ohio University

**NM-MoP-35** Tuning Interface Sharpness and Superconductivity at Oxide Heterostructures, ***Y. Eren Suyolcu****,* Max Planck Institute for Solid State Research, Germany*; G. Kim,* Max Planck Institute for Solid State Research*; Y. Wu, G. Logvenov, P. van Aken,* Max Planck Institute for Solid State Research, Germany

**NM-MoP-37** Molecular Beam Epitaxial Growth of GaInAs, GaNAs and GaInNAs Nanowires over 2-inch Si(111) Substrate Showing Emission at Near Infrared Regime, ***Keisuke Minehisa****, H. Hashimoto, K. Nakama, F. Ishikawa,* Hokkaido University, Japan

**NM-MoP-38** Tunable Superconductivity in Hybrid Interface $FeTe_{1-x}Se_x/Bi_2Te_3$ Grown by Molecular Beam Epitaxy, ***An-Hsi (Jane) Chen****,* Oak Ridge National Laboratory, USA*; Q. Lu, R. Moore, M. Brahlek,* Oak Ridge National Laboratory

**NM-MoP-39** Van Der Waals Epitaxy of 2D Ferromagnetic $Fe_{5-x}GeTe_2$ Films with Curie Temperature Above Room Temperature on Graphene, ***Joao Marcelo J. Lopes****, H. Lv, A. Kassa, A. da Silva, J. Herfort, M. Hanke, A. Trampert, R. Engel-Herbert, M. Ramsteiner,* Paul-Drude-Institut für Festkörperelektronik, Leibniz-Institut im Forschungsverbund Berlin, Germany

**NM-MoP-40** Molecular Beam Epitaxy of $MnBi_2Te_4$ and $Bi_2Te_3$/ $MnBi_2Te_4$ Heterostructures, ***Hyunsue Kim****,* University of Texas at Austin*; M. Liu,* Harvard University*; L. Frammolino, Y. Li, F. Zhang,* University of Texas at Austin*; W. Lee,* University of Chicago*; X. Li, A. MacDonald, C. Shih,* University of Texas at Austin

**NM-MoP-41** Effect of Spin-Orbit Field on the Magnetization Reversal in a Crystalline (Ga,Mn)(As,P) Ferromagnetic Layer, ***Seongjin Park****, K. Lee, S. Lee,* Korea University, Republic of Korea*; X. Liu,* Unversity of Notre Dame*; M. Dobrowolska, J. Furdyna,* University of Notre Dame

**NM-MoP-42** Unraveling the Role of Dopant Clustering in Magnetic Impurity Doped Monolayers of Transition Metal Dichalcogenides, ***Rehan Younas****, G. Zhou, C. Hinkle,* University of Notre Dame

**NM-MoP-43** Atomic Layer Molecular Beam Epitaxy Growth of Kagome Ferrimagnet $RMn_6Sn_6$ (R = Rare Earth) Thin Films, ***Shuyu Cheng****, W. Zhou, R. Kawakami,* Ohio State University

**NM-MoP-44** Investigating Phase Transformations and Stability of Pt-Te Van Der Waals Materials Through Pt Vapor Exposure and Post-Growth Annealing, ***Kinga Lasek****,* Purdue University; University of South Florida

**NM-MoP-45** Layer-Dependent Optical Properties of MBE-Grown $ZrTe_2$ Determined by in-Situ Spectroscopic Ellipsometry, *E. Houser,* ***Frank Peiris****,* Kenyon College*; A. Richardella, M. Stanley, N. Samarth,* Pennsylvania State University

**NM-MoP-46** Bi Heteroantisites at Ga(As,Bi)/(Al,Ga)As Interface: Role of the Surface Reconstruction?, ***Esperanza Luna****, A. da Silva, K. Biermann,* Paul-Drude-Institut für Festkörperelektronik, Leibniz-Institut im Forschungsverbund Berlin e.V., Germany*; J. Puustinen, J. Hilska, M. Guina,* Optoelectronics Research Centre, Tampere University, Finland*; P. Laukkanen, M. Punkkinen,* University of Turku, Finland*; A. Trampert,* Paul-Drude-Institut für Festkörperelektronik, Leibniz-Institut im Forschungsverbund Berlin e.V., Germany

**NM-MoP-47** Substrate Preparation Methods for the MBE Growth of Van Der Waals Materials, ***Ryan Trice****, M. Yu, A. Richardella, M. Hilse, S. Law,* Penn State University

**NM-MoP-49** Comparison of the Optoelectronic Properties of InGaAs and GaAsSb Absorbers on InP for 1.55 µm Avalanche Photodiodes, ***Nathan Gajowski****,* The Ohio State University*; P. Webster,* Air Force Research Lab*; S. Lee,* The Ohio State University*; P. Grant,* Air Force Research Lab*; S. Krishna,* The Ohio State University

**NM-MoP-50** Transmission Electron Microscopy Studies of the Formation of $In_2Se_3$ Layers via Selenium Passivation of InP(111)B Substrates, ***Kaushini Wickramasinghe****, C. Forrester,* City College of New York, City University of New York*; M. McCartney, D. Smith,* Arizona State University*; M. Tamargo,* City College of New York, City University of New York

## Science and Technology of MBE
## Room Hall of Ideas E-J - Session ST-MoP
## Science and Technology of MBE Poster Session
## 5:15 – 7:00 pm

**ST-MoP-1** Shadow Mask Molecular Beam Epitaxy, ***Shagorika Mukherjee****, S. Sitaram, X. Wang,* University of Delaware*; S. Law,* Penn State University

**ST-MoP-2** Strain Relaxation of Graded InGaN and AlGaN, ***Reem Alhelais****, F. Mais de Oliveira, H. Stanchu, M. Sarollahi, Y. Mazur, N. Al-Hosainy, M. Ware,* University of Arkansas

**ST-MoP-3** Improved N-Type Doping Activation in AlGaAs:Si Through Digital Alloy Growth, ***Xizheng Fang****, B. Kim, D. Montealegre, Y. Wang, A. Birge, M. Lee,* University of Illinois at Urbana Champaign

**ST-MoP-4** Metal Contact Etch Process Optimization of Metal Contact Etching in 3D Integration Devices, ***Sung Gyu Pyo****,* CAU, Republic of Korea

# Tuesday Morning, September 19, 2023

| | Room Ballroom A | |
|---|---|---|
| 7:45am | **Welcome and Sponsor Thank Yous** | **Novel Materials**<br>**Session NM-TuM1**<br>**Novel Materials, Optoelectronics**<br>**Moderator:**<br>**Jason Kawasaki**, University of Wisconsin - Madison |
| 8:00am | **INVITED: NM-TuM1-2** NAMBE Young Investigator Awardee Talk: Dislocation Dynamics in InGaSb Graded Buffers on GaSb Grown by MBE, ***Stephanie Tomasulo***, *M. Twigg, S. Maximenko, I. Vurgaftman, J. Nolde,* U.S. Naval Research Laboratory | |
| 8:15am | | |
| 8:30am | **NM-TuM1-4** Emergent Ferromagnetism in Altermagnetic Candidate MnTe Films Grown on InP (111), ***Matthew Brahlek***, Oak Ridge National Laboratory | |
| 8:45am | **NM-TuM1-5** Growth Parameters Impact on Electronic and Optical Properties of ErAs:InGaAlBiAs Materials, ***Wilder Acuna***, *W. Wu, J. Bork, M. Jungfleisch, L. Gundlach, J. Zide,* University of Delaware | |
| 9:00am | **NM-TuM1-6** Heteroepitaxial Growth of Site-determined Quantum Emitters in 2D GaSe Films, ***Mingyu Yu***, University of Delaware; *S. Law,* Pennsylvania State University | |
| 9:15am | **NM-TuM1-7** Evaluating (001) and (111)A InAs Quantum Emitters at Telecommunication Wavelengths Grown by Droplet Epitaxy, ***Margaret Stevens***, US Naval Research Laboratory; *W. McKenzie, G. Baumgartner,* Laboratory for Telecommunication Sciences; *J. Grim, A. Bracker,* US Naval Research Laboratory | |
| 9:30am | **NM-TuM1-8** Growth of InSb Quantum Well on InAs Using AlInSb Buffer Layer Assisted by Interfacial Misfit Dislocation Arrays, ***Fatih Furkan Ince***, *A. Newell, T. Rotter, G. Balakrishnan,* University of New Mexico; *M. McCartney, D. Smith,* Arizona State University | |
| 9:45am | **NM-TuM1-9** Molecular Beam Epitaxy of Kagome Antiferromagnetic $Mn_3GaN$ grown on MgO(001), ***Ali Abbas***, *A. Shrestha, A. Smith,* Ohio University | |
| 10:00am | **BREAK & EXHIBITS** | |
| 10:15am | | |
| 10:30am | **NM-Tu2-12** Doping the Undopable: Hybrid Molecular Beam Epitaxy Growth, n-type Doping, and Field-Effect Transistor using $CaSnO_3$, ***Fengdeng Liu***, University of Minnesota, USA; *P. Golani,* University of Minnesota; *T. Truttmann,* University of Minnesota, USA; *I. Evangelista,* University of Delaware; *M. Smeaton,* Cornell University; *D. Bugallo,* Drexel University; *J. Wen,* University of Minnesota; *A. Kamath Manjeshwar,* University of Minnesota, USA; *S. May,* Drexel University; *L. Kourkoutis,* Cornell University; *A. Janotti,* University of Delaware; *S. Koester,* University of Minnesota; *B. Jalan,* University of Minnesota, USA | **Novel Materials**<br>**Session NM-TuM2**<br>**Thin Film Membranes**<br>**Moderator:**<br>**Roman Engel-Herbert**, Paul Drude Institute, Germany |
| 10:45am | **NM-TuM2-13** Controlling the Balance between Remote, Pinhole, and van der Waals Epitaxy of Heusler Films on Graphene/Sapphire, ***Taehwan Jung***, *Z. LaDuca, D. Du, S. Manzo, K. Su, X. Zheng, V. Saraswat,* University of Wisconsin - Madison; *J. McChesney,* Argonne National Lab; *M. Arnold, J. Kawasaki,* University of Wisconsin - Madison | |
| 11:00am | **NM-TuM2-14** Synthesis of Flexomagnetic GdAuGe Membranes via Van Der Waals Epitaxy on Graphene Terminated Germanium, ***Zachary LaDuca***, *S. Manzo, T. Jung, T. Samanta, K. Su, M. Arnold, J. Kawasaki,* University of Wisconsin - Madison | |
| 11:15am | **NM-TuM2-15** Flexomagnetism and Strain Induced Superconductivity in Rippled GdAuGe Heusler Membranes, ***Tamalika Samanta***, *Z. LaDuca, D. Du, T. Jung, S. Manzo, K. Su, M. Arnold, J. Kawasaki,* University of Wisconsin - Madison | |
| 11:30am | **NM-TuM2-16** Growth Mechanism of $SrTiO_3$ on a Graphene-covered Substrate Using Hybrid MBE, ***Sooho Choo***, University of Minnesota, Republic of Korea; *H. Yoon,* University of Minnesota, USA, Republic of Korea; *B. Matthews,* Pacific Northwest National Laboratory; *S. Sharma,* University of Minnesota, USA; *S. Spurgeon, S. Chambers,* Pacific Northwest National Laboratory; *R. James, B. Jalan,* University of Minnesota, USA | |
| 11:45am | **NM-TuM2-17** Synthesis of Free-Standing Membranes Using a Sacrificial Layer Method Grown by Hybrid MBE, ***Shivasheesh Varshney***, *S. Choo, Z. Yang, J. Wen, S. Koester, B. Jalan,* University of Minnesota, USA | |

# Tuesday Afternoon, September 19, 2023

| | Room Ballroom A | |
|---|---|---|
| 1:30pm | **GD-TuA1-1** InSb-Based Dilute-Bismide Alloys Towards Long-Wave Infrared Sensing, ***Corey White***, *M. Bergthold, T. Leonard, A. Ricks, D. Wasserman, S. Bank,* The University of Texas at Austin | **MBE-Grown Devices**<br>**Session GD-TuA1**<br>**Solar Cell and Quantum Computing**<br>**Moderator:**<br>**Minjoo Larry Lee**, University of Illinois Urbana-Champaign |
| 1:45pm | **GD-TuA1-2** Abrupt Te Doping of MBE-Grown GaInP for Solar Cell Applications, ***Brian Li***, *Y. Sun, R. Hool, M. Lee,* University of Illinois, Urbana-Champaign | |
| 2:00pm | **GD-TuA1-3** MBE Growth of Metamorphic 1 eV InGaAs Solar Cells with Low Threading Dislocation Density, ***Adrian Birge***, *M. Kim, B. Kim, D. Montealegre, M. Lee,* University of Illinois at Urbana-Champaign, USA | |
| 2:15pm | **GD-TuA1-4** Strained Superlattice InAlGaAs/AlGaAs Spin-Polarized Photocathodes Implemented with Random and Digital Alloying, ***Aaron Engel***, University of California, Santa Barbara; *M. Stutzman,* Thomas Jefferson National Accelerator Facility; *J. Dong,* University of California, Santa Barbara; *C. Palmstrøm,* University of California, Santa Barabara | |
| 2:30pm | **GD-TuA1-5** Molecular Beam Epitaxy Growth and Characterization of InAs Quantum Wells Grown on Metamorphic III-V Buffer Layers, *I. Levy,* ***Patrick Strohbeen***, *W. Strickland, M. Hatefipour, J. Issokson, L. Baker,* New York University; *M. Mikalsen,* new york University; *S. Farzaneh*, *J. Shabani,* New York University | |
| 2:45pm | **GD-TuA1-6** Cryogenic Growth of Superconducting Thin Films on GaAs, Si, and Sapphire Substrates, ***Teun van Schijndel***, *A. Engel,* University of California Santa Barbara; *J. Dong,* University of California at Santa Barbara; *A. McFadden,* NIST-Boulder; *C. Palmstrøm,* University of California Santa Barbara | |
| 3:00pm | **BREAK & EXHIBITS** | |
| 3:15pm | | |
| 3:30pm | **NM-TuA2-9** $TaO_2$ - The New Kid on the 5*d* Block, ***Yorick Birkhölzer***, *A. Park, M. Barone, D. Schlom,* Cornell University | **Novel Materials**<br>**Session NM-TuA2**<br>**Novel Oxides and Superconductors**<br>**Moderator:**<br>**Matthew J. Brahlek**, Oak Ridge National Laboratory |
| 3:45pm | **NM-TuA2-10** Growth of $KTaO_3$, $KNbO_3$ and $KNb_xTa_{1-x}O_3$ solid solutions by Suboxide Molecular-Beam Epitaxy, ***Tobias Schwaigert***, Cornell University; *S. Hazra,* Penn State University; *S. Salmani-Razaie,* Cornell University; *T. Kuznetsova,* Penn State University; *S. Ganschow,* Leibniz-Institut für Kristallzüchtung, Germany; *H. Paik,* Oklahoma State University; *D. Muller,* Cornell University; *R. Engel-Herbet,* Paul Drude Institute, Germany; *V. Gopalan,* Penn State University; *D. Schlom,* Cornell University; *K. Ahadi,* North Carolina State University | |
| 4:00pm | **NM-TuA2-11** Studying Electronic Structures of Pure $SrCoO_x$ Thin Films, Ordered Phases, and Heterostructures, ***Jibril Ahammad***, *G. Rimal,* Auburn University; *J. Sadowski,* Brookhaven National Laboratory; *G. Sterbinsky,* Argonne National Laboratory; *M. Boebinger,* Oak Ridge National Laboratory; *R. Comes,* Auburn University | |
| 4:15pm | **NM-TuA2-12** Synthesizing Metastable Ruddlesden-Popper Titanates by Mbe in Pursuit of Next-Generation Millimeter-Wave Tunable Dielectrics, ***Matthew Barone***, Cornell University; *Z. Tian,* University of California at Berkeley; *M. Papac,* National Institute of Standards and Technology, Boulder; *B. Goodge, E. Fleck, G. Olsen,* Cornell University; *K. Lee,* Hongik University, Republic of Korea; *L. Kourkoutis,* Cornell University; *N. Orloff,* National Institute of Standards and Technology, Boulder; *L. Martin,* University of California at Berkeley; *D. Schlom,* Cornell University | |
| 4:30pm | **NM-TuA2-13** MBE Synthesis and UV Raman Characterization of hexagonal $ScFeO_3$ films, ***Nicholas Parker***, *D. Schlom,* Cornell University; *D. Tenne,* Boise State University; *M. Barone,* Cornell University | |
| 4:45pm | **NM-TuA2-14** Growth and Characterization of Complex Nickelates with High Sr Concentration, *B. Paudel, L. Wang, Z. Yang, M. Bowden,* Pacific Northwest National Laboratory; *J. Liu,* Shanghai Institute of Microsystem and Information technology, China; *K. Koirala, T. Kaspar, P. Sushko, S. Chambers,* ***Yingge Du***, Pacific Northwest National Laboratory | |
| 5:00pm | **NM-TuA2-15** Sharpening the Superconducting Transition of $Bi_2Sr_2Ca_{n-1}Cu_nO_{2n+4}$ Films with $n$=1–3 Grown by MBE, ***Y. Eren Suyolcu***, *Y. Li, D. Schlom,* Cornell University | |
| 5:15pm | **NM-TuA2-16** High-Temperature Superconductor FeSe Films Enabled Through Temperature and Flux Ratio Control, ***Maria Hilse***, *H. Yi, C. Chang, N. Samarth,* The Pennsylvania State University; *R. Engel-Herbert,* Paul-Drude-Institut für Festkörperelektronik, Germany | |

# Wednesday Morning, September 20, 2023

| | Room Ballroom A | |
|---|---|---|
| 8:00am | **ST-WeM1-2** Thermal Laser Epitaxy - the Universal Epitaxy Tool(?), ***Wolfgang Braun,*** *D. Kim, F. Hensling, T. Smart, L. Majer, B. Faeth, S. Smink, D. Dereh,* Max Planck Institute for Solid State Research, Germany*; H. Boschker,* Epiray GmbH, Germany*; J. Mannhart,* Max Planck Institut for Solid State Research, Germany | **Science and Technology of MBE**<br>**Session ST-WeM1**<br>**Advancement in MBE Growth Approaches**<br>**Moderator:**<br>**Darrell Schlom**, Cornell University |
| 8:15am | **ST-WeM1-3** Routes Towards Making $BaZrSe_3$ Thin Films in the Perovskite Structure by MBE, ***Ida Sadeghi,*** *K. Ye, J. Van Sambeek, R. Jaramillo,* MIT | |
| 8:30am | **ST-WeM1-4** Adsorption Controlled Homoepitaxial Growth of *c*-Plane Sapphire by Thermal Laser Epitaxy, ***Felix Hensling,*** *L. Majer, S. Smink, J. Mannhart, W. Braun,* Max Planck Institute for Solid State Research, Germany | |
| 8:45am | **ST-WeM1-5** Prediction of MBE-grown Oxide Film Composition Using Neural Networks and Big Data Analytics, ***Patrick Gemperline,*** *R. Paudel, S. Thapa, S. Provence, S. Battles, R. Markland,* Auburn University*; R. Vasudevan,* Oak Ridge National Laboratory*; R. Comes,* Auburn University | |
| 9:00am | **ST-WeM1-6** Autonomous Synthesis in the MBE Using Real-Time Artificial Intelligence, ***Tiffany Kaspar,*** *L. Wang, J. Christudasjustus, M. Sassi, B. Helfrecht, J. Pope, A. Harilal, S. Akers, S. Spurgeon,* Pacific Northwest National Laboratory | |
| 9:15am | **ST-WeM1-7** The Role of Optical Excitation on Misfit Dislocations in Epitaxial ZnS on GaP, ***Alexandra Fonseca Montenegro,*** *M. Baan, A. Blackston, R. Myers, T. Grassman,* The Ohio State University | |
| 9:30am | **BREAK** | |
| 9:45am | | |
| 10:00am | **ST-WeM2-10** Doping and Surfactant Behavior of Antimony and Gallium in Molecular Beam Epitaxy Grown Germanium-Tin, ***Amanda Lemire,*** *K. Grossklaus, C. Jamison, V. Vazquez, P. Hennessey, T. Vandervelde,* Tufts University | **Science and Technology of MBE**<br>**Session ST-WeM2**<br>**Fundamentals of MBE Growth**<br>**Moderator:**<br>**Stephanie Law**, University of Delaware |
| 10:15am | **ST-WeM2-11** $SiO_2$ Surface Planarization for Selective Area Regrowth of High Aspect Ratio Microstructures, ***Ashlee Garcia,*** *A. Skipper, M. Bergthold, S. Bank,* University of Texas at Austin | |
| 10:30am | **ST-WeM2-12** InP Lateral Epitaxial Overgrowth by Solid-Source Molecular Beam Epitaxy, ***Yiteng Wang,*** *R. Hool, W. North, S. Pandey, E. Raftery, K. Choquette, M. Lee,* University of Illinois at Urbana-Champaign | |
| 10:45am | **ST-WeM2-13** Effect of Molecular Beam Epitaxy (Mbe) Growth Conditions on the Structural and Magnetic Properties of High Curie Temperature $(MnSb_2Te_4)_x(Sb_2Te_3)_{1-x}$ Magnetic Topological Insulators, ***Candice Forrester,*** The City college of New York, Lehman College*; C. Testelin,* Institute des NanoSciences de Paris, France*; K. Wickramasinghe,* The City College of New York*; I. Levy,* New York University*; X. Ding, L. Krusin-Elbaum,* The City College of New York*; G. Lopez,* Lehman College*; M. Tamargo,* The City College of New York | |
| 11:00am | **ST-WeM2-14** Evolution of Antiferromagnetic Spin Texture in MBE-Grown Epitaxial Multiferroic BiFeO3, ***Maya Ramesh,*** 105 Worth Street*; P. Meisenheimer,* University of California, Berkeley*; S. Zhou,* Brown University*; P. Stevenson,* Northeastern University*; L. Caretta,* Brown University*; R. Ramesh,* Rice University*; D. Schlom,* Cornell University | |
| 11:15am | **ST-WeM2-15** Adsorption-Controlled Growth of $SrTiO_3$ by Oxide MBE, ***Dylan Sotir,*** *M. Barone, D. Schlom,* Cornell University | |
| 11:30am | **ST-WeM2-16** MBE of $Ba_2BiTaO_6$,a Candidate *p*-type Oxide Semiconductor, ***Anna Park,*** *Y. Birkhölzer, M. Barone, D. Schlom,* Cornell University | |

**Novel Materials**
**Room Ballroom A - Session NM-WeA**
**Low Dimensional and Topological Materials**
**Moderator: Joshua Zide**, University of Delaware

| | | |
|---|---|---|
| 12:15pm | **NM-WeA-1** Piezo- and Flexoelectricity Arising from Extreme Strain Gradients in Bent GaAs Nanowires, *F. Marin, O. Brandt,* ***Lutz Geelhaar,*** Paul-Drude-Institut für Festkörperelektronik Leibniz-Institut im Forschungsverbund Berlin, Germany | |
| 12:30pm | **NM-WeA-2** InAs Quantum Dot Nucleation on Finite Surface for Scalable Quantum Light Sources, ***Chen Shang,*** *Y. Pang, M. Kennedy,* University of California Santa Barbara*; G. Moody, J. Bowers,* University of California at Santa Barbara | |
| 12:45pm | **NM-WeA-3** Epitaxial $Cd_3As_2$ Heterostructures for Vertical Device Architectures, ***Anthony Rice,*** *J. Nelson, A. Norman, K. Alberi,* National Renewable Energy Laboratory | |
| 1:00pm | **Closing Remarks and Thank Yous** | |

# Author Index

## Bold page numbers indicate presenter

# Author Index

# Author Index



## — M —



## — N —



## — O —



## — P —



## — Q —



## — R —

# Author Index

# Author Index

# Advanced Heterogeneous Integration Enabled by Remote Epitaxy

Jeehwan Kim

Associate Professor of Mechanical Engineering

Associate Professor of Materials Science and Engineering


For future of electronics such as bioelectronics, 3D integrated electronics, and bendable electronics, needs for flexibility and stackability of electronic products have substantially grown up. However, conventional wafer-based single-crystalline semiconductors cannot catch up with such trends because they are bound to the thick rigid wafers such that they are neither flexible nor stackable. Although polymer-based organic electronic materials are more compatible as they are mechanically complaint and less costly than inorganic counterparts, their electronic/photonic performance is substantially inferior to that of single-crystalline inorganic materials. For the past half a decade, my research group at MIT has focused on mitigating such performance-mechanical compliance dilemma by developing methods to obtain cheap, flexible, stackable, single-crystalline inorganic systems. In today's talk, I will discuss about our strategies to realize such a dream electronic system and how these strategies unlock new ways of manufacturing advanced electronic systems. I will highlight our remote epitaxy technique that can produce single-crystalline freestanding membranes including III-nitrides, III-V and complex oxide system with their excellent semiconducting performance. In addition, I will present unprecedented artificial heterostructures enabled by stacking of those freestanding 3D material membranes, e.g., world's smallest vertically-stacked full color micro-LEDs, world's best multiferroic devices, battery-less wireless e-skin, and heat dissipating system GaN power devices.

**Biography**

Prof. Jeehwan Kim is a tenured faculty at MIT. His research group's focuses on material innovations for next generation computing and electronics. Prof. Kim joined MIT in September 2015. Before joining MIT, he was a Research Staff Member at IBM T.J. Watson Research Center in Yorktown Heights, NY since 2008 right after his Ph.D. He worked on next generation CMOS and energy materials/devices at IBM. Prof. Kim is a recipient of 20 IBM high value invention achievement awards. In 2012, he was appointed a "Master Inventor" of IBM in recognition of his active intellectual property generation and commercialization of his research. After joining MIT, he continuously worked nanotechnology for advanced electronics/photonics. As its recognition, he received LAM Research foundation Award, IBM Faculty Award, DARPA Young Faculty Award, and DARPA Director's Fellowship. He is an inventor of > 200 issued/pending US patents and an author of > 50 articles in peer-reviewed journals. He currently serves as Associate Editor of *Science Advances*, AAAS. He received his B.S. from Hongik University, his M.S. from Seoul National University, and his Ph.D. from UCLA, all of them in Materials Science.

# Flexomagnetism And Strain-Induced Superconductivity in Rippled GdAuGe Heusler Membranes

Tamalika Samanta, Zachary LaDuca, Dongxue Du, Taehwan Jung, Sebastian Manzo, Katherine Su, Michael Arnold, and Jason Kawasaki

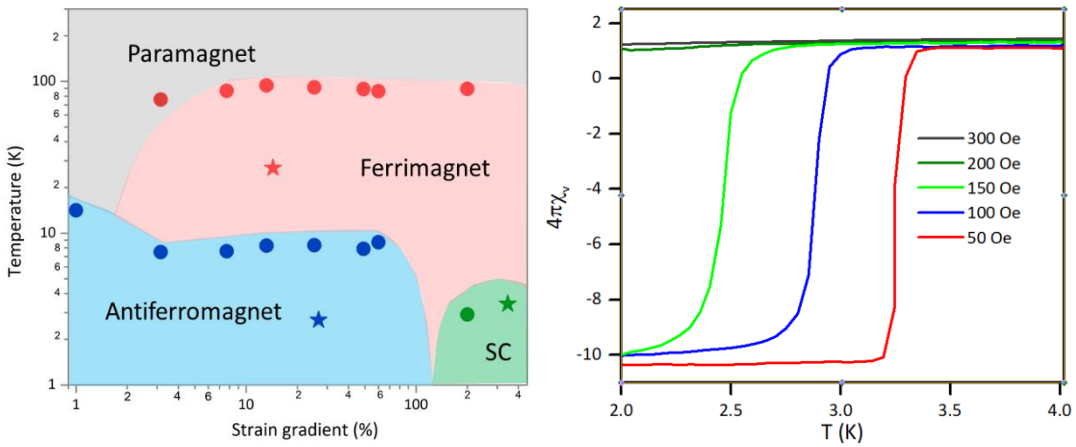


*Figure 1: (a) Phase diagram for rippled GdAuGe membranes. The circle and star denote differently exfoliated rippled membranes. (b) The field-dependent onset of diamagnetism in a rippled membrane shows the Meissner response, implying superconductivity.*

# Supplementary Material

*Figure 1. SEM image of a 60-nm-thick $YbRh_2Si_2$ film on a Ge(001) substrate.*

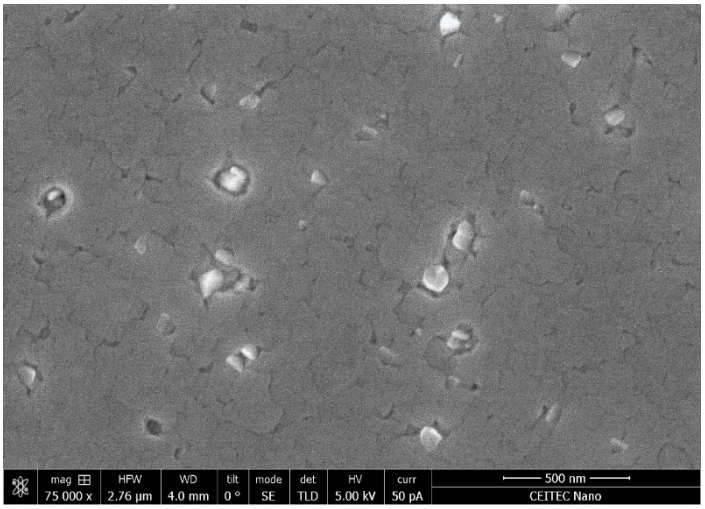


*Figure 2. AFM image of the $5 \times 5\mu m^2$ surface morphology of a 10- nm-thick $YbRh_2Si_2$ film on Ge after a sub-monolayer Yb soak, RMS = 1.8 nm*

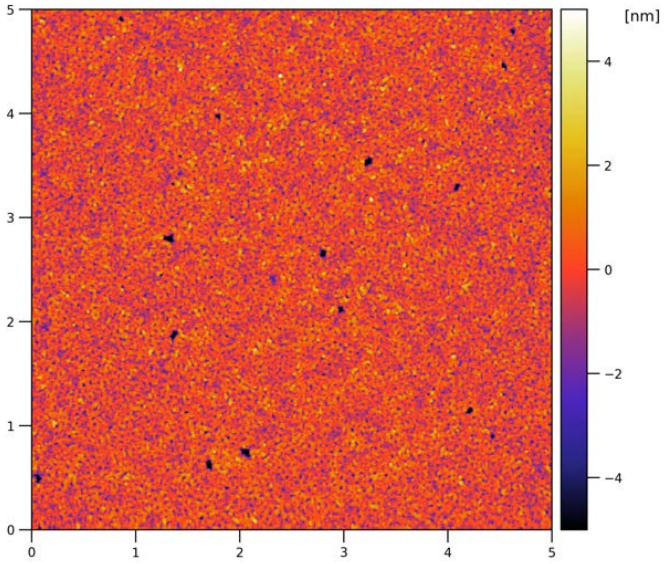

*Figure 3 XRD scan of $Ce_3Bi_4Pd_3$ on sapphire. The RMS roughness of the sample, measured by AFM, is 2.8 nm*

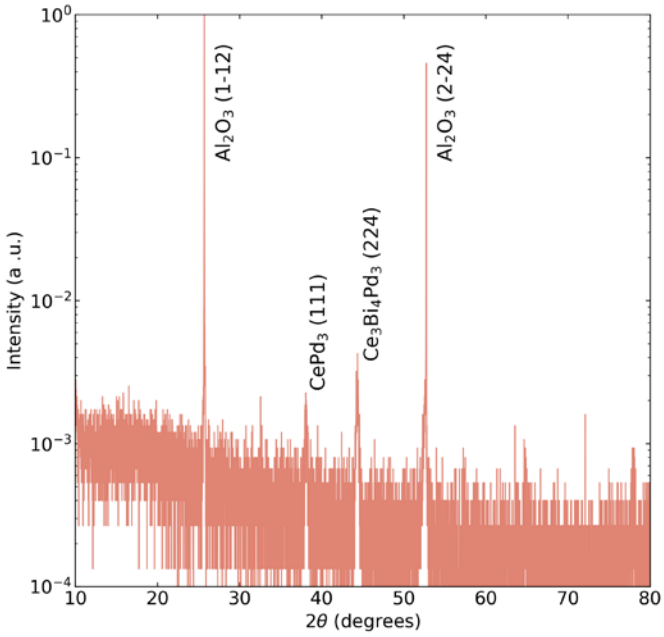

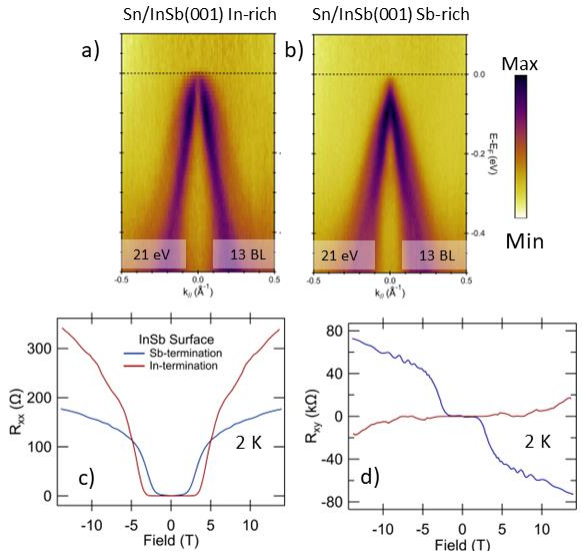


*Figure 1 Control of doping in α-Sn films via surface termination of the InSb(001) substrate. a) ARPES measurement of 13 BL α-Sn grown in the In-rich c(8x2) reconstruction. b) ARPES measurement of 13 BL α-Sn grown in the Sb-rich c(4x4) reconstruction. A photon energy of 21 eV is chosen to accentuate the surface states. A clear shift in chemical potential from below the Dirac node to at the Dirac node is evident from a) to b). c) shows $R_{xx}$ and d) shows $R_{xy}$ measurements of 56 BL α-Sn grown on the same InSb surface terminations. Conductive InSb substrates make quantification difficult, but a clear change in carrier type is evident, showing the change in doping in a), b) is carried through to the bulk α-Sn.*

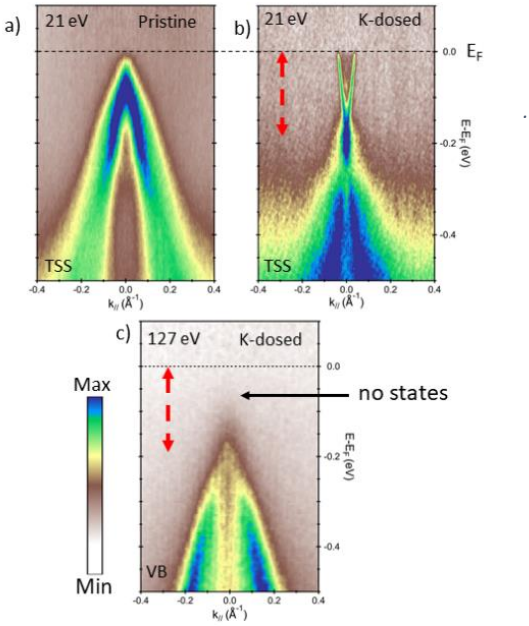


*Figure 2 Confirmation of 3D topological insulator-like phase. ARPES measurement at 21 eV before a) and after b) potassium dosing the surface. Potassium dosing effectively electron dopes the surface, allowing to see further above the surface Dirac node. The surface Dirac node is preserved without a gap opening. c) ARPES measurement at 127 eV after potassium dosing the surface. At this photon energy the bulk states at the bulk Γ point are observed. There is clear evidence of the valence band, but no conduction band evident below the Fermi level. This indicates at least a 200 meV bulk band gap. This film is thus 3D topological insulator-like.*

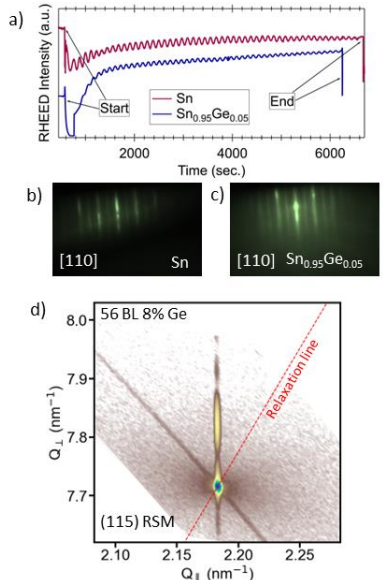


*Figure 3 Growth of α-SnGe thin films. a) RHEED oscillations showing preservation of layer by layer growth mechanism when the Sn films are alloyed with Ge. b) RHEED pattern of (2x1)/(1x2) in 50 BL α-Sn. c) The same as b) in 50 BL α-SnGe. d) High resolution XRD reciprocal space map around the InSb(115) peak showing the α-SnGe is fully strained. Pendellosung fringes in the (00l) direction are clear, indicative of high-quality interfaces.*

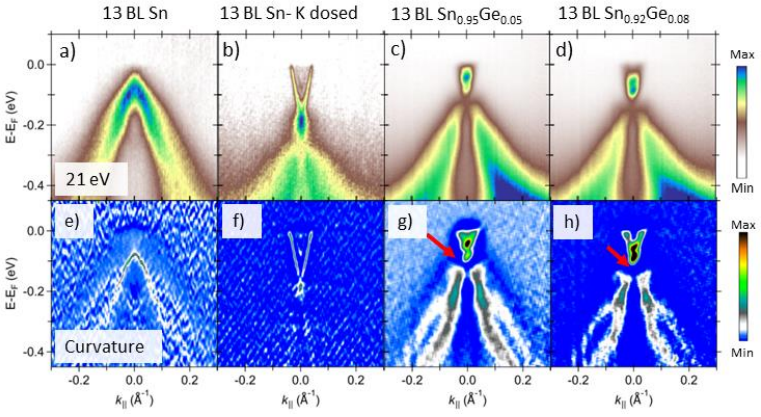


*Figure 4 Topological phase transition upon Ge alloying α-Sn films studied via ARPES measurements at 21 eV to accentuate the surface states. a) Pristine 13 BL Sn, b) Potassium dosing the film in a). c) 5% Ge alloying, resulting in about +0.5% strain. d) 8% Ge alloying, resulting in about +0.9% strain. A small gap opens at the surface Dirac node. A double peak is evident just above the gapped Dirac node. The exact cause is unclear, but is likely an additional, unpredicted surface state. e)-h) shows the curvature of a)-d), enhancing the contrast of the bands.*

## Improving MBE $(Bi,Sb)_2(Te,Se)_3$ Topological Materials Via Resonant and Magnetic Dopants

*Patrick Taylor[1], Brandi Wooten[2], Jos Heremans[2], Mahesh Neupane[1], Harry Hier[1], Owen Vail[1], Paul Corbae[3], Aaron Engel[3], Patrick Folkes[1], Christopher J. Palmstrøm[3]*

1. *DEVCOM US Army Research Laboratory, Adelphi, MD 20783*
2. *Materials Department, The Ohio State University, Columbus, OH*
3. *University of California Santa Barbara, Santa Barbara, CA*

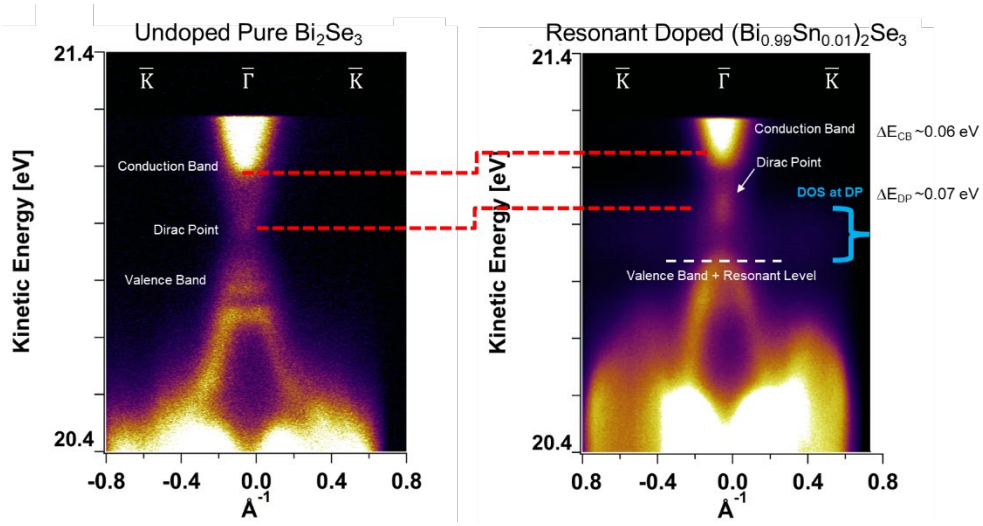


**Figure 1:** In-situ ARPES measurements from pure $Bi_2Se_3$ (left) and $Bi_2Se_3$ doped with resonant Sn (right) showing the behavior predicted by DFT calculations.

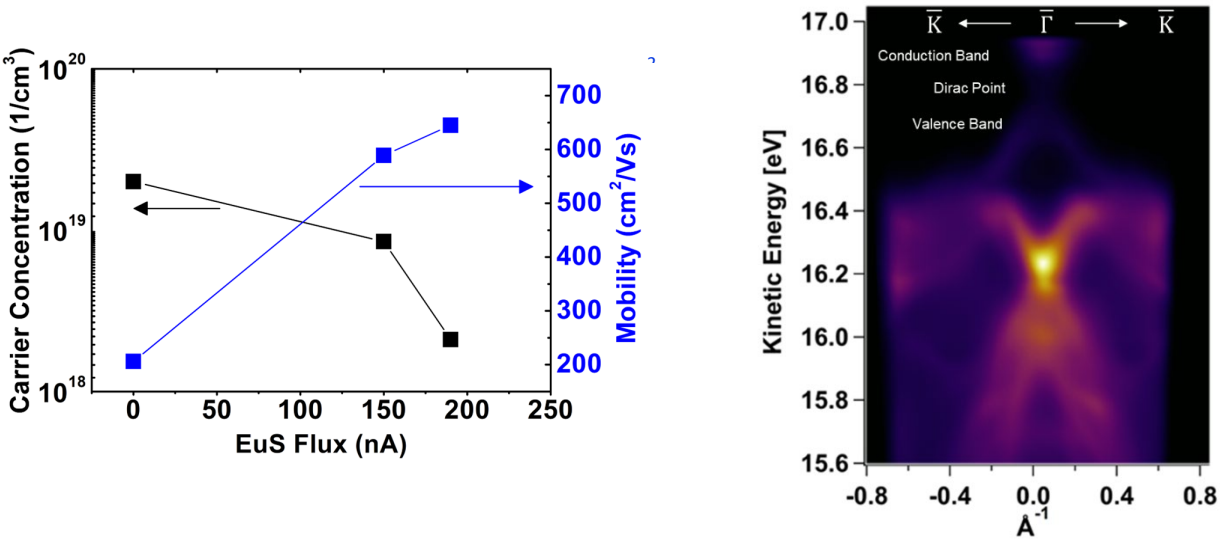


**Figure 2:** The improvement in transport properties of $(Bi,Sb)_2(Te,Se)_3$ doped with europium sulfide showing the desired reduction of bulk carriers (left), and near complete elimination of conduction band states with the Fermi level approaching the Dirac-like states.

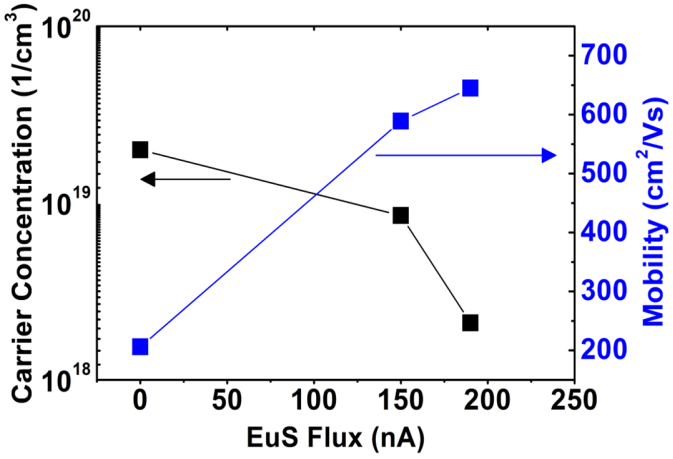
Carrier Concentration (1/cm$^3$)
$10^{20}$
$10^{19}$
$10^{18}$
0
50
100
150
200
250
EuS Flux (nA)
700
600
500
400
300
200
Mobility (cm$^2$/Vs)

# Quasi Van der Waals Epitaxy of Magnetic Topological Insulators on a GaAs (111) Substrate

**Yuxing Ren,**[1] Lixuan Tai,[2] Kaicheng Pan,[1] Sidharth Srivastava,[1]

Ya-Hong Xie, [1] Mark Goorsky, [1] Kang L. Wang [1,2]

[1] *Materials Science and Engineering Department, University of California, Los Angeles, CA, USA*
[2] *School of Electrical and Computer Engineering, University of California, Los Angeles, CA, USA*

Magnetic topological insulator could achieve quantum anomalous Hall (QAH) effect and spin-orbit torque (SOT) switching in the same structure. This is promising for its future applications in memory or switching with its robust surface properties by topological protection. Considering the van der Waals nature of the epitaxial layers, it has very weak van der Waals bonding with the substrate. This gives rise to a novel quasi Van der Waals epitaxial growth mode at the interface of GaAs (111) substrates and the epitaxial layers, which has the advantages of both good crystallinity from substrate confinement, and a less influence from defects and roughness on the substrate surfaces. This is very crucial for achieving the quantization regime.

In this work we have done hetero-epitaxy of Cr:$(Bi_xSb_{1-x})_2Te_3$ and other magnetic topological insulators on GaAs (111) substrates by MBE (Molecular Beam Epitaxy). Unlike the pure Van der Waals epitaxy which has more freedom at the interfaces epitaxial layer and substrates, we found out that in this quasi Van der Waals growth mode, strain exist and relaxes quickly within the 1$^{st}$ epitaxial layer. While the surface defects quickly get screened within the 1$^{st}$ layer, the surface confinement also gives the epitaxial layer a uniform in-plane orientation which is important for achieving a single crystalline structure. Growth mechanism and the influence on its transport properties are also discussed.

**Figure 1. qvdWE of Cr: $(Bi_xSb_{1-x})_2Te_3$ (CBST) on GaAs (111)**

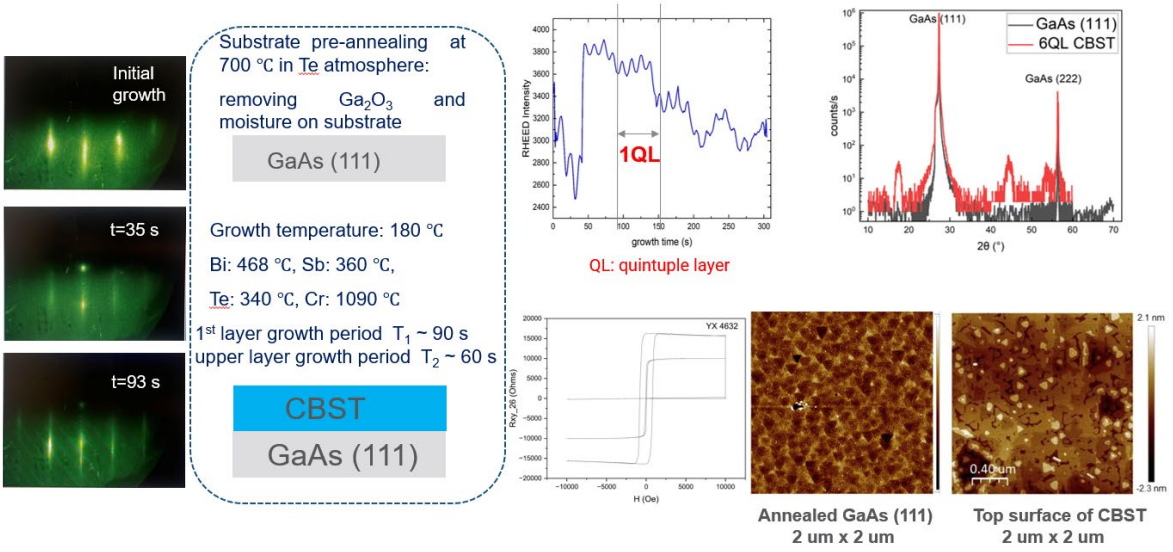


**Figure 2. Reciprocal Space Mapping (RSM) for 6 QL CBST on GaAs (111)**

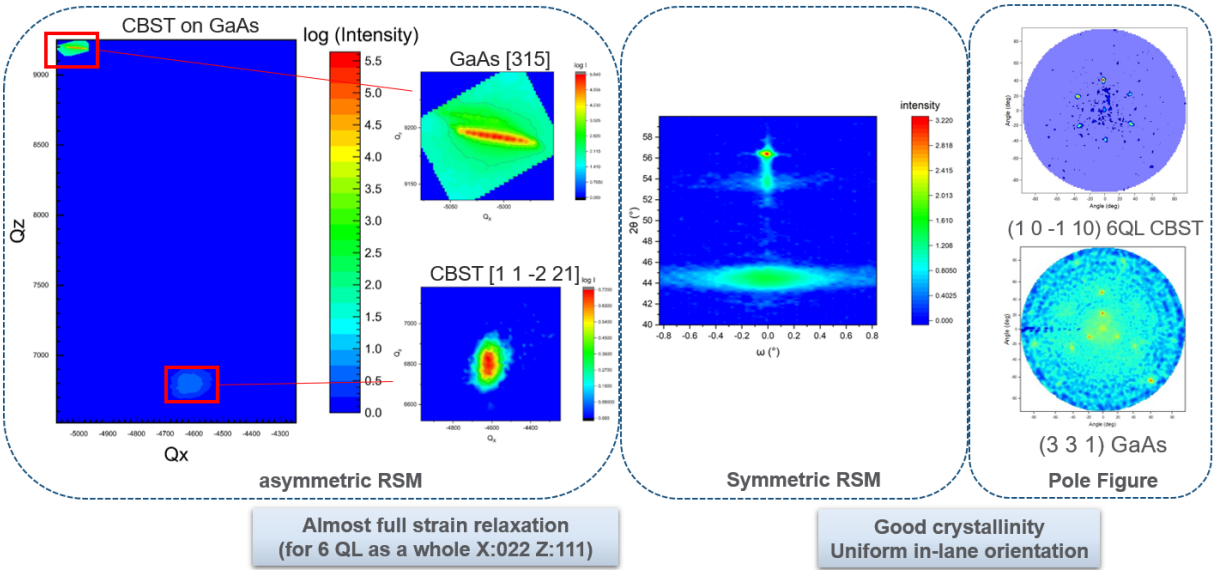


[1] Alaskar Y, Arafin S, Martinez-Velis I, Wang KL. Heteroepitaxial growth of III–V semiconductors on 2D materials. Two-dimensional Materials-Synthesis, Characterization and Potential Applications. 2016 Aug 31

[2] arXiv:2103.09878

+ Author for correspondence: yxren@g.ucla.edu

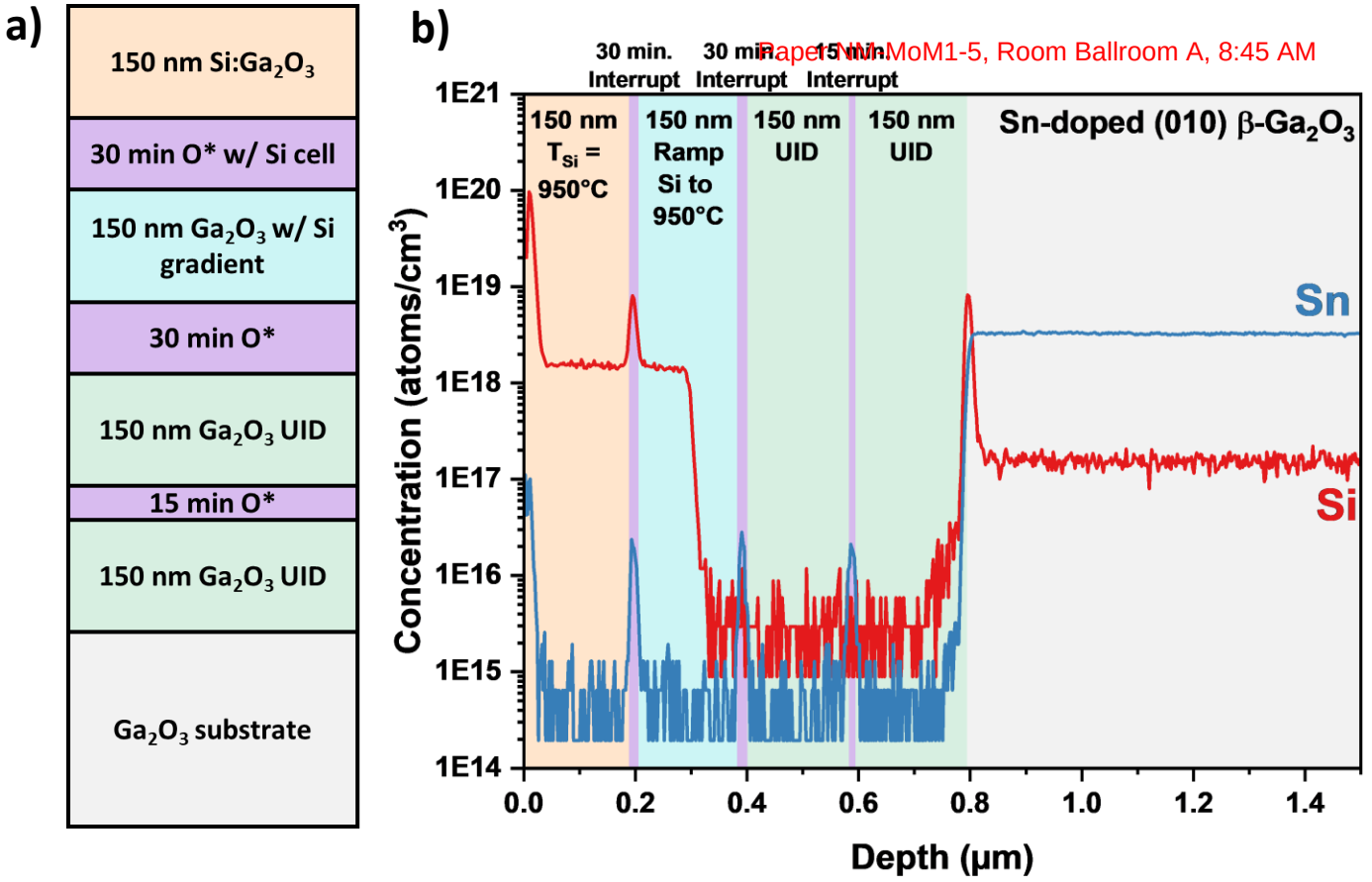


**Figure 1** – a) Schematic structure of test structure to study impacts of plasma bulbs and Si dopant source during growth interrupts. b) TOF-SIMS depth profile showing Si only accumulates at the sample surface during growth interrupts while the Si cell was hot enough to provide a Si flux while no Si accumulated regardless of exposure time to just the quartz plasma bulb with a 250W O plasma.

**Ga Beam Flux = 1 × $10^{-7}$ Torr "Gallium Rich" Regime**

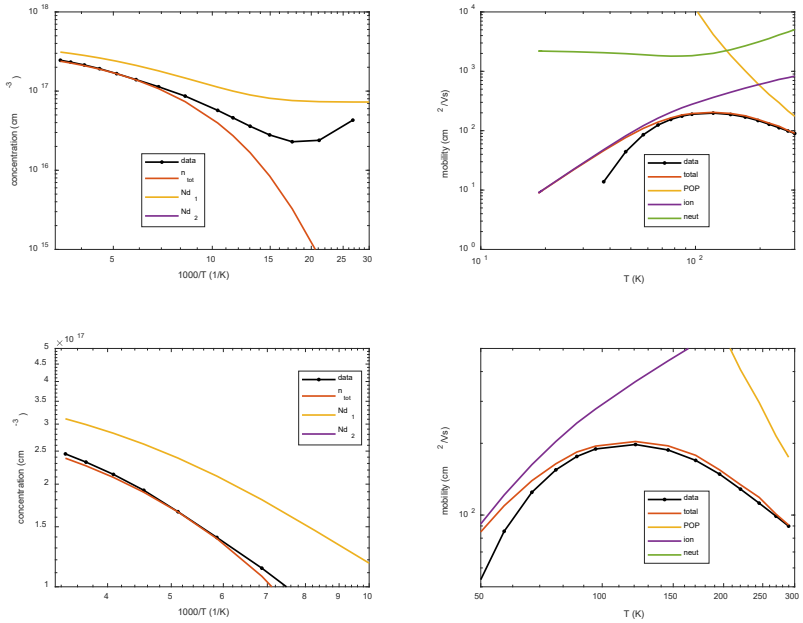


*Figure 1: Transport of a gallium rich film and the fits to quantify defects and donors. A donor at 27 meV shows a concentration of 4.25 × $10^{17}$ $cm^{-3}$ and an acceptor of 7.26 × $10^{16}$ $cm^{-3}$.*

**Ga Beam Flux = 6 × $10^{-8}$ Torr "Oxygen Rich" Regime**

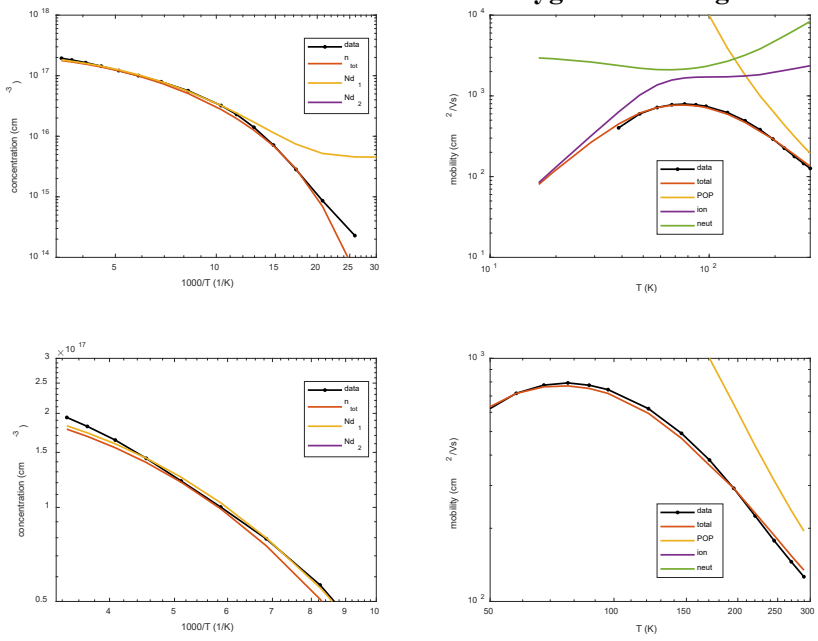


*Figure 2: Transport of a gallium rich film and the fits to quantify defects and donors. A donor at 38 meV shows a concentration of 2.6 × $10^{17}$ $cm^{-3}$ and an acceptor of 4.5 × $10^{15}$ $cm^{-3}$.*

**Molecular Beam Epitaxy of Binary and Ternary Manganese and Chromium Nitrides.**

Kevin D. Vallejo[1], Krzysztof Gofryk[1], Sandra Julieta Gutiérrez-Ojeda[2], Gregorio H. Cocoletzi[3], Brelon J. May[1]
[1]Idaho National Laboratory, ID, USA
[2]Universidad Nacional Autónoma de México, Baja California, México
[3]Benemérita Universidad Autónoma de Puebla, Puebla, Mexico

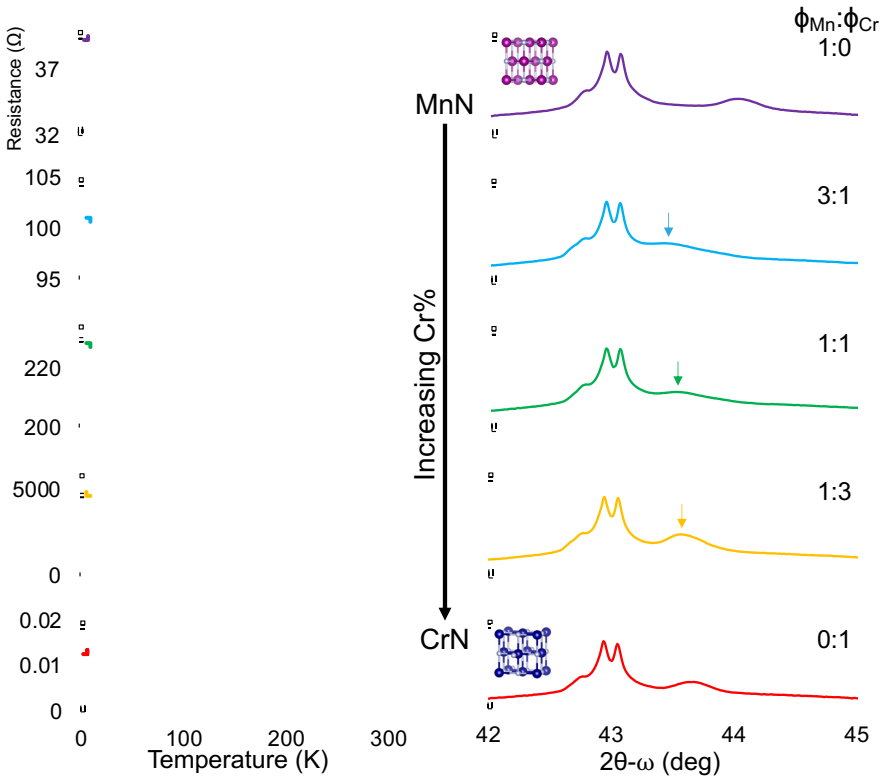


Left column: Resistance vs temperature for $Mn_xCr_yN$ with increasing amounts of Cr (purple to red). The binary compounds are metallic, while the ternaries are semiconducting.

Right column: X-ray diffraction for the same $Mn_xCr_yN$ samples deposited on MgO (001) substrates, the corresponding beam equivalent pressure ratio ($\Phi_{Mn}$:$\Phi_{Cr}$) are shown in the top right of each panel. The ternary compounds fall outside of the two binaries, suggesting a non-rocksalt phase.

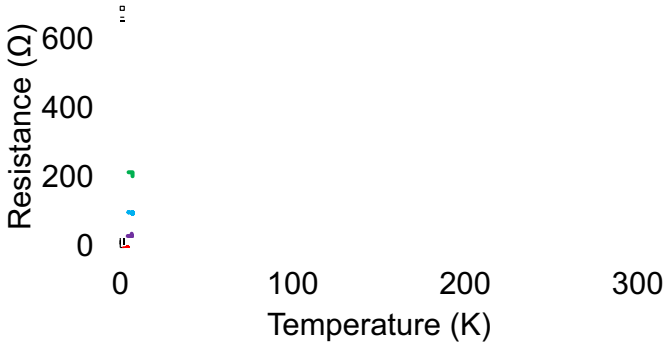


The same resistance vs temperature data as shown above, but on the same y-axis. The $Mn_xCr_yN$ sample with $\Phi_{Mn}$:$\Phi_{Cr}$ of 1:3 shows the largest drop in resistance

# Achieving Atomically Ordered GaN/AlN Quantum Heterostructures: The Role of Surface Polarity

Yuanpeng Wu[1], Peng Zhou[1], Yixin Xiao[1], Kai Sun[2], Ding Wang[1], Ping Wang[1], and Zetian Mi*[,1]
1) Department of Electrical Engineering and Computer Science, University of Michigan, Ann Arbor, MI 48109, USA
2) Department of Materials Science and Engineering, University of Michigan, Ann Arbor, MI 48109, USA
*Corresponding author: ztmi@umich.edu

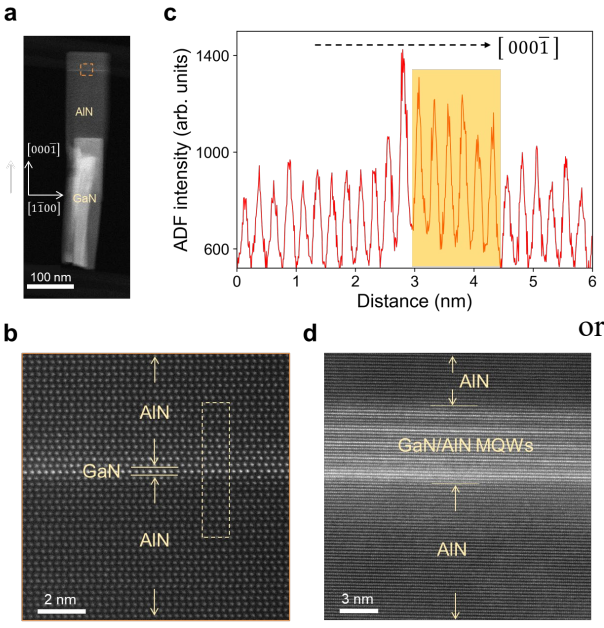


**Figure 1. Structural characterization of GaN/AlN quantum heterostructures on *c*-plane.** (a) Low-magnification HAADF-STEM image of monolayer GaN incorporated on the *c*-plane of an AlN nanowire. (b) High-resolution HAADF-STEM image of the orange-boxed region in (a). The ML GaN as well as the AlN barriers are indicated by the arrows. (c) ADF intensity analysis of the yellow-boxed region in (b). The yellow-shaded region indicates the cation intermixing region. (d) HAADF-STEM image of GaN/AlN digital alloys of 2 MLs GaN/6 MLs AlN (Sample A2).

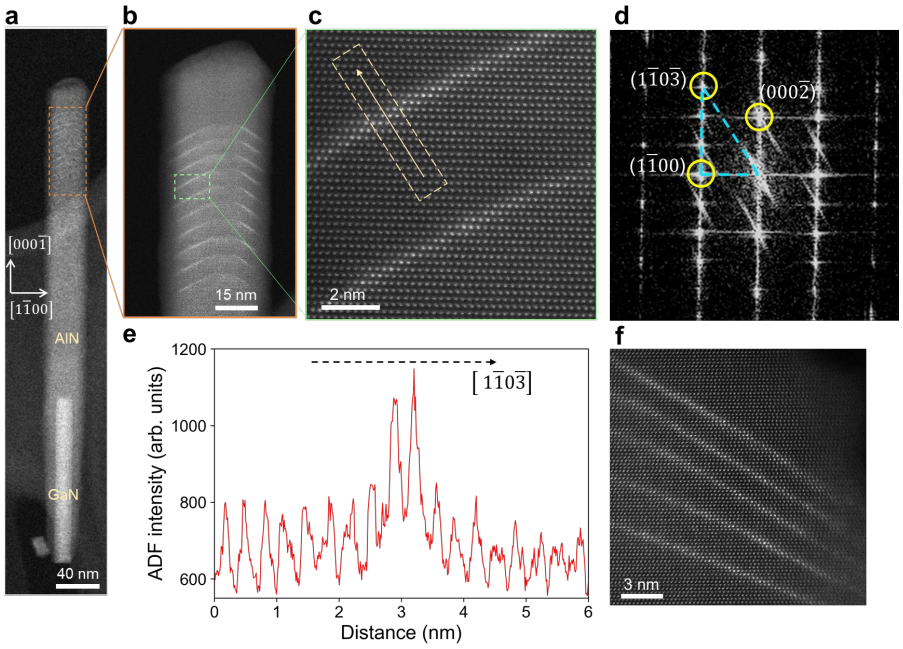

**Figure 2. Structural characterization of GaN/AlN quantum heterostructures on the semipolar plane.** (a) Low-magnification HAADF-STEM image of 10 periods of GaN/AlN digital alloys embedded in an AlN nanowire. (b) HAADF-STEM image of the orange-boxed region in (a). (c) High-resolution HAADF-STEM image of the green-boxed region in (b). (d) Fast Fourier transform of (c). (e) ADF intensity analysis of the yellow-boxed region in (c). (f) HAADF-STEM image of the active region of Sample B2 consisting of 2 MLs GaN/6 MLs AlN.

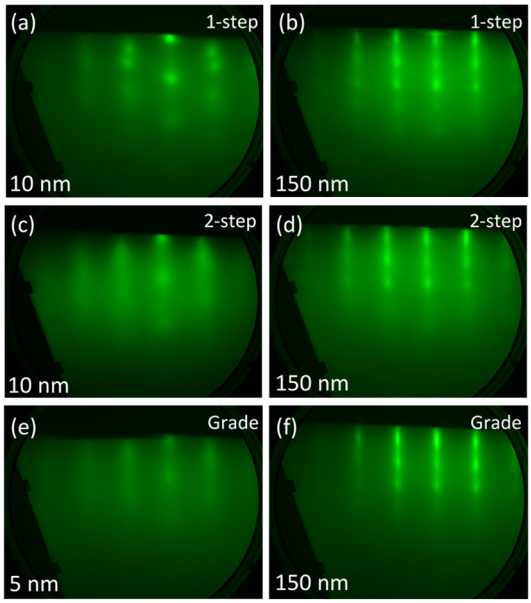


Fig. 1. RHEED images of the (a, b) 1-step $Sc_{0.40}Al_{0.60}N$ sample, (c, d) 2-step $Sc_{0.32}Al_{0.68}N/Sc_{0.40}Al_{0.60}N$ sample, and (e, f) graded $Sc_{0.32\rightarrow0.40}Al_{0.68\rightarrow0.60}N/Sc_{0.40}Al_{0.60}N$ sample taken (a, c, e) just after nucleation and (b, d, f) after growth of the 150-nm total-thickness film.

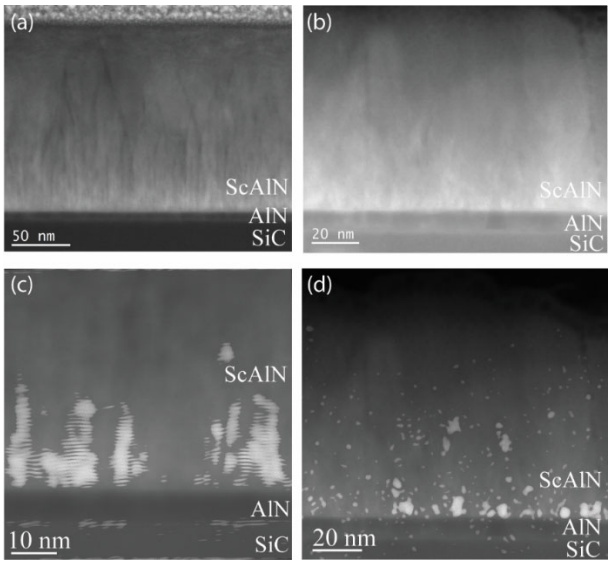


Fig. 2. (a, b) Transmission electron micrographs of a 1-step and graded start $Sc_{0.40}Al_{0.60}N$ sample, respectively. (c, d) Bragg-filtered images of the same regions on each sample highlighting the presence of rock-salt grains.

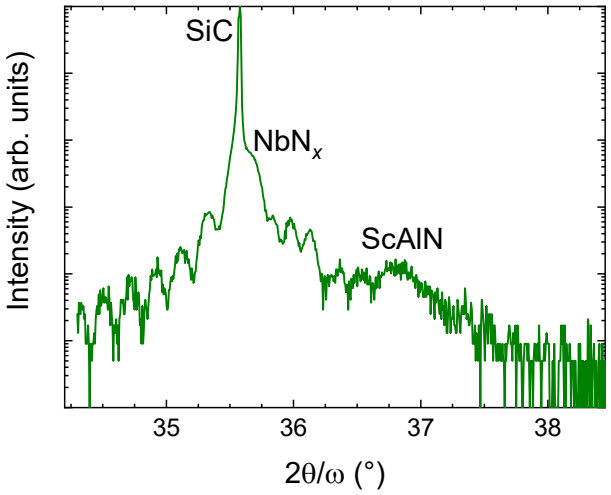


Fig. 3. 2θ/ω XRD scan about the 0002 reflection of a $Sc_{0.40}Al_{0.60}N$ sample having a graded initiation layer, an AlN interlayer and an NbN epitaxial metal layer grown on SiC.

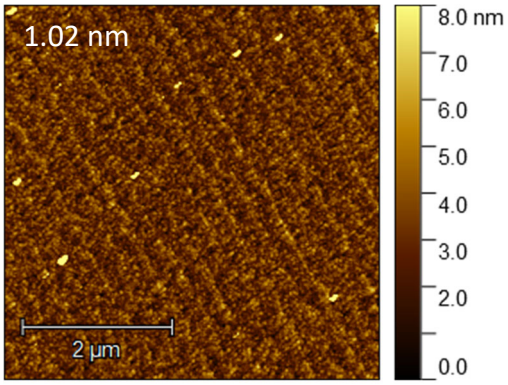


Fig. 4. Atomic force microscopy image of a $Sc_{0.40}Al_{0.60}N$ sample having a graded initiation layer, an AlN interlayer and an NbN epitaxial metal layer grown on SiC. The rms roughness from the 5 µm × 5 µm scan was 1.02 nm.

# High efficiency micrometer scale green and red light emitting diodes

Yixin Xiao[1], Reddeppa Maddaka[1], Yuanpeng Wu[1], Yakshita Malholtra[1], Yifu Guo[1], Samuel Yang[1], Jiangnan Liu[1], Kai Sun[2], Ayush Pandey[1], Jungwook Min[1], and Zetian Mi*[,1]

1) Department of Electrical Engineering and Computer Science, University of Michigan, Ann Arbor, MI 48109, USA

2) Department of Materials Science and Engineering, University of Michigan, Ann Arbor, MI 48109, USA

*Corresponding author: ztmi@umich.edu

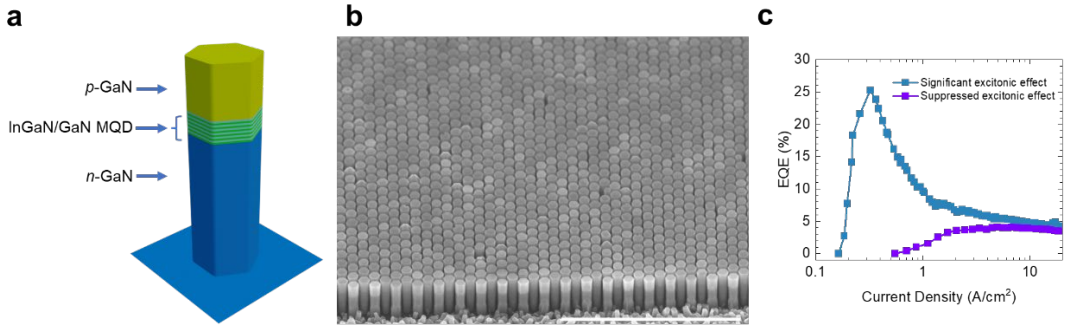


**Figure 1.** Ultrahigh efficiency green emitting μLEDs. (a) Schematic of the nanowire LED design, with a green InGaN/GaN multiple-quantum-dot (MQD) structure serving as the active region. (b) Scanning electron microscope of such a nanowire array. Scale bar: 3 μm. (c) Variation in external quantum efficiency due to differences in nanowire diameters, with the navy blue curve coming from a thin nanowire diameter array and the purple curve coming from a larger diameter array. The thinner diameter array allows for more active region formation on the semi-polar plane rather than the polar c-plane, thus allowing for radiative excitonic recombination channels that are more efficient than traditional free carrier radiative recombination for InGaN.

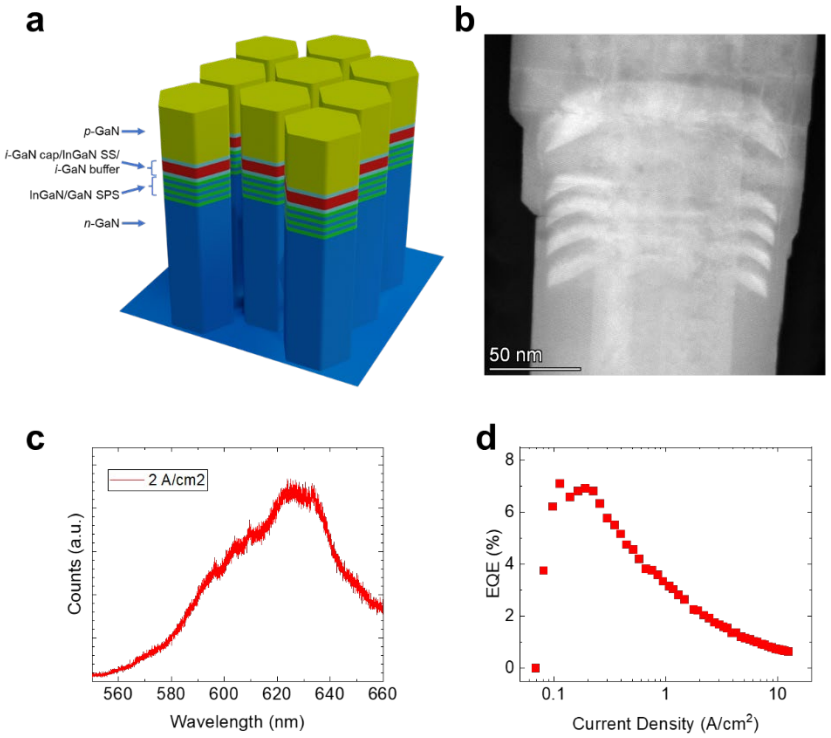


Figure 2. High efficiency red emitting μLEDs. (a) Schematic of the nanowire design, which employs a short-period superlattice (SPS) that allows for high levels of In incorporation in the single segment (SS) active region. (b) High angle annular dark field scanning transmission electron micrograph of such one such nanowire, where the four layers of SPS InGaN and the single segment active region InGaN are clearly visible at a higher contrast, as InGaN has a higher atomic number than GaN. (c) Electroluminescence of a red emitting μLED at 2 A/cm$^2$. (d) The external quantum efficiency (EQE) of such red emitting μLED devices can reach >7%.

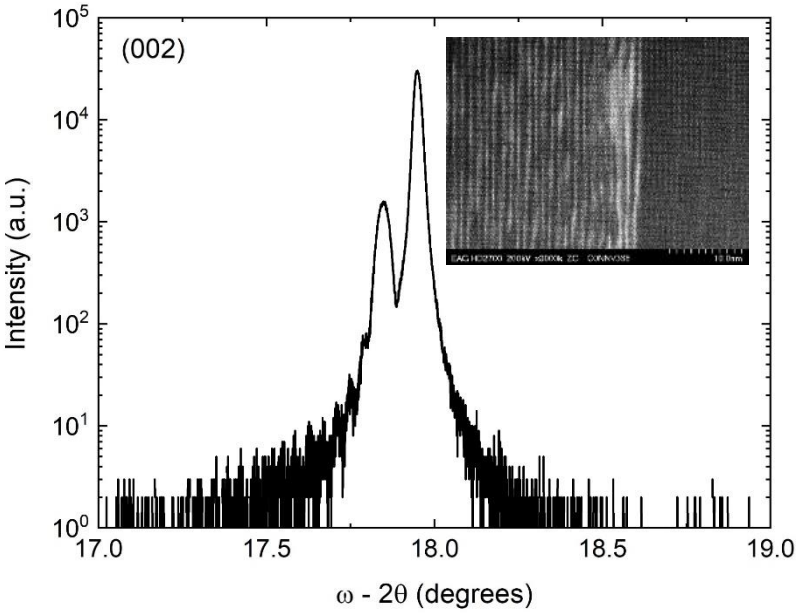


**Figure 1**: XRD coupled scan of the first attempt at a think layer SPSL. Shows faint Pendelosung fringes. Inset image shows a cross-sectional TEM image of the sample, highlighting the strong ALN/GaN intermixing.

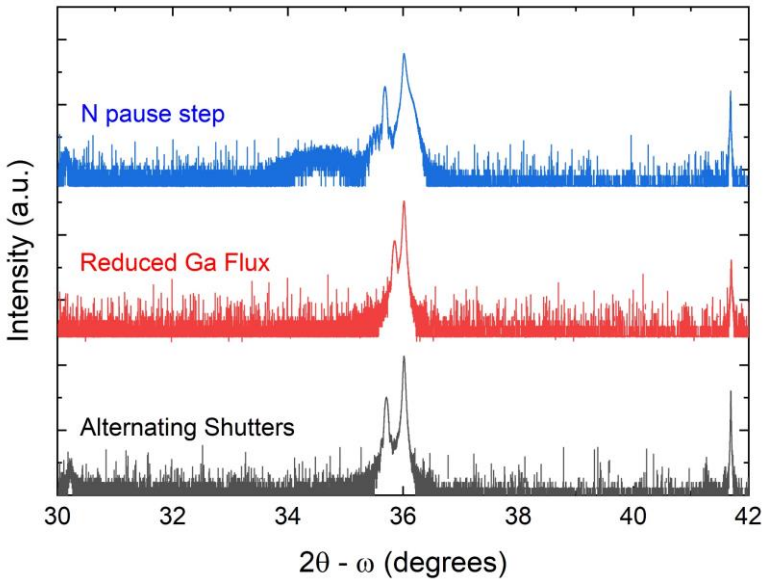


**Figure 2**: XRD coupled scans of the samples using various growth conditions used. The introduction of a N only pause step generates 2 regions of SPSL uniformity.

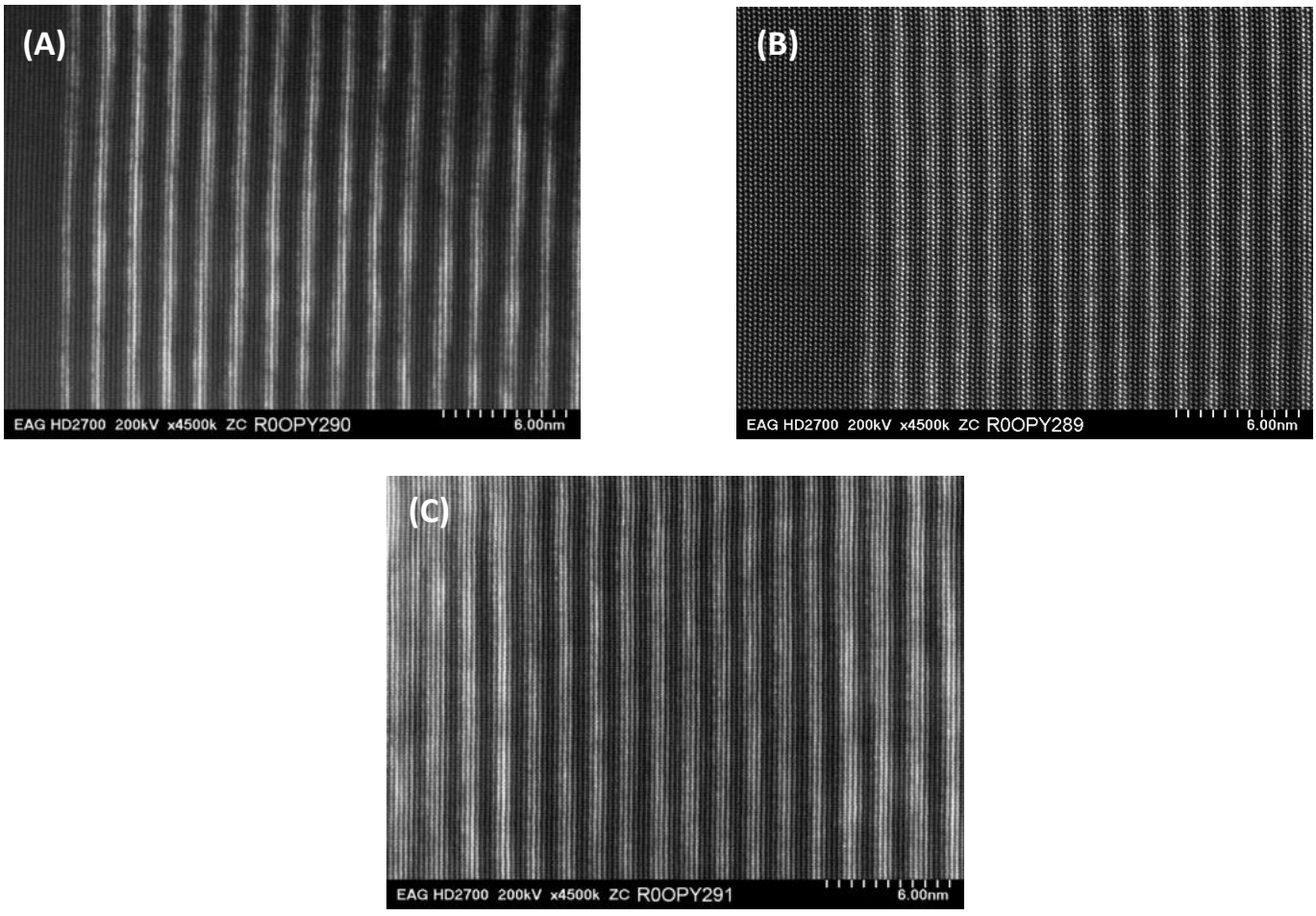


**Figure 3**: TEM images of the various altered growth conditions. A) Grown using alternating Al and Ga shutters. Resulting AlN and AlGaN layer thicknesses are approximately 5 ML and 3 ML respectively B) Grown using half the normal Ga flux. Resulting AlN and AlGaN layer thicknesses are the same as (A) but there is more variation in the AlN thickness C) Grown using alternating shutter conditions with an additional N-pause step. Shows 2 regions: strong intermixing (left) and strong layer uniformity (right). AlN and AlGaN layer thicknesses are 3 ML and 4 ML respectively.

# Separate Absorption, Charge, and Multiplication Avalanche Photodiodes With InGaAs/GaAsSb Type-II Superlattices Grown by Molecular Beam Epitaxy.

H. Jung[1], S. Lee[1], X. Jin[2], Y. Liu[2], T. J. Ronningen[1], C. H. Grein[3], J. P. R. David[2], and S. Krishna[1*]

[1]Department of Electrical and Computer Engineering, The Ohio State University, Columbus, Ohio, 43210, USA
[2]Department of Electronic and Electrical Engineering, University of Sheffield, Sheffield S1 3JD, UK
[3]Department of Physics, University of Illinois, Chicago, Illinois 60607, USA
[*]Corresponding author: Sanjay Krishna, krishna.53@osu.edu

**Abstract**

Avalanche photodiodes (APDs) can be used in remote sensing applications, such as atmospheric greenhouse gas monitoring, free-space optical communications, and medical diagnostics, including the extended short-wavelength infrared (eSWIR) range between 1.3 μm and 2.5 μm. APDs have internal multiplication characteristics that allow them to detect weak signals. However, traditional *p-i-n* structure APDs, commonly used for longer infrared wavelengths (1.55 – 3.4 μm), can be performance-limited by the high dark currents due to band-to-band tunneling when subject to high electric fields. A separate absorption, charge, and multiplication (SACM) structure can be employed to improve their performance. The SACM structure decouples the absorption region from the multiplication regions, maintaining the absorber region below the tunneling threshold while keeping a high electric field only in the multiplier. In this work, we designed, grew, and fabricated an eSWIR SACM APD. The epitaxial layers grown by molecular beam epitaxy consist of a 5 nm-$In_{0.53}Ga_{0.47}As$/5 nm-$GaAs_{0.51}Sb_{0.49}$(InGaAs/GaAsSb) type-II superlattice (SL) absorber and 1000 nm-thick $Al_{0.85}Ga_{0.15}AsSb$ (AlGaAsSb) multiplier on a InP substrate. The development of the SL involved the growth of InGaAs with a growth rate of 1 μm/hr and a V/III beam equivalent pressure (BEP) ratio of ~10, along with GaAsSb grown at a rate of 0.47 μm/hr and a V/III BEP ratio of ~20. Both were grown at a temperature of 470 °C, as measured by the Bandit system. Meanwhile, AlGaAsSb was grown at a rate of 0.6 μm/hr and a temperature of 500 °C. The X-ray diffraction (XRD) result of our devices is presented in Figure 1, which reveals a mismatch of -440 arcsec and -260 arcsec for AlGaAsSb and SL, respectively. The period of the SL was calculated from a distance between the satellite peaks, determined to be 9.75 nm. These devices have a cut-off wavelength of 2.4 μm, a gain of up to 60 at room temperature, and a resulting quantum efficiency of 600% at 2 μm. as shown in Figure 3. Furthermore, the excess noise factor of our AlGaAsSb-based SACM APD stays below 2.2, up to a gain of 30. This value is considerably lower than competing technologies, with 2 times lower than InAlAs-based SACM APD and 1.2 times lower than InAlAsSb SACM APD on GaSb at the gain of 10.

These results demonstrate the potential of AlGaAsSb-based SACM APDs with InGaAs/GaAsSb SLs for various eSWIR detection applications and provide insight into the design and fabrication of SACM APDs with good noise and sensitivity characteristics, making them suitable for a range of remote sensing applications in the eSWIR range. These results have significant implications for developing highly sensitive and low-noise APDs for use in various applications.

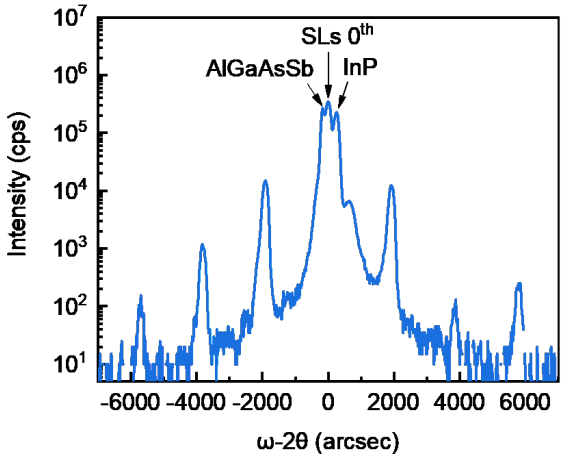


Figure 1. The XRD result of our SACM APDs with AlGaAsSb multiplier and InGaAs/GaAsSb SL on the InP substrate.

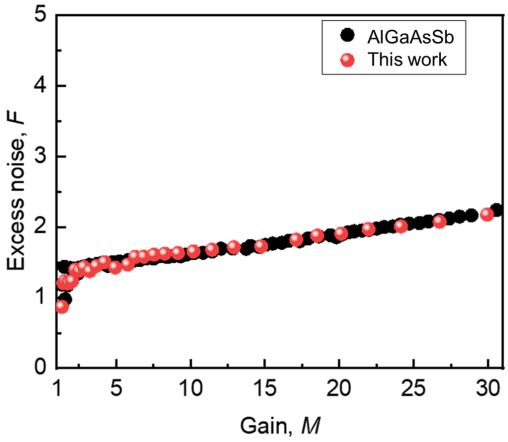


Figure 2. Excess noise as a function of gain for the SACM APD described in this work, compared with a 1000-nm thick AlGaAsSb *p-i-n* APD.

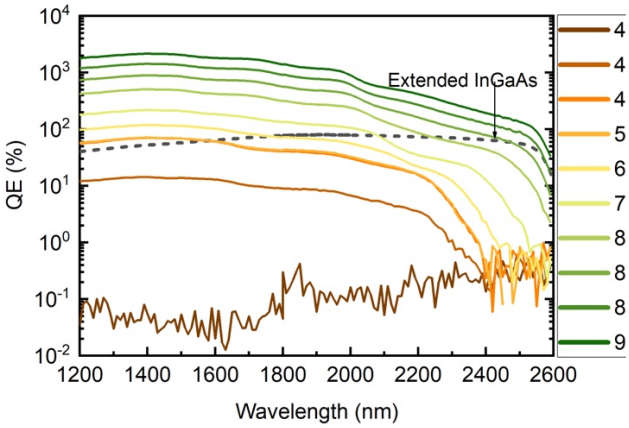


Figure 1. External quantum efficiency of an eSWIR AlGaAsSb-based SACM APDs with InGaAs/GaAsSb SL absorber at various reverse biases. The dotted line is for a commercial extended InGaAs photodiode with a cut-off wavelength of 2.6 µm.

**ACKNOWLEDGMENTS**

This work was supported by the Advanced Component Technology (ACT) program of NASA's Earth Science Technology Office (ESTO) under Grant No. 80NSSC21K0613.

# Growth of MWIR ICLEDs on Silicon using Molecular Beam Epitaxy

**M. Frost,[1] T. J. Rotter,[1] F. F. Ince,[1] G. Balakrishnan,[1] M. R. McCartney,[2] D. J. Smith,[2] C. L. Canedy,[3] W. W. Bewley,[3] S. Tomasulo,[3] C. S. Kim,[3] M. Kim,[4] I. Vurgaftman,[3] and J. R. Meyer.[3]**

*[1] University of New Mexico, Albuquerque, NM 87108*
*[2] Department of Physics, Arizona State University, Tempe, AZ 85287*
*[3] U.S. Naval Research Laboratory, Washington, DC 20375*
*[4] Jacobs Corporation, Hanover, MD 21076, USA.*

Previously, interband cascade light-emitting diodes (ICLEDs) grown on GaSb substrates have been demonstrated as useful emitters in the mid-wave infrared (MWIR) region of 3 – 5 µm for room-temperature (RT) continuous wave (CW) operation [1,2]. Transferring this technology to growth on Silicon substrates would be advantageous for applications in chemical sensing and IR scene projectors (IRSPs), providing improved manufacturability through direct integration onto these circuits. This presentation will discuss the comparison of high-performance ICLEDs grown at NRL on GaSb/Si buffers that were grown at UNM and on lattice-matched GaSb substrates, including L-I characteristics, cross-section transmission electron microscopy (XTEM) and x-ray reciprocal space mapping (RSM).

The growth of GaSb/Si involves GaSb buffer layers which were grown on Silicon (001) with a 4° offcut towards (111). The native oxide was removed using a dilute HF solution to obtain a hydrogen-passivated surface. To achieve III-V nucleation on Silicon, a ~10 nm thick AlSb layer was grown at a substrate temperature of 500°C followed by a 1 µm buffer layer and an antimony cap to prevent oxidation. The GaSb/Si wafers were then transferred to NRL where an additional 2-3 µm GaSb buffer and the ungrouped active ICLED stages were grown. This same 22-stage structure was grown on a GaSb substrate as a control sample. Accounting for differences in architecture, the ICLED structures grown on Silicon show efficiencies that are 75% of those measured in ICLEDs grown on GaSb. At 100 mA, 200-µm-diameter mesas produce 184 µW CW at 25°C and 140 µW at 85°C.

Threading dislocations were observed in GaSb buffer grown on Si from the XTEM images, showing a higher density near the Silicon substrate but reduced near the ICLED. Individual dislocations which reached the active ICLED layers exhibited a multiplying effect throughout the structure. Another growth artifact seen in these images was a slow-varying oscillation in the ICLED layers. Our presentation will provide a detailed explanation for both mechanisms and a comparison of the ICLEDs grown on Silicon to those grown on GaSb. Possible strategies for improving the epitaxial quality and device performance will also be discussed.

[1] C. S. Kim et al., Opt. Engr. 57, 011002 (2018).
[2] N. Schäfer et al., Opt. Engr. 58, 117106 (2019).
[+] Author for correspondence: mdfrost@unm.edu

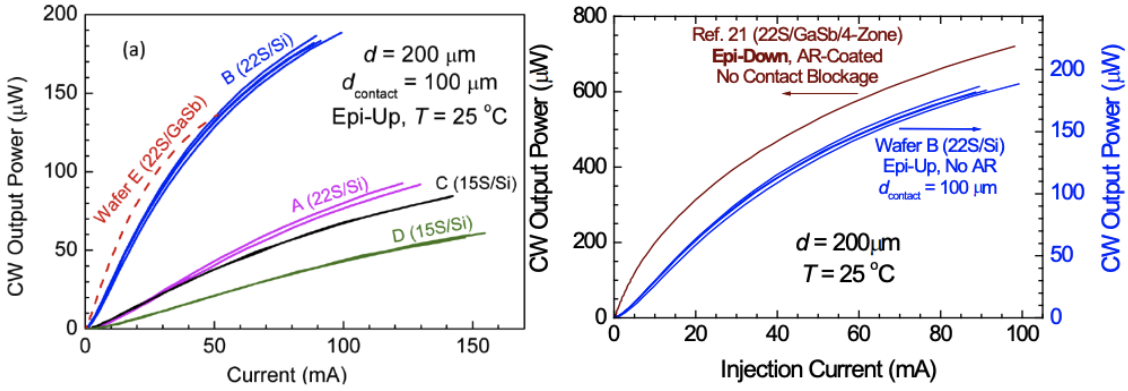


Figure 1 (left) – CW L-I characteristics at room temperature for multiple 200-µm-diameter ICLEDs from Wafers A-D on silicon and control Wafer E on GaSb. Figure 2 (right) - RT CW L-I characteristics of multiple epi-up ICLEDs on Silicon, compared to that for an epi-down and AR-coated ICLED on GaSb, all 200 µm mesa diameter. Adjustment of the right power scale by a factor of 3.3 accounts for architectural differences.

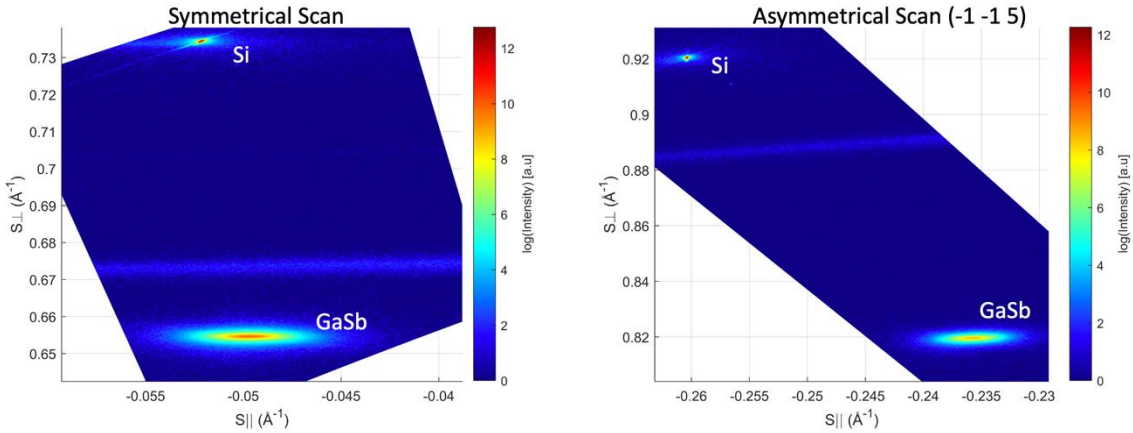


Figure 3 – XRD Reciprocal Space Map of GaSb on Silicon buffer grown at UNM. Threading dislocation density is ~ $10^8$/cm$^3$ and the GaSb is 99.2% relaxed.

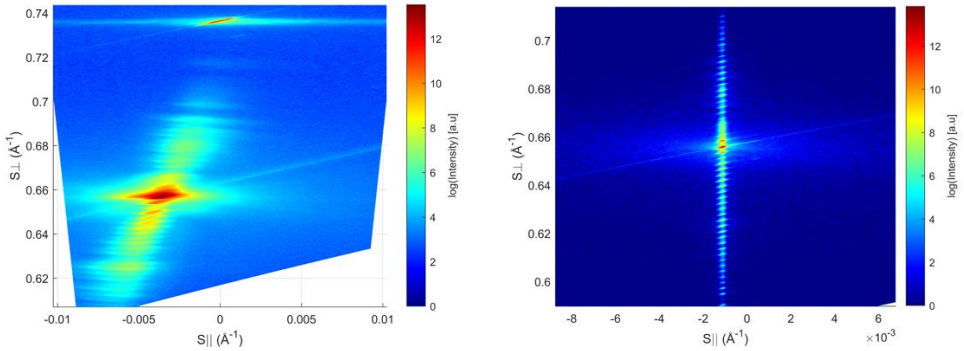


Figure 4 – (left) RSM of ICLED grown on GaSb buffer on Silicon and (right) RSM of ICLED grown lattice matched on GaSb. There is a reduction in the number of fringes in the metamorphic growth due to undulations in the ICLED structure.

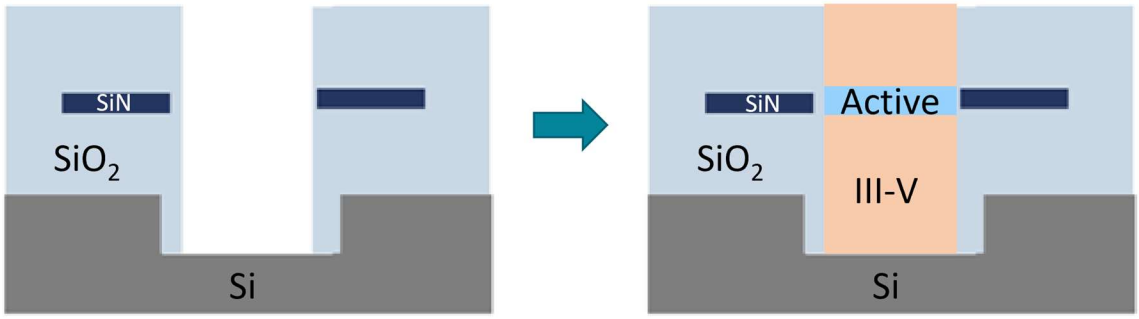


Figure 1: Sketch of the III-V laser stack grown in a pocket on a silicon photonics wafer with the active region aligned to a silicon nitride waveguide.

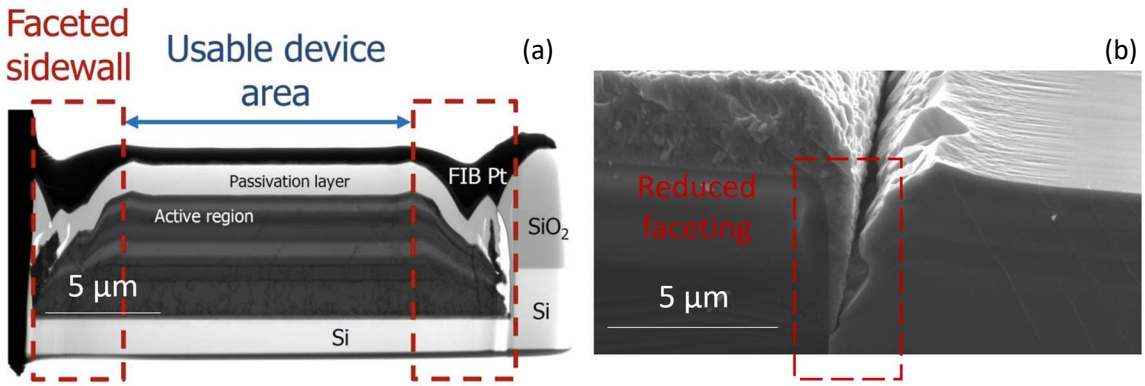


Figure 2: Cross-sectional scanning electron microscope images showing a laser grown under conventional growth conditions with a large gap (a) and a laser grown with a selective buffer and a reduced gap (b).

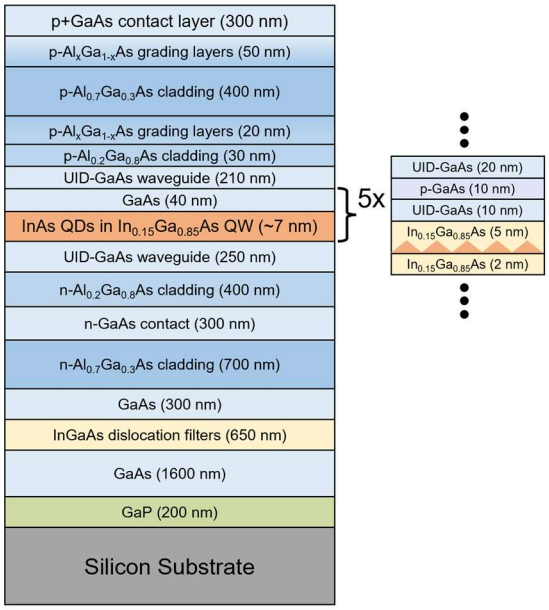


Figure 3: Layer stack of the III-V InAs quantum dot laser structure grown on silicon.

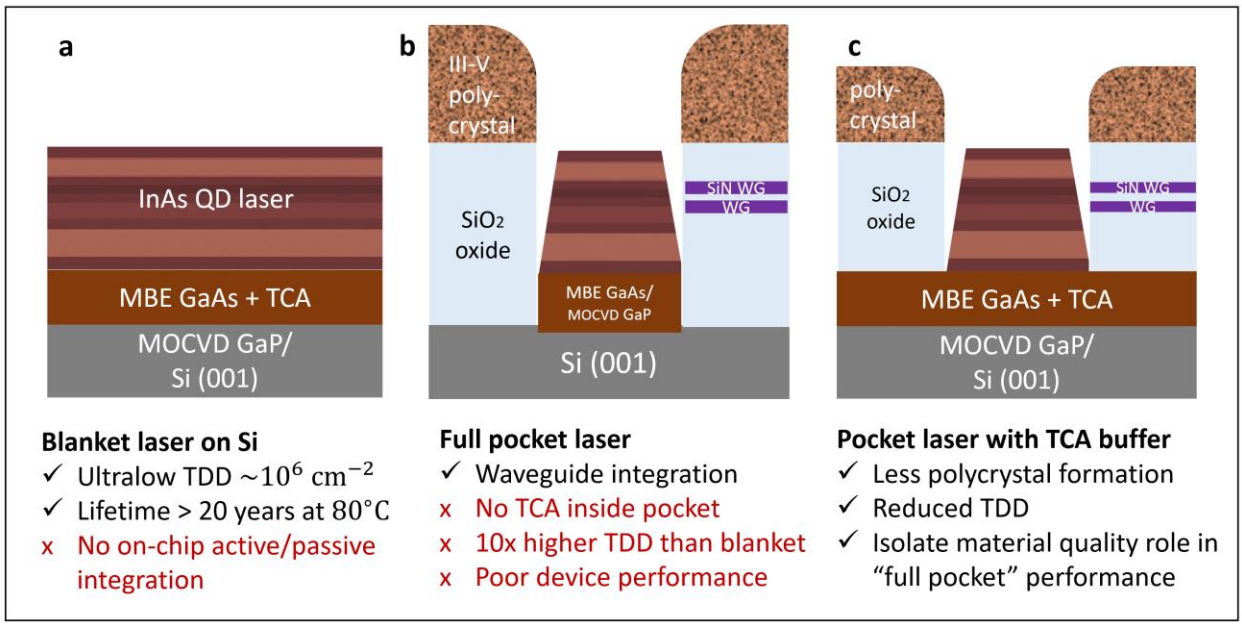


Figure 1. (a) Cross sectional schematic of blanket-grown laser on planar GaP/Si substrate with ultralow threading dislocation density (TDD) after thermal cyclic annealing (TCA). (b) Pocket-grown laser directly on $SiO_2$/Si. (c) New platform for reduced TDD and reduced polycrystal formation, where TCA is applied to a planar buffer prior to $SiO_2$ and passive structure deposition.

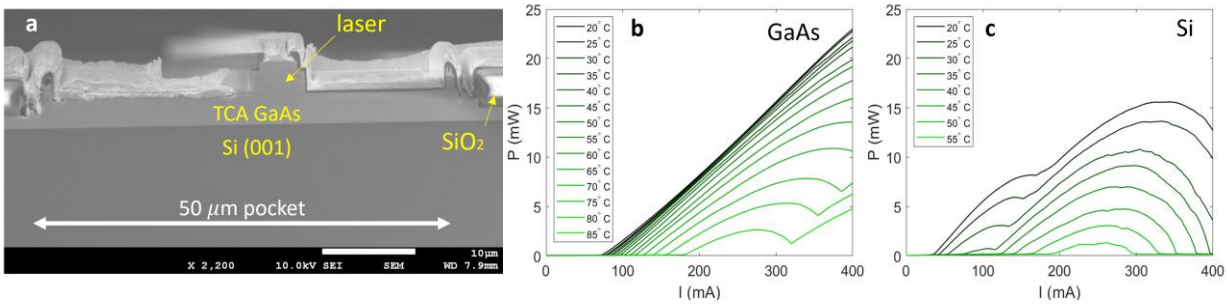


Figure 2. (a) Cross sectional scanning electron microscope image of pocket laser on TCA GaAs/GaP/Si. (b) Comparison of laser light-current characteristics at elevated temperature for blanket GaAs or (c) Si pocket-grown substrate devices.

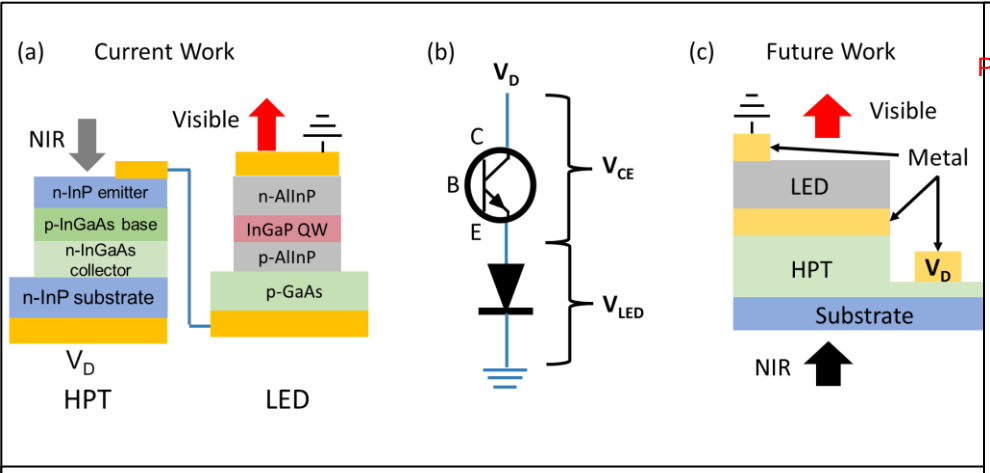


Figure 1: (a) Schematic of the NIR upconverter components in series, as demonstrated in this work. (b) Circuit diagram of the NIR upconverter where $V_D$, $V_{LED}$, and $V_{CE}$ refer to voltage drops across the full device, the LED, and HPT, respectively. (c) Schematic showing future work where the LED will be metal-metal bonded to the HPT with the LED substrate removed.



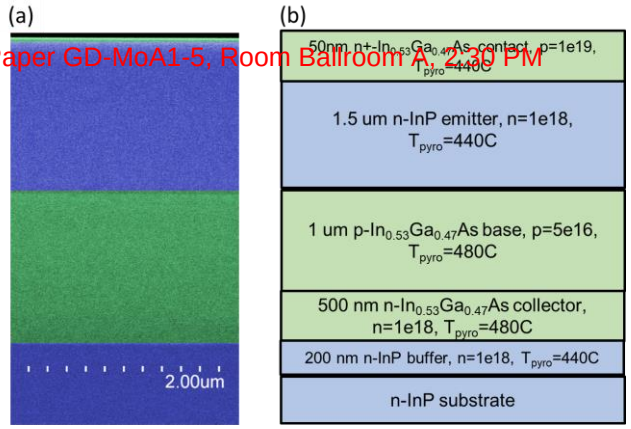


Figure 2: (a) False color cross-sectional SEM of the HPT and (b) stack diagram of the HPT growth labeling the layer composition, thickness, growth temperature, and nominal bulk doping.

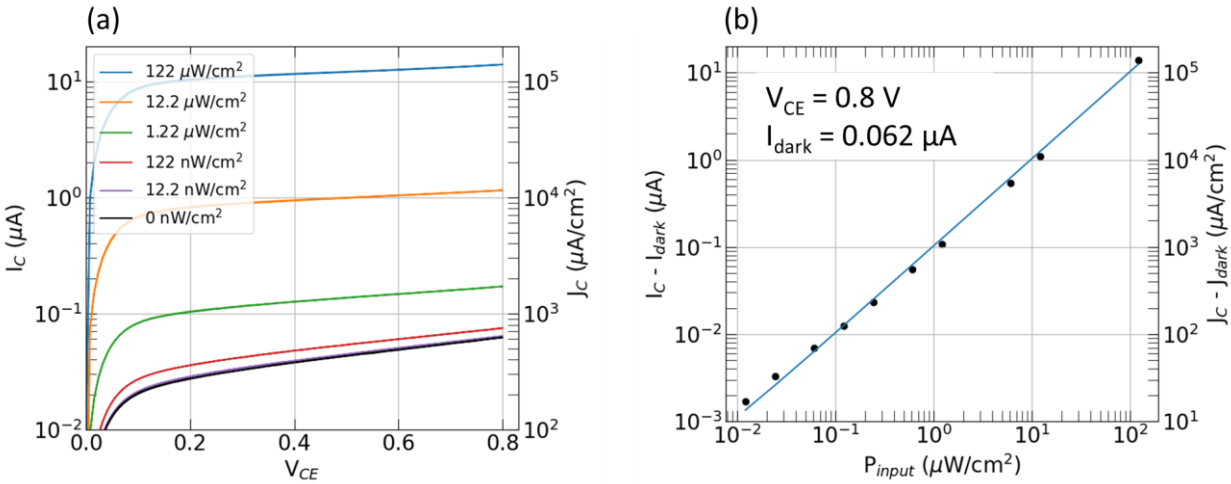


Figure 3: (a) IV characteristics of the HPT under different input powers (λ=1.55 μm). An input power density as low as 12.2 nW/cm² generates a current signal $I_C$ that is distinguishable from the dark current. (b) Current above dark current vs input power ($V_{CE}$ = 0.8V) showing linear response.

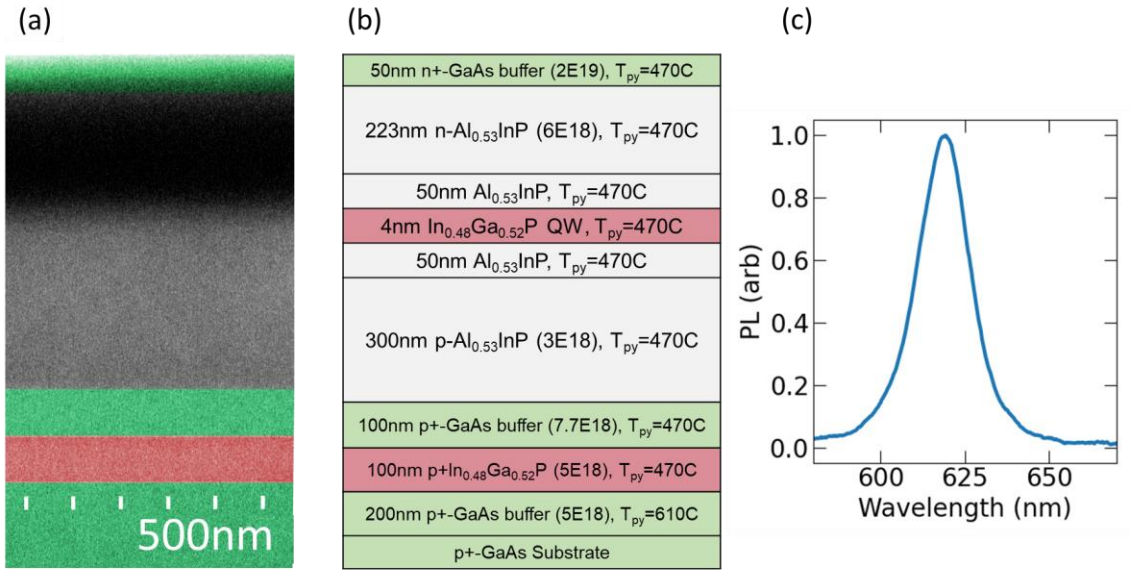


Figure 4: (a) False-color cross-sectional SEM of the visible LED. (b) Stack diagram of the LED growth labeling the layer composition, thickness, growth temperature, and nominal bulk doping. (c) PL spectrum of the RTA'd LED.

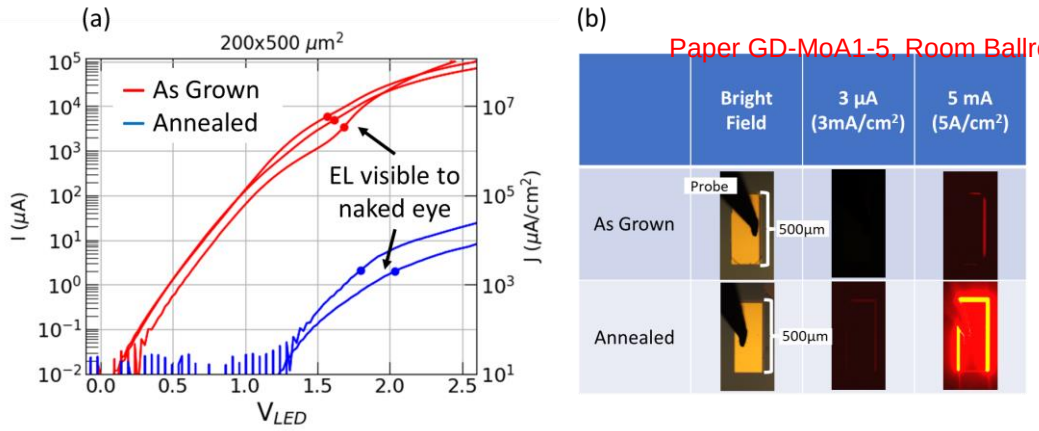


Figure 5: (a) IV characteristics of the LED comparing the device with and without annealing; the RTA'd LED shows high series resistance, which will be addressed in future work. Points indicate where the LED starts to emit light visible to the dark-adapted naked-eye. (b) Images of the devices under a microscope under different operating currents.

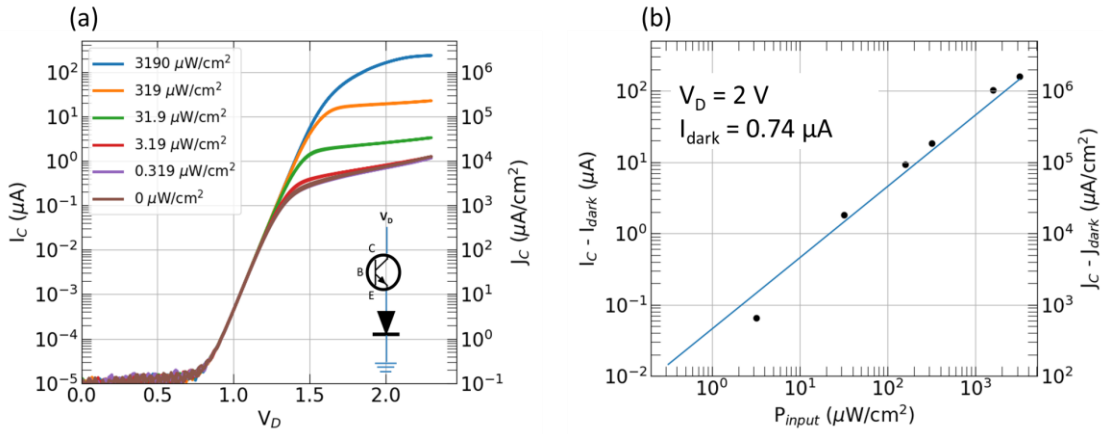


Figure 6: (a) IV characteristics of an HPT and LED in series [as in Fig. 1(b)] under different input powers (λ=1.55 μm). Amplified photocurrent from the HPT turns on the visible LED, clearly demonstrating up-conversion. (b) Current above dark current vs input power ($V_D$ = 2 V). The curve deviates from linearity for input power < 32 μW/cm², but 3.2μW/cm² is still distinguishable from dark current.

Bibliography

1. Spitzer, Cary R., and Cary Spitzer, eds. *Digital Avionics Handbook*. CRC press, (2000): 126-135.

# Supplementary Pages

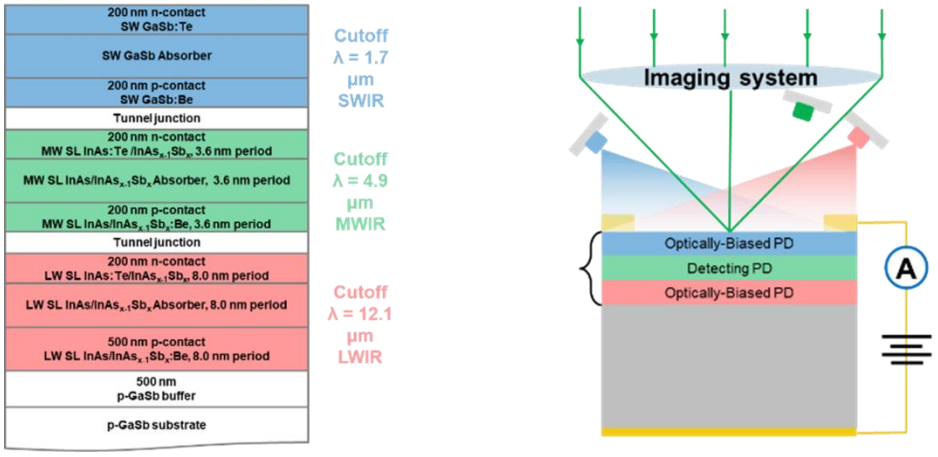


Figure 1: (Left) Triple-band PD layer structure, and (right) its operating principle under optical addressing.

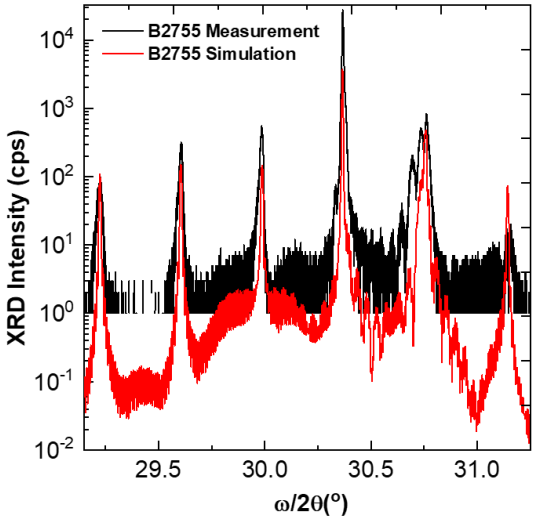


Figure 2: ω/2θ XRD scan of a strain-balanced MWIR T2SL device structure on a GaSb substrate.

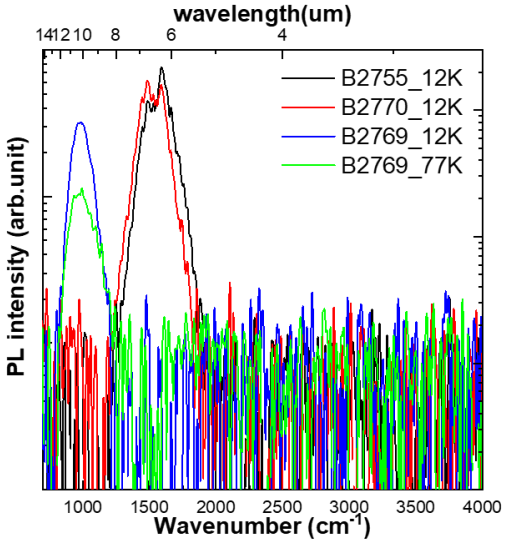


Figure 3: PL spectra of MWIR and LWIR T2SL measured by FTIR showed peaks at 6 10 μm for MWIR and LWIR, respectively.

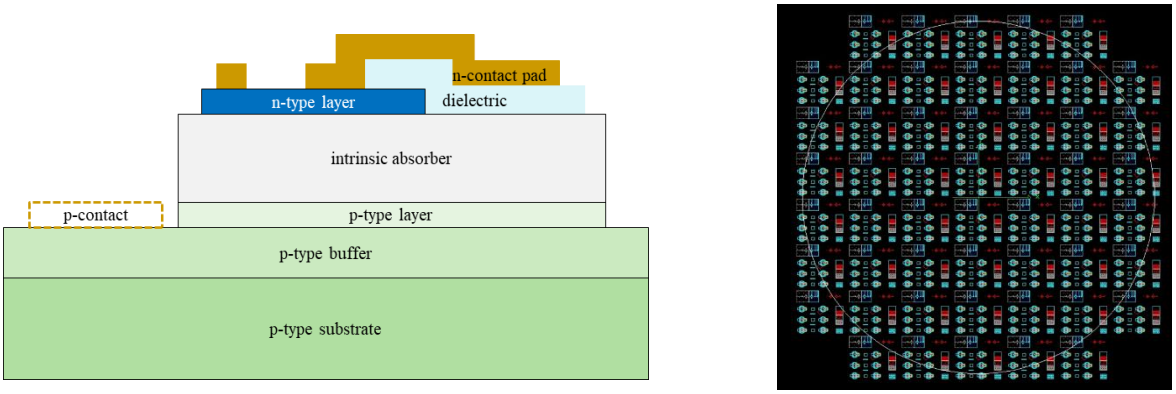


Fig. 4. (left) Cross-section of the PD device design, and device layout (up to 4-inch wafers) with aperture sizes 200, 100, 50μm and metal contact pads.

# Parity-time symmetry single-mode double-microdisk InGaAs quantntum dot lasers

K. F. Lin, C.Y. Xu, and T. S. Lay*,

*Department of Electrical Engineering and Graduate Institute of Optoelectronic Engineering,*

*National Chung Hsing University, Taichung , Taiwan*

*Email: tslay@dragon.nchu.edu.tw

We successfully demonstrate the parity-time symmetry (PT-symmetry) single-mode lasing operation of laterally coupled double-microdisk lasers. The microdisk lasers of disk diameter = 2.85 μm are fabricated by using MBE-grown InGaAs quantum dots as the gain medium. The gain materials of dots-in-a-well (DWELL) structures are grown on (001) $n^+$-GaAs substrate by molecular beam epitaxy. The wafer structure consists of a 1 μm-thick $Al_{0.5}Ga_{0.5}As$ sacrifice layer, and an active layer comprised of a stack of six InGaAs DWELLs. In spite of the lasing output of multiple whispering-gallery modes (WGMs) from the single microdisk lasers, the laterally coupled double-microdisk lasers achieve single WGM lasing under gain-loss contrast pumping condition, literally pumping only one disk for the double- microdisk. We change the air gap distance (*d*) for the coupled double-microdisk structures to change the coupling strength (*k*) between the microdisks. Under single selective pumping (gain-loss contrast) at room temperature, the laterally coupled double microdisk lasers of *d* = 150nm, and 200nm show single lasing mode at WGM m = 1, 21 (λ = 1199nm). We also fabricate the double-microdisk lasers by coating the microdisks with $HfO_2$ to change the coupling strength *k*. Under single selective pumping, the $HfO_2$–coated double microdisk lasers show a single lasing mode at WGM m = 1, 20 (λ= 1277nm).

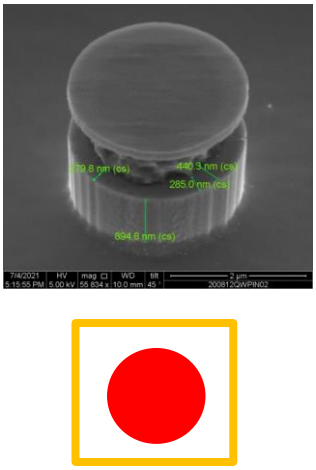

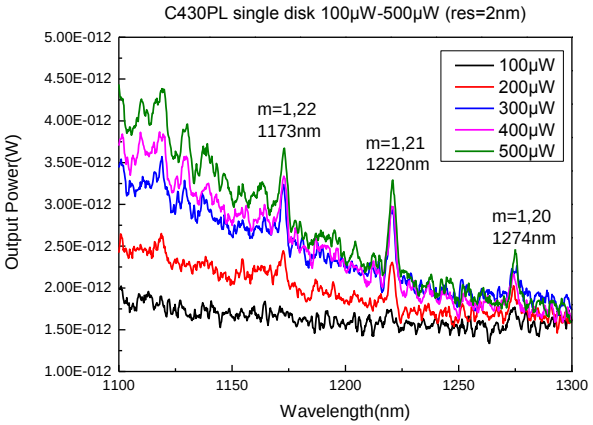


Fig. 1. SEM picture fora single microdisk of diameter = 2.85 μm, and the lasing output of multiple WGMs .

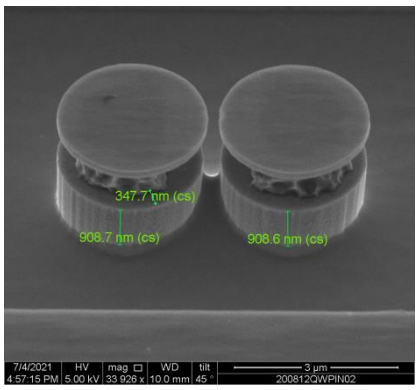


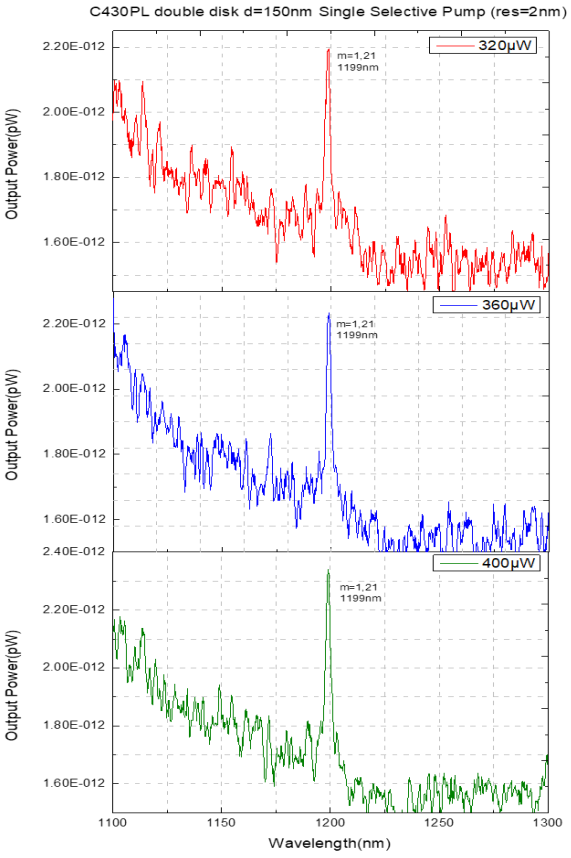


Fig. 2. Under single selective pumping (gain-loss contrast) at room temperature, single lasing mode at WGM m = 1,21 (λ = 1199nm) is obtained for the laterally coupled double- microdisk laser of *d* = 150nm.

# Impact Ionization Coefficients of $Al_xGa_{1-x}AsSb$ ($x$=0 – 1) Lattice Matched to InP Substrates

S. Lee[1], X. Jin[2], H. Jung[1], J. P. R. David[2], and S. Krishna[1*]

[1]Department of Electrical and Computer Engineering, The Ohio State University, Columbus, Ohio, 43210, USA
[2]Department of Electronic and Electrical Engineering, University of Sheffield, Sheffield S1 3JD, UK
[*]Corresponding author: krishna.53@osu.edu

**Abstract**

Impact ionization is a crucial process in the physics of semiconductors that influences the operation and performance of various semiconductor devices. It is utilized in avalanche photodiodes (APDs) to increase signal-to-noise ratio, but it can also lead to avalanche breakdown in electronic devices. To ensure reliable device operation, it is vital to determine the impact ionization coefficients of electrons and holes ($\alpha$ and $\beta$), respectively. In this study, we present the $\alpha$ and $\beta$ for a range of $Al_xGa_{1-x}AsSb$ compositions, covering $x$ from 0 to 1, as determined through measurements of avalanche multiplication. Additionally, we explore the relationship between the impact ionization coefficients and the bandgap ($E_g$) change ($\Gamma$ and $X$ points) along with the indirect-to-direct transition. This is because the impact ionization process is influenced by the material's band structure and the $E_g$.

Four PIN $Al_xGa_{1-x}AsSb$ APDs with $x$ of 0, 0.5, 0.65 and 0.85 were grown on InP using the RIBER Compact 21DZ molecular beam epitaxy, and standard photolithography with a citric-based wet-etch technique was used to fabricate devices for electrical characterizations. The measured photocurrent spectra of the four APDs are presented in Fig. 1 (a), which illustrates that the cut-off tail moves toward lower energy as the $x$ gradually decreases. To investigate the behavior of the $E_g$ with various Al compositions, the $E_{g,\Gamma}$ and $E_{g,X}$ were extracted, as shown in Fig. 1 (b), and compared with the theoretical change in $E_g$ proposed by Adachi [1]. The discrepancy of $E_g$ between the theory and experiment may come from the alloy disorder that can induce lower $E_g$ than expected in the theoretical calculation. The result suggests that the cross-over should happen around $x$=0.5 which is similar value predicted by Adachi [1].

The $\alpha$ and $\beta$ for $Al_xGa_{1-x}AsSb$ with $x$=0, 0.85 [2], and 1 [3] were plotted as a function of inverse electric field as shown in Fig. 2 (a). Fig. 2 (b) illustrates the $\alpha$ and $\beta$ for $Al_xGa_{1-x}AsSb$ with $x$=0, 0.85, and 1 as a function of $x$ at 290 kV/cm. The α remains fairly constant until $x$=0.85, where it jumps up at $x$=0, while the $\beta$ gradually increases as the $x$ decreases from 1 to 0. This suggests that the $\alpha$ can change abruptly at a critical $x$ point, and a similar point may exist for the rate of change in the $\beta$, as seen in other material systems such as AlGaInP and AlGaAs on GaAs [4]. To gain more insight, we will explore the behavior of $E_g$ and $\alpha$ and $\beta$ for additional $x$=0, 0.2, 0.4, 0.45, 0.50, 0.55, 0.65, 0.75, 0.85, and 1 in $Al_xGa_{1-x}AsSb$. Knowing these coefficients and $E_g$ parameters will allow engineers and scientists to design and optimize the performance of optoelectronic and electronic devices.

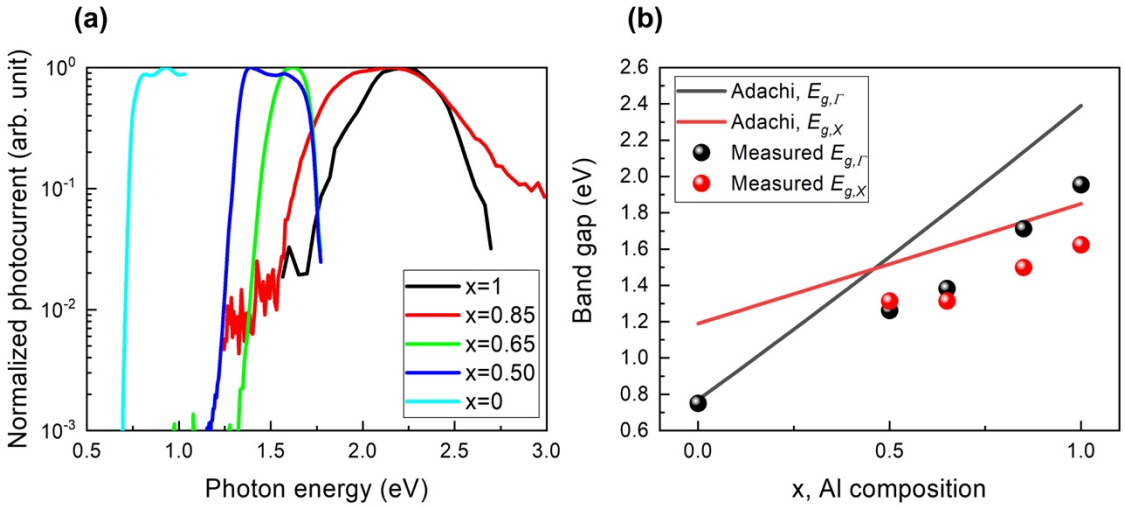


Figure 1 (a) The photocurrent spectra of $Al_xGa_{1-x}AsSb$ (x=0, 0.5, 0.65, 0.85, and 1) and (b) their band gap change as a function of Al composition. The measured bandgaps were compared with the ones theoretically calculated by Adachi.

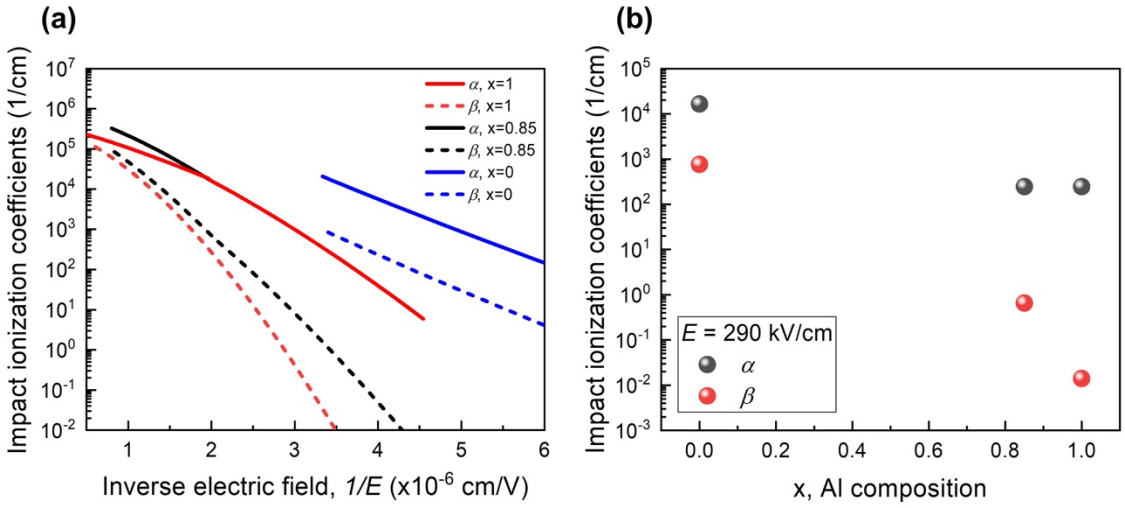


Figure 2 (a) Impact ionization coefficients ($\alpha$ and $\beta$) of $Al_xGa_{1-x}AsSb$ (x=0, 0.85, and 1) as a function of inverse electric field. (b) The $\alpha$ and $\beta$ values extracted at 290 kV/cm as a function of Al composition.

## References

[1] S. Adachi, *Properties of semiconductor alloys: group-IV, III-V and II-VI semiconductors*. John Wiley & Sons, 2009.

[2] B. Guo *et al.*, "Impact ionization coefficients of digital alloy and random alloy Al 0.85 Ga 0.15 As 0.56 Sb 0.44 in a wide electric field range," *Journal of Lightwave Technology,* vol. 40, no. 14, pp. 4758-4764, 2022.

[3] X. Yi *et al.*, "Extremely low excess noise and high sensitivity AlAs 0.56 Sb 0.44 avalanche photodiodes," *Nature Photonics,* vol. 13, no. 10, pp. 683-686, 2019.

[4] H. I. Lewis *et al.*, "Impact Ionization Coefficients in (Al x Ga 1-x) 0.52 In 0.48 P and Al x Ga 1-x As Lattice-Matched to GaAs," *IEEE Transactions on Electron Devices,* vol. 68, no. 8, pp. 4045-4050, 2021.

## Acknowledgement

This work was supported by the Advanced Component Technology (ACT) program of NASA's Earth Science Technology Office (ESTO) under Grant No. 80NSSC21K0613.

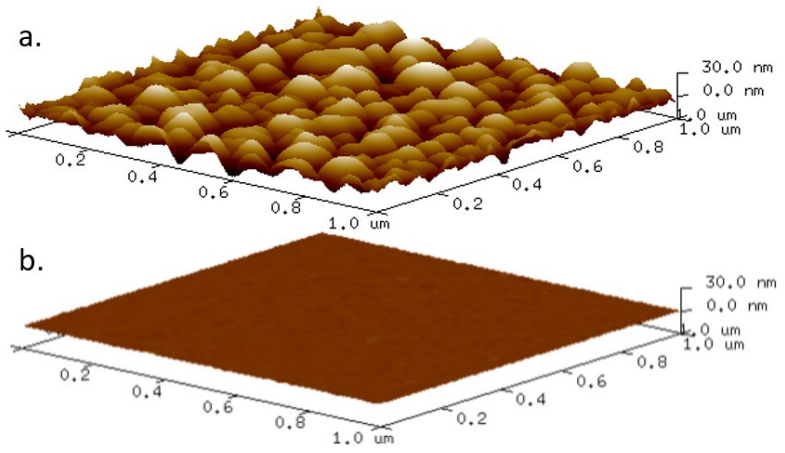


AFM scans of two aluminum layers grown on $In_{0.75}Ga_{0.25}As/In_{0.53}Ga_{0.47}As$ (6nm/100nm) on the InP(001) substrate. **In both cases, the nominal thickness of the Al layer was 10 nm.**

a. The layer was deposited at 0.5 Å/s.
b. The layer was deposited at 3.0 Å/s.

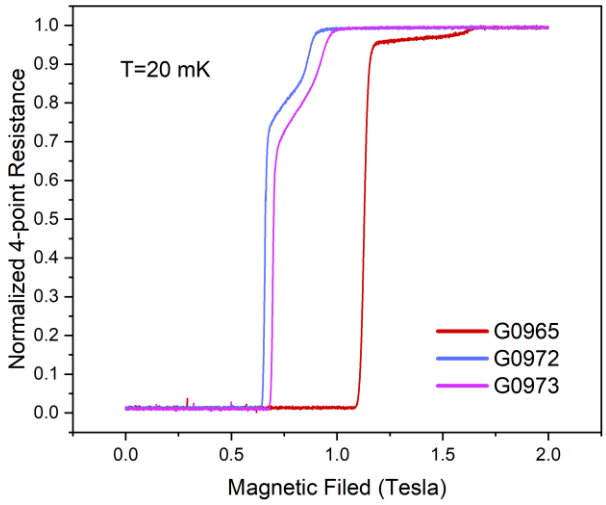


Superconducting to normal phase transition signatures for three Al layers:

G0972 was deposited at 3.0 Å/s (10 nm thick)
G0973 was deposited at 2.0 Å/s (10 nm thick)
G0965 was deposited at 2.0 Å/s (8.6 nm thick)

**Layers deposited at lower growth rates did not show superconductive behavior.**

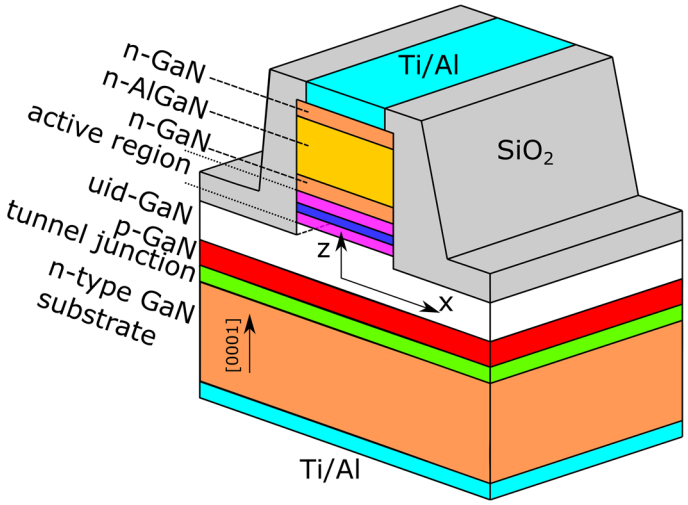


Figure 1. Schematic image of the bottom tunnel junction laser diode.

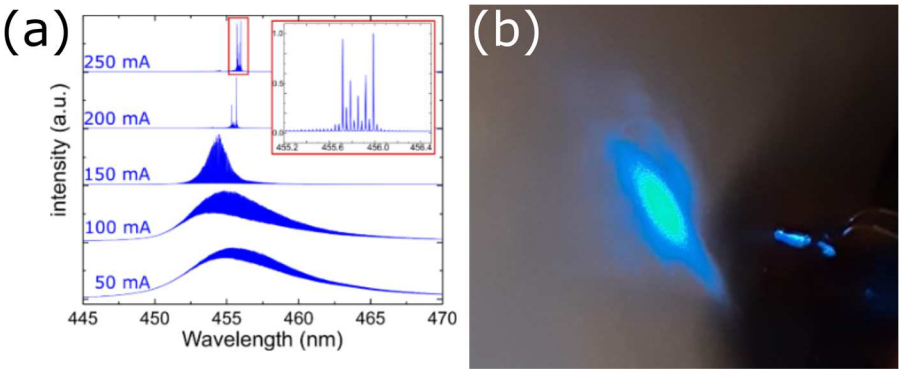


Figure 2. (a) Emission spectra for different driving currents with inset showing zoomed-in spectra at 250 mA. (b) Real-color picture of the farfield of the bottom tunnel junction laser diode directed onto sheet of paper.

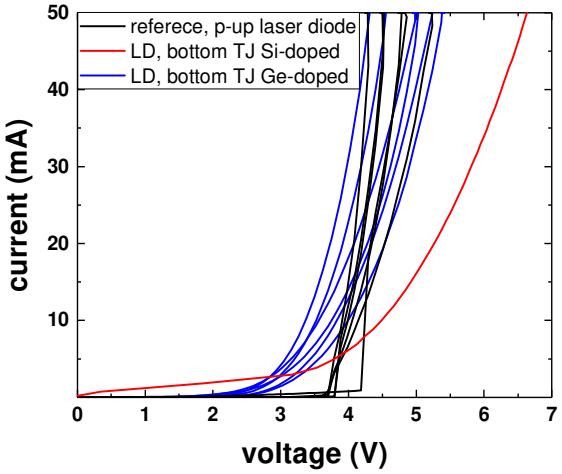


Figure 3. Comparison of current-voltage characteristics for the reference p-up laser diode with Si- and Ge-doped bottom tunnel junction laser diode.

**Title:** Zeeman Field-Induced Two-Dimensional Weyl Semimetal Phase in Cadmium Arsenide Thin Films


## Abstract

We report a topological phase transition in MBE-grown, quantum-confined cadmium arsenide ($Cd_3As_2$) thin films under an in-plane Zeeman field when the Fermi level is tuned into the topological gap via an electric field. Symmetry considerations in this case predict the appearance of a two-dimensional Weyl semimetal (2D WSM), with a pair of Weyl nodes of opposite chirality at charge neutrality that are protected by space-time inversion ($C_2T$) symmetry. We show that the 2D WSM phase displays unique transport signatures, including saturated resistivities on the order of $h/e^2$ that persist over a range of in-plane magnetic fields. Moreover, applying a small out-of-plane magnetic field, while keeping the in-plane field within the stability range of the 2D WSM phase, gives rise to a well-developed odd integer quantum Hall effect, characteristic of degenerate, massive Weyl fermions. A minimal four-band $k \cdot p$ model of $Cd_3As_2$, which incorporates first-principles effective $g$ factors, qualitatively explains our findings.


## Figure

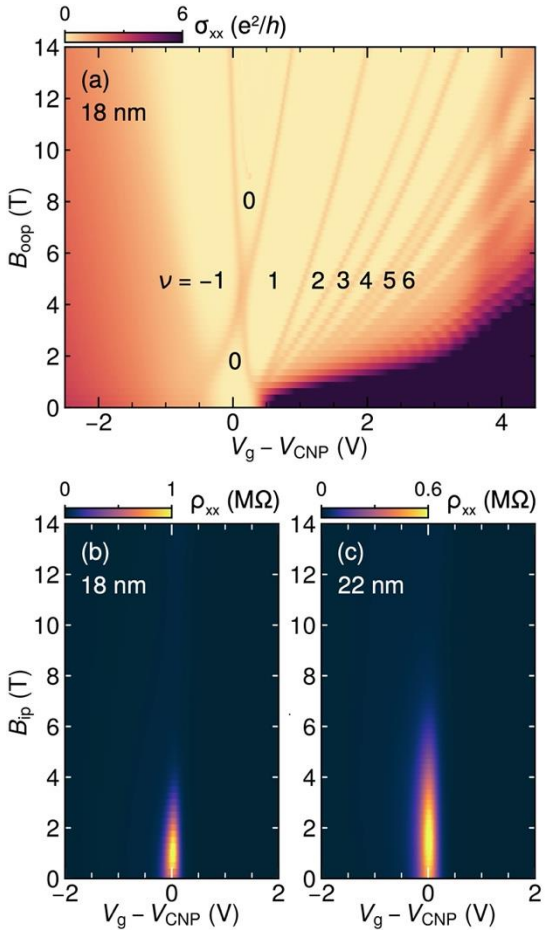


## Caption

Out-of-plane and in-plane magnetotransport. **(a)** Longitudinal conductivity $\sigma_{xx}$ as a function of the out-of-plane field $B_{oop}$ and the scaled (relative to $V_{CNP}$) top-gate voltage for the 18 nm $Cd_3As_2$ sample (device, hb1). Quantum Hall plateau regions are indexed by their filling factor ν up to 6. The measured voltage $V_g$ is offset by $V_{CNP}$, which corresponds to the charge neutrality condition. **(b)** Longitudinal resistivity $\rho_{xx}$ as a function of the in-plane field $B_{ip}$ and the top-gate voltage for the 18 nm $Cd_3As_2$ sample (device, hb1). The same is shown in (c) for the 22 nm sample. $V_{CNP} = -1.35$ V for the 18 nm sample, $V_{CNP} = -1.165$ V for the 22 nm sample. Measurements were done at $T = 2$ K in the transverse configuration.

## Reference:


B. Guo … S. Stemmer, *Phys. Rev. Lett.* 131, 046601 (2023)

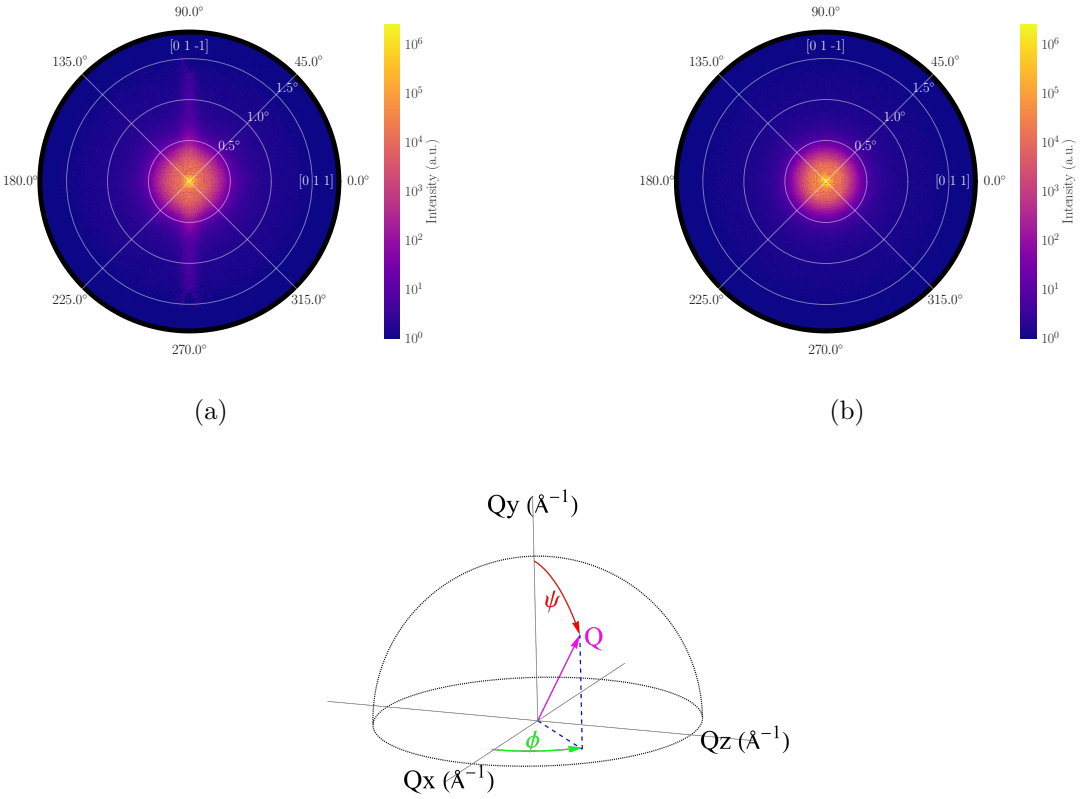


Figure 1: Two Polar plots of reciprocal space. The two coordinates of each point on the plot correspond to, an amount of tilt, $\psi$, away from the exact (001) planes and also an azimuthal angle, $\phi$, that indicates the direction of the tilt. The relative intensities of points on the plot reveal what proportion of the crystal structure is tilted in that direction. Figure (a) corresponds to sample A and Figure (b) corresponds to sample B. The tilt $\psi$ is measured as the radius and $\phi$ is the azimuthal angle measured counter-clockwise from the positive x axis. At $\phi = 0°$ the incident X-ray beam is travelling in the [011] crystallographic direction. Figures (a) and (b) can be thought of as a 2D projection of the surface of the hemisphere shown in (c).

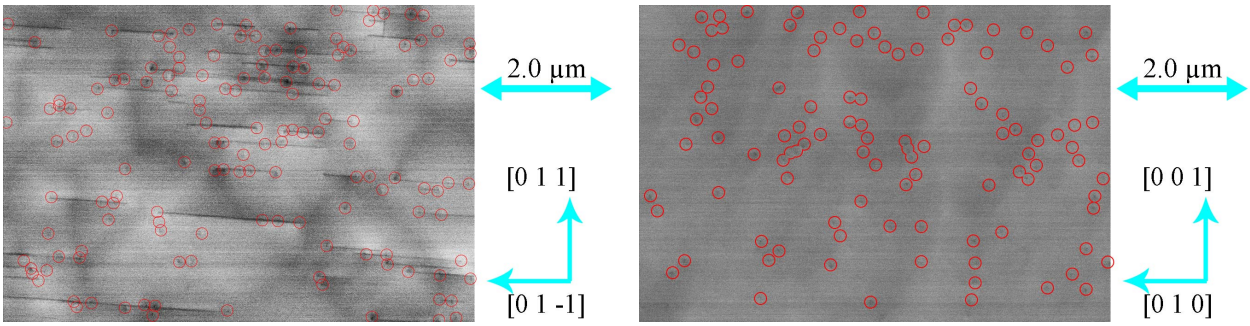


Figure 2: Scanning electron microscope ECCI images for (a) sample A and (b) sample B. Small dots of increased contrast caused by TDD are circled in red. The corresponding crystallographic directions and image scale are indicated by the blue arrows on the right.

# Multicolor micrometer scale light emitting diodes monolithically grown on the same chip

Yifu Guo[1], Yixin Xiao[1], Yakshita Malholtra[1], Yuanpeng Wu[1], Samuel Yang[1], Jiangnan Liu[1], Ayush Pandey[1], and Zetian Mi*,[1]
1) Department of Electrical Engineering and Computer Science, University of Michigan, Ann Arbor, MI 48109, USA
*Corresponding author: ztmi@umich.edu

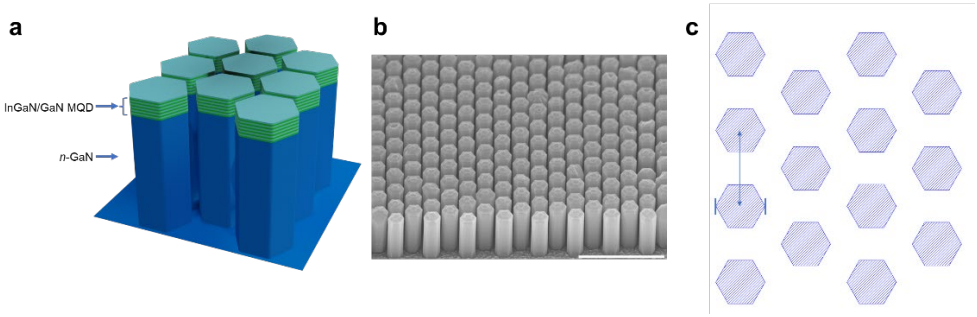


**Figure 1.** Schematics and structural characterization of a nanowire array. (a) Schematic of the nanowire array with a green InGaN/GaN multiple-quantum-dot (MQD) design for the active region. (b) A sample scanning electron microscopy of such a nanowire array. The scale bar (in white) is 1 micron. (c) Layout of the two-dimensional honeycomb shaped photonic crystal, which is parametrized by nanowire diameter and lattice constant. The two vertical lines indicate the nanowire diameter length, and the vertical double-headed arrow indicates the lattice constant length in this sample crystal design.

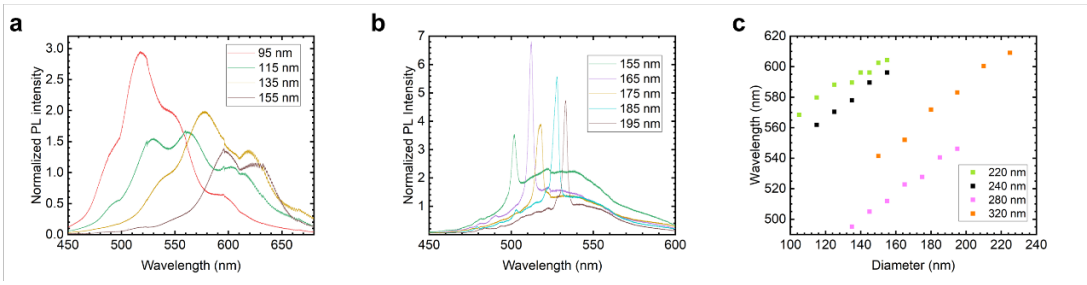


**Figure 2.** Variation in photoluminescence peak wavelength due to varying nanowire diameter. (a) Photoluminescence spectra for nanowire arrays with a classic multiple-quantum-disk design but different nanowire diameters. The lattice constant is 240 nm

for all curves here. (b) The peak wavelength of photonic crystal mode emissions can be modulated with the nanowire diameter as well. The lattice constant is 280 nm for all curves here. (c) Scatterplot showing the effect of peak wavelength modulation persists for different lattice constants.

## References

[1] A. W. Bett and O. V. Sulima. GaSb photovoltaic cells for applications in TPV generators. *Semiconductor Science and Technology*, 18(5):S184, April 2003.

[2] T. N. Danilova, B. E. Zhurtanov, A. N. Imenkov, and Yu. P. Yakovlev. Light-emitting diodes based on GaSb alloys for the 1.6–4.4 m mid-infrared spectral range. *Semiconductors*, 39(11):1235–1266, November 2005.

[3] Daniel Kandel and Efthimios Kaxiras. The surfactant effect in semiconductor thin film growth, January 1999. arXiv:cond-mat/9901177.

[4] Shouzhu Niu, Zhipeng Wei, Xuan Fang, Dengkui Wang, Xinwei Wang, Xian Gao, and Rui Chen. Brief Review of Epitaxy and Emission Properties of GaSb and Related Semiconductors. *Crystals*, 7(11):337, November 2017. Number: 11 Publisher: Multidisciplinary Digital Publishing Institute.

[5] B. Z. Nosho, B. R. Bennett, E. H. Aifer, and M. Goldenberg. Surface morphology of homoepitaxial GaSb films grown on flat and vicinal substrates. *Journal of Crystal Growth*, 236(1):155–164, 2002.

## RESULTS AND DISCUSSION:

The $Al_{0.34}Ga_{0.66}N/GaN$ microfabricated Hall sensor [**Fig. 1(b)**], where evaluation of the 2-DEG is achieved by investigating the Hall voltage which has direct influence on drift velocity of carrier, as a function of thermal aging time. Fabricated Micro-Hall sensor sensitivity tested under constant current and voltage bias mode for all thermal annealing protocol, corresponding data presented in **Fig. 2(a & b)**. The efficiency of $Al_{0.34}Ga_{0.66}N/GaN$ micro-Hall sensor under thermal aging, we calculated the Absolute Sensitivity ($S_A$), of a Hall device is defined as the change in output Hall voltage ($V_H$) divided by the change in applied magnetic field (H) i.e., $S_A = G_H \frac{r_H}{qN_{2deg}} I_b --(1)$. Similarly, Supply Current Related Sensitivity ($S_{scrs}$) expressed as $S_{scrs} = G_H \frac{r_H}{qN_{2deg}} --(2)$, and Supply Voltage Related Sensitivity ($S_{svrs}$) can be defined as $S_{svrs} = G_H \frac{r_H}{RqN_{2deg}} --(3)$ which implies that $S_{svrs} = \mu_H G_H \frac{r_H}{\left(\frac{L}{W}\right)} --(4)$. From above relation, it is clear that current-related sensitivity ($S_{scrs}$) is inversely proportional to ($n_s$) and the voltage-related sensitivity ($S_{svrs}$) is directly proportional to electron mobility. The measured taken current-related sensitivity ($S_{scrs}$) were found to be 74 $VA^{-1}T^{-1}$ and 82 $VA^{-1}T^{-1}$ (SCRS), and voltage-related sensitivity ($S_{svrs}$) are measured to be 0.053 $T^{-1}$ and 0.051 $T^{-1}$ (SVRS) for pristine sample and after 2800 hours thermal aging at 200 $^oC$ in air. As we seen from **Fig. 2** there will be ~2% improvement in SCRS and ~2% change in SVRS of the Hall sensor after a prolonged baking times of 2800 hours at 200 $^oC$. As expected, the Hall sensor has the ability to survive at 200 $^oC$ in air for an extended period of time. The slight increasing trend of SCRS and decreasing trend of SVRS with heating due to the combined changes in sheet carrier density and mobility ($n_s\mu$).

## CONCLUSIONS:

We have investigated the temperature response of $Al_{0.34}Ga_{0.67}N/GaN$ Hall sensors, in terms of the Hall sensitivity, and Ohmic contacts during thermal aging at 200 $^oC$ for up to 2800 hours under atmospheric conditions. The MBE grown $Al_{0.34}Ga_{0.67}N/GaN$ Hall sensors were characterized by using HR-XRD, micro-Raman, and XPS on Hall sensor device before and after thermal aging time. To compare the performance of the Hall sensor we have correlated the structural evolution in $Al_{0.34}Ga_{0.67}N/GaN$ Hall sensor heterostructures with measured electric response of Hall device. Results indicate that the $Al_{0.34}Ga_{0.67}N/GaN$ Hall sensor provides stable performance for as long as 2800 hours aging at 200 $^oC$ without any significant degradation to the sensitivity, and Ohmic contacts. However, this study conducted for Hall sensor device does not have surface passivation, though we have noticed the out-diffusion of 'Ga' and 'Al' does not affect much on performance of the Hall sensor. Addition we have found initial stage of contacts resistance droop which could be due to out 'Ga' or Al diffusion process may be consequence of a reduction of oxygen concentration at the GaN/Ti interface resulting in a reduced contacts barrier height. The 'Pt' based ohmic contact enables bumpy free surface morphology after 800$^oC$ RTA.

**FIGURES:**

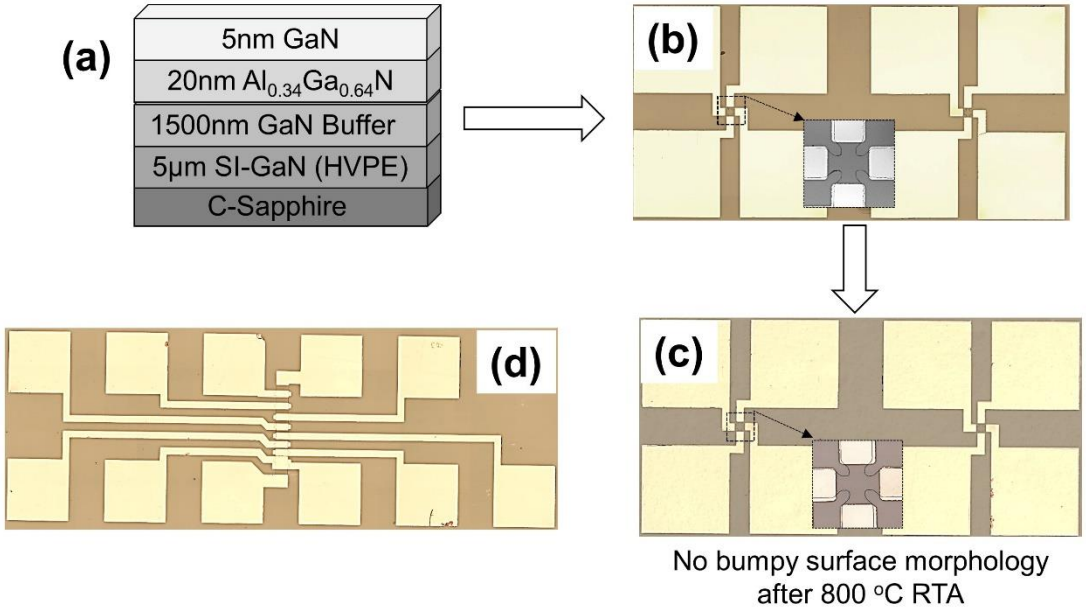


**Fig. 1. (a)** Cross-sectional growth diagram of AlGaN/GaN Hall sensor, **(b)** Plan view of Greek-Cross Hall sensor device before RTA, **(c)** Plan view of Greek-Cross Hall sensor device after Ohmic contact after RTA annealing **(d)** TLM structure used for contact resistance measurement.

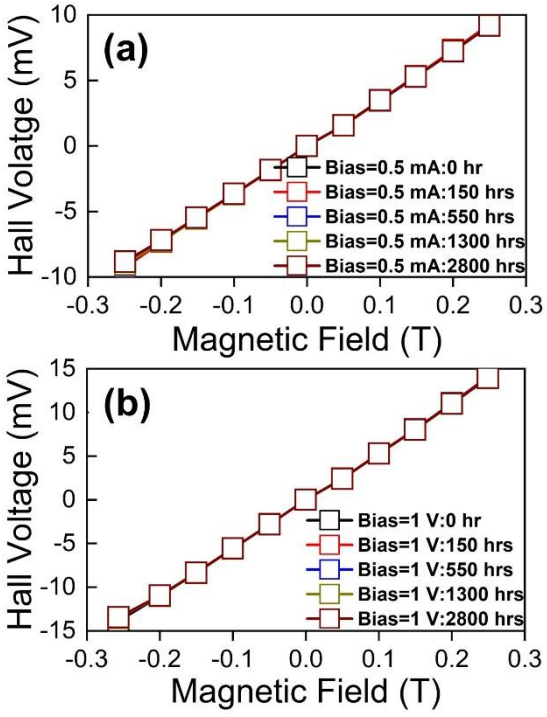


**Fig. 2.** Measured **(a-b)** Micro-Hall sensor have a linear response to magnetic field, both in current and voltage bias mode over a wide range of thermal annealing time at 200 °C in atmospheric condition.

# Optimization of Heteroepitaxial $ZnGeN_2$/GaN Quantum Wells for Green LEDs

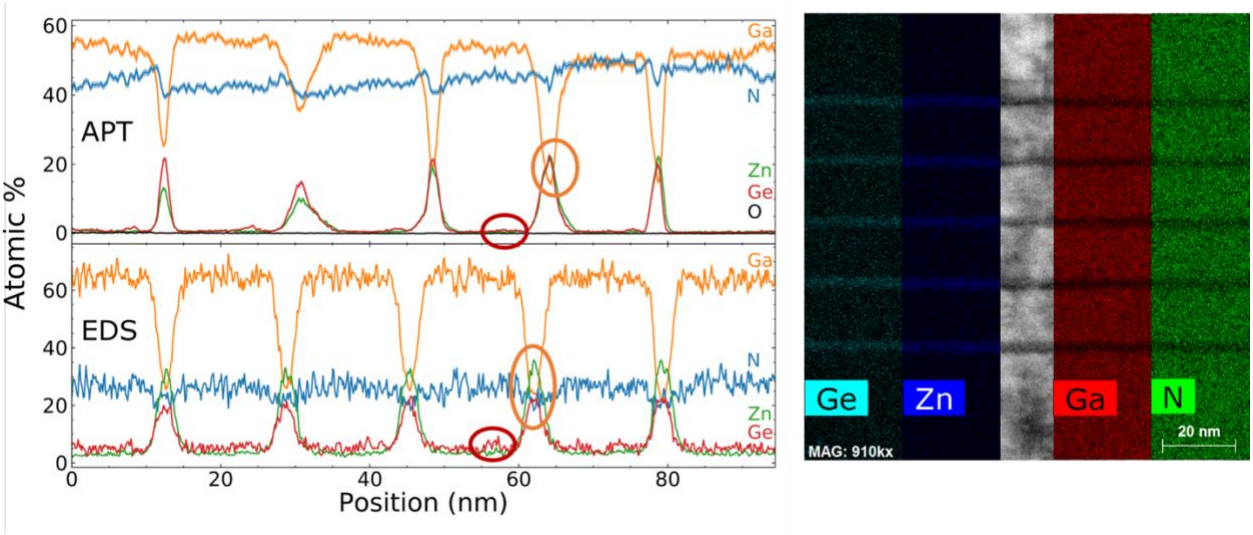


Figure 1: (left) APT (top) and EDS (bottom) of the $ZnGeN_2$/GaN five-unit quantum well, showing unintentional incorporation of Ge and Ga; (right) STEM/EDS of a 5 MQW $ZnGeN_2$/ GaN heterostructure showing clear abrupt interfaces.

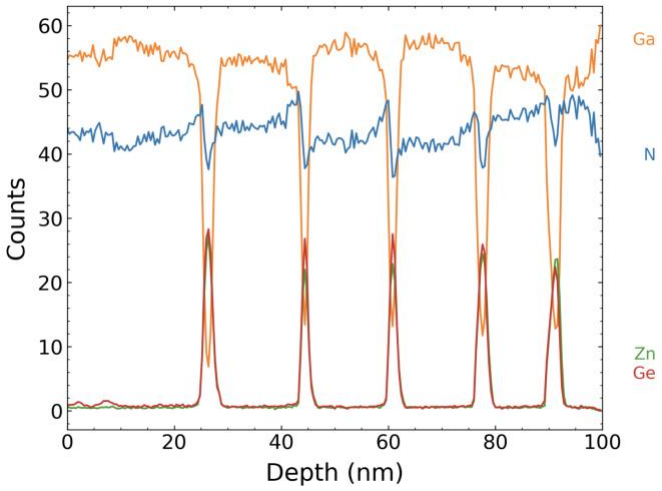


Figure 2: APT of the optimized $ZnGeN_2$/GaN five-unit quantum well, showing reduced unintentional incorporation of Ge and Ga.

Machine Learning Analysis and Predictions of PAMBE III–Nitride Growth

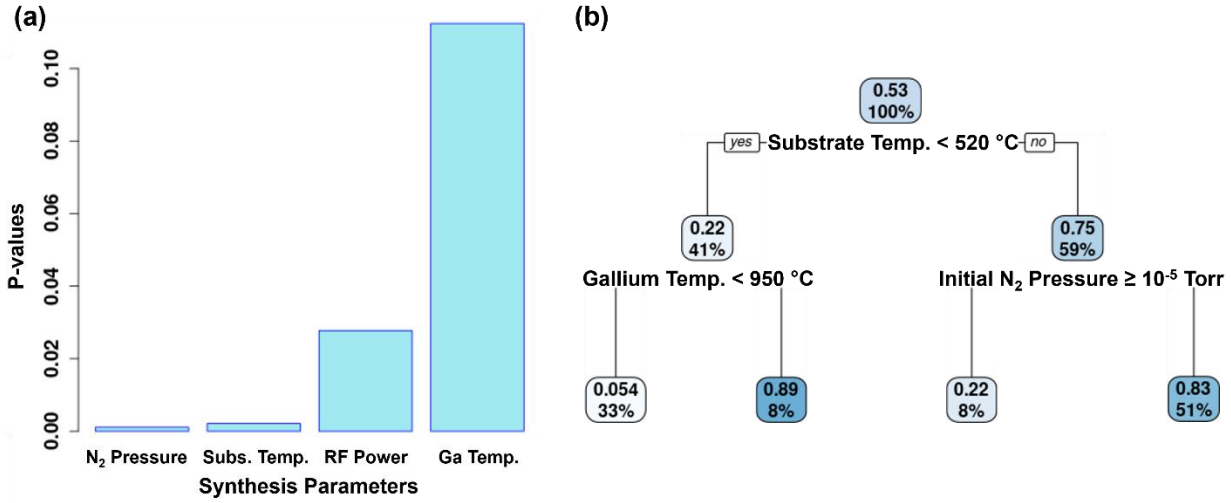


Figure 1: (a) P–values for GaN growth parameters – initial nitrogen pressure, substrate temperature, RF plasma source power, and gallium effusion cell temperature – measured with respect to the crystallinity value. (b) Decision tree fit to the GaN synthesis parameter data indicating the splitting rules which most accurately predict the crystallinity value in the GaN growth data.

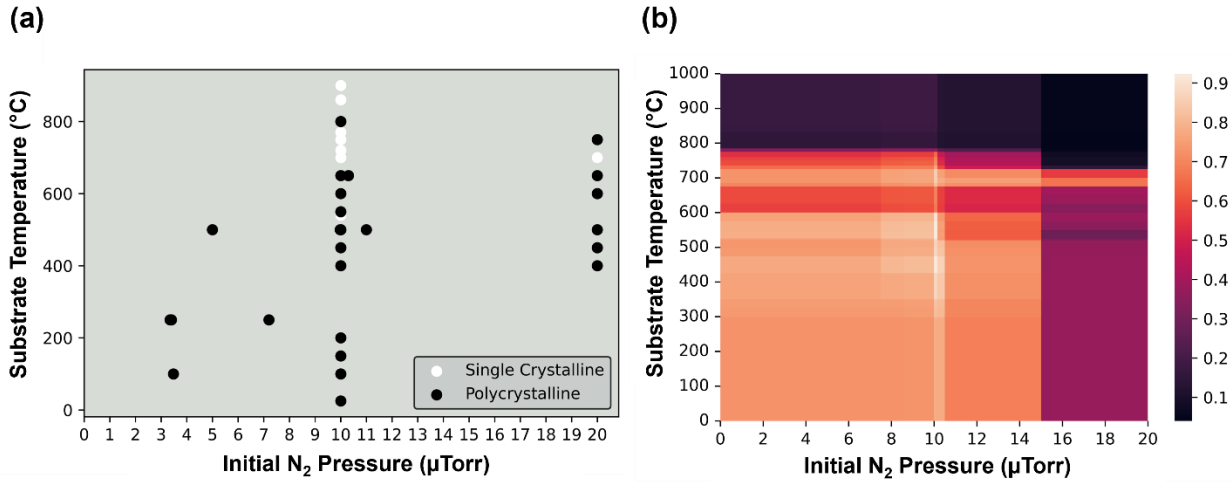


Figure 2: (a) Distribution of GaN training data points across a synthesis space of the two most statistically significant growth variables. (b) Class conditional probability value of a GaN sample growing as single crystalline as predicted by a random forest ensemble algorithm trained upon the growth data. During these predictions, the gallium effusion cell temperature was held constant at 960 °C and the RF plasma power was held constant at 350 W.

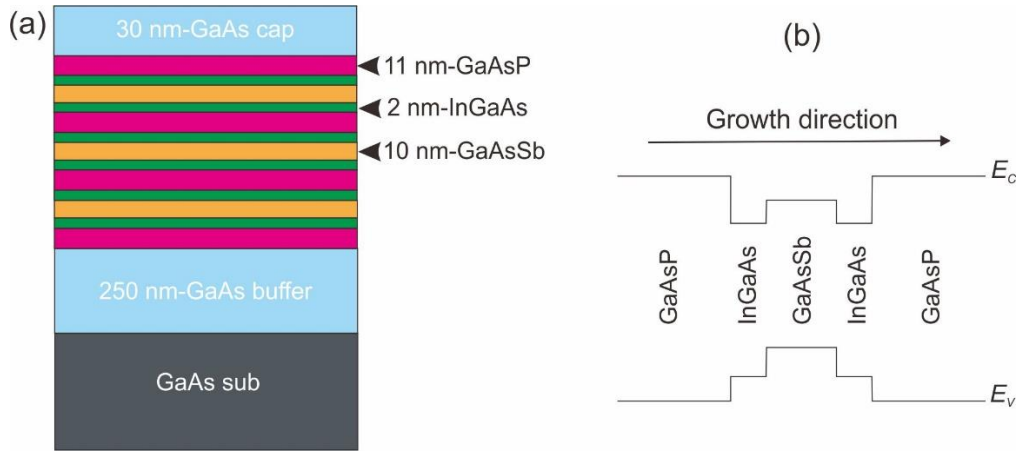


**Fig. 1.** Schematic diagrams of (a) sample layer structure of three cycles of the InGaAs/GaAsSb/InGaAs W-QW and (b) band alignment of one cycle of the W-QW with GaAsP strain-compensation layers.

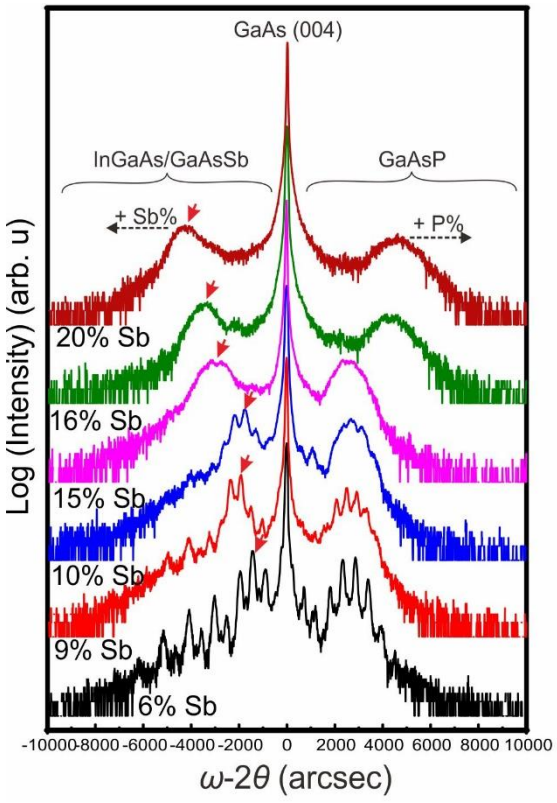


**Fig. 2.** X-ray rocking curves of W-QW with various Sb compositions in the GaAsSb layer. The red arrows show the shift of the rocking curves as a function of different Sb compositions.

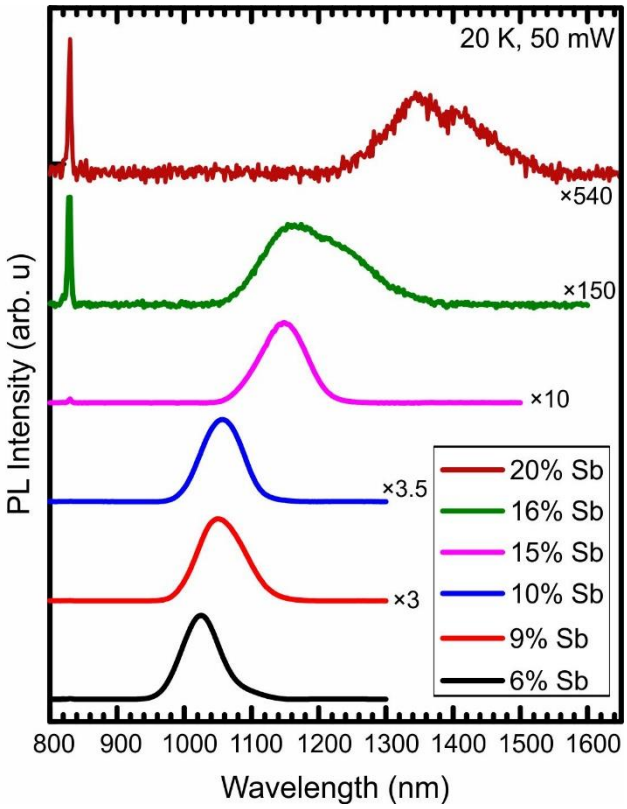


**Fig. 3.** Low-temperature PL (excitation power of 50 mW) of W-QW with various Sb compositions. The spectra are shifted vertically for clarity.

# Growth of Cobalt-containing Compounds for Back-End-of-Line Interconnects

**Yansong Li, Guanyu Zhou, Christopher Hinkle**
**University of Notre Dame**

(a)

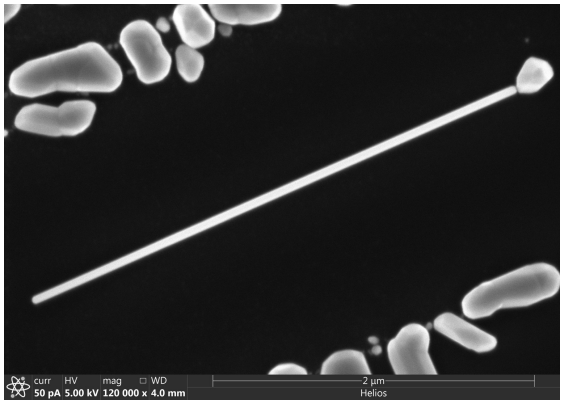


(b)

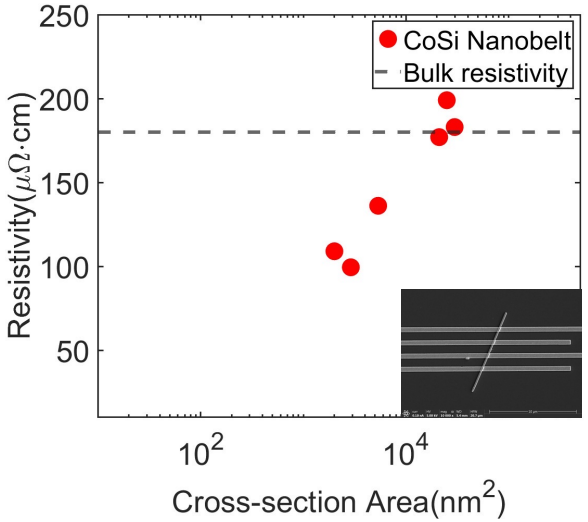


FIG. 1. (a) SEM image of as-grown CoSi nanobelt on HOPG substrate. (b) Dimension-dependent resistivity curve of CoSi nanobelts.

(a)

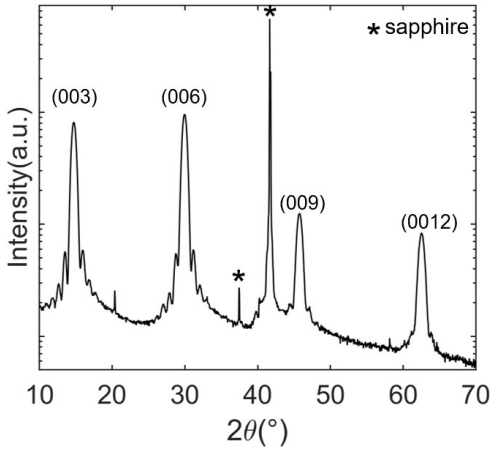


(b)

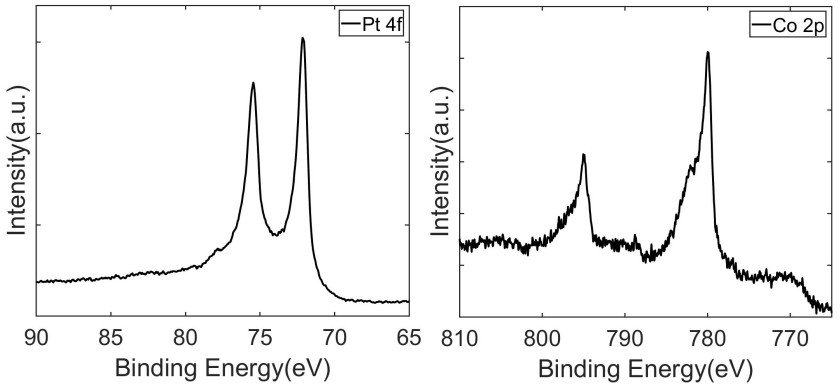


FIG. 2. (a) $\theta - 2\theta$ XRD of $PtCoO_2$ thin film. (b) XPS spectra of Pt 4f and Co 2p for the $PtCoO_2$ thin film.

## References

[1] Y. Liu *et al.*, "Valence band engineering of GaAsBi for low noise avalanche photodiodes," *Nat. Commun.*, vol. 12, no. 1, 2021.

[2] R. D. Richards, "Molecular beam epitaxy growth and characterisation of GaAsBi for photovoltaic applications," no. September, p. 197, 2014.

## Supplementary Material

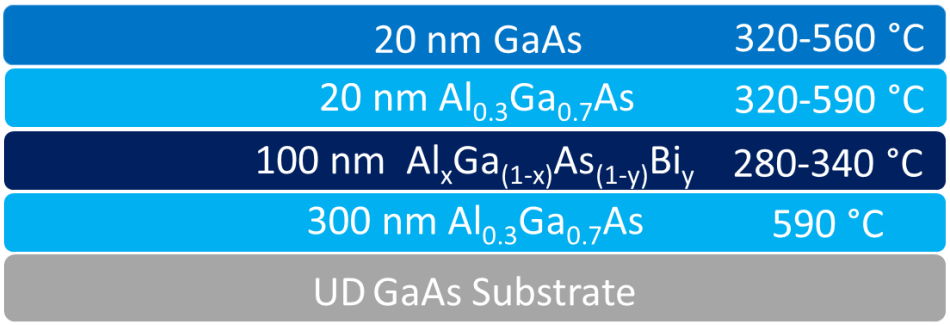


*Figure 1 Sample architecture for $Al_xGa_{(1-x)}As_{(1-y)}Bi_y$ growth investigation. Capping growth temperature varied only for purpose of annealing investigation.*

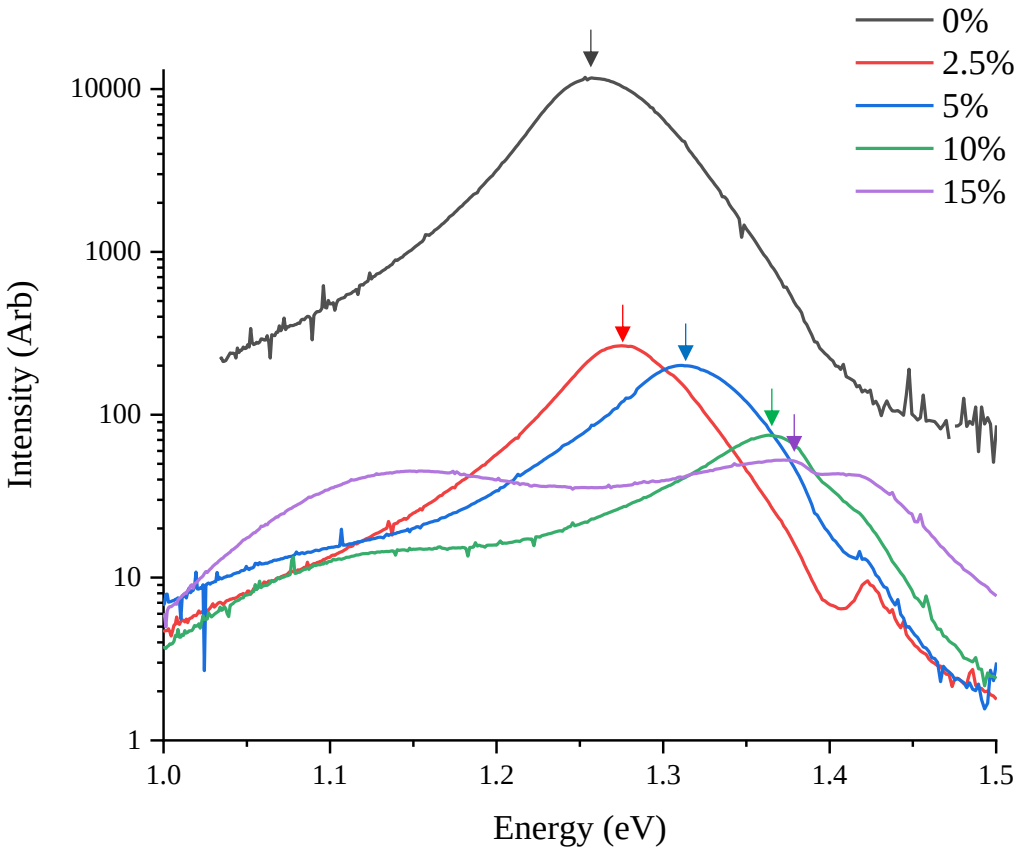


*Figure 2 Room Temperature Photoluminescence Spectra of $Al_xGa_{(1-x)}As_{(1-y)}Bi_y$ samples with varied Al contents between 0-15%. Bi content between 2.3-2.7% across the series with the main peak of interested marked.*

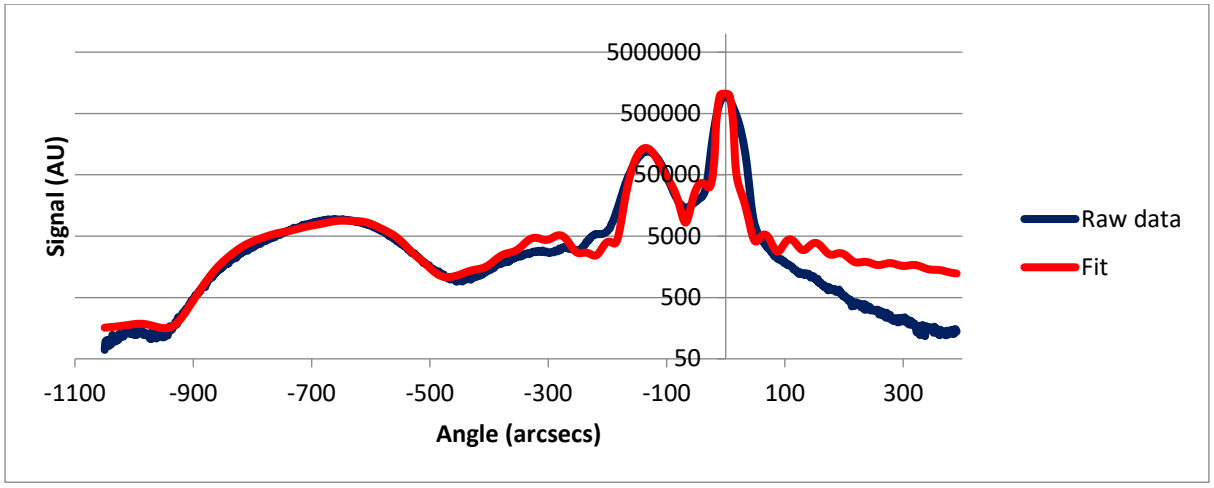


*Figure 3 X-Ray Diffraction of* $Al_{0.05}Ga_{0.95}As_{0.976}Bi_{0.024}$


*Figure 4 Normaski microscope Images of sample surfaces A,B & C for X= 0.0, 0.05 & 0.15* $Al_xGa_{(1-x)}As_{(1-y)}Bi_y$ *alloys respectively with 300µm scale bar.*

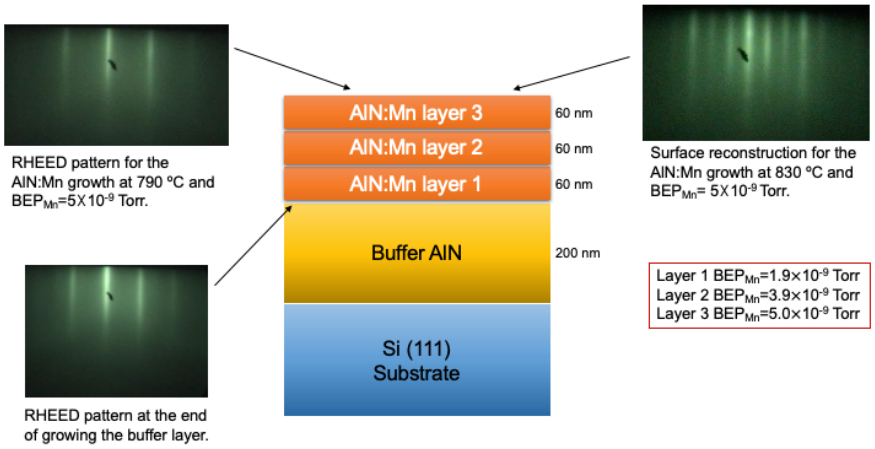


*Figure 1. Samples structure and RHEED patterns observed at different stages of AlN growth.*

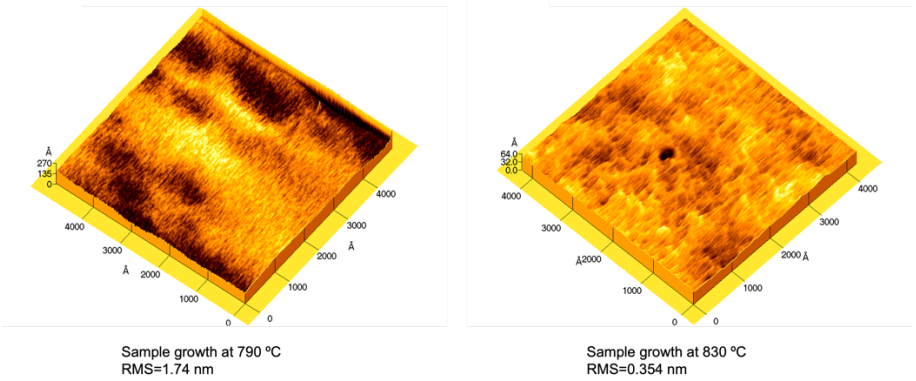


*Figure 2. AFM surface micrographs of samples grown at 790 and 830 ºC.*

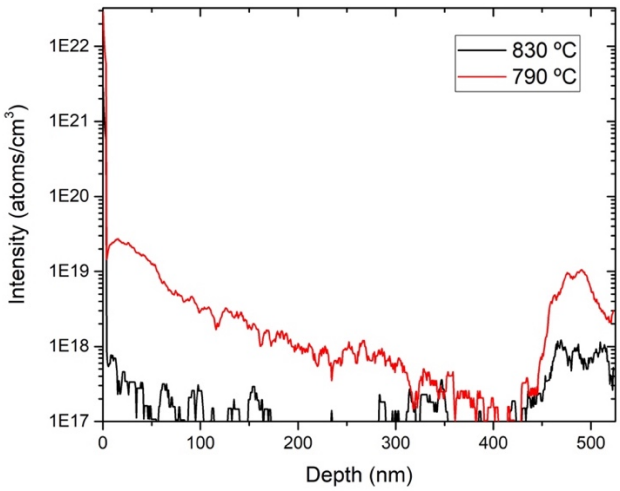


*Figure 3. SIMS depth profile of Mn in the samples grown at 790 and 830 ºC.*

# Growth and scattering mechanisms of metamorphic $In_{0.81}Ga_{0.19}As$ quantum wells

**Jason T. Dong[1], Yilmaz Gul[2], Aaron N. Engel[1], Connor P. Dempsey[3], Shirshendu Chatterjee[3], Michael Pepper[2] Christopher J. Palmstrøm[1,3]**

*[1]Materials Department, University of California, Santa Barbara, CA 931063*

*[2]London Centre for Nanotechnology, University College London, 17-19 Gordon Street, London WC1H 0AH, United Kingdom*

*[3]Deparment of Electrical and Computer Engineering, University of California, Santa Barbara, CA 93106*

Supplementary Figures:

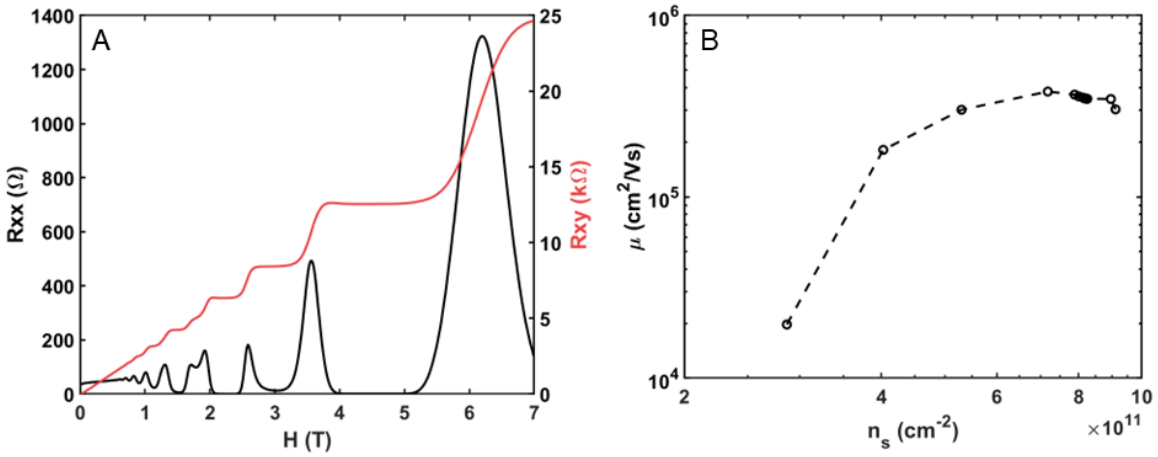


Figure 1: a) Low temperature (2 K) magnetotransport of an $In_{0.81}Ga_{0.19}As$ quantum well. b) Electron mobility as a function of carrier density of a gated $In_{0.81}Ga_{0.19}As$ quantum well.

# Supplementary Materials

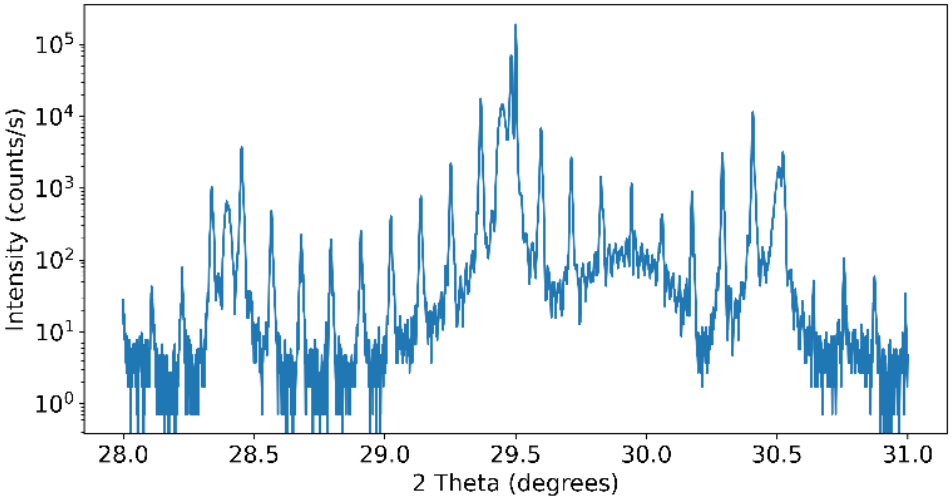


*Figure 1. XRD of an InAs/AlSb QCD grown strain balanced on GaSb with a designed absorption wavelength of 4.3 µm.*

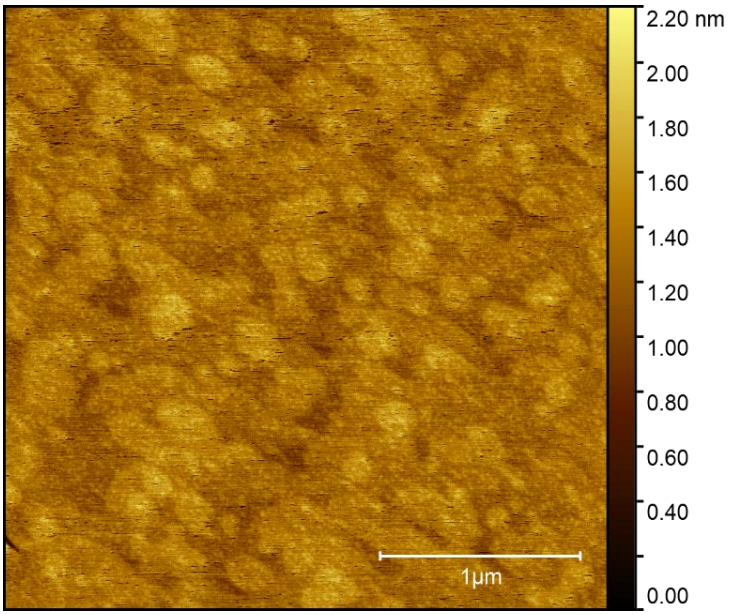


*Figure 2. AFM of a 3×3 µm surface of the InAs/AlSb QCD grown strain balanced on GaSb. The RMS surface roughness of this scan is 0.189 nm*

**Supplemental document: Impact of unintentional Sb in the tensile electron well of type-II InAs/InAsSb superlattices grown on GaSb by molecular beam epitaxy**

Marko S. Milosavljevic, Preston T. Webster, and Shane R. Johnson

The figure below shows the photoluminescence spectra from four 5.3 µm midwave and four 12.0 µm longwave InAs/InAsSb superlattices, measured at 80 K with an 808 nm pump power of 200 mW. The solid vertical lines indicate the superlattice bandgap energy extracted from each spectra. The dashed lines indicate the expected bandgap position for a structure with a pure tensile InAs layer. The blue shift in the measured bandgap indicates the presence of unintentional Sb in the tensile InAs layer.

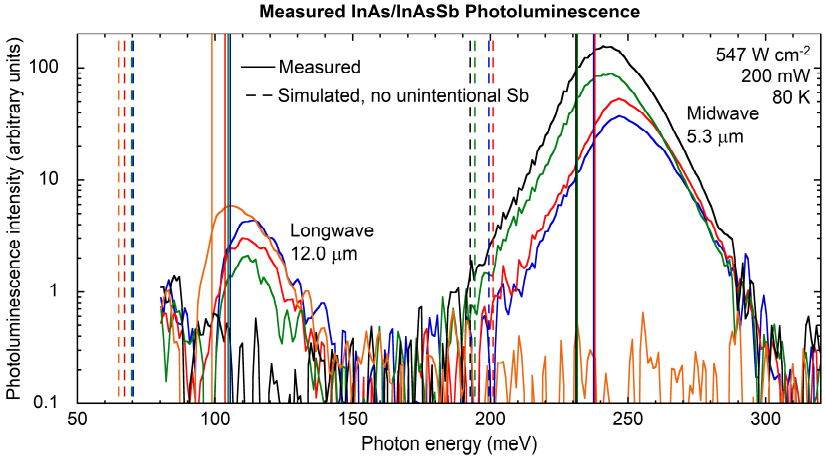


In the figure below, left panel (a) shows measured Sb mole fractions in the compressive layer as open black circles and the tensile layer as open red circles for the mid and long wave structures. The fit to the model is shown as solid black and red curves for the tensile and compressive layers respectively. The mole fraction versus monolayer number is shown in panels (b) and (c) for the mid and long wave InAs/InAsSb superlattices; the Sb profile is in red and the average of the profile is in black.

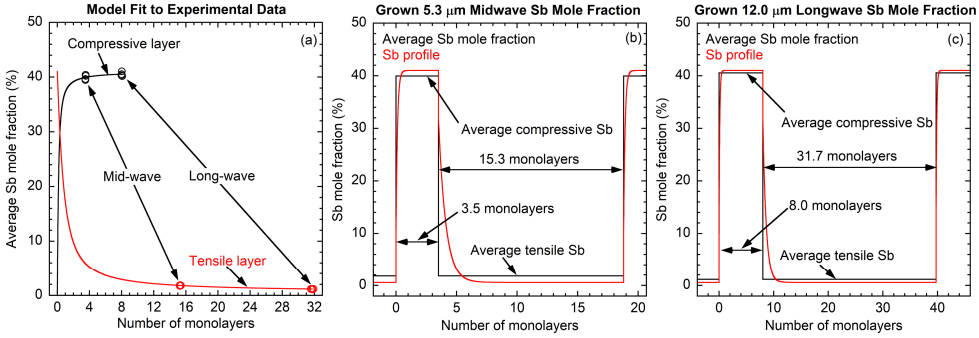


The average structure of the grown midwave and longwave InAs/InAsSb superlattices is shown in the table below. The layer thicknesses and Sb mole fractions are averages and are labeled as the "Grown" structure. For comparison, an "Ideal" structure with no unintentional Sb in the tensile InAs layer is also shown. The 80 K bandgap, compressive Sb mole fraction, and tetragonal distortion are the same for both the grown and ideal structures. The grown structures have a significantly thicker tensile layer. a slightly thinner compressive layer, and a smaller electron-hole wavefunction overlap.

| Superlattice type | Superlattice tetragonal distortion (%) | 80 K Bandgap (meV) | 80 K Bandgap (µm) | Structure | Sb mole fraction (%) Tensile InAs(Sb) | Sb mole fraction (%) Comp. InAsSb | Thickness (nm) Tensile InAs(Sb) | Thickness (nm) Comp. InAsSb | Electron-hole overlap squared (%) |
|---|---|---|---|---|---|---|---|---|---|
| Mid-wave | -0.0013 | 233 | 5.3 | Grown | 1.8 | 40.0 | 4.61 | 1.12 | 58.2 |
| | | | | Ideal | 0 | 40.0 | 3.87 | 1.18 | 63.1 |
| Long-wave | 0.0269 | 103 | 12.0 | Grown | 1.2 | 40.5 | 9.56 | 2.56 | 22.2 |
| | | | | Ideal | 0 | 40.5 | 8.54 | 2.62 | 24.8 |

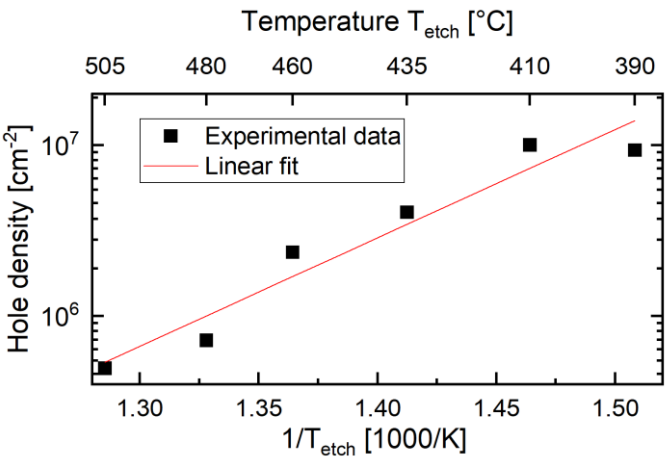


**Fig. 1**: Surface density of etched nanoholes vs. the inverse etching temperature $T_{etch}$. Data points were generated by counting nanoholes at 2,000x magnification in an SEM evaluating at least 40 nanoholes per temperature.

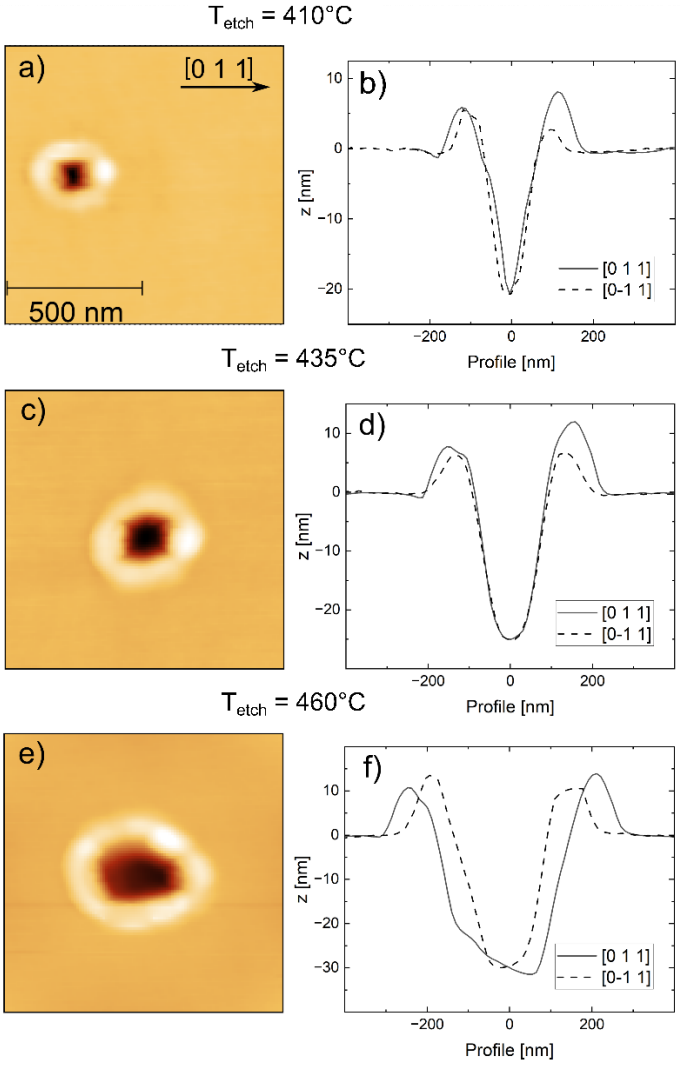


**Fig. 2**: AFM images and line profiles for samples overgrown with 50 nm $In_{0.52}Al_{0.48}As$ and etched at 410°C ( a) and b)), at 435°C ( c) and d)), and at 460°C ( e) and f)), respectively. Etching was performed with 4.1 ML of InAl. The size of the AFM images is 1×1 µm$^2$.

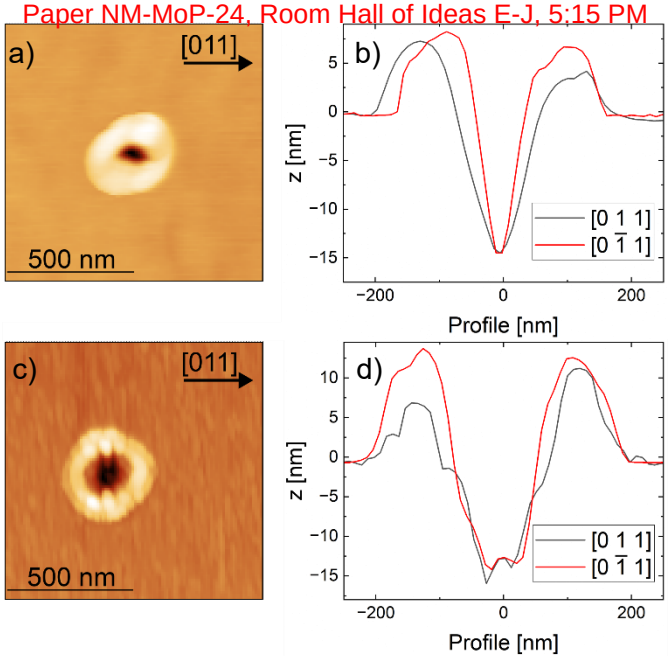


**Fig. 3**: AFM images and profiles for nanoholes etched with approximately 2 ML of Al ( a) and b)) and 2 ML of In ( c) and d)). The etching temperature $T_{etch}$ was in both cases 435°C. Holes etched with Al are significantly more elongated along the [011] direction as can be seen from the image a) and the line scans along the high symmetry directions b).

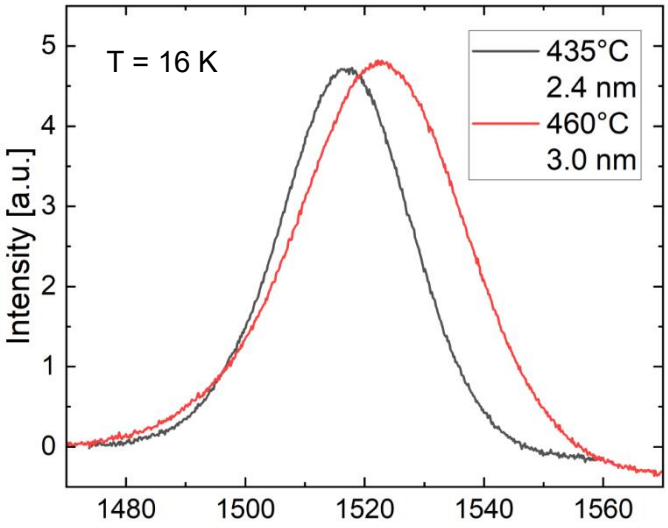


**Fig. 4**: Ensemble photoluminescence from quantum dots generated by $In_{0.53}Ga_{0.47}As$ filling of nanoholes etched at 435°C and 460°C and 50 nm $In_{0.52}Al_{0.48}As$ overgrowth (see Fig. 2 c) - f)). The filled holes have been capped by 100 nm $In_{0.52}Al_{0.48}As$. The $In_{0.53}Ga_{0.47}As$ deposition amount is given in the figure as an equivalent homogeneous layer deposition and corresponds to the maximum possible filling amount for nanoholes generated at these temperatures, which was found by investigating uncapped holes filled with the same parameters.

# Strain-mediated Sn incorporation and segregation in compositionally graded $Ge_{1-x}Sn_x$ epilayers grown by MBE at different temperature

Nirosh M. Eldose,[1,*] Hryhorii Stanchu,[1] Subhashis Das[1], Satish Shetty[1], Chen Li[1], Yuriy I. Mazur[1], Shui-Qing Yu,[2] and Gregory J. Salamo[1]

[1] *Institute for Nanoscience and Engineering, University of Arkansas, Fayetteville, Arkansas 72701, USA*

[2] *Department of Electrical Engineering, University of Arkansas, Fayetteville, Arkansas 72701, USA*

Group IV alloys of Ge and Sn are extensively studied for various electronic and optoelectronic applications on a Si platform. $Ge_{1-x}Sn_x$ with α-Sn concentrations as low as 6% [1] allows for a transition from an indirect bandgap to a direct optical. Higher Sn content makes possible mid and even long-range infrared optical emission and detection [2]. At the same time, due to the low solid solubility of Sn in Ge (~1%), as well as the large lattice mismatch of α-Sn with Ge (~14%), the realization of high-quality Sn-rich $Ge_{1-x}Sn_x$ structures has proved challenging. In this study, we demonstrate enhanced Sn content using molecular beam epitaxy (MBE) growth of compositionally graded $Ge_{1-x}Sn_x$ on Ge (001). High-quality GeSn alloys with Sn composition reaching 6% at constant temperature. The maximal fraction of Sn was further increased to 9.0% when the growth temperature was continuously lowered while increasing the Sn flux. The analysis of surface droplets and SIMS (secondary ion mass spectrometry) profiles of elemental composition give evidence of Sn rejection during the growth, potentially associated with a critical energy of elastic strain. The intentional reduction of the coherent strain by decreasing the Sn flux near the sample surface has shown to trap a higher fraction of Sn in the $Ge_{1-x}Sn_x$ layer and lower surface segregation. Supporting data (Fig.2) shows an approach for XRD spectra simulation was developed for strain and composition characterization.

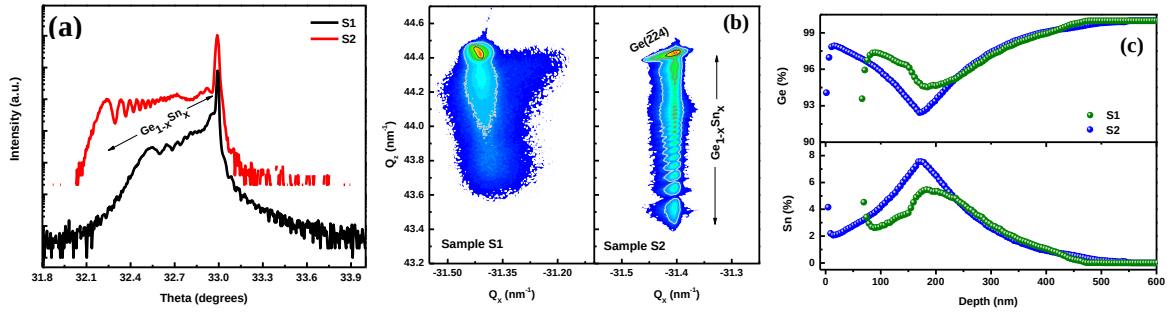


**Fig. 1.** (a) XRD (004) ω/2θ scans, (b) ($\bar{2}\bar{2}4$) RSMs of samples G1 and G2 and (c) The SIMS profiles of Sn and Ge in the $Ge_{1-x}Sn_x$ epilayer of samples S1 and S2.

[1] S. Wirths, D. Buca, S. Mantl, Prog. Cryst. Growth Charact. Mater. 2016, 62 (1), 1−39.
[2] J. Bass, H. Tran, W. Du, R. Soref, S.-Q. Yu, Opt. Exp. 2021, 29 (19),30844-30856.

[+] Author for correspondence: nmeckama@uark.edu

# Supplementary Pages (Optional)

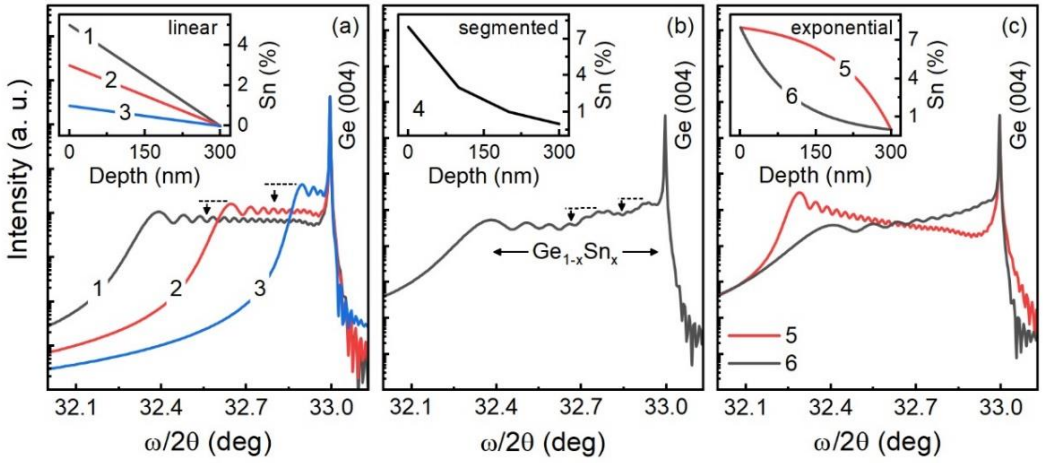


**Fig. 2**. Calculated X-ray diffraction 004 ω/2θ spectra for several pseudomorphic compositionally graded $Ge_{1-x}Sn_x$/Ge heterostructures showing the effect of (a) linear grading, (b) stepwise grading, and (c) exponential grading on the scattered intensity.

# Growth and Characterization of GaAs (111) on 4H-SiC for Infrared Sensor

**Subhashis Das,[1,2] Nirosh M Eldose,[1] Hryhorii Stanchu[1], Fernando Maia de Oliveira[1], Chen Li[1], Mourad Benamara[1], Yuriy I. Mazur[1], Gregory Salamo[1,2]**

[1] *Institute for Nanoscience and Engineering, University of Arkansas, Fayetteville, AR, 72701, USA.*

[2] *Department of Physics, University of Arkansas, Fayetteville, AR, 72701, USA.*

Epitaxial growth of III-V semiconductors on 4H-SiC would potentially allow the integration of optical sensors on SiC based power devices. We report on the growth of high-quality crystalline GaAs layer on the SiC hexagonal substrate by molecular beam epitaxy (MBE). For fabrication on SiC, a 5 nm AlAs nucleation layer was grown at 700 °C followed by a 60 nm GaAs layer buffer grown at 600 °C. We will discuss the surface morphology, structural quality, and the optical properties of the MBE grown samples. The ω-2θ scan result (fig.1. (a)) corroborates the crystalline growth of GaAs (111) on 4H-SiC. The structural quality is further illustrated by the cross-sectional TEM image in fig. 1(b). It consists of a high-quality GaAs layer and a highly defected interface region between GaAs and the 4H-SiC substrate. This defect region is attributed to the lattice and crystal structure mismatch between substrate and film. Fig. 1(c) shows the temperature dependent photoluminescence properties of the grown structure. Good free-exciton (FE) emission has been observed at room temperature (300 K) and lower temperature (77 K). Excitingly, the optical results were comparable with the same structure grown on a GaAs substrate. Overall, these observations exhibit potential to achieve an optical emitter for sensors integrated on SiC based power device platform.

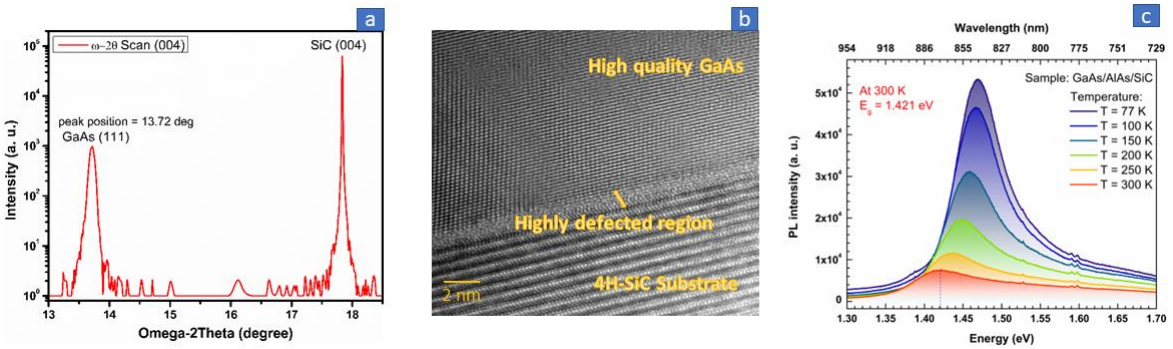


Figure 1. (a) XRD (ω-2θ) scan, (b) cross-sectional TEM image, (c) temperature dependent photoluminescence spectra of GaAs/SiC structure.

[1] S. K. Saha, R. Kumar, A. Kuchuk, M. Z. Alavijeh, Y. Maidaniuk, Y. I. Mazur, S.-Q. Yu, and G. J. Salamo, Cryst. Growth Des., **19**, 5088−5096 (2019).

+ Author for correspondence: subhashis.ds@email.com

# Suplementary Pages (Optional)

Fig. 2 depicts the nominal structure of the GaAs grown on 4H-SiC. A 5 nm AlAs nucleation layer was grown at 700 °C whereas, the buffer layer of 60 nm GaAs was grown at 600 °C. All the growth temperatures were measured by the thermocouple. Fig. 3 illustrates reflection high energy electron diffraction (RHEED) images before growth (fig. 3(a)) and after growth (fig. 3(b). A streaky RHEED image is evidence of high cleanliness and smoothness of substrate surface. The spotty pattern from fig. 3(b) indicates the 3D growth mode and the existence of twining.

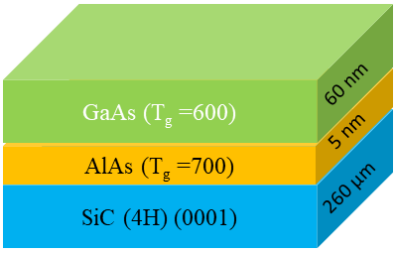


Fig. 2. Schematic structure of GaAs/SiC.

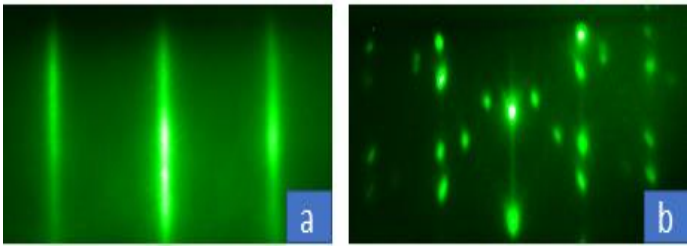


Fig. 3. RHEED images of GaAs/SiC structure (a) before growth and (b) after growth.

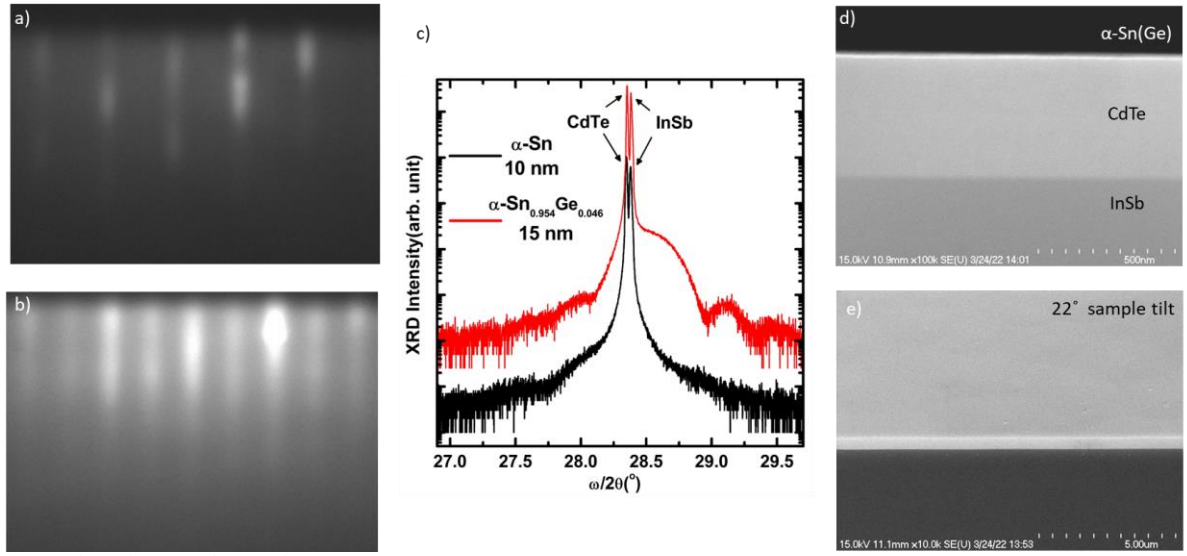


Fig. 1. After a few monolayers of α-Sn(Ge) growth, RHEED becomes a streaky (2x2) pattern (a,b). The thickness and Ge composition were determined from XRD simulation and Pendellösung fringes (c). Cross sectional SEM imaging confirmed thickness and showed single crystal layers with abrupt interfaces between α-Sn(Ge)/CdTe/InSb (d) and smooth surfaces (e).

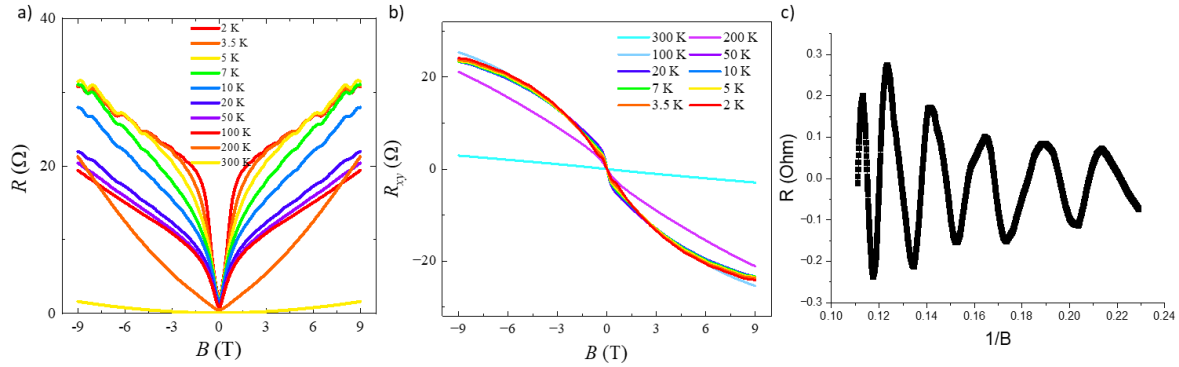


Fig. 2. α-Sn and dilute Ge alloys exhibit large magnetoresistance, Shubnikov-de Haas oscillations and weak antilocalization (a,b). Expanded Shubnikov-de Haas quantum oscillations as a function of inverse magnetic field (c).

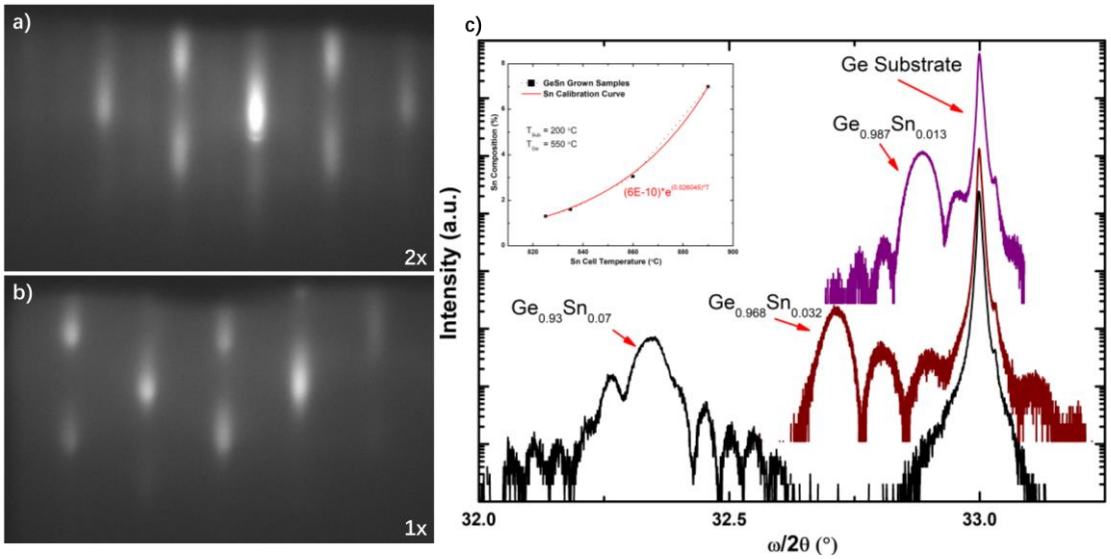


Fig. 3. RHEED reconstruction changes from (2x) to (1x) with increasing Sn composition (a,b). XRD spectra of GeSn samples towards achieving *k*-SCS with increasing Sn content, showing nice Pendellösung fringes (c). (inset) Sn composition versus Sn cell temperature calibration curve for constant substrate and Ge cell temperature.

[1] D. Zhang, H. Wang, J. Ruan, G. Yao, and H. Zhang, "Engineering topological phases in the Luttinger semimetal *α*-Sn," *Physical Review B*, vol. 97, no. 19, p. 195139, 05/21/ 2018

[2] T. T. McCarthy, Z. Ju, S. Schaefer, S.-Q. Yu, and Y.-H. Zhang. "Momentum(k)-Space Carrier Separation Using SiGeSn Alloys for Photodetector Applications" *Journal of Applied Physics* **130**, 223102 (2021)

# Supplemental Material

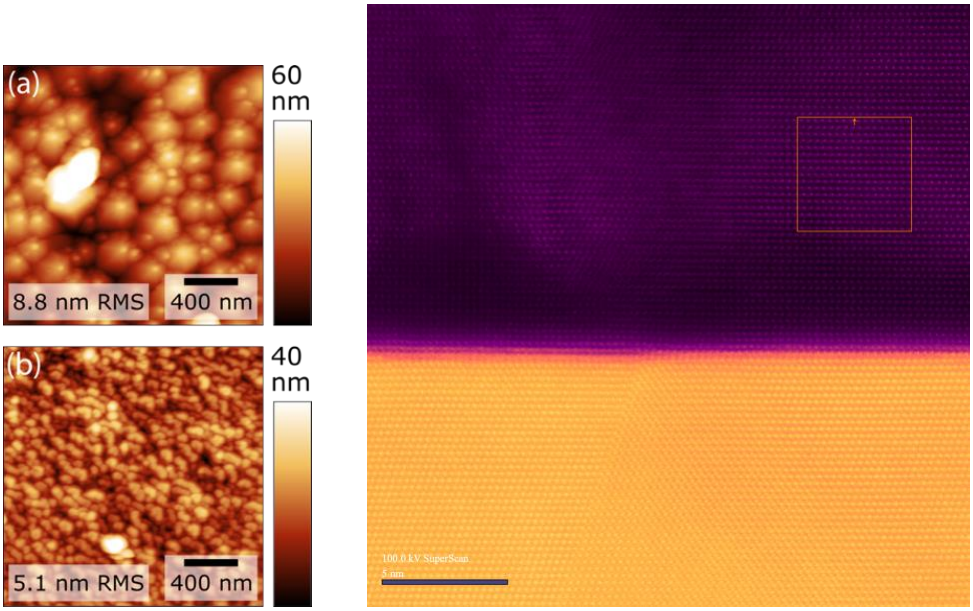


(left) AFM of $Al_{0.7}Ga_{0.3}N$ grown on TaC (a) and AlN (b) showing spiral hillocks indicative of step-flow growth and a large dislocation density. (right) STEM image of a defect propagating from TaC to AlGaN

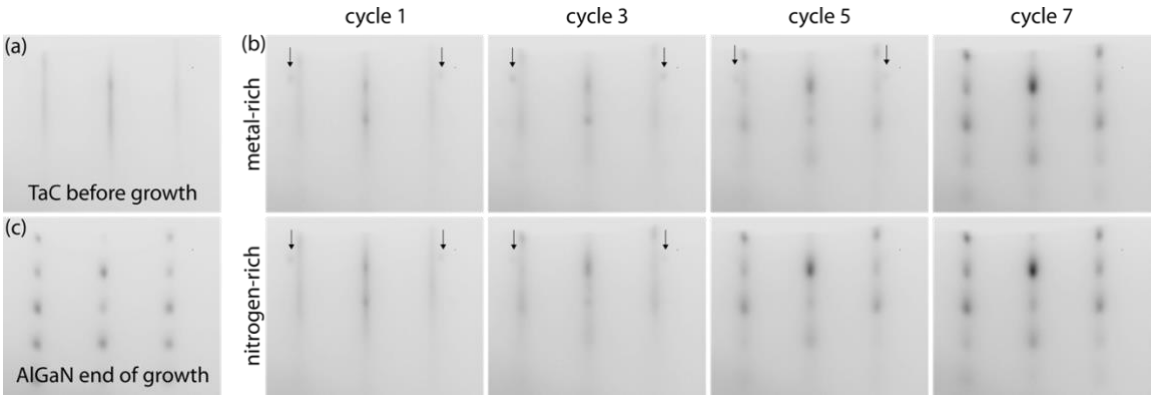


RHEED images of $Al_{0.7}Ga_{0.3}N$ nucleation on TaC. (a) shows the streaky-smooth TaC surface before growth. (b) shows RHEED captures from the first few cycles of metal-modulated epitaxy. The arrows point to an incommensurate spot which is more pronounced in metal-rich conditions and is not seen after 7 cycles. (c) shows the AlGaN at the end of growth.

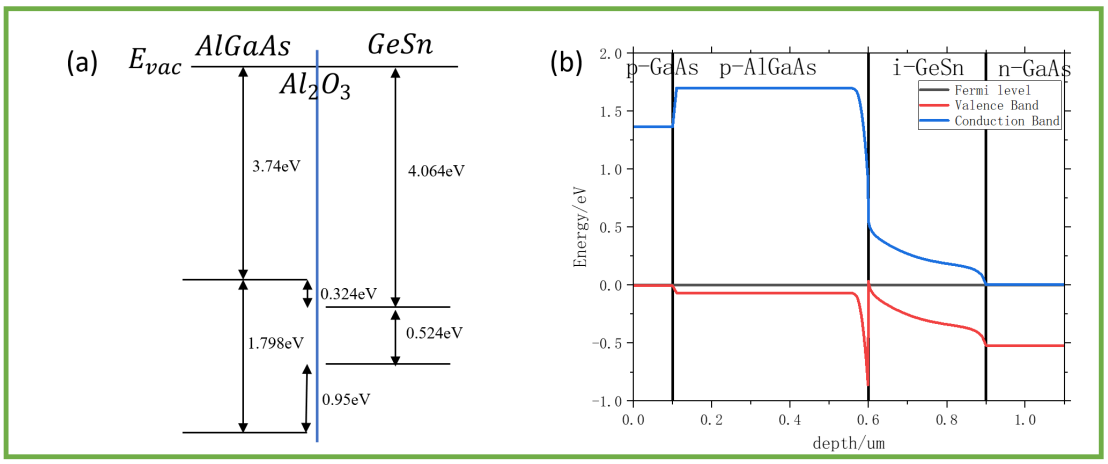


Figure 1: (a) AlGaAs /GeSn heterostructure band diagram (b) Silvaco simulated band structure

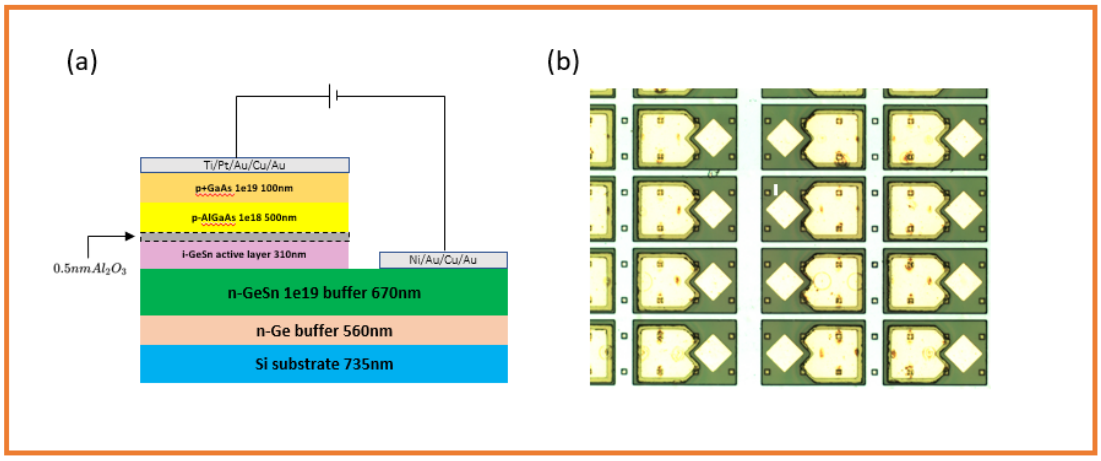


Figure 2: (a) AlGaAs/GeSn diode device structure (b) Optical microscope image of the diodes

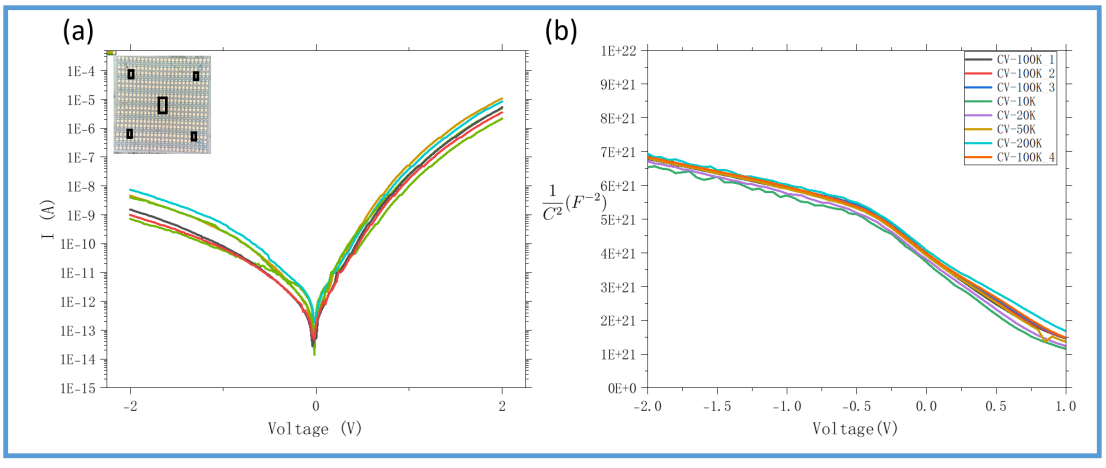


Figure 3: (a)I-V performances from -2V to 2V from the different regions of the sample

(b) C-V performances under frequency from 10KHz to 200KHz(100KHz was measured multiple times to check the stability)

# Van der Waals epitaxy of 2D ferromagnetic $Fe_{5-x}GeTe_2$ films with Curie temperature above room temperature on graphene

Joao Marcelo J. Lopes*, Hua Lv, Atekelte A. Kassa, Alessandra da Silva, Jens Herfort, Michael Hanke, Achim Trampert, Roman Engel-Herbert, Manfred Ramsteiner

Paul-Drude-Institut für Festkörperelektronik, Leibniz-Institut im Forschungsverbund Berlin e.V, 10117 Berlin, Germany

*** Presenter/Corresponding Author: lopes@pdi-berlin.de**
Hua Lv: lv@pdi-berlin.de
Atekelte Kassa: kassa@pdi-berlin.de
Alessandra da Silva: dasilva@pdi-berlin.de
Jens Herfort: herfort@pdi-berlin.de
Michael Hanke: hanke@pdi-berlin.de
Achim Trampert: trampert@pdi-berlin.de
Roman Engel-Herbert: engel-herbert@pdi-berlin.de
Manfred Ramsteiner: ramsteiner@pdi-berlin.de

**Desired session: NM9: Van der Waals Materials**
**Preferred Presentation Type: Oral**

## Abstract

Van der Waals (vdW) heterostructures combining layered ferromagnets and other two-dimensional (2D) crystals such as graphene and transition metal dichalcogenides are promising building blocks for the realization of ultra-compact devices with integrated magnetic, electronic and optical functionalities. Their implementation in various technologies depends strongly on the development of a bottom-up, scalable synthesis approach allowing to realize highly uniform heterostructures with well-defined interfaces between different 2D layered materials. It also requires that each material component of the heterostructure remains functional, which ideally includes ferromagnetic order above room temperature for 2D ferromagnets. In this contribution, we will present our recent results on van der Waals (vdW) epitaxy of the 2D itinerant ferromagnetic metal $Fe_{5-x}GeTe_2$ (FGT, $x \sim 0$) on single crystalline epitaxial graphene using molecular beam epitaxy. For the growth of FGT films (with thickness ranging from 10 to 15 nm), elemental Fe, Ge, and Te were co-supplied from conventional effusion cells, and a growth temperature of 300 °C was employed. As a substrate, epitaxial graphene on 4H-SiC(0001), synthesized via SiC surface graphitization, was employed. Morphological and structural characterization using methods such as atomic force microscopy, synchrotron-based grazing incidence X-ray diffraction, and scanning transmission electron microscopy (STEM) revealed that epitaxial FGT films exhibiting very good surface morphology, high crystalline quality, and a sharp interface to graphene could be realized. Interestingly, stacking faults related to the presence of single FGT layers with thicknesses exceeding those expected for the $Fe_5GeTe_2$ phase could be identified by STEM. We expect these to be novel FGT metastable phases with Fe composition higher than 5 and potentially enhanced magnetic properties. Temperature-dependent magneto-transport measurements and superconducting quantum interference device (SQUID) magnetometry were employed to assess the magnetic properties of the samples. Ferromagnetic order with a predominant out-of-plane magnetization was shown to persist above 350 K. Furthermore, magneto-transport also revealed that the epitaxial graphene continues to exhibit a high electronic quality. These results represent an important advance beyond non-scalable flake exfoliation and stacking methods, thus marking a crucial step toward the implementation of ferromagnetic 2D materials in practical applications.

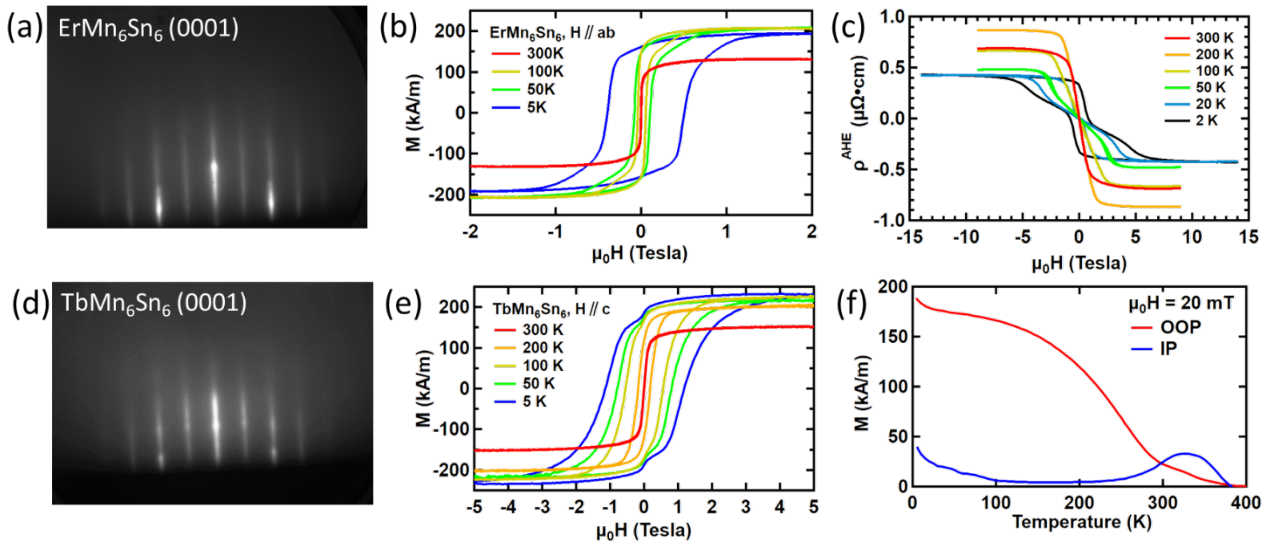


(a). RHEED pattern of $ErMn_6Sn_6$(0001) thin films. (b). In-plane hysteresis loops of $ErMn_6Sn_6$ thin films at different temperatures taken with SQUID. (c). AHE hysteresis loops of $ErMn_6Sn_6$ thin films at different temperatures. (d). RHEED pattern of $TbMn_6Sn_6$(0001) thin films. (e). Out-of-plane hysteresis loops of $TbMn_6Sn_6$ thin films at different temperatures taken with SQUID. (f). Temperature dependence of remanence magnetization of $TbMn_6Sn_6$ thin films, suggesting out-of-plane to in-plane spin reorientation above T = 300 K.

# Layer-dependent Optical Properties of MBE-grown $ZrTe_2$ Determined by in-situ Spectroscopic Ellipsometry

**Elizabeth Houser and Frank Peiris**
*Department of Physics, Kenyon College, Gambier, OH 43022, USA*

**Anthony Richardella, Max Stanley, and Nitin Samarth**
*Materials Research Institute, Pennsylvania State University, PA 1680, USA*

Two-dimensional transition metal dichalcogenides (TMDCs) are an interesting platform to interrogate fundamental physics questions as well as to advance the development of optoelectronic technologies. Both these endeavors are heavily dependent on having high-quality TMDCs, realized only after employing extensive growth optimization procedures. In this work, we investigated the growth and the optical properties of $ZrTe_2$, a candidate topological Dirac semimetal. During the growth of 12 unit cells (u.c.) of $ZrTe_2$ on a sapphire substrate, we obtained in-situ spectroscopic ellipsometry after the deposition of each u.c. After the deposition of the $ZrTe_2$, we deposited a Te capping layer to protect the TMDC film. X-ray reflectivity measurements performed subsequently indicated that the total thickness of $ZrTe_2$ and the thickness of Te to be 5.95 nm and 19 nm, respectively.

A standard inversion technique was used to model the ellipsometry spectra by specifying a three layer model (i.e., sapphire substrate, $ZrTe_2$ layer and the Te capping layer) to fit the final ellipsometry spectra. The thicknesses obtained from X-ray reflectivity allowed us to obtain the precise dielectric function of the final $ZrTe_2$ layer (i.e., 12 u.c.). Subsequently, we fit the remaining ellipsometry spectra obtained for 11 u.c. through 1 u.c. $ZrTe_2$ and obtain their dielectric functions. Clearly, the dielectric functions show a noticeable change with the thickness of the $ZrTe_2$ layers, where the absorption depicted by the imaginary part of the dielectric function increases with the thickness of $ZrTe_2$. Additionally, the layer-dependent dielectric functions were analyzed by incorporating a Drude oscillator to account for the free electrons and two Kramers-Kronig-consistent oscillators to represent the band-to-band transitions. Interestingly, we find that the Drude contribution reduces as the thickness of $ZrTe_2$ gets smaller, suggesting that its metallic character diminishes as the thickness reduces. Further analysis of the optical conductivity verifies this observation.

The work at Kenyon is funded by DMR-2004812 and the work at The Pennsylvania State University Two-Dimensional Crystal Consortium – Materials Innovation Platform (2DCC-MIP) is supported by NSF cooperative agreement DMR-1539916 and DMR-2039351.

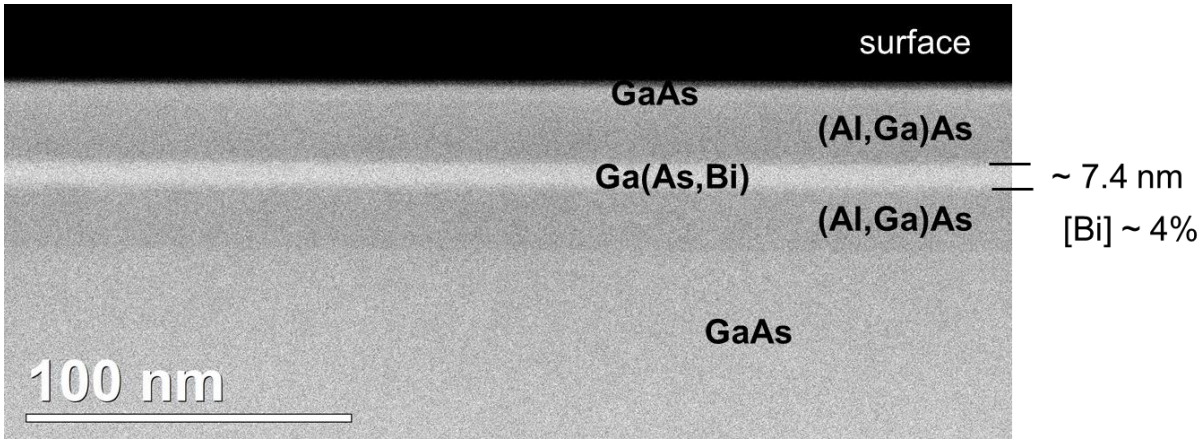


Fig. 1. High-angle annular dark-field (HAADF) image with atomic number Z-contrast of the 7 nm thick Ga(As,Bi) QW with 20 nm thick (Al,Ga)As barriers. The expected HAADF bright contrast of the QW is due to the presence of Bi, $Z_{Bi} = 83$, in the layer.

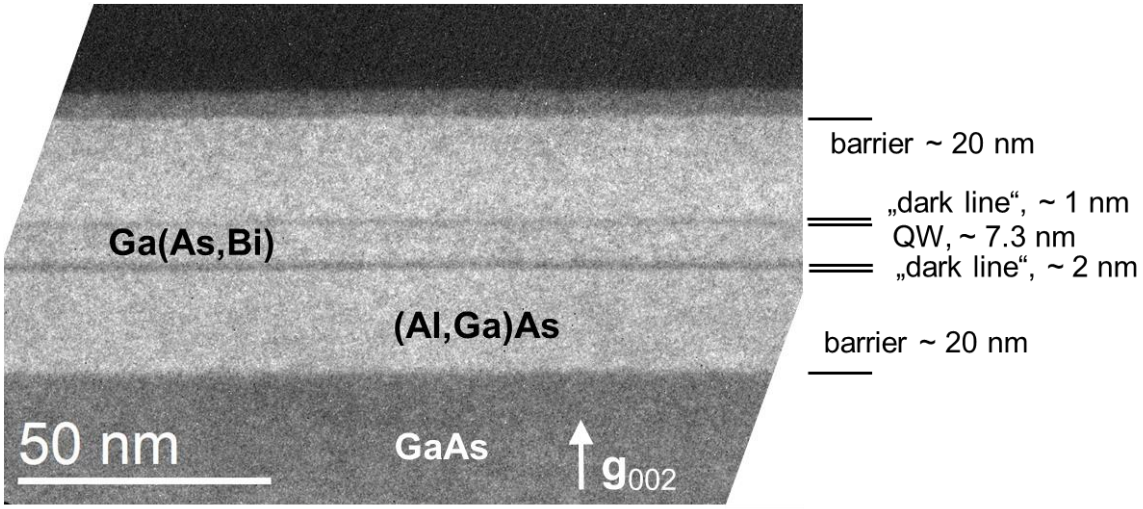


Fig. 2. Chemically-sensitive $\mathbf{g}_{002}$ dark-field TEM micrograph of the Ga(As,Bi) QW with 20 nm thick (Al,Ga)As barriers. Note the presence of two lines with darker contrast delimiting the interface position, at the location of the growth interruptions (GI).

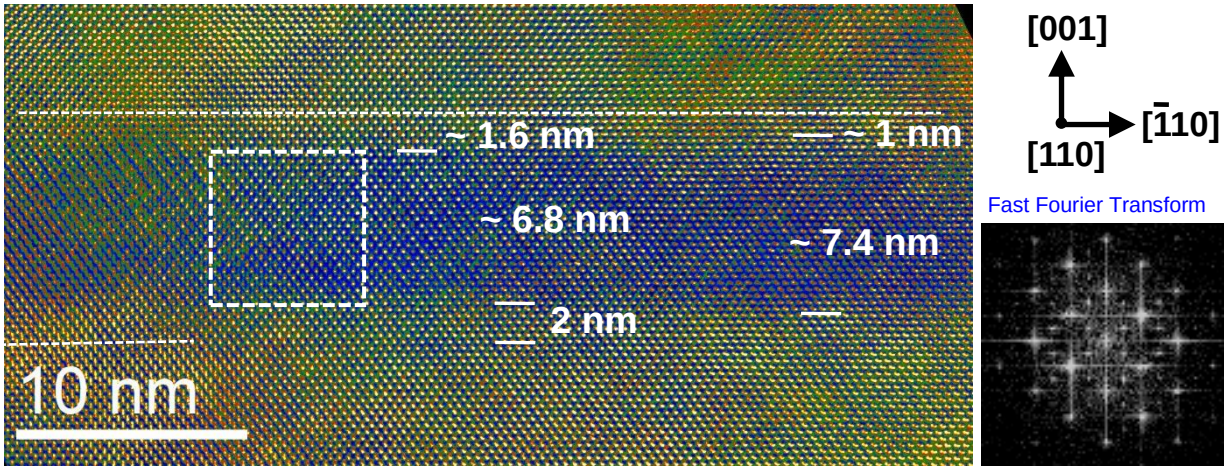


Fig. 3. High-resolution (HR) TEM micrograph of the Ga(As,Bi) QW. $CuPt_B$ atomic ordering is detected inside the 7-nm-thick QW but not at two unintentional layers before and after the QW, at the GI positions.

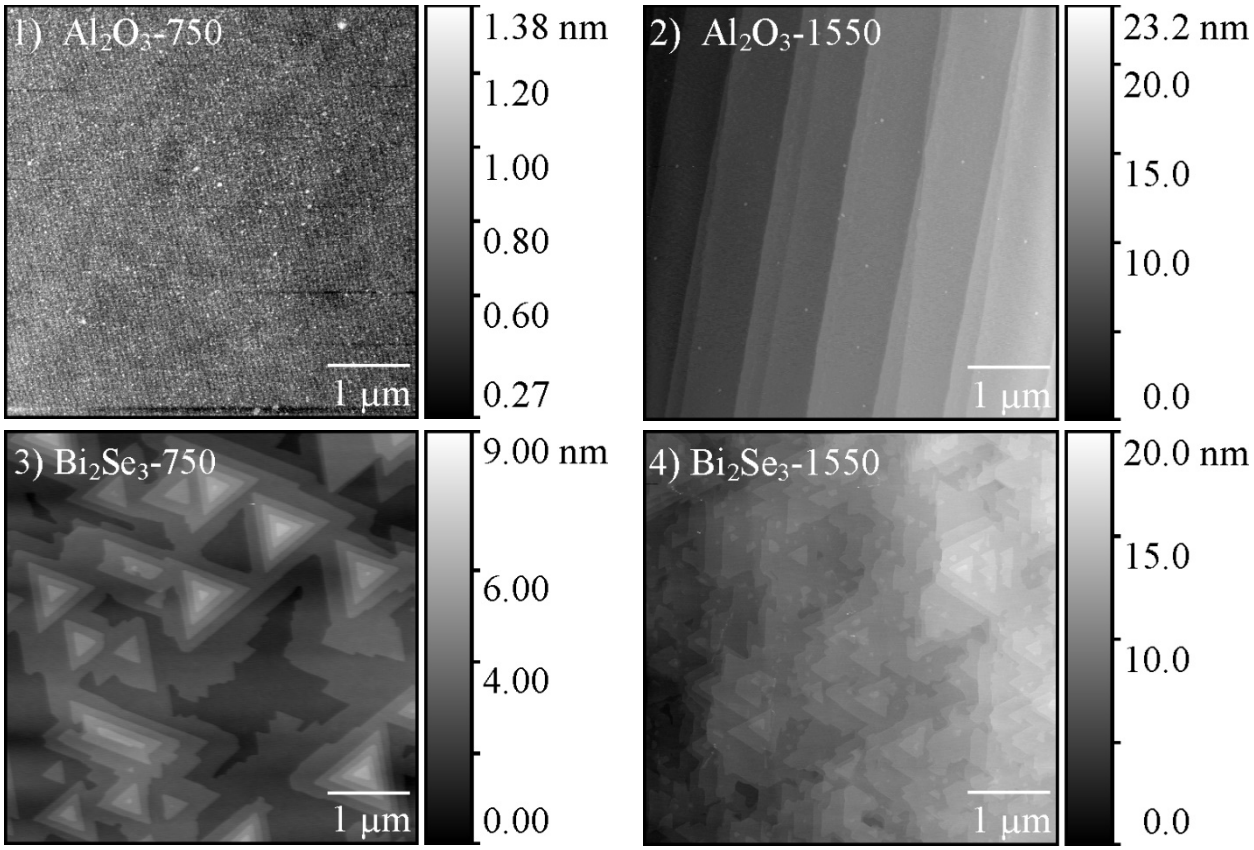


Figure 1: Sapphire surface structure annealed at 750°C (1) and 1550°C (2). Growth of $Bi_2Se_3$ on sapphire annealed at 750°C (3) and 1550°C (4). The sample grown on sapphire annealed at 1550°C appears to have less vertical island growth with slightly larger, less distinctive, domains. This sample also clearly grows on the same terraced step structure as the base sapphire.

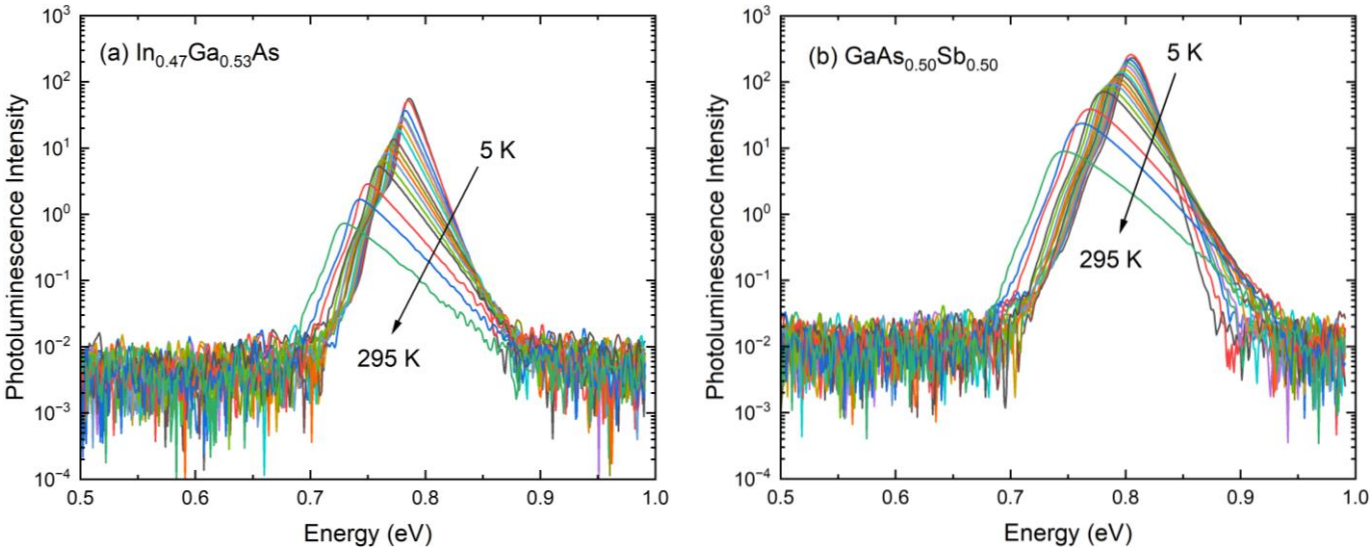


**Fig. 1** Photoluminescence spectra for unintentionally doped $In_{0.47}Ga_{0.53}As$ (a) and $GaAs_{0.50}Sb_{0.50}$ (b) on InP substrate as a function of temperature from 5 K to room temperature.

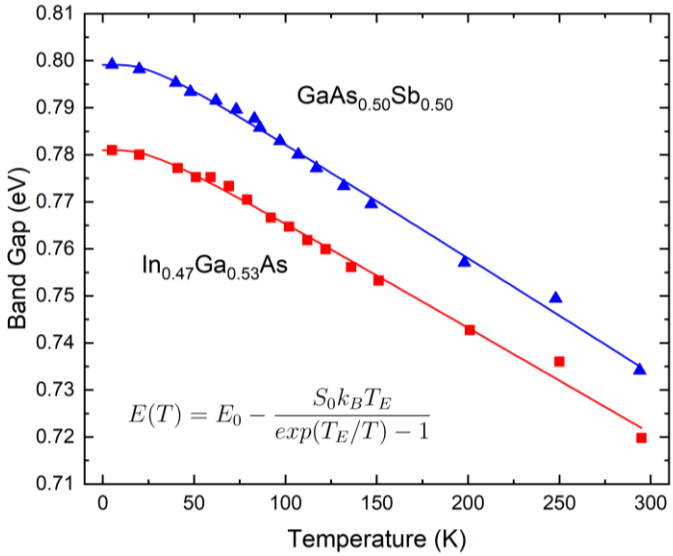


**Fig. 2** Temperature-dependent band gap extracted from photoluminescence for both $In_{0.47}Ga_{0.53}As$ and $GaAs_{0.50}Sb_{0.50}$ samples lattice matched to InP (triangles and squares). The data was fit to the Einstein single oscillator equation shown for each sample (solid lines).

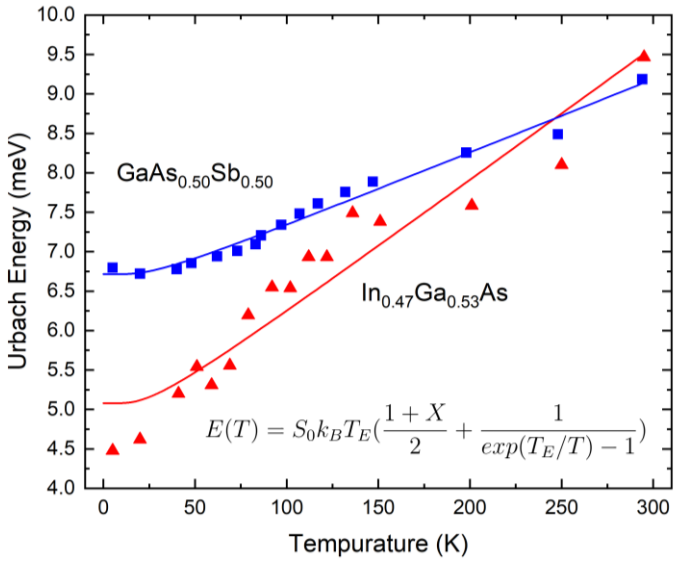


**Fig. 3** Urbach Energy extracted from the sub band gap slope of the photoluminescence as a function of temperature for both $In_{0.47}Ga_{0.53}As$ and $GaAs_{0.50}Sb_{0.50}$ samples lattice matched to InP (triangles and squares). The data was fit to the Einstein single oscillator equation shown for each sample (solid lines).

**Table 1** Einstein single oscillator fit parameters for the band gap as a function of temperature for unintentionally doped $In_{0.47}Ga_{0.53}As$ and $GaAs_{0.50}Sb_{0.50}$.

| *Sample* | $T_E$ $(K)$ | $S_0$ | $E_0$ $(meV)$ |
|---|---|---|---|
| GaAsSb | 70 | 2.855 | 779.1 |
| InGaAs | 69 | 2.618 | 781.0 |

**Table 2** Einstein single oscillator fit parameters for the Urbach Parameter as a function of temperature for unintentionally doped $In_{0.47}Ga_{0.53}As$ and $GaAs_{0.50}Sb_{0.50}$.

| *Sample* | $T_E$ $(K)$ | $S_0$ | $X$ |
|---|---|---|---|
| GaAsSb | 75 | 0.109 | 18.04 |
| InGaAs | 69 | 0.196 | 7.65 |

*Kaushini S. Wickramasinghe et al.,* Transmission Electron Microscopy Studies of the Formation of $In_2Se_3$ Layers via Selenium Passivation of InP(111)B Substrates

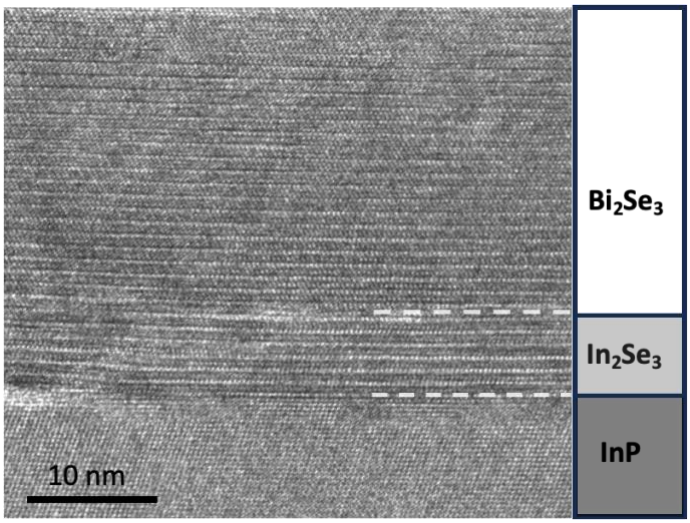


Figure 1. Cross-sectional HR-TEM image of $Bi_2Se_3$ on $In_2Se_3$ layer grown via selenium passivation of InP(111)B substrate showing abrupt interfaces between the layers.

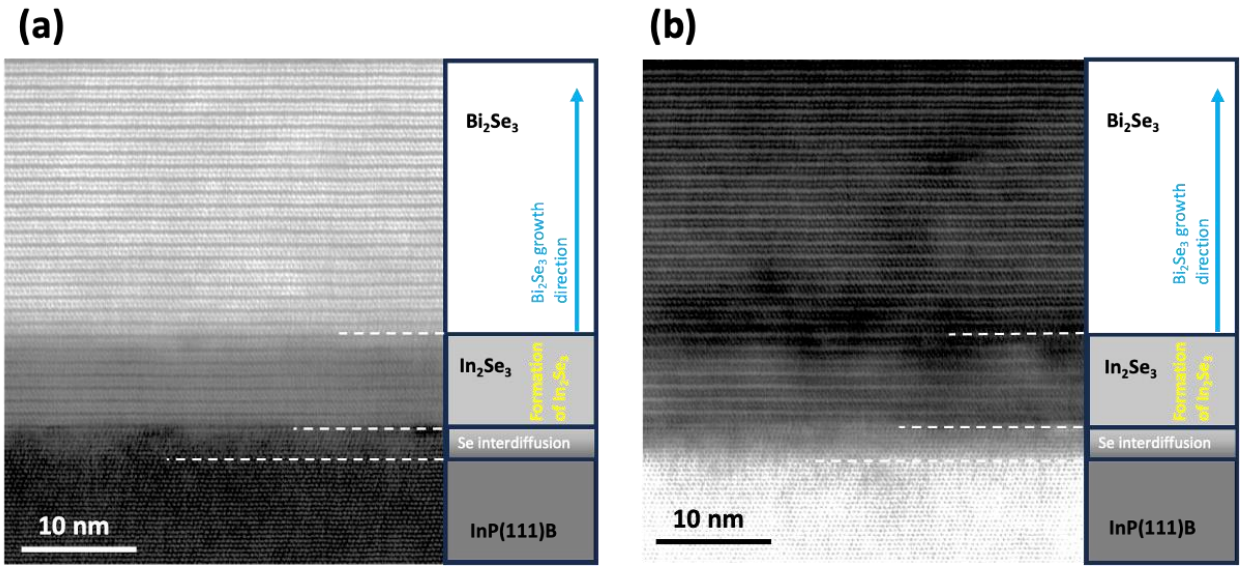


Figure 2. Cross-sectional (a)HAADF and (b) BF image of $Bi_2Se_3$ on $In_2Se_3$ layer grown via selenium passivation of InP(111)B substrate clearly showing abrupt interface between $Bi_2Se_3$ and $In_2Se_3$ layers and the zinc blende InP lattice and the rhombohedral $In_2Se_3$ layer. Images also show selenium diffusion further into the substrate without changing the crystal structure of zinc blende InP.

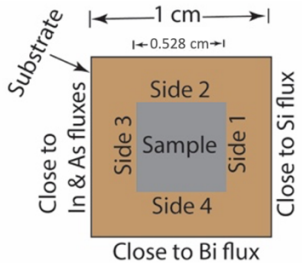


Fig. 1: Schematic of sample (top view of in-plane GPM sample). The sides indicate the elemental cells they face during the growth of the film.

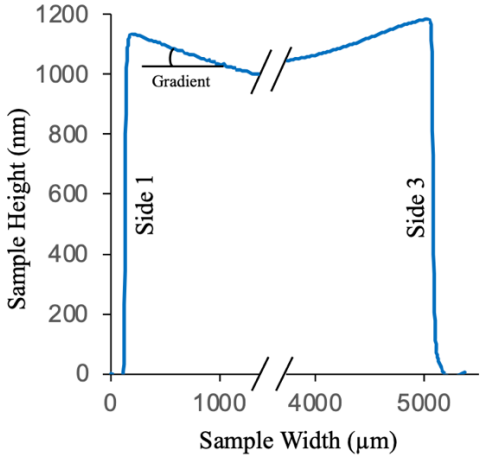


Fig. 2: Surface profile of in-plane GPM sample in the direction of side1 to side3. This figure represents the thickness gradient of the sample. The thickness gradient gives rise to composition gradient, which in turn gives rise to doping gradient leading to permittivity gradient in the sample.

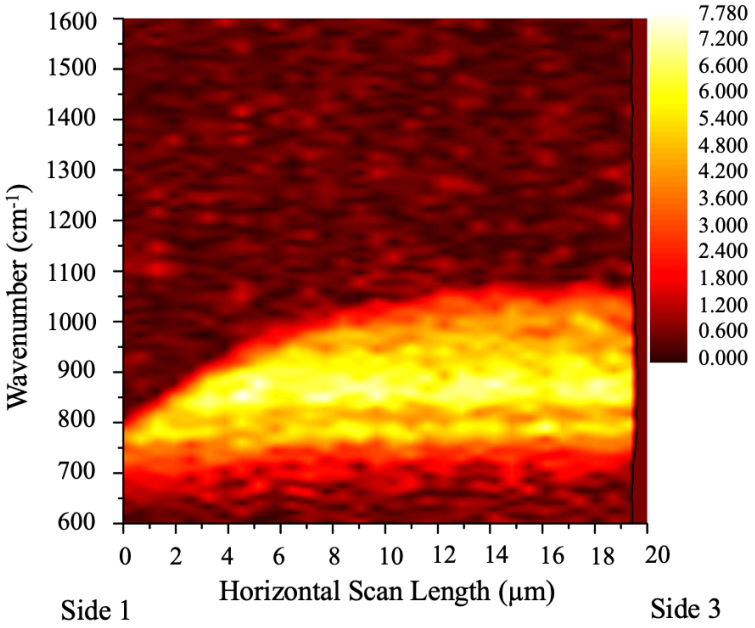


Fig. 3: Characterization by s-SNOM (scattering-type scanning near-field optical microscopy) using mid-IR light source on in-plane GPM. This figure illustrates that the GPM confines different wavelengths of light (corresponding to the gradient in wavenumber) with respect to distinctive in-plane positions in the GPM.

# Strain relaxation of graded InGaN and AlGaN

Reem E. Alhelais[1 2], Fernando Maia de Oliveira[3], Hryhorii V. Stanchu[3], Mohammad Zamani-Alavijeh[4], Mirsaeid Sarollahi[6], Yuriy I. Mazur[3], Najm Al-Hosainy[2], Morgan E. Ware[1 3 5]

[1] Department of Materials Science and Engineering, University of Arkansas, Fayetteville, AR, 72701, USA

[2] Department of Physics, Taif University, Taif, 21944, Saudi Arabia

[3] Institute for Nanoscience and Engineering, University of Arkansas, Fayetteville, AR 72701, USA

[4] Department of Physics, University of Arkansas, Fayetteville, AR, 72701, USA

[5] Department of Electrical Engineering, University of Arkansas, Fayetteville, AR, 72701, USA

[6] Department of Physics, University of Idaho, Moscow, 83843, USA

E-mail: meware@uark.edu, realhela@uark.edu

III-nitride semiconductor materials have proved to be ideal materials for high-power, high-frequency, and high-temperature applications because of their tunable direct band gaps, high breakdown voltage, high absorption coefficient, resistance to defects, lattice match, and polarization characteristics. These materials form a continuous alloy system with direct bandgaps from 6.2 eV (AlN) through 3.4 eV (GaN) to 0.7 eV (InN). The compositionally graded Group III-nitride alloy enables access to large range of energies through varying the bandgap. This change in bandgap is achieved through varying the indium and aluminum composition during growth, which yields excellent compatibility for various optoelectronic applications.

The growth and quality of mismatched heteroepitaxial III-Nitrides layers are generally influenced by strain relaxation mechanisms that release the accumulated strain energy. Plastic relaxation is generally started by the formation of misfit dislocations above the critical thickness. This has been well studied and is generally understood for heteroepitaxial films with fixed composition. Graded composition films have been investigated recently for potential incorporation into semiconductor devices, however the issue of plastic relaxation for graded III-Nitride semiconductors has not been thoroughly investigated.
Graded InGaN and AlGaN can be grown pseudomorphically strained to its substrate until some critical amount of strain energy is built up. This can happen either as a result of reaching a maximum composition or a maximum growth thickness. These two parameters are not independent in terms of their contribution to the buildup of strain energy, and the goal of this study is to determine both the range over which these alloy layers can be grown without relaxation and the mechanisms by which they exhibit relaxation.

In the present work, we have grown both graded InGaN and AlGaN layers with 30 % of In and Al composition of increasing thicknesses for 15 min, 30 min, and 60 min on GaN substrates. We investigated their properties through X-ray diffraction reciprocal space mapping (RSM). With increasing the thickness of these graded layers, the InGaN or AlGaN signature in the RSM shifts from a fully strained position. Atomic force microscopy will be also used to characterize the

sample surface of interest, including dislocation density, while transmission electron microscopy will be used to understand the nature of relaxing defects that is formed in these layers. How these introduced dislocations impact the electrical and optical properties will be demonstrated through photoluminescence and Raman spectroscopy.

- X-ray diffraction reciprocal space mapping (RSM)

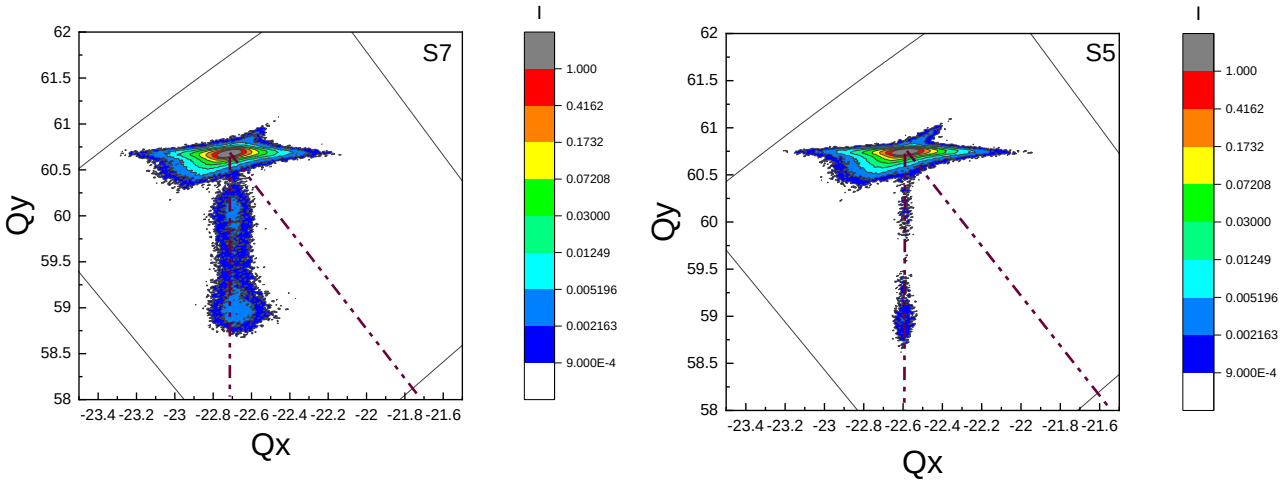


With increasing the thickness of these graded layers, the InGaN or AlGaN signature in the RSM shifts from a fully strained position.

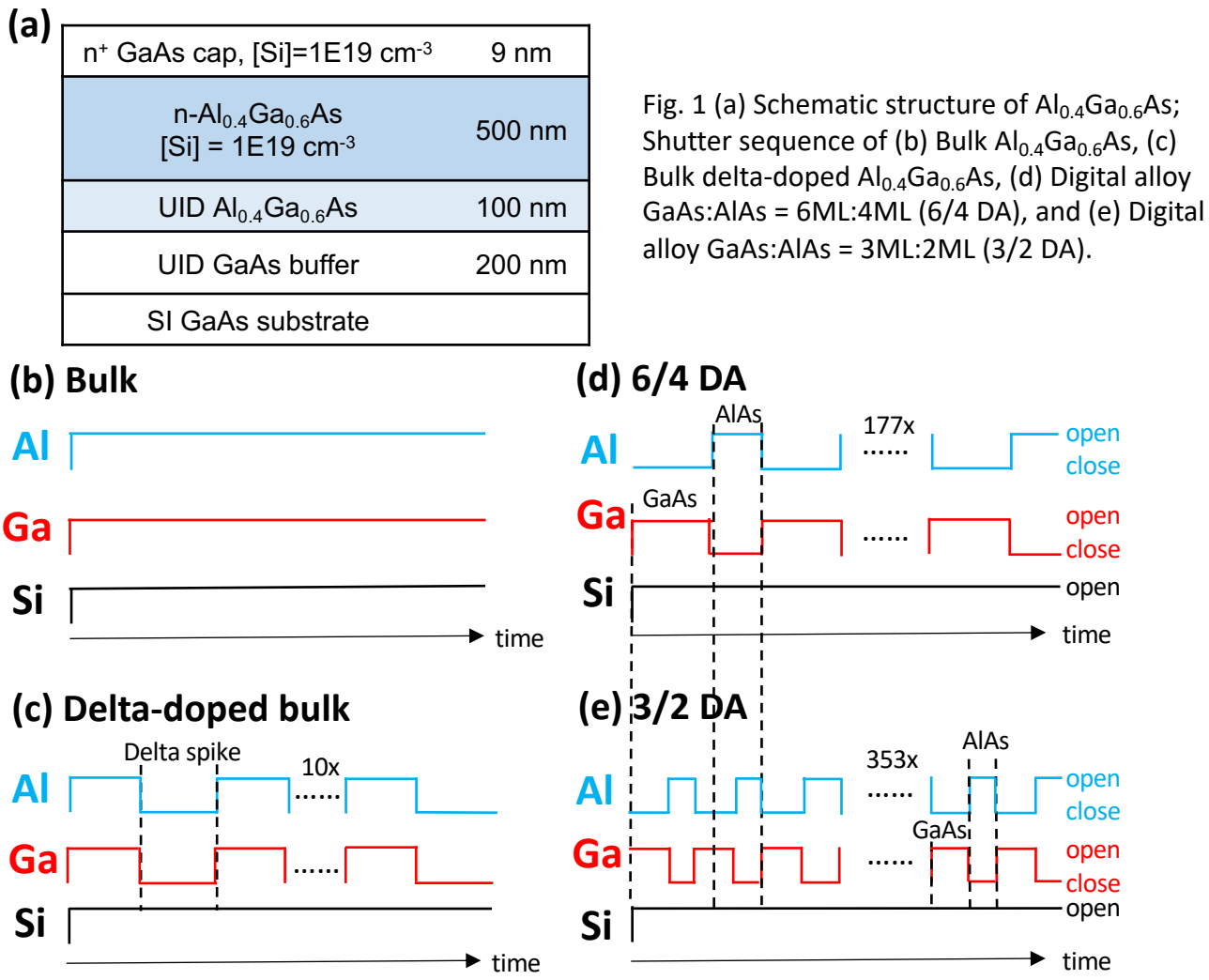


Fig. 1 (a) Schematic structure of $Al_{0.4}Ga_{0.6}As$; Shutter sequence of (b) Bulk $Al_{0.4}Ga_{0.6}As$, (c) Bulk delta-doped $Al_{0.4}Ga_{0.6}As$, (d) Digital alloy GaAs:AlAs = 6ML:4ML (6/4 DA), and (e) Digital alloy GaAs:AlAs = 3ML:2ML (3/2 DA).

| Growth Method | $n_0$ ($cm^{-3}$) | Doping enhancement over bulk alloy | Activation (%) | $T_{sub}$ (°C) | $T_{Si}$ (°C) | RMS (nm) |
|---|---|---|---|---|---|---|
| Bulk Alloy | 7.3E15 | 1 | 0.073 | 610 | 1223 | 2.1 |
| Delta doped | 1.0E16 | 1.4 | 0.10 | 610 | 1191 | 4.0 |
| 6/4 DA | 1.9E16 | 2.6 | 0.19 | 610 | 1223 | 1.0 |
| 3/2 DA | 1.0E17 | 14 | 1.0 | 500 | 1219 | / |
| 3/2 DA | 2.5E17 | 34 | 2.5 | 610 | 1223 | 1.4 |

Table 1. Description of bulk, delta-doped, and DA samples in this work. Activation = bulk doping/target doping = bulk doping/1E19 $cm^{-3}$.

Supplemental Document placeholder continued for Abstract 77550, Paper ST-MoP-3 (page 2 of 2)

**$T_{sub}$=455 °C** **$T_{sub}$=495 °C**

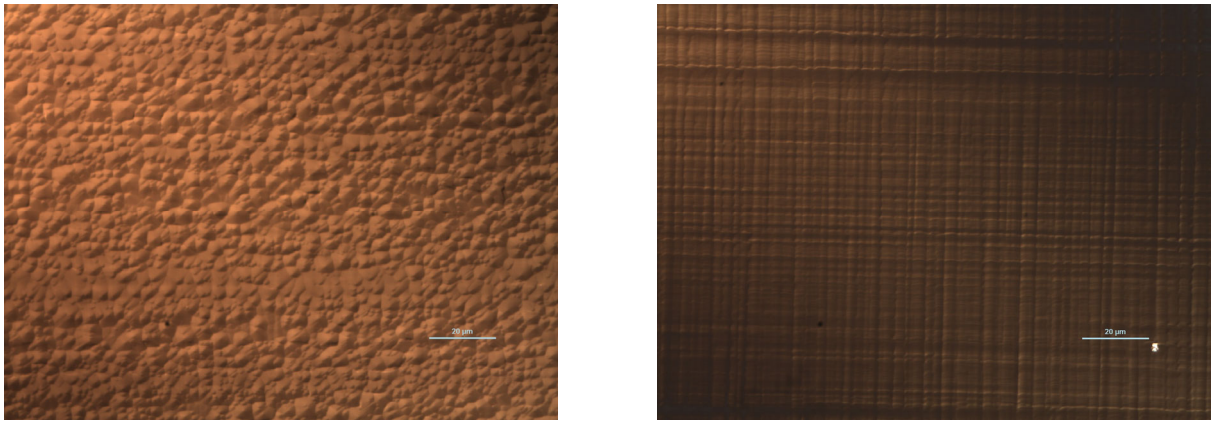

Nomarski microscopy images of InGaSb graded buffers grown at $T_{sub}$= 455 °C (left) and 495 °C (right)

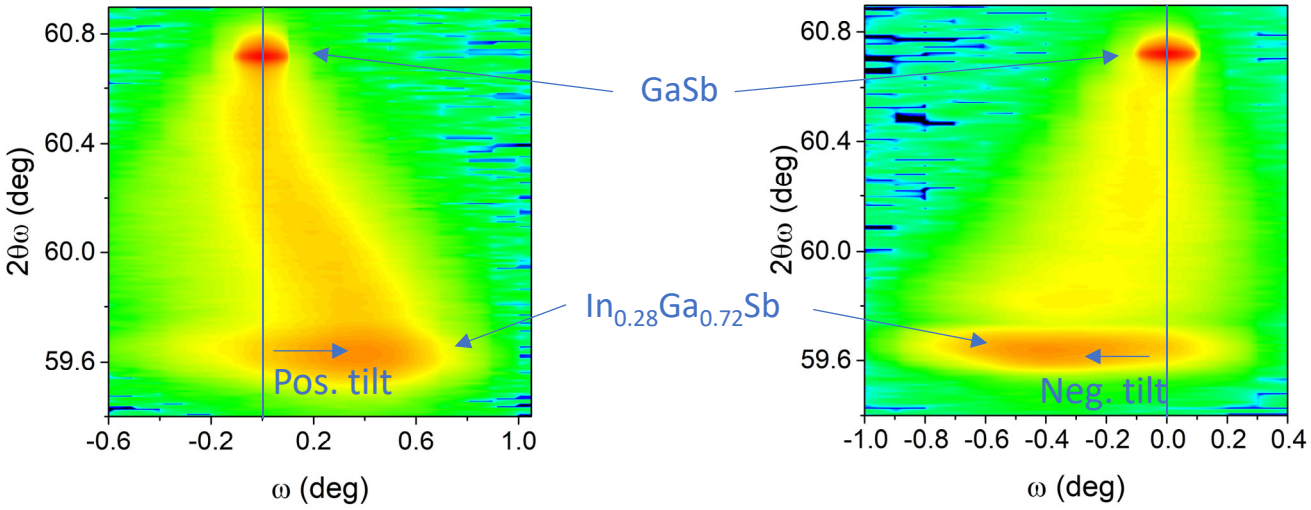


(004) Reciprocal space maps of InGaSb graded buffers with $T_{sub}$= 455 °C (left) and 495 °C (right) taken along [110], revealing positive tilt and negative tilt, respectively.

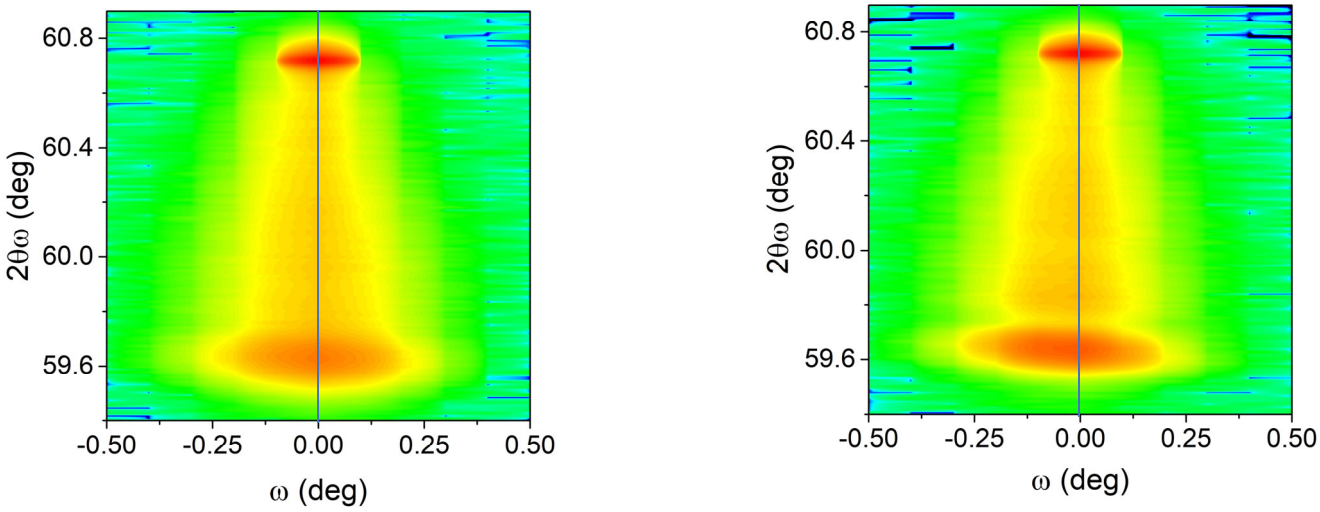


(004) Reciprocal space maps of InGaSb graded buffers with $T_{sub}$= 455 °C (left) and 495 °C (right) taken along [1$\bar{1}$0], revealing little tilt.

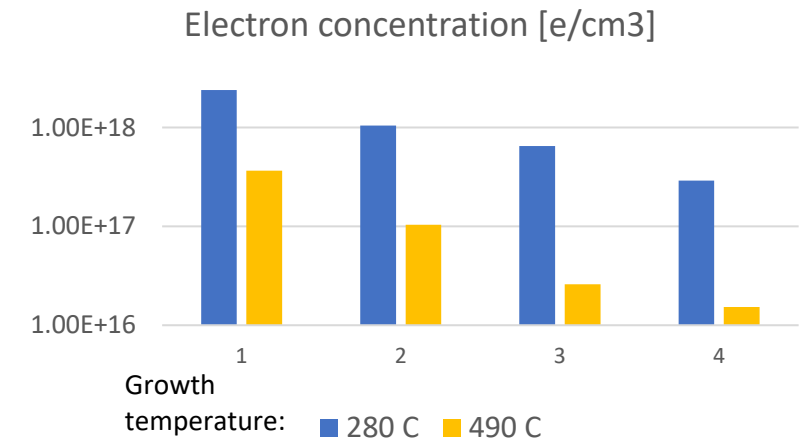


**Figure 1.** Impact of Er incorporation and growth temperature on InGaAs materials.
**1.** Co-deposition. ErAs ~1.7%
Interrupt growth:
**2.** 20 nm period InGaAs, As shutter always open. ErAs~0.3%
**3.** 22 nm period InGaAs, As closed during Er deposition + 30 s all shutters close. ErAs~1.3%
**4.** 30 nm period InGaAs, As closed during Er deposition + 30 s all shutters close. ErAs~1%

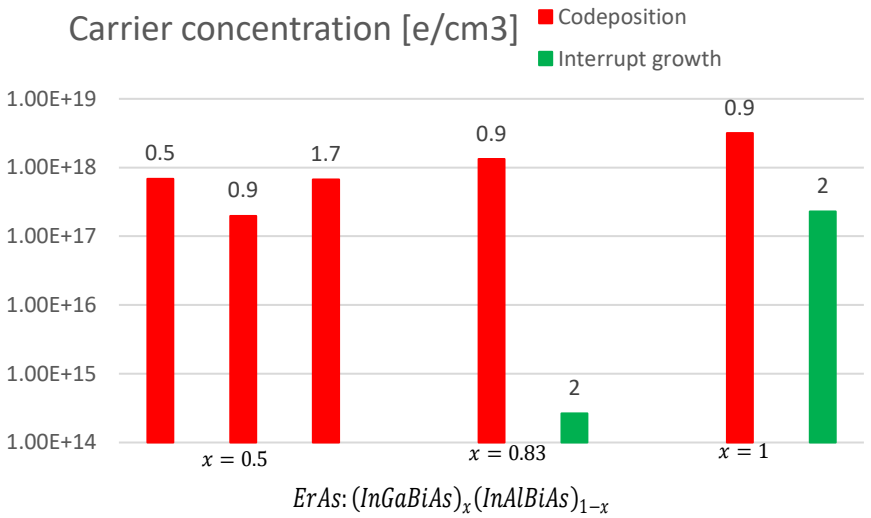


**Figure 2.** Carrier concentration in ErAs:InGaAlBiAs digital alloys. For interrupt growth, the matrix period is 30 nm and Er shutter was open for 45 s without As, plus 30 s with all shutters close. (Data labels on top correspond to the approximated %ErAs composition)



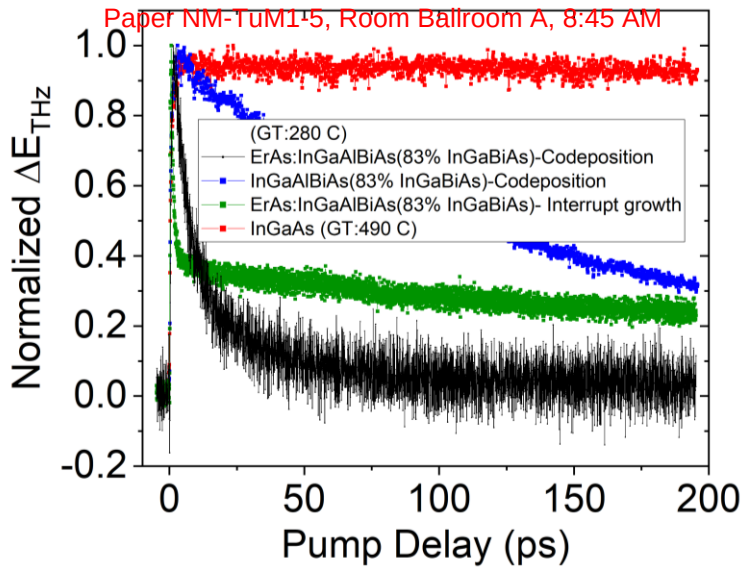


**Figure 3.** Optical pump (800 nm) THz probe on ErAs:InGaAlBiAs materials, showing a fast decay component of a few ps in samples with Er. We have also achieved sub-picosecond dynamics.

# Supplementary Pages (Optional)

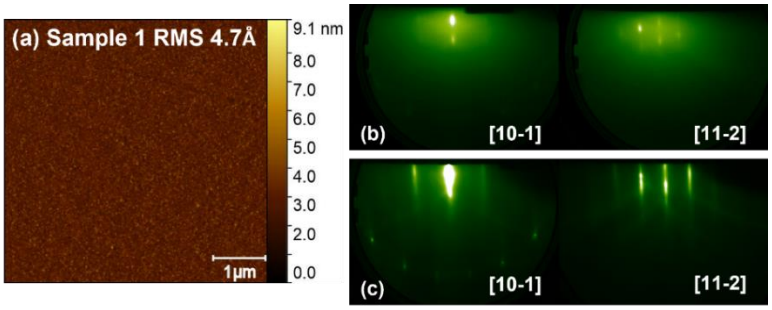


Fig. S1 (a) Atomic force microscope (AFM) image ($5\times5\mu m^2$) of sample 1, a deoxidized GaAs(111)B substrate. *In-situ* reflection high energy electron diffraction (RHEED) patterns of the GaAs(111)B before (b) and after (c) deoxidation. Root mean square (RMS) surface roughness of sample 1 is 4.7Å. [10-1] and [11-2] are the in-plane orientations of GaAs(111).

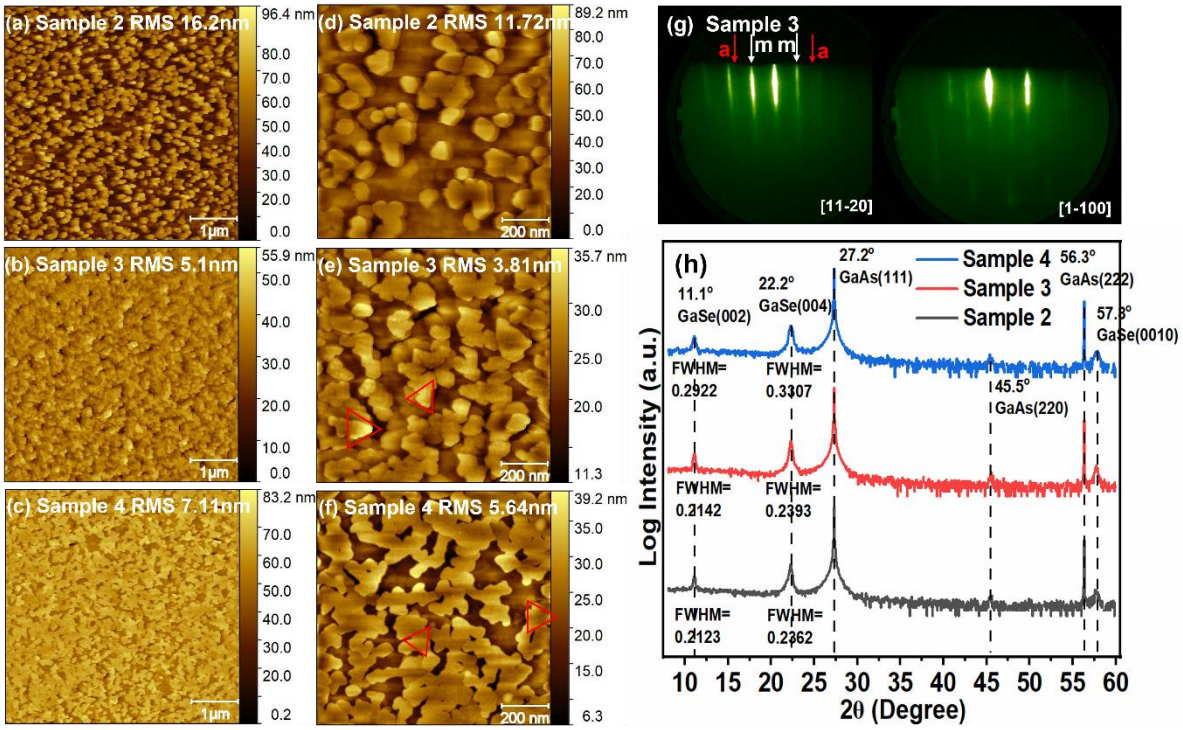


Fig. S2 AFM images ($5\times5\mu m^2$) of samples 2 (a), 3 (b), and 4 (c). AFM images ($1\times1\mu m^2$) of samples 2 (d), 3 (e) and 4 (f). The red triangle boxes mark typical GaSe nucleation domains. (g) *In-situ* RHEED patterns taken at the end of growth of sample 3, along two in-plane orientations of GaSe. The red and white arrows indicate a-plane and m-plane diffractions, respectively. (h) $2\theta/\omega$ X-ray diffraction curves of samples 2-4. FWHM (full width at the half maximum) indicates the crystallite sizes. Samples 2-5 were grown using the same Se:Ga flux ratio and growth rate. Samples 2 and 3 were grown at 375°C, but sample 3 was annealed in Se at 375°C for 30min before growth. Sample 4 was grown via 2-step method: initially grew at 375°C for 8min, then grew at 450°C for 60min. Sample 5 was grown at 375°C for 8min (the first step of growing sample 4).

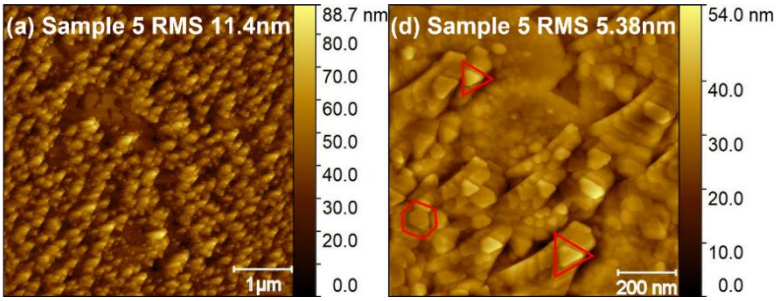


Fig. S3 AFM images ($5\times5\mu m^2$) (a) and ($1\times1\mu m^2$) (b) of sample 5. It used same growth conditions as sample 2, but used a freshly cleaved GaAs(111)B substrate. Red boxes mark GaSe nucleation domains.

[1] M. Yu, L. Murray, M. Doty, and S. Law, J. Vac. Sci. Technol. A 41 (3), 2023.

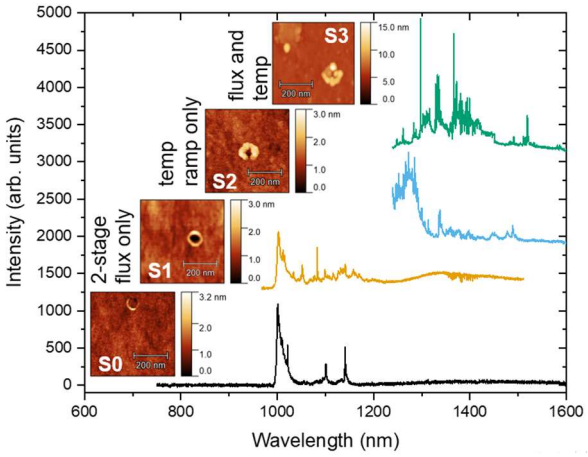


**Fig S1**: Photoluminescence spectra at 4 K of InAs droplet epitaxy structures with different morphologies. By varying the flux and temperature conditions during the crystallization stage of droplet epitaxy, the resulting emission is redshifted into the telecommunication wavelength ranges. Figure modified from Stevens et al. *JVSTA* **41** 032703 2023.

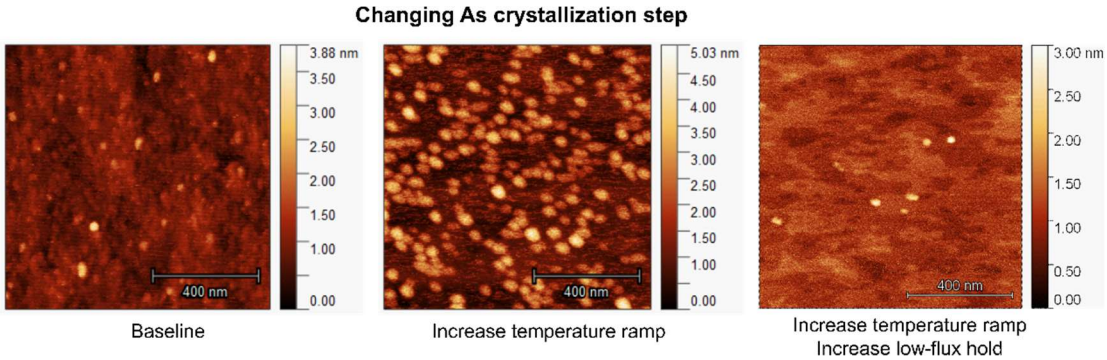


**Fig S2**: Atomic force microscopy images of quantum dots formed during different manipulations of the As crystallization step. Increasing the temperature ramp results in a high density of larger quantum dots. Increasing the temperature ramp and increasing the low-flux hold time reduces the quantum dot density.

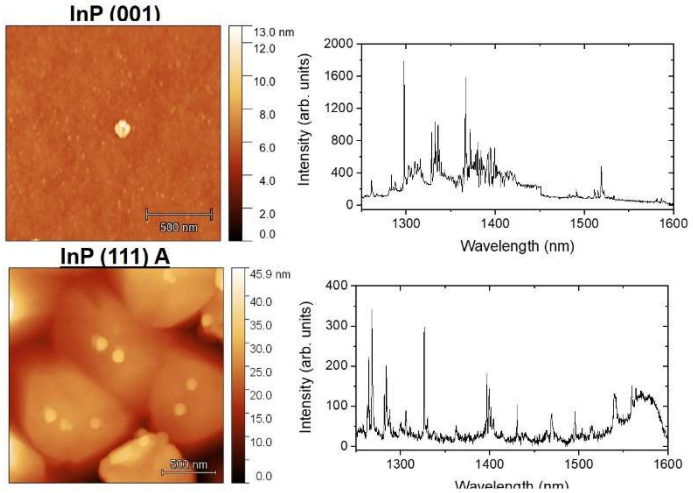


**Fig S3**: AFM images and PL spectroscopy of DE structures on InP (001) substrates compared to InP (111)A substrates.

# Supplementary Pages

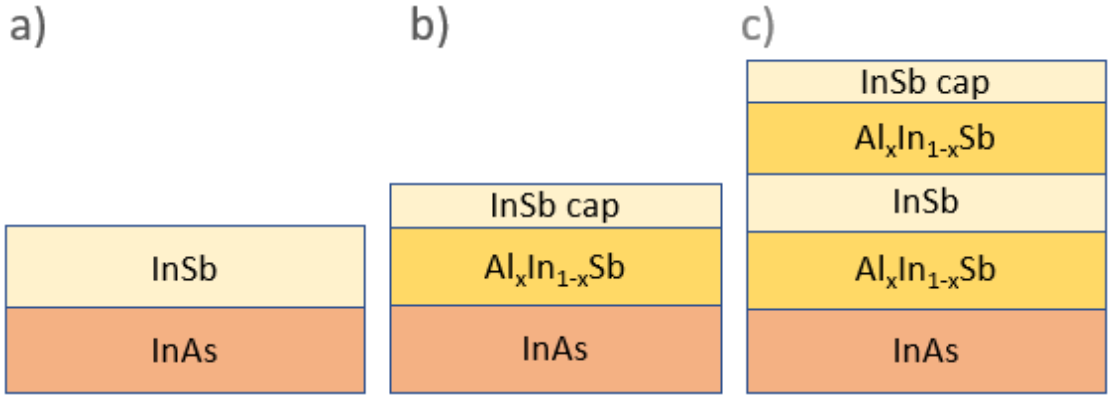


Figure 1: Schematic of different configurations of the IMF samples

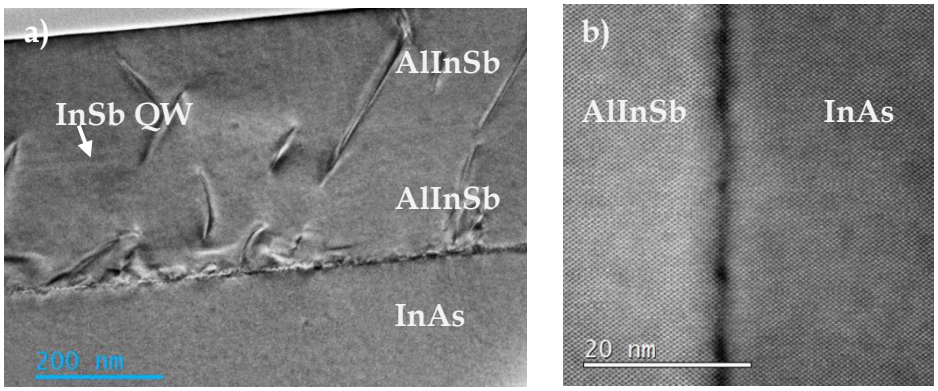


Figure 2: TEM image of InSb QW using AlInSb buffer shown (a). Interfacial misfit dislocations at the AlInSb/InAs interface

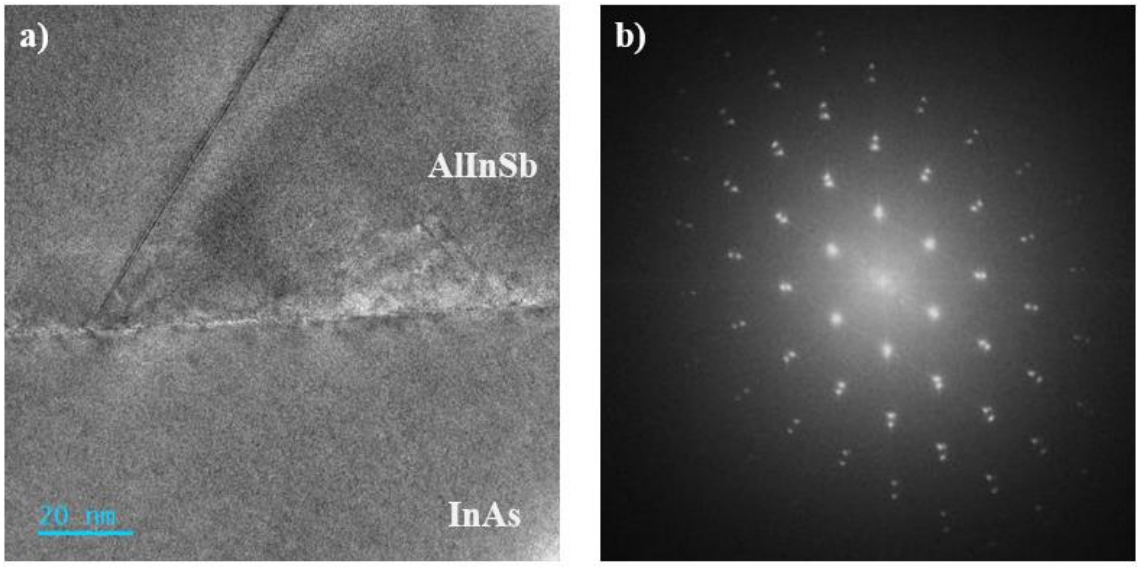


Figure 3: *TEM of the $Al_{0.2}In_{0.8}Sb$/InAs buffer layer interface showing a stacking fault formation and FFT of the image shows two distinct lattice parameters $Al_{0.2}In_{0.8}Sb$ and InAs*

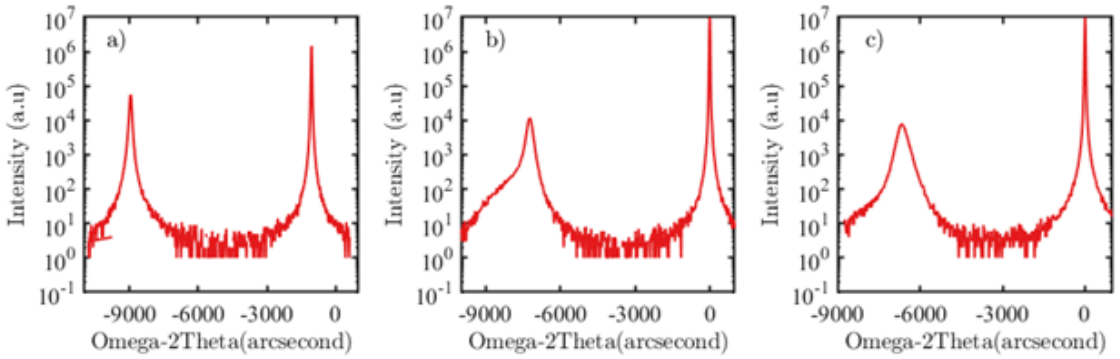


Figure 4 – *HR-XRD ω-2θ scans of a) InSb/InAs b) $Al_{0.1}In_{0.9}Sb$ and c) $Al_{0.2}In_{0.8}Sb$ buffer layers*

# Flexomagnetism And Strain-Induced Superconductivity in Rippled GdAuGe Heusler Membranes

Tamalika Samanta, Zachary LaDuca, Dongxue Du, Taehwan Jung, Sebastian Manzo, Katherine Su, Michael Arnold, and Jason Kawasaki

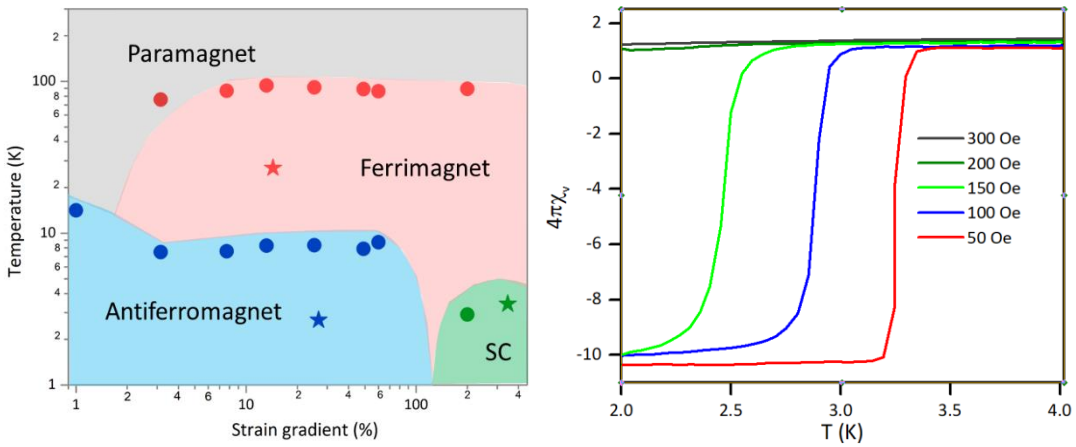


*Figure 1: (a) Phase diagram for rippled GdAuGe membranes. The circle and star denote differently exfoliated rippled membranes. (b) The field-dependent onset of diamagnetism in a rippled membrane shows the Meissner response, implying superconductivity.*

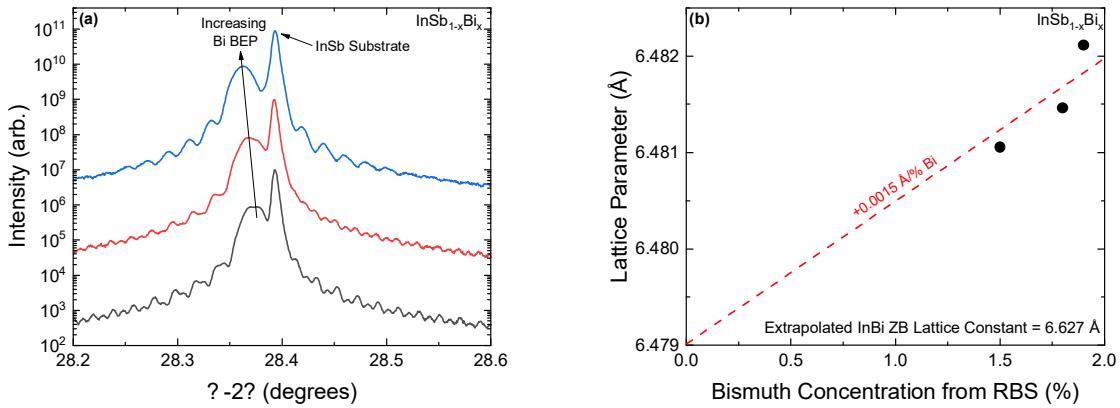


**Fig. 1 (a)** Coupled XRD ω-2θ scans about the (004) peak of InSb of three $InSb_{1-x}Bi_x$ films demonstrating a shift to greater angles with increasing bismuth beam equivalent pressure (BEP). **(b)** The effective strained mismatch between the $InSb_{1-x}Bi_x$ layer peaks and the InSb substrate was converted to a lattice parameter. The lattice parameter increased as a function of total bismuth concentration, as measured by RBS, enabling linear extrapolation of the lattice parameter of InBi yielding a value of 6.627 Å.

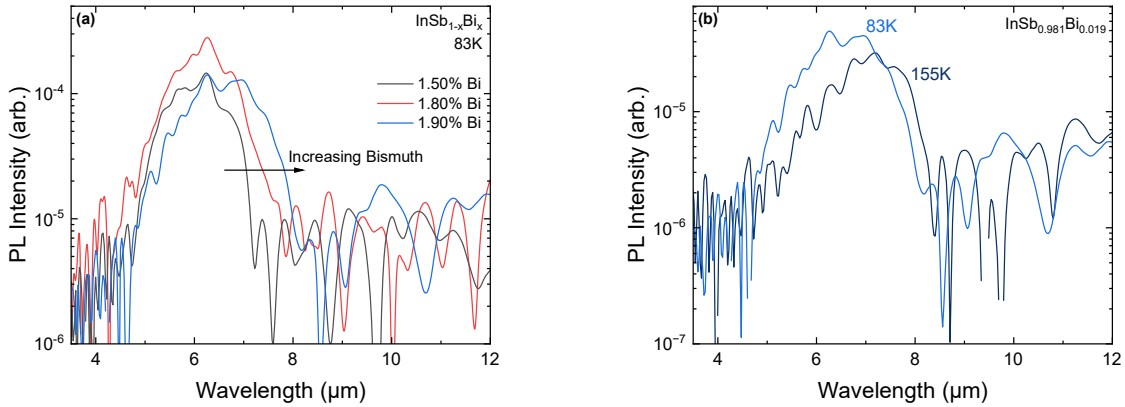


**Fig. 2 (a)** PL spectra measured at 83 K for the $InSb_{1-x}Bi_x$ films demonstrating wavelength extension with increasing bismuth concentration as expected due to the bismuth-induced bandgap reduction. **(b)** PL spectra for the film with the highest bismuth content exhibiting increasing wavelength extension with increasing temperature consistent with an optical interband transition as expected for a III-V alloy.

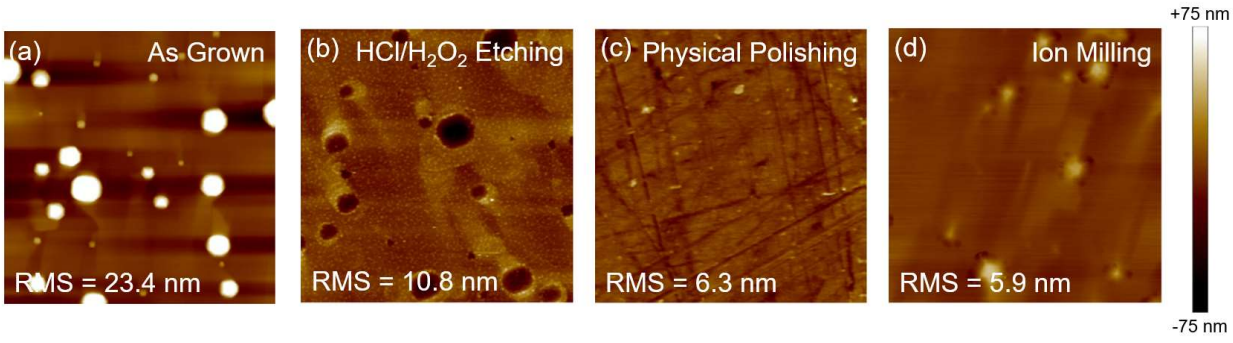


**Fig. 3** 5 μm × 5 μm atomic force microscopy scans of **(a)** InSb with large bismuth droplets as grown; as well as individual pieces of the same sample after **(b)** 3 cycles of $HCl/H_2O_2$ digital etching leaving pits remaining where the droplets had been **(c)** physical polishing showing scratches left behind and **(d)** ion milling with remnants of droplets still present on the surface.

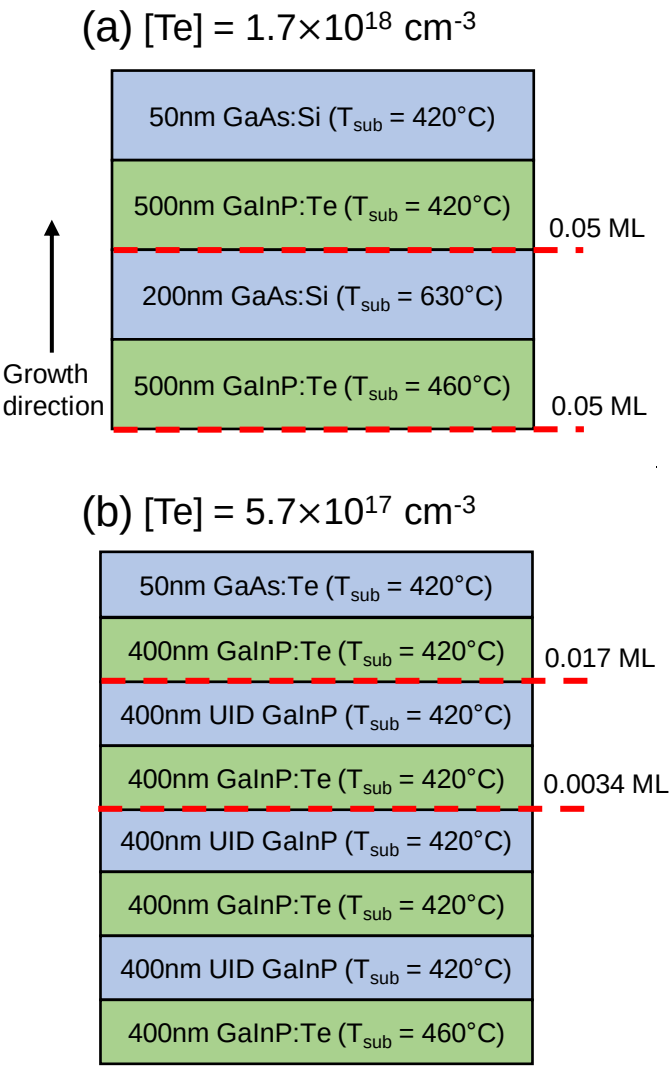


Figure 1: Growth structures for GaInP:Te SIMS profiling, grown on GaAs (001) substrates (not shown). Te pre-dose values indicated by dotted lines in monolayers (ML). (a) target [Te] = $1.7\times10^{18}$ cm$^{-3}$ with GaAs spacer to absorb excess Te. (b) target [Te] = $5.7\times10^{17}$ cm$^{-3}$ with unintentionally doped (UID) GaInP spacers to absorb excess Te.

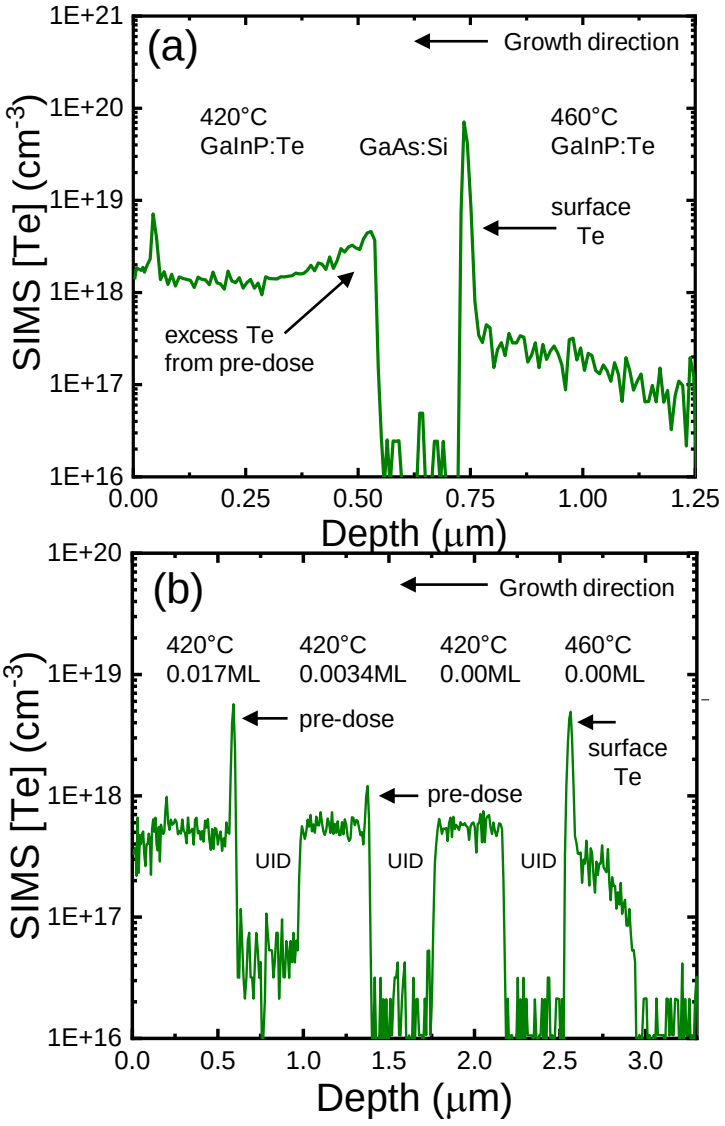


Figure 2: SIMS profiles corresponding to growth structures in Figure 1. (a) SIMS for target [Te] = $1.7\times10^{18}$ cm$^{-3}$ shows greatly reduced but visible segregation at $T_{sub}$ = 420 °C. (b) SIMS for [Te] = $5.7\times10^{17}$ cm$^{-3}$ shows complete suppression of surface segregation at $T_{sub}$ = 420 °C, as seen by abrupt Te pre-dose spikes.

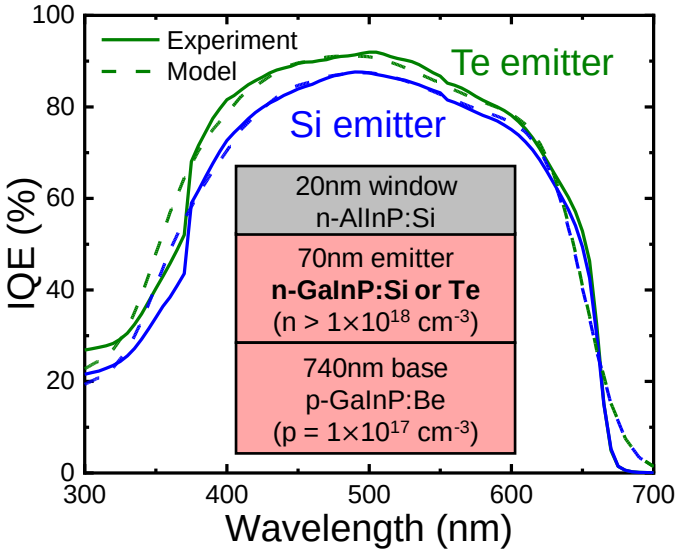


Figure 3: IQE of GaInP solar cells with GaInP:Si and GaInP:Te emitters, experimental (solid) and modeled (dotted). The model indicates a ~4× improved carrier lifetime for n-GaInP:Te. Inset simplified cell structure shows AlInP window and n/p GaInP absorber region.

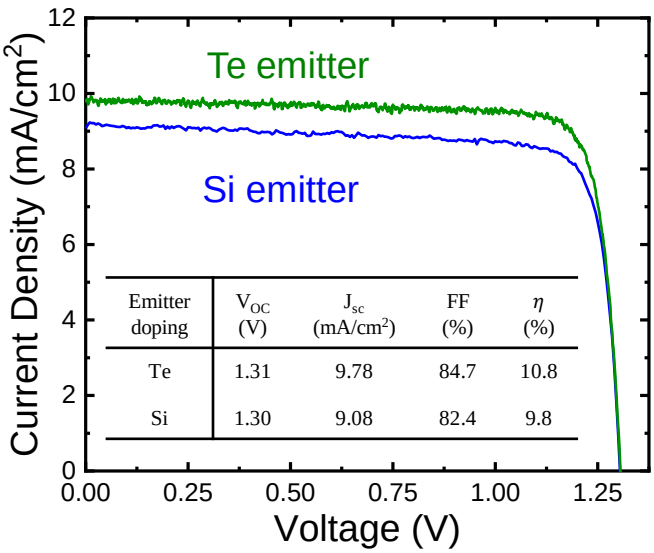


| Emitter doping | $V_{OC}$ (V) | $J_{sc}$ (mA/cm$^2$) | FF (%) | $\eta$ (%) |
|---|---|---|---|---|
| Te | 1.31 | 9.78 | 84.7 | 10.8 |
| Si | 1.30 | 9.08 | 82.4 | 9.8 |

Figure 4: Lighted IV curves of GaInP cells with GaInP:Si and GaInP:Te emitters, and figures of merit of open-circuit voltage ($V_{OC}$), short-circuit current density ($J_{sc}$), fill factor (FF), and efficiency ($\eta$).

# References in abstract

[1] M. A. Green *et al.*, "Solar cell efficiency tables (Version 61)," *Prog. Photovoltaics Res. Appl.*, vol. 31, no. 1, pp. 3–16, 2023.

[2] Y. Sun, B. D. Li, R. D. Hool, S. Fan, M. Kim, and M. L. Lee, "Improving the performance of GaInP solar cells through rapid thermal annealing and delta doping," *Sol. Energy Mater. Sol. Cells*, vol. 241, no. August 2021, p. 111725, 2022.

[3] K. Takahashi, S. Yamada, Y. Minagawa, and T. Unno, "Improved efficiency of Al0.36Ga0.64As solar cells with a pp-n-n structure," *Sol. Energy Mater. Sol. Cells*, vol. 66, no. 1–4, pp. 517–524, 2001.

[4] E. E. Perl *et al.*, "Development of a 2.0 eV AlGaInP solar cell grown by OMVPE," *2015 IEEE 42nd Photovolt. Spec. Conf.*, pp. 1–6, 2015.

[5] O. Kumagai, H. Kawai, Y. Mori, and K. Kaneko, "Chemical trends in the activation energies of DX centers," *Appl. Phys. Lett.*, vol. 45, no. 12, pp. 1322–1323, 1984.

[6] K.-J. Lee, H. K. Chen, and J. C. Chen, "Photoluminescence of the Se and Si DX centers in (AlxGa1-x)0.5In0.5P grown by metalorganic vapor phase epitaxy," *J. Appl. Phys.*, vol. 82, no. 3, pp. 1350–1351, 1997.

[7] I. García, I. Rey-Stolle, B. Galiana, and C. Algora, "Analysis of tellurium as n-type dopant in GaInP: Doping, diffusion, memory effect and surfactant properties," *J. Cryst. Growth*, vol. 298, no. SPEC. ISS, pp. 794–799, 2007.

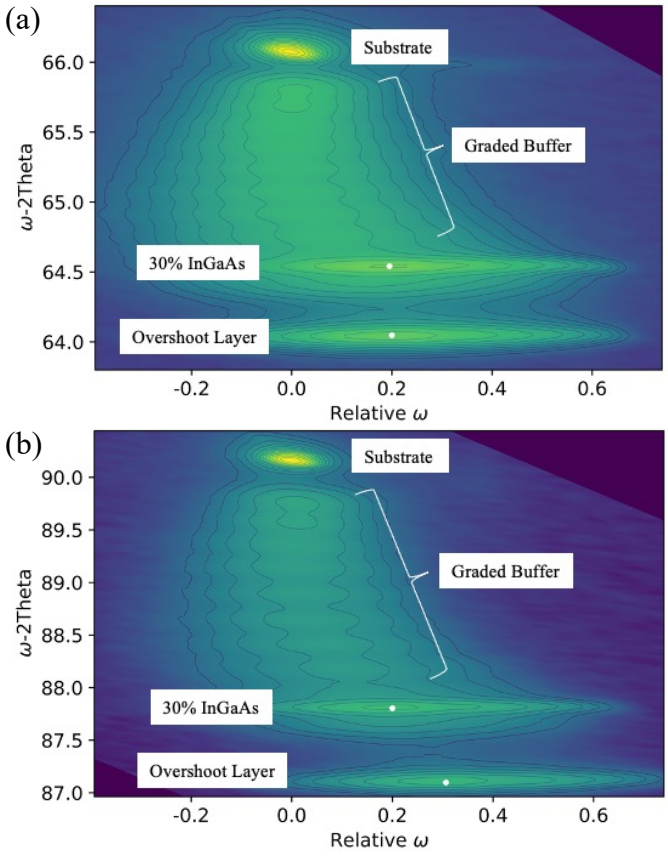


Figure 1: Reciprocal space maps (RSM) of the (a) 004 and (b) 115 lattice planes of the InGaAs graded buffer. A linear grade of 3% In composition intervals with a 0.7%/um grade rate and an overshoot layer of $In_{0.35}Ga_{0.65}As$ were used to realize 97.9% relaxation (-0.04% strain) in the $In_{0.30}Ga_{0.70}As$ cap. The change of relative omega in the graded buffer for both lattice planes is caused by epilayer tilt. ~100% relaxation is indicated by the vertical alignment of the $In_{0.30}Ga_{0.70}As$ cap and overshoot layer in the 004 RSM and an offset in omega between the $In_{0.30}Ga_{0.70}As$ cap and overshoot layer in the 115 RSM.

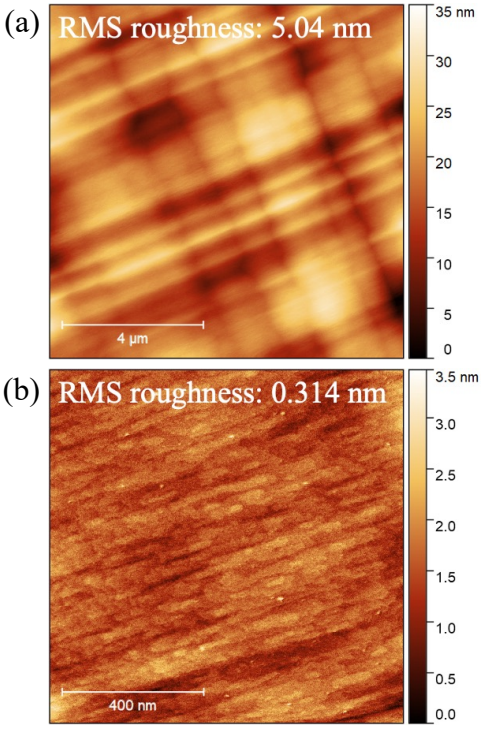


Fig 3: 10x10 μm² (a) and 1x1 μm² (b) atomic force microscopy of the $In_{0.30}Ga_{0.70}As$ graded buffer cap.

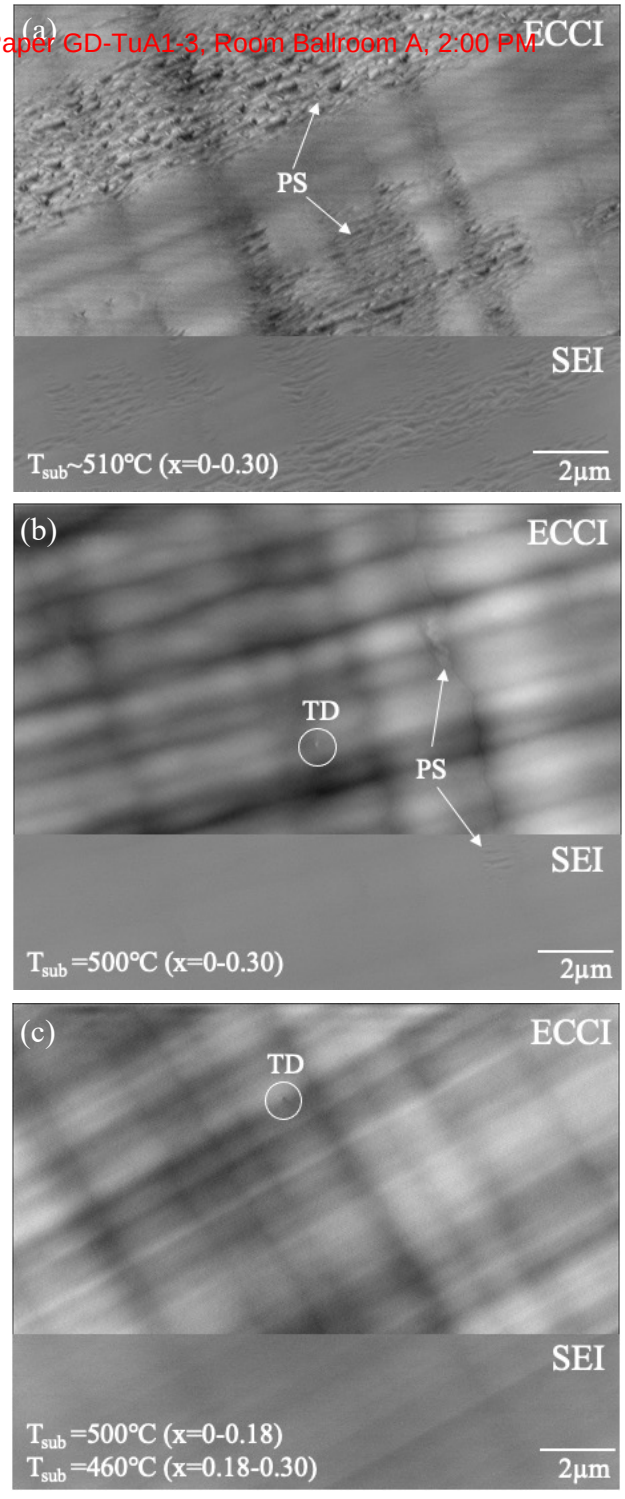


Figure 2: ECCI (top) and SEI (bottom) micrographs of $In_xGa_{1-x}As$ graded buffers grown at various temperatures. At ~510°C (a), rampant PS causes large-scale dislocation nucleation. At 500°C (b), dislocation nucleation is suppressed, but small patches of PS are present. Finally, when growing at 500°C for x=0-0.18 and 460°C for x=0.18-0.30 (c), PS is eliminated and the TDD of $7.0x10^5$ $cm^{-3}$ is comparable to the lowest reported values for $In_{0.30}Ga_{0.70}As$.

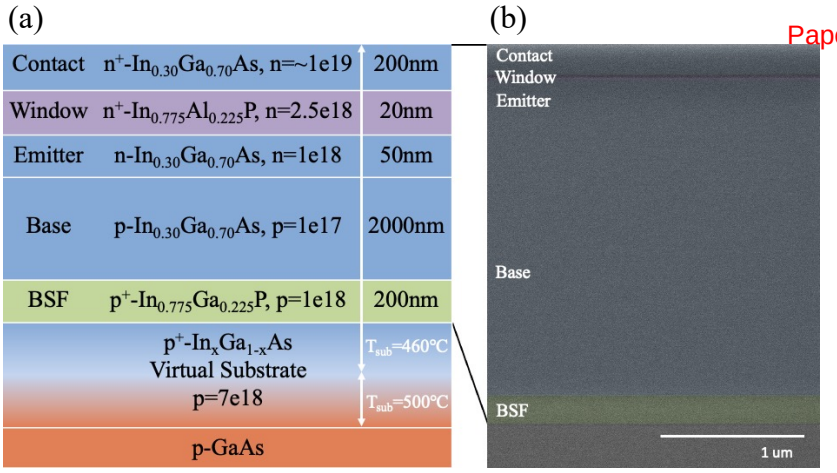


Figure 4: (a) Layer structure of 1 eV InGaAs solar cell grown on a two-step graded buffer. All layers of the device were grown at 460°C. (b) Cross-sectional SEM micrograph of the as-grown solar cell.

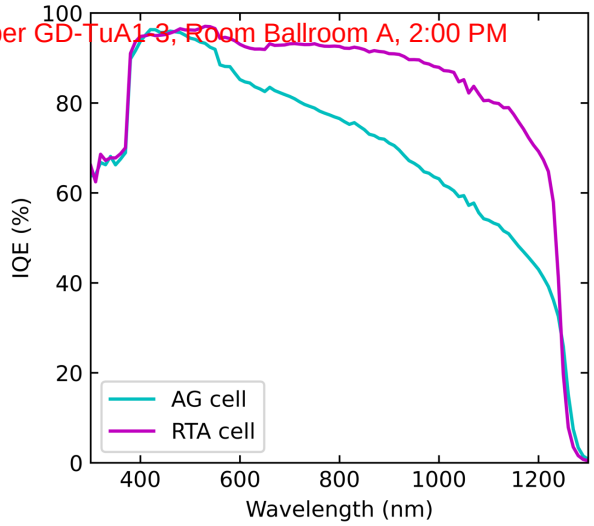


Figure 5: IQE spectra of AG and RTA'd cells. IQE of the RTA'd cell is significantly higher than the AG cell at longer wavelengths due to improved minority electron diffusion length in the base.

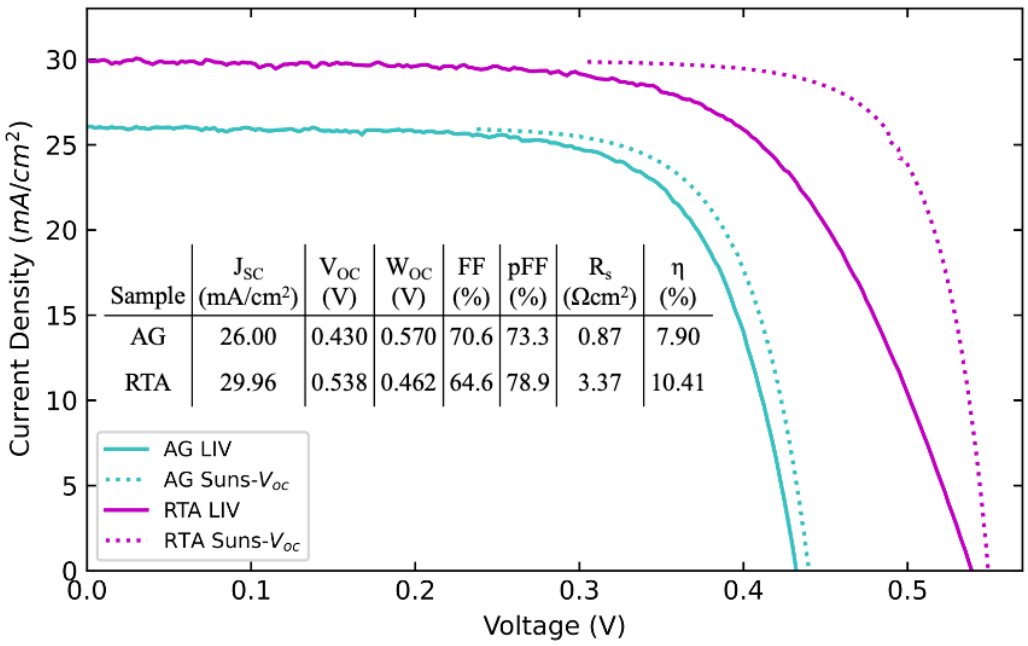


| Sample | $J_{SC}$ (mA/cm²) | $V_{OC}$ (V) | $W_{OC}$ (V) | FF (%) | pFF (%) | $R_s$ (Ωcm²) | η (%) |
|---|---|---|---|---|---|---|---|
| AG | 26.00 | 0.430 | 0.570 | 70.6 | 73.3 | 0.87 | 7.90 |
| RTA | 29.96 | 0.538 | 0.462 | 64.6 | 78.9 | 3.37 | 10.41 |

Figure 6: LIV curves under 1-sun AM1.5 and Suns-$V_{oc}$ curves of the AG and RTA'd cells; the Suns-$V_{OC}$ method allows a 'pseudo IV' curve to be collected without series resistance ($R_S$). No anti-reflection coatings were used. The RTA'd cell has similar $J_{SC}$ and $V_{OC}$ to other MBE-grown 1eV solar cells[6], but series resistance hinders its FF. However, the pFF extracted from Suns-$V_{oc}$ measurements indicates potential for improvement of the cell if series resistance can be reduced.

[1] N. J. Quitoriano and E. A. Fitzgerald, J. Appl. Phys. **102**, 033511 (2007).
[2] M. Kim *et al., in 2021 IEEE 48th Photovoltaic Specialists Conference (PVSC)*, 1762 (2021).
[3] L. Yang *et al., J. Crystal Growth* **324**, 103-109 (2011).
[4] Y. Sun *et al., Solar Energy Materials and Solar Cells* **241**, 111725 (2022).
[5] R. M. France *et al., Joule* **6**, 1121-1135 (2022).
[6] R. Oshima *et al., J. Crystal Growth* **447**, 267-271 (2017).

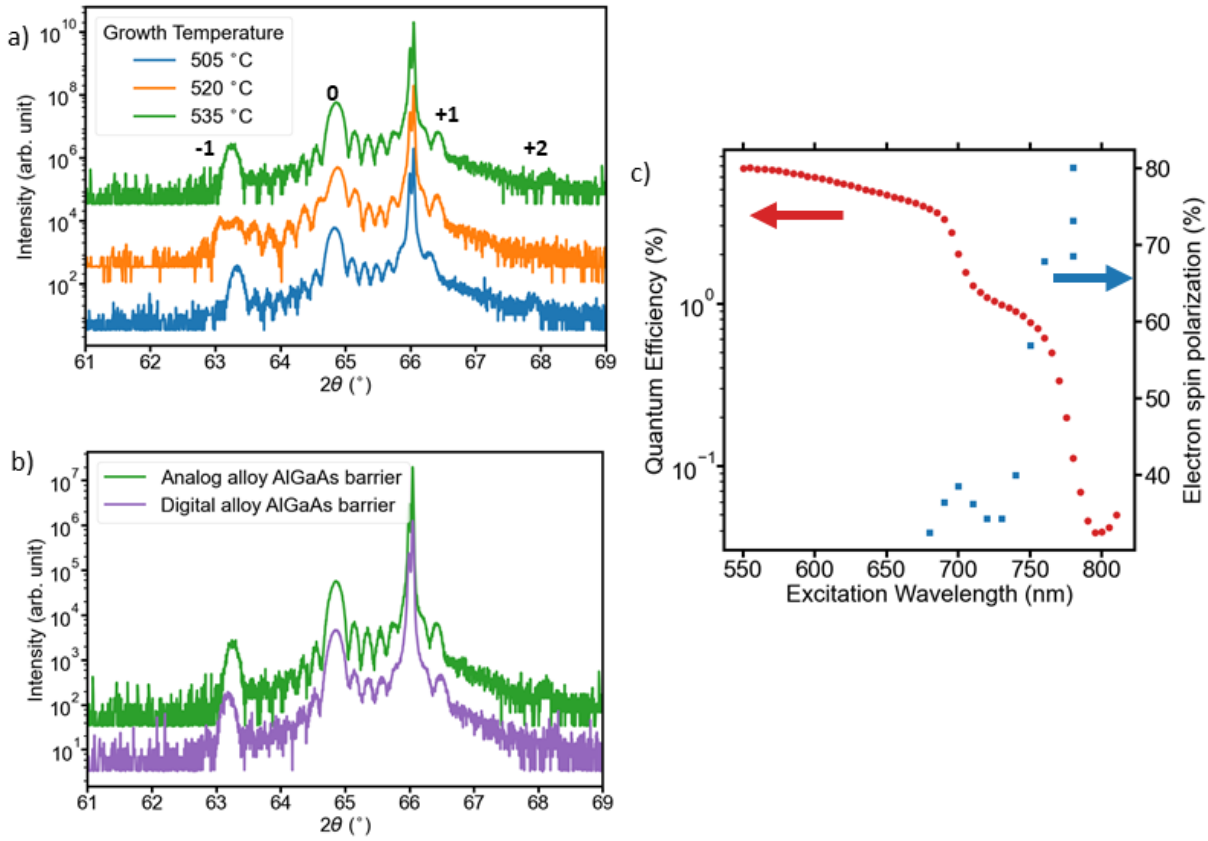


Initial characterization of strained superlattice InAlGaAs/AlGaAs photocathode structures grown pseudomorphically on GaAs(001)

a) X-ray diffraction measurements around the GaAs(004) peak for the same photocathode structure at three different growth temperatures. The sample grown at 520 °C likely had a poorly calibrated temperature, resulting in some phase segregation and the splitting of the **-1** peak. The other films show good superlattice ordering.

b) The same measurement comparing a photocathode grown with analog AlGaAs barriers and digital alloy AlGaAs barriers. The overall superlattice structure is preserved in the digital alloy scheme.

c) Quantum efficiency and spin polarization measured in a photocathode fabricated from the sample grown at 520 °C with phase segregation. Despite this, the peak figure of merit measured is only slightly worse than the state-of-the-art

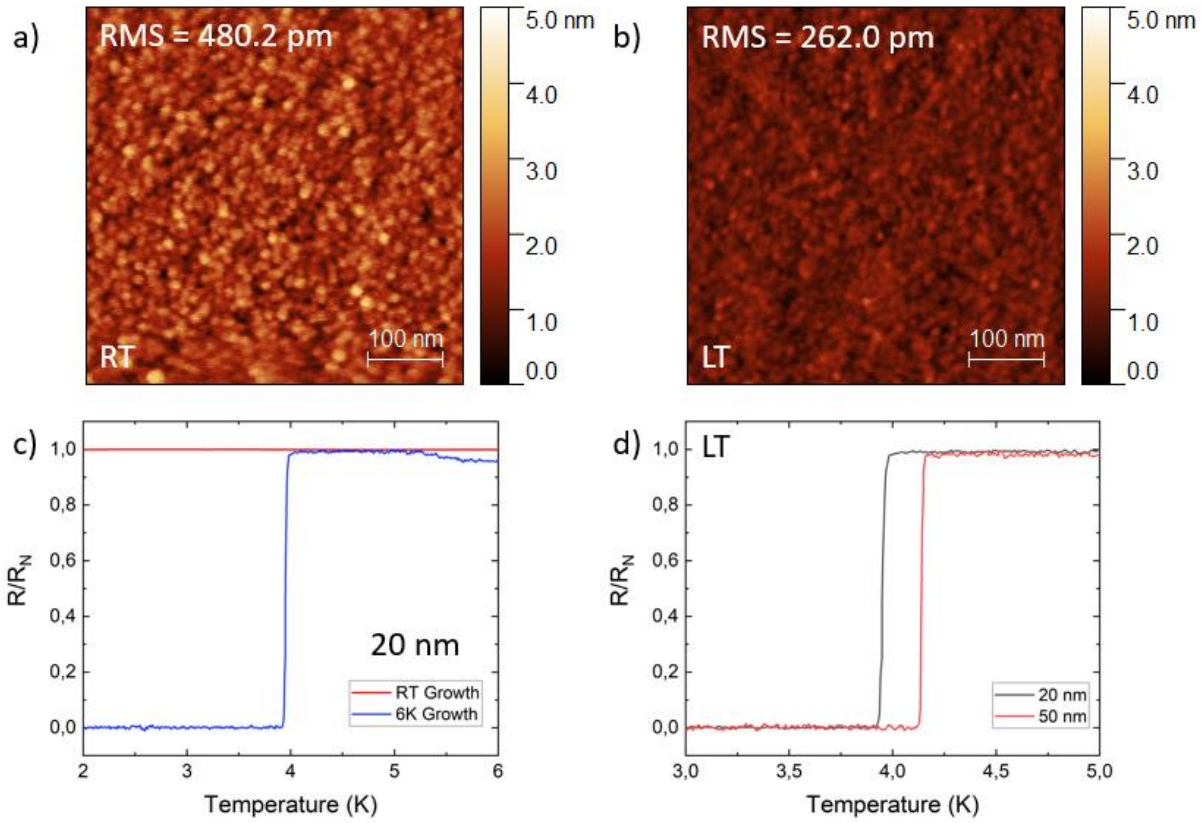


**Fig 1. Initial structural and electrical characterization of Ta thin film.** *a) Atomic Force Microscopy (AFM) image of the 20 nm tantalum grown at RT on $SiO_2$/Si. From this 500 x 500nm scan, the roughness is calculated to be RMS = 480.2 pm. b) AFM image of the tantalum grown at LT. From this 500 x 500nm scan, the roughness is calculated to be RMS = 262.0 pm. c) Four-probe resistance measurement of RT (red) and LT (blue) grown tantalum for a 20 nm thick film. Superconducting transition is observed at 3.95K. d) Four-probe resistance measurement LT grown tantalum for a 20 (black) and 50 (red) nm thick film. Superconducting transition for 50 nm thick film is observed at 4.14K.*

*Supplemental Material*

**Studying Electronic Structures of Pure $SrCoO_x$ Thin Films, Ordered Phases, And Heterostructures**

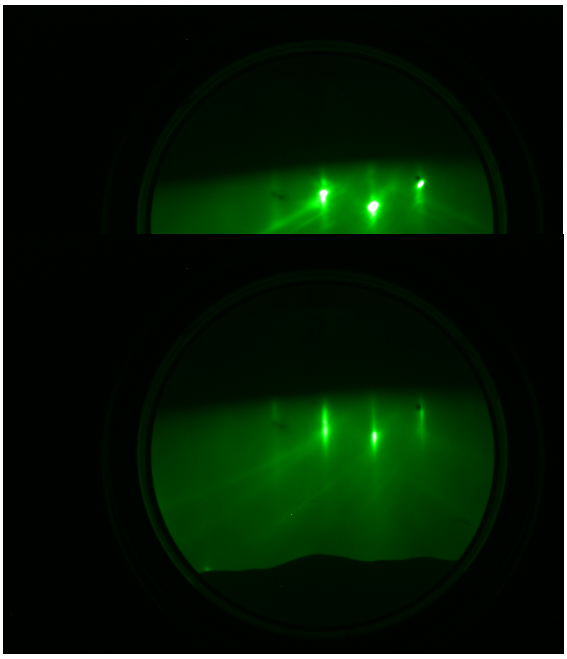

Fig 1: $LaAlO_3$ (LAO) substrate before growth (*top*), $SrCoO_x$ (SCO) film grown on LAO (*bottom*)

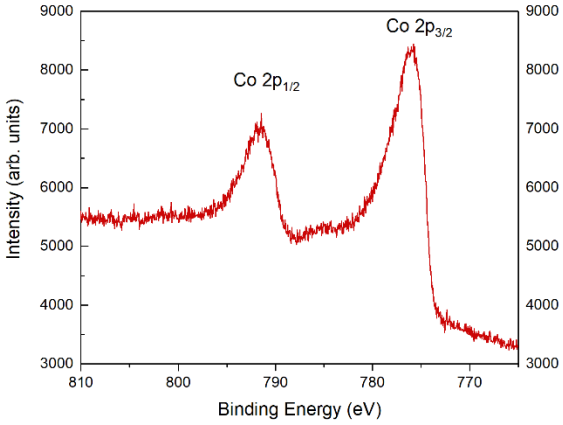


Fig 2: XPS spectra of Co 2p

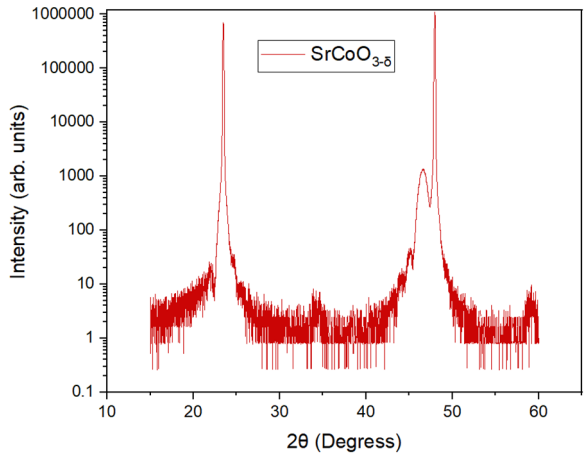


Fig 3: XRD analysis of SCO film grown on LAO

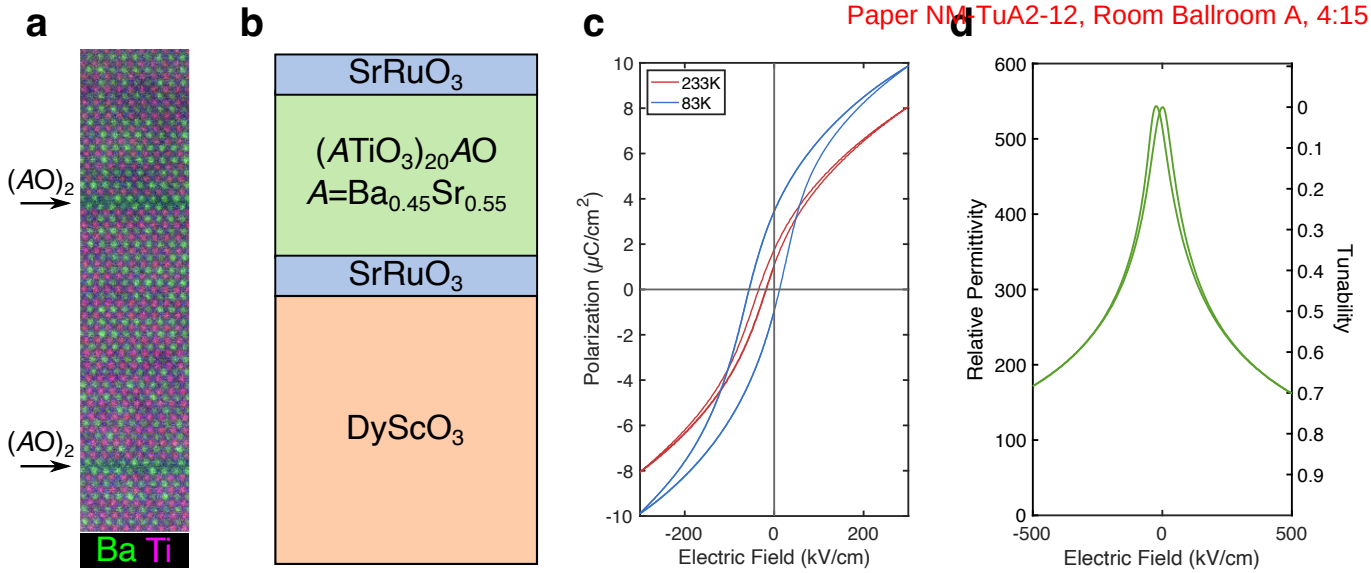


**Figure 1 (a)** Scanning transmission electron microscopy with spatially resolved electron energy loss spectroscopy (STEM-EELS) of an $(ATiO_3)_{20}AO$ film with $A = Ba_{0.6}Sr_{0.4}$. Barium atoms are shown in green and titanium atoms in magenta. Arrows indicate the $(AO)_2$ layers of the Ruddlesden-Popper phases separated by 20 perovskite unit cells. **(b)** Diagram of an MIM capacitor heterostructure. **(c)** Hysteresis loops measured from the MIM heterostructure represented by (b) at 233 K and 83 K. **(d)** Room temperature dielectric tunability of the same MIM heterostructure.

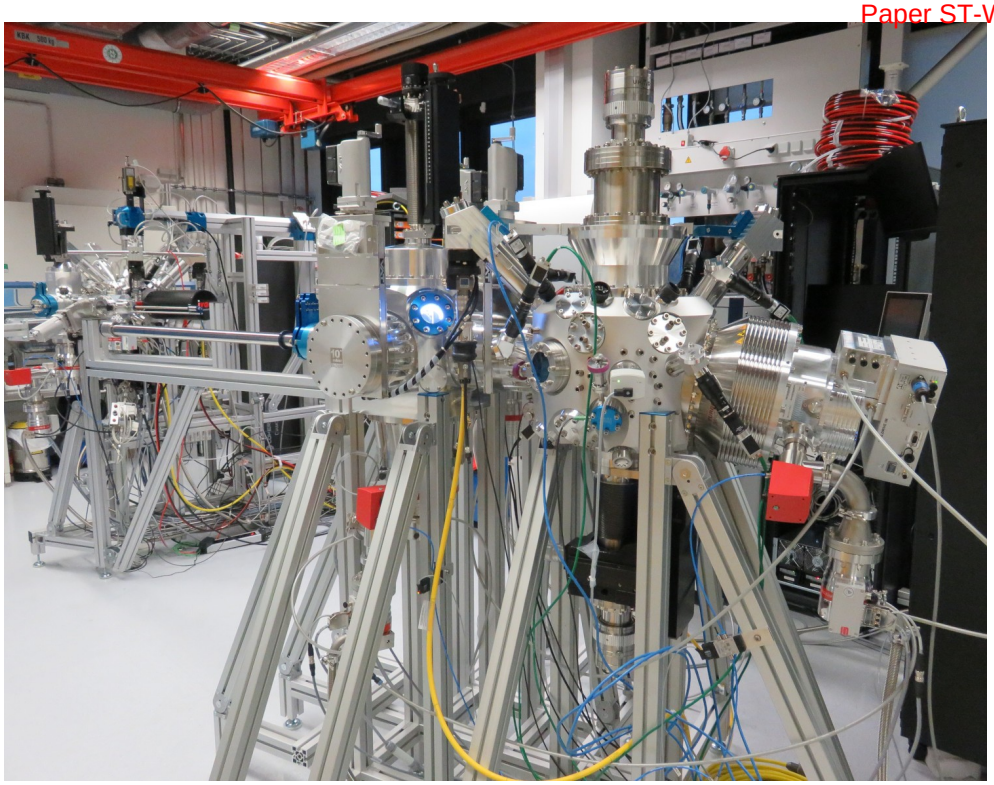

Fig. 1: State of the art triple-chamber TLE research systems. The smaller system in the back is designed for substrate sizes up to 2", the larger one in the front for substrate sizes up to 4". The 1 µm wavelength source heating lasers are coupled to the machine via the yellow fiber cables, 10 µm wavelength $CO_2$ beamline-guided lasers are used for substrate heating.
The compact design ensures high pumping speeds and small footprints. The sources are transferred into and out of the growth chamber via a single transfer mechanism also used for sample transfer. They may be stored in the middle chamber for high purity and rapid exchange.

Fig. 2: Growth rates of TLE Al sources (12 mm diameter sapphire crucibles) at three different $O_2$ background pressures as a function of laser power for a fixed spot diameter on the source of about 0.7 mm FWHM. In the presence of $10^{-3}$ hPa $O_2$, the flux deviates from the approximately straight line measured in UHV at low powers, indicating the formation of a volatile suboxide at the source surface depending on the oxygen pressure (not shown) and the metallic area as defined by either a stationary (bottom) or circularly moving beam (top).

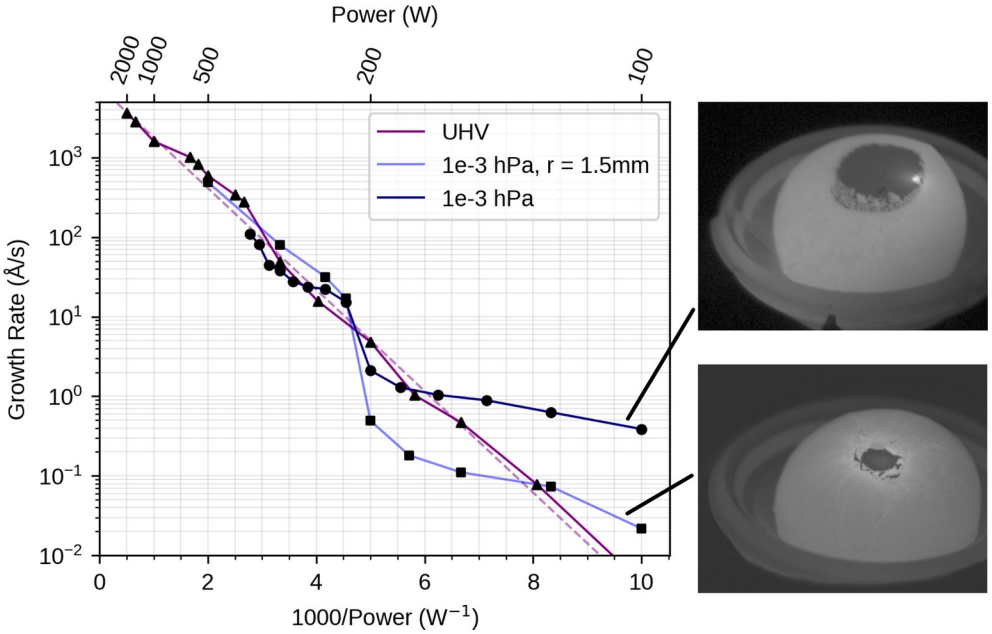


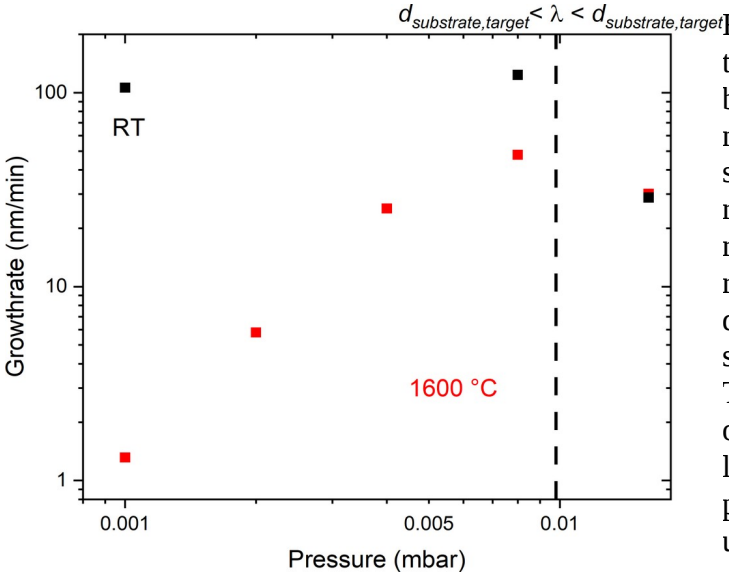


Fig. 3: Transition of $Al_2O_3$ growth from the ballistic to the diffusive transport regime at around $10^{-2}$ hPa $O_2$ background pressure. This transition corresponds to the mean free path of the $O_2$ dropping below the source-sample distance of 80 mm. RT denotes deposition at room temperature, the red points show the deposition rate in the adsorption-limited homoepitaxial growth regime at a substrate temperature of 1600 °C. For details on the adsorption-limited epitaxy, refer to the submission by Felix Hensling.
The very high dynamic range of TLE sources, spanning over 5 orders of magnitude in flux for a factor of 20 in laser power (see Fig. 2), combined with very rapid power modulation allows high growth rate deposition at ultrahigh quality with economic use of source material.

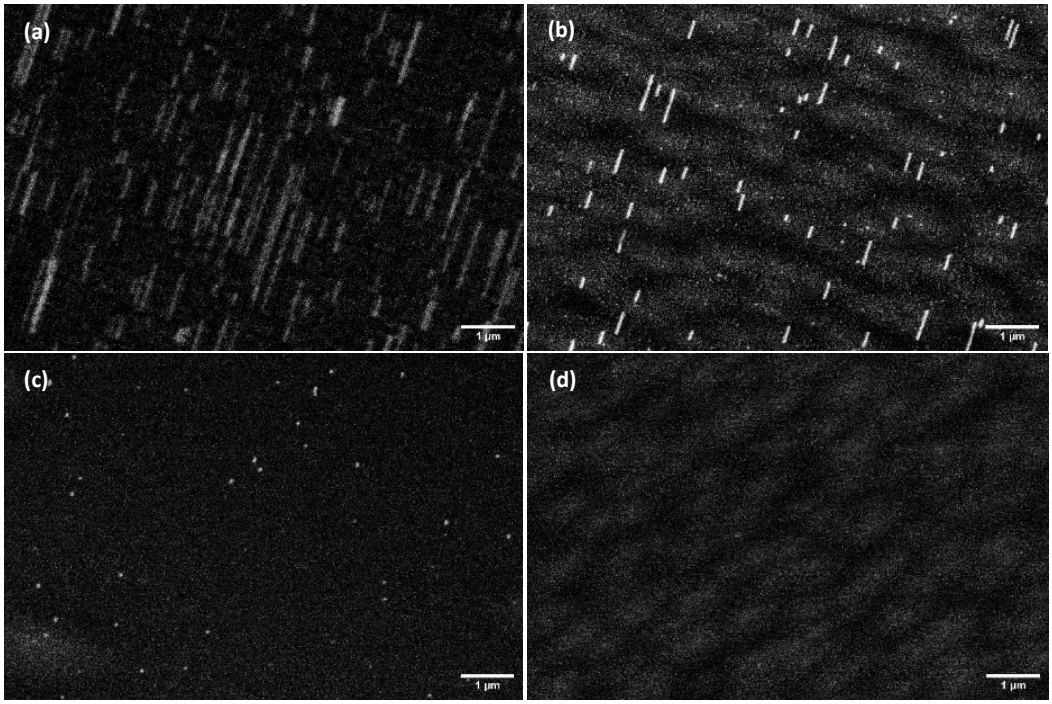


Electron channeling contrast imaging (ECCI) of ZnS on GaP (100) thin films at (a) 50, (b) 25, (c) 20, and (d) 15 nm shows misfit dislocations along (220) directions.

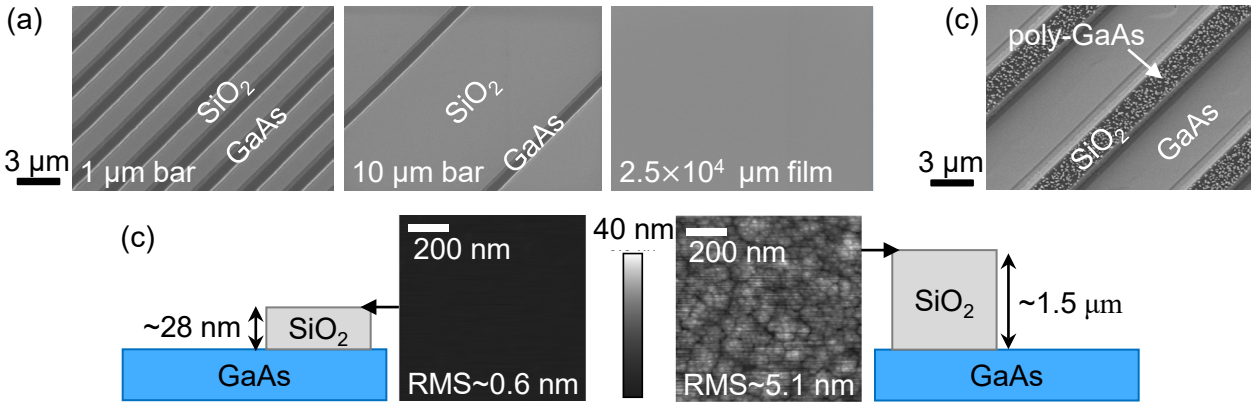


Figure 1. (a) Scanning electron microscopy (SEM) images of silica gratings and film (~28 nm height) show no polycrystal formation after 100 nm of 10% PSE growth of GaAs at 600˚C demonstrating feature-size independent selective growth. (b) Poly-GaAs formation observed on 1.5 μm tall gratings after same growth was performed. (c) Atomic force microscopy of respective $SiO_2$ surfaces indicates that increased roughness of 1.5 μm features promotes nucleation of poly-GaAs in this growth regime.

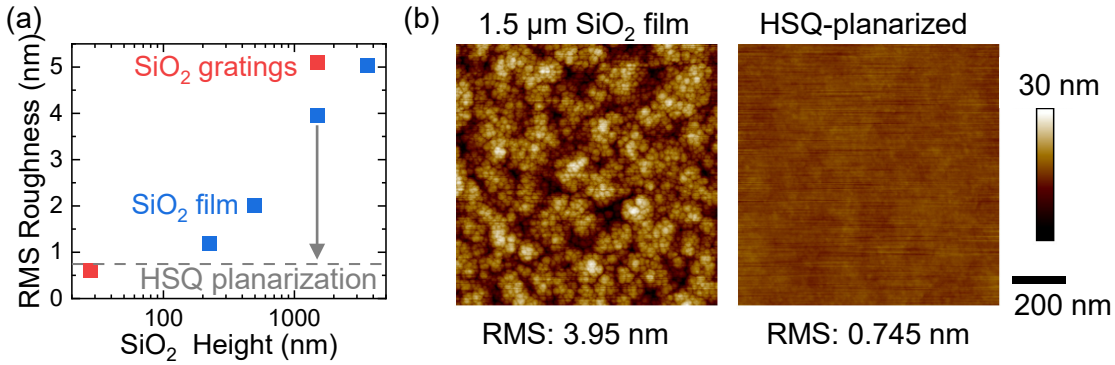


Figure 2. (a) Root-mean-square surface roughness of $SiO_2$ deposited by plasma-enhanced chemical vapor deposition (PECVD) compared to HSQ planarization. (b) Atomic force microscopy of a 1.5 μm $SiO_2$ film (left) before and (right) after planarization by 100 nm hydrogen silsesquioxane (HSQ) layer.

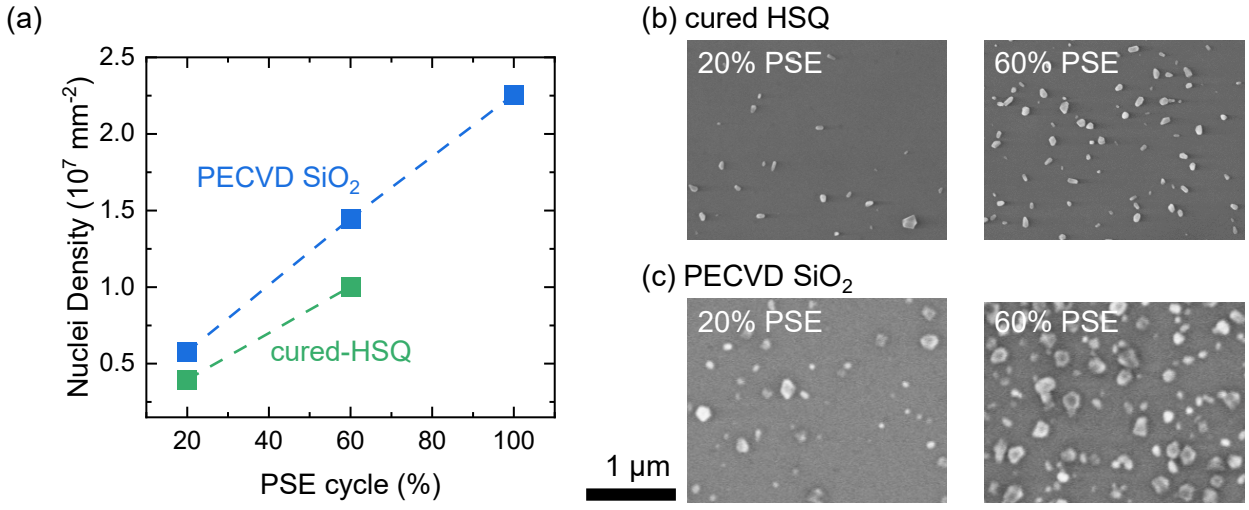


Figure 3. (a) Resulting poly-GaAs nuclei densities on cured HSQ and PECVD $SiO_2$ films after 100 nm GaAs was grown with varying PSE cycles ($t_{cycle}$ = 60 s) at 600˚C. Scanning electron microscope images of poly-GaAs on (b) cured HSQ and (c) PECVD $SiO_2$.

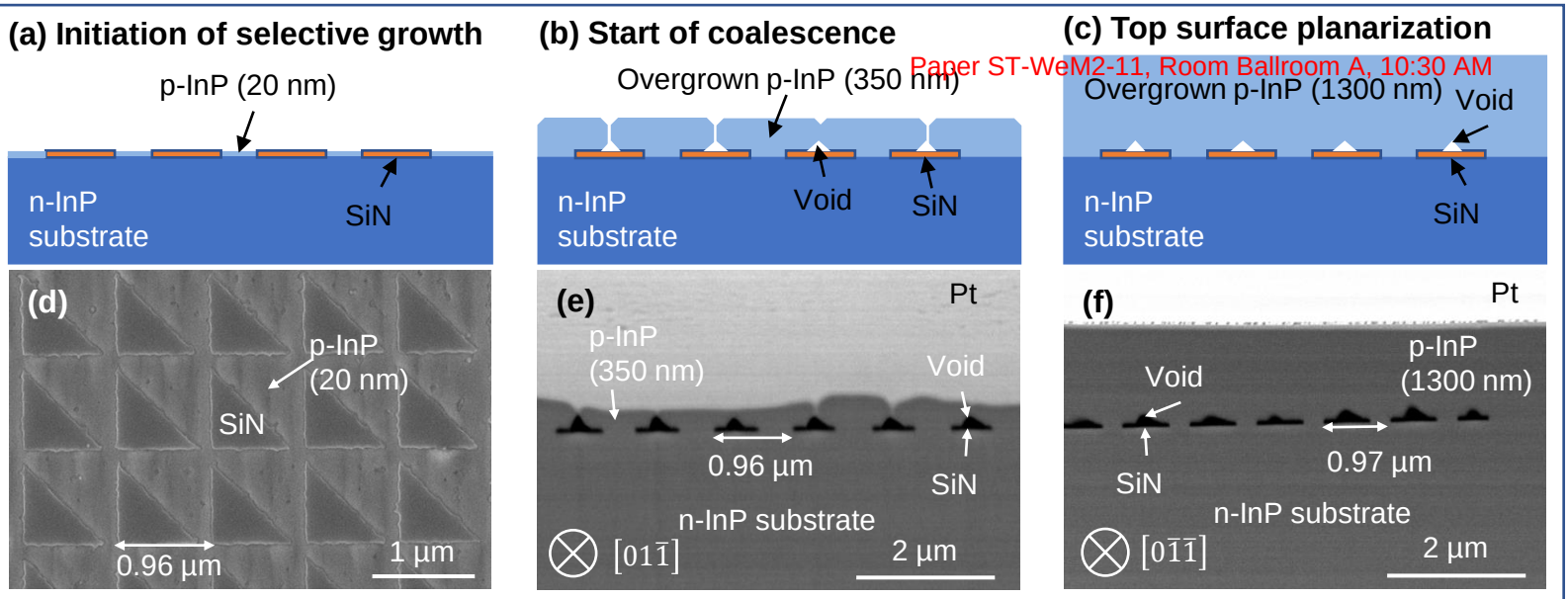


Fig. 1. (a)-(c) Cross-sectional schematics after 20, 350, and 1300 nm of p-InP ($p=10^{18}cm^{-3}$) growth on patterned n-InP substrate. Pattern consists of isosceles-right-triangles (side length = 965 nm) of SiN (40 nm thick); (d) plan-view SEM after 20 nm growth showing selectivity; (e) and (f) XSEM after 350 and 1300 nm of p-InP growth.

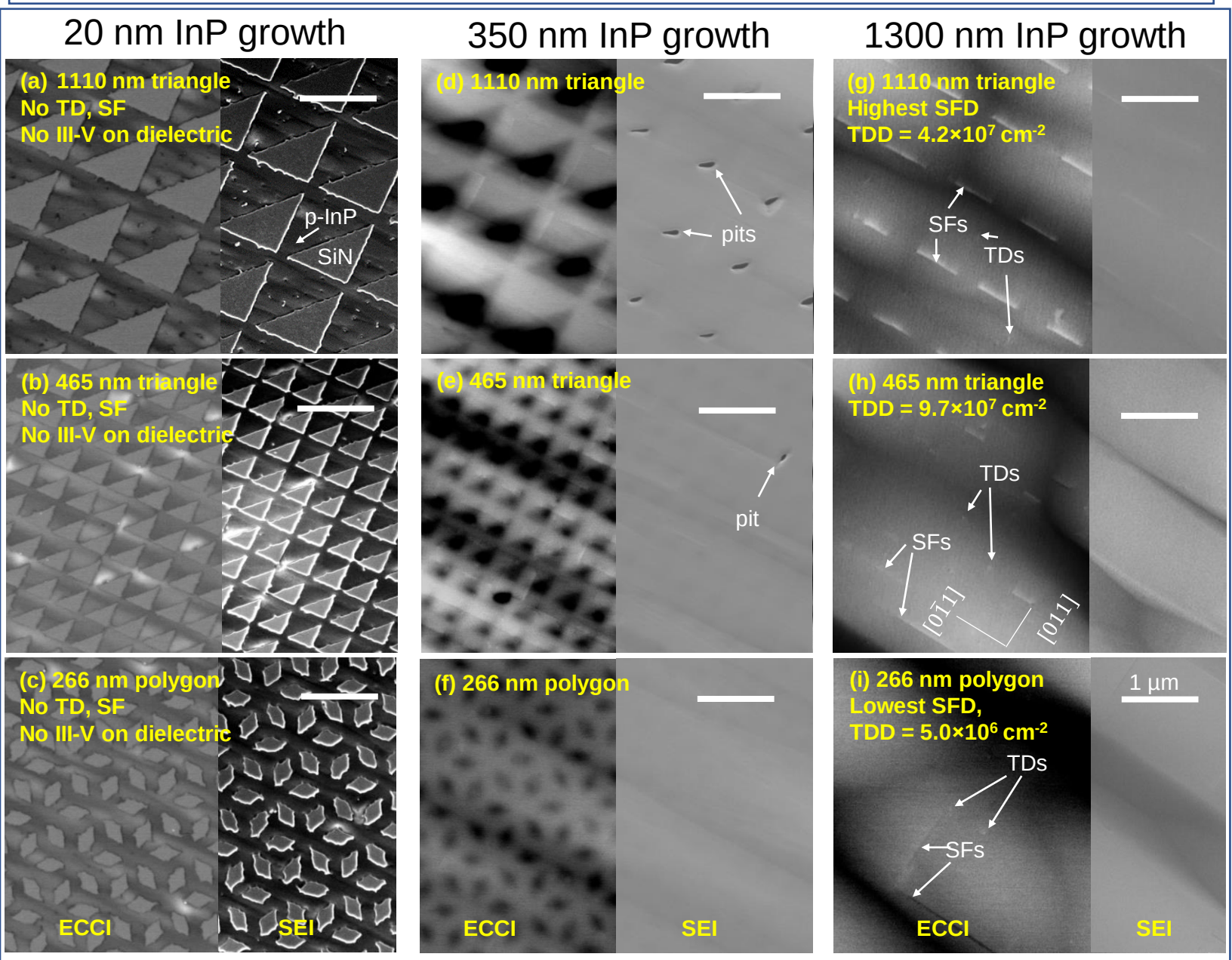


Fig. 2. (a) - (c) ECCI/SEI of 20 nm p-InP grown on patterned SiN/n-InP substrate with feature size of (a) 1110 nm, (b) 465 nm, and (c) 266 nm; (d) - (f) ECCI/SEI of 350 nm p-InP grown on similar patterns; (g) - (i) ECCI/SEI of 1300 nm p-InP grown on similar patterns. SF = Stacking fault, TD = threading dislocation, SFD/TDD refers to density. Scalebar = 1µm.

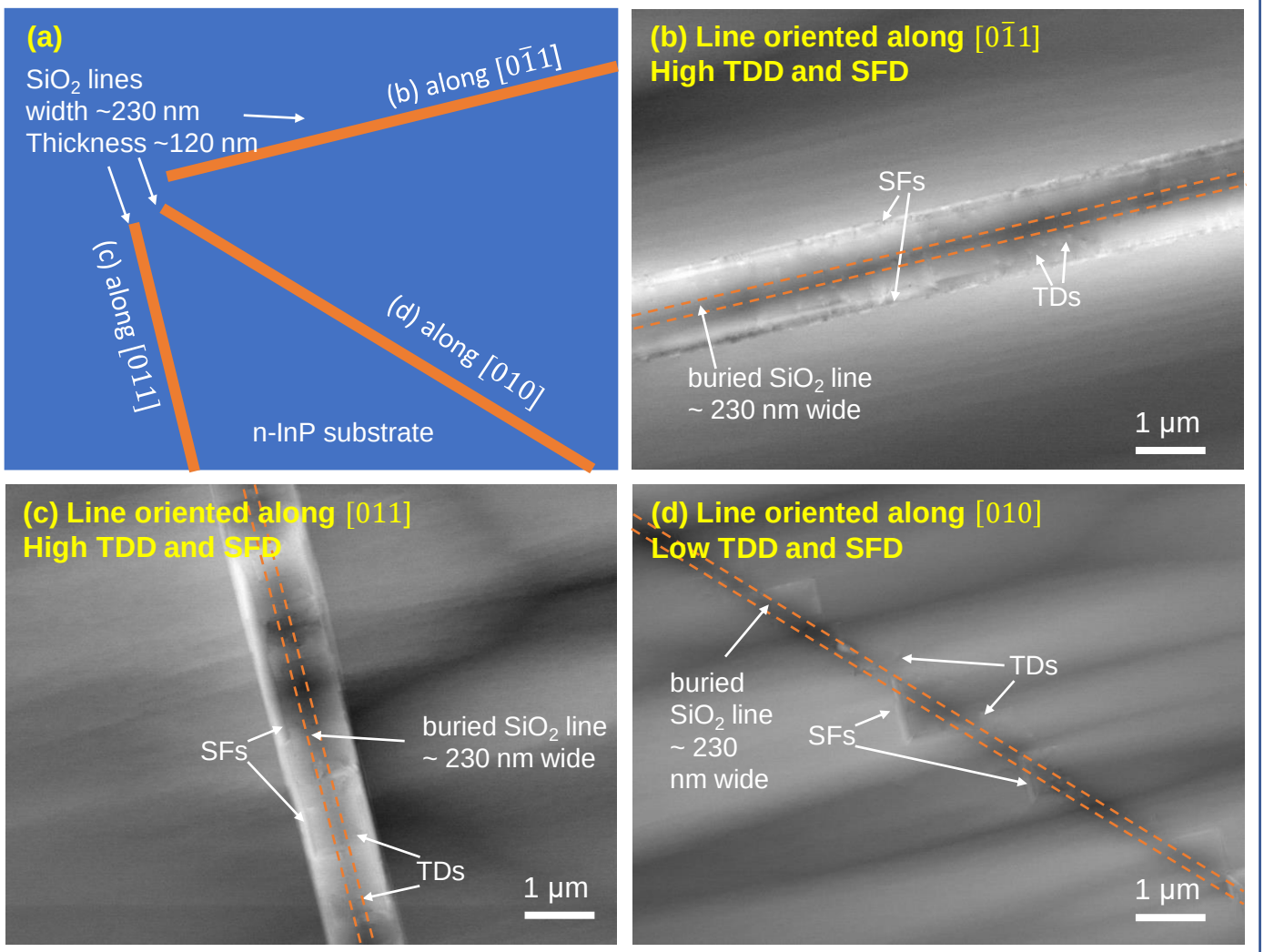


Fig. 3. (a) Plan-view schematics of patterned $SiO_2$/n-InP substrate (line pattern); (b) - (d) ECCI of 580 nm p-InP grown on the same substrate with $SiO_2$ line oriented along (b) [0 -1 1], (c) [0 1 1], and (d) [0 1 0] crystallographic directions. Dashed line represent the two sides of buried $SiO_2$ lines. The [0 1 0] stripes show the lowest defect density.

References

[1] K. Hirose et al., *Nature Photonics* 8, no. 5 (May 2014): 406–11.
[2] Z. Wang et al., *Materials Science and Engineering: B* 177, no. 17 (October 2012): 1551–57.
[3] D. Ironside et al., *Progress in Quantum Electronics* 77 (May 2021): 100316.
[4] M. Fahed et al., *Nanotechnology* 26, no. 29 (July 24, 2015): 295301.

Candice Forrester et al., *Effect of molecular beam epitaxy (MBE) growth parameters on the structural and magnetic properties of high Curie temperature $(MnSb_2Te_4)_x(Sb_2Te_3)_{1-x}$ magnetic topological insulators*

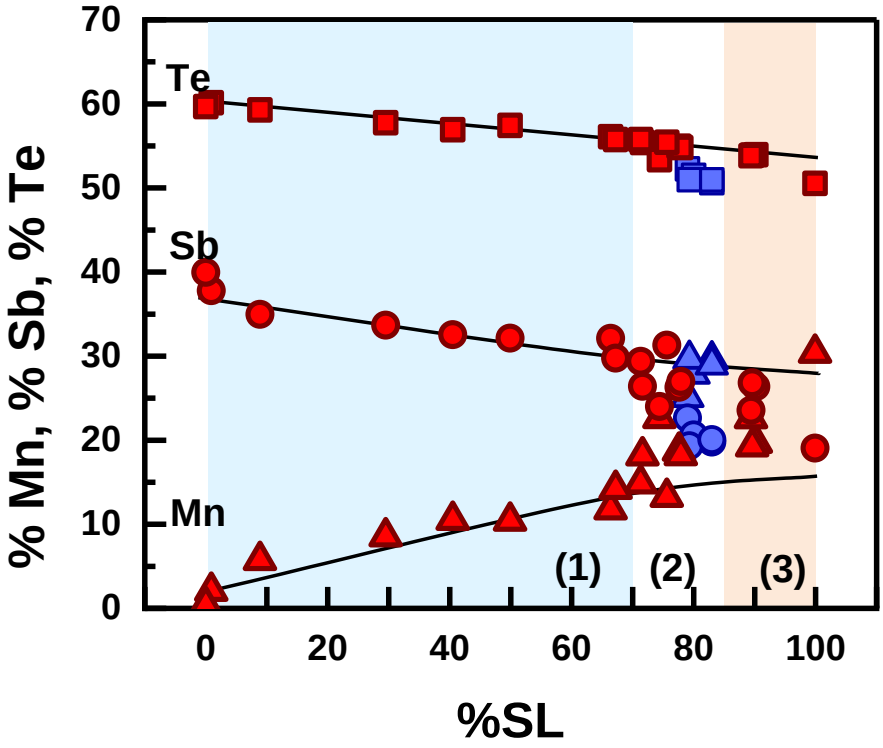


Figure 1: Energy Dispersion X-Ray Spectroscopy (EDS) study exploring the elemental contribution of Mn, Sb and Te to the crystal structure as a function of percent of septuple layers. The black lines represent stochiometric $(MnSb_2Te_4)_x(Sb_2Te_3)_{1-x}$. For $(MnSb_2Te_4)_x(Sb_2Te_3)_{1-x}$ samples with $0.7 < x < 0.85$ and grown with a **fast GR (red)**, Mn and Sb intermixing was observed. However for samples $(MnSb_2Te_4)_x(Sb_2Te_3)_{1-x}$ samples with $0.7 < x < 0.85$ and grown with a **slow GR (blue),** not only, showed increased Sb and Mn intermixing, but also, some Mn and Te intermixing.

# Adsorption-Controlled Growth of $SrTiO_3$ by Oxide MBE

Dylan Sotir[1,2], Matthew Barone[1,2], Darrell Schlom[1,2,3,4]

[1] Department of Materials Science and Engineering, Cornell University
[2] Platform for the Accelerated Realization, Analysis, and Discovery of Interface Materials (PARADIM), Cornell University
[3] Kavli Institute at Cornell for Nanoscale Science
[4] Leibniz-Institut für Kristallzüchtung

Historically, the growth of stoichiometric $SrTiO_3$ by conventional molecular-beam epitaxy (MBE), utilizing elemental sources, has been challenging due to the precise calibration required. It would be useful if there were a thermodynamic regime where the composition of $SrTiO_3$ was self-regulating. One demonstrated way to achieve such automatic control of stoichiometry in $SrTiO_3$ is by supplying an excess of the volatile organometallic precursor titanium isopropoxide to grow $SrTiO_3$ by metalorganic MBE (MOMBE). Another means, and the one investigated here, is to stick with elemental sources but increase the substrate temperature. When $SrTiO_3$ is heated to high temperature, it does not evaporate congruently; rather, it loses more strontium than titanium. This difference in the vapor pressures of the volatile species suggests that adsorption-controlled growth of $SrTiO_3$ may be possible by conventional MBE. We report a thermodynamic window in which $SrTiO_3$ can be grown via adsorption control by conventional MBE. A new high-temperature laser substrate heater installed in Cornell University's PARADIM Thin Film Facility allows substrate temperatures to reach up to 2000 ℃.

We show that the growth window for our highest quality adsorption-controlled $SrTiO_3$ is from approximately 1450-1475℃, with a Sr:Ti ratio of 5:1. All films were grown on $LaAlO_3$ (100) substrates. Figure 1 shows XRD data for samples grown at several temperatures including the adsorption-control window.

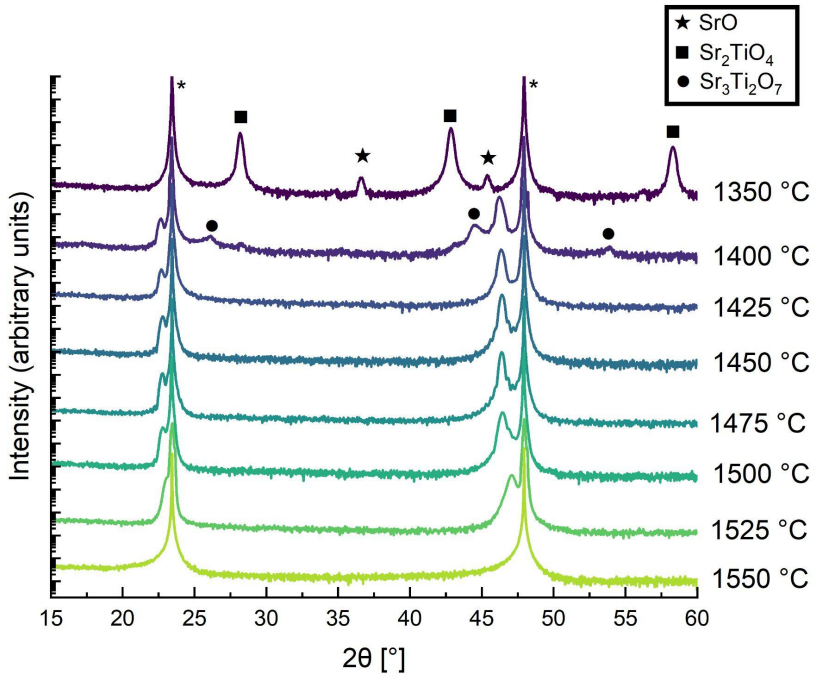


Figure 1: θ-2θ x-ray diffraction scan showing approximately 33 nm thick films of $SrTiO_3$ grown by MBE on $LaAlO_3$ (100) at a range of temperature from 1350-1550 ℃ at a background pressure of 10% ozone of $1\times10^{-6}$ Torr.

**Supplemental to: Piezo- and flexoelectricity arising from extreme strain gradients in bent GaAs nanowires**

Francisca Marin, Oliver Brandt, and Lutz Geelhaar
*Paul-Drude-Institut für Festkörperelektronik, Leibniz-Institut im Forschungsverbund Berlin e.V., Hausvogteiplatz 5-7, 10117 Berlin, Germany*

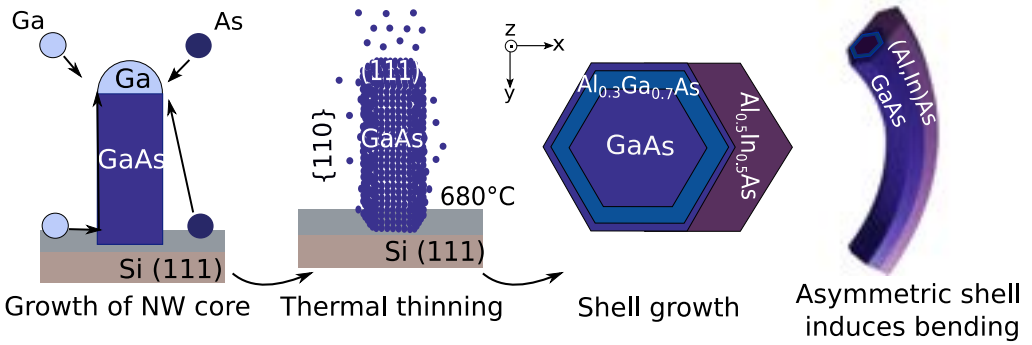


Fig. 1: Schematic illustrating the growth of bent GaAs nanowires (NWs). NWs are grown under Ga droplets, their diameter is thinned by thermal evaporation, and a lattice-matched symmetric (Al,Ga)As shell is grown for surface passivation. Last, a lattice-mismatched (Al,In)As stressor shell is grown and induces bending by strain partitioning.

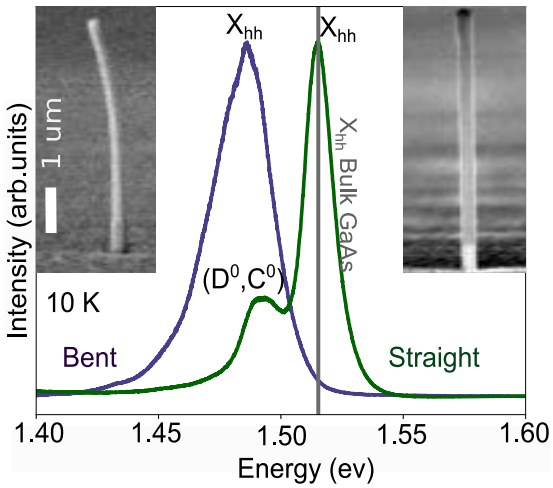


Fig. 2: Low-temperature photoluminescence (PL) spectra for single straight and bent GaAs NWs with low degree of polytypism. Only the donor-acceptor pair ($D^0$,$C^0$) and the free exciton $X_{hh}$ transition are observed. The insets are side-view micrographs of the corresponding NWs.

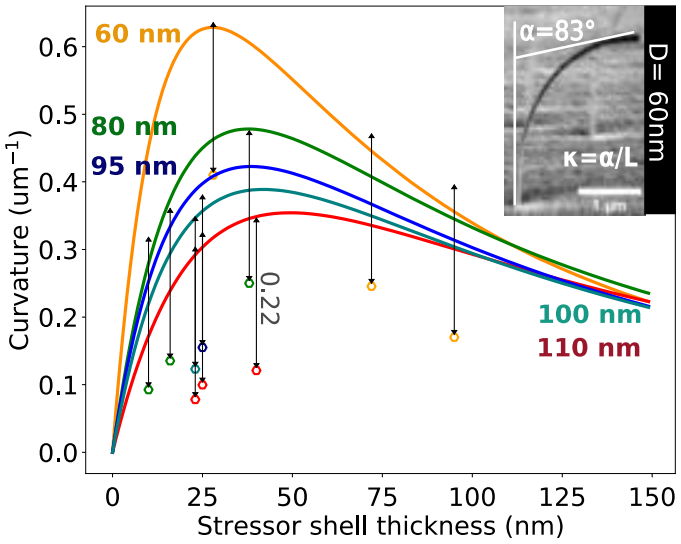


Fig. 3: NW curvature as a function of stressor shell thickness. The curves correspond to elastic strain calculations for different diameters. Data points represent experimental values, and the double arrows indicate a constant offset from the model.

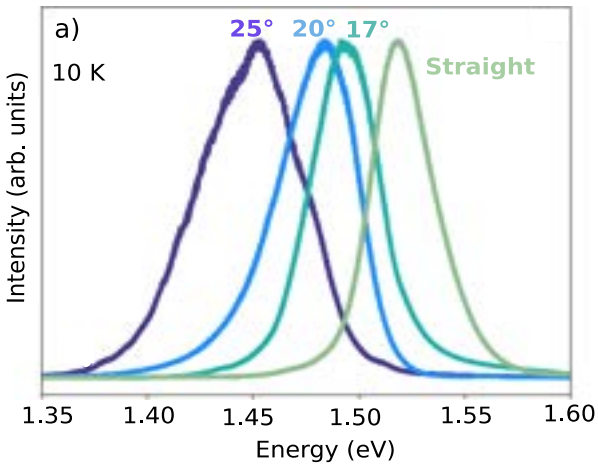


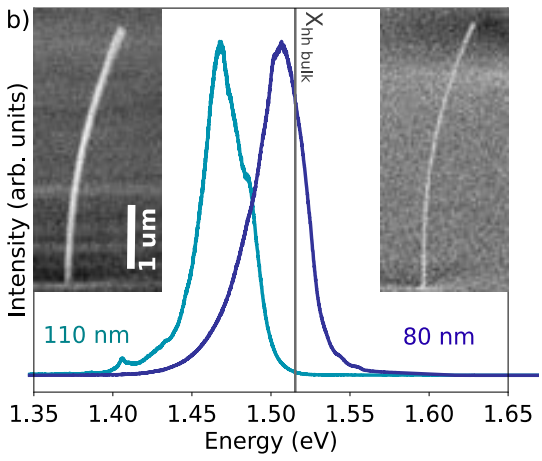


Fig. 4: Low-temperature PL spectra of single bent GaAs NWs. a) Same diameter, different curvature, as indicated by the bending angles. b) Similar curvature, different diameter as given by labels. The insets are side-view micrographs of the corresponding NWs.

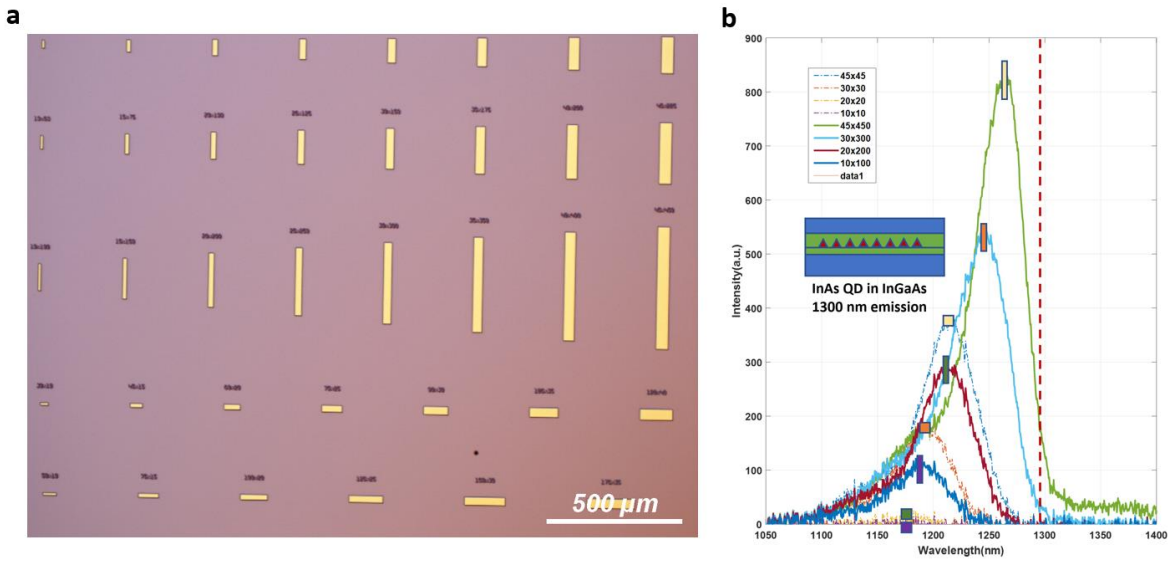


Figure 1: (a) Nomarski image of the as-fabricated oxide pattern on GaAs. The pocket size various between 45 µm × 450 µm to 1 µm × 1 µm. (b) Example room temperature PL spectra of the as-grown material. The legend is structured as "W×L" in micrometers. The red vertical dashed line indicates the emission wavelength of the QDs grown on planar GaAs.

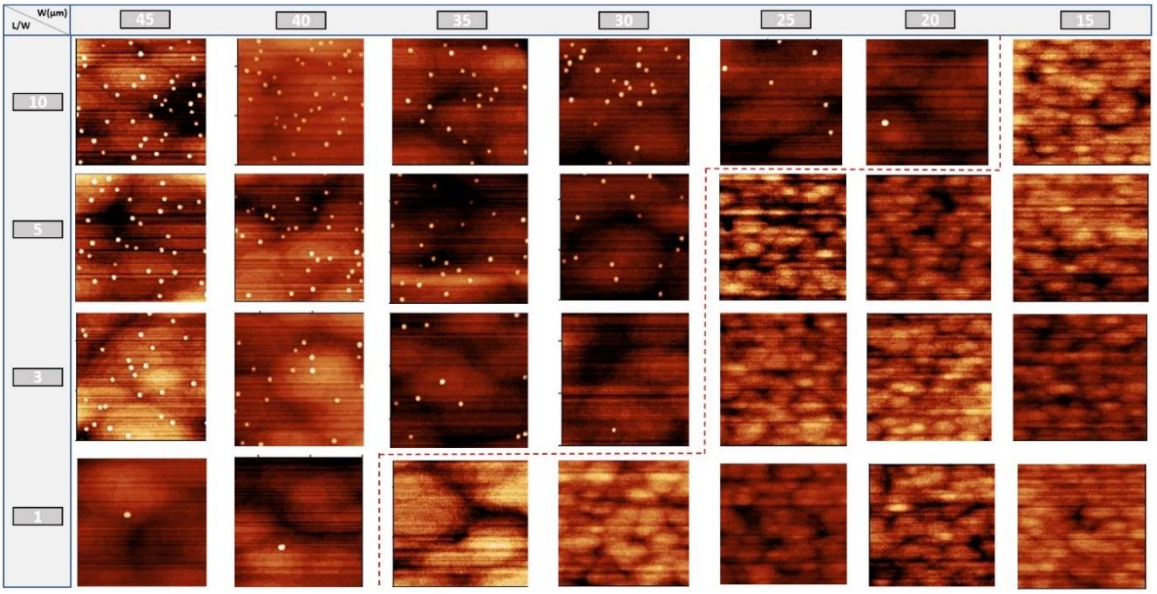


Figure 2: AFM scan of the exposed surface dots. The top roll indicates the widths of the pockets. Each AFM image shows a 500 nm × 500 nm scan area. The red dashed line indicates a "boundary" between the pocket with and without observed dots.

Table 1: QD surface density ($cm^{-2}$) measured in pocket with various dimensions. The reference density is approximately $5\times10^{10}$ $cm^{-2}$ on planar GaAs substrate

| L/W \ W(μm) | 45 | 40 | 35 | 30 | 25 | 20 | 15 |
|---|---|---|---|---|---|---|---|
| 10 | 1.60E+10 | 1.58E+10 | 1.10E+10 | 9.20E+09 | 2.40E+09 | 2.00E+07 | 0.00E+00 |
| 5 | 1.53E+10 | 1.44E+10 | 8.80E+09 | 6.10E+09 | 0.00E+00 | 0.00E+00 | 0.00E+00 |
| 3 | 1.04E+10 | 7.60E+09 | 4.40E+09 | 1.00E+07 | 0.00E+00 | 0.00E+00 | 0.00E+00 |
| 1 | 4.00E+06 | 1.00E+06 | 0.00E+00 | 0.00E+00 | 0.00E+00 | 0.00E+00 | 0.00E+00 |

Table 2: Typical dot height (nm) measured in pocket with various dimensions. The reference height is 8 to 9 nm on planar GaAs substrate

| L/W \ W(μm) | 45 | 40 | 35 | 30 | 25 | 20 | 15 |
|---|---|---|---|---|---|---|---|
| 10 | 4.6 | 4.6 | 4.8 | 4.8 | 5.35 | 6.6 | N/A |
| 5 | 4.6 | 4.6 | 5.1 | 5.25 | N/A | N/A | N/A |
| 3 | 4.6 | 4.6 | 5.3 | 5.55 | N/A | N/A | N/A |
| 1 | 4.6 | 5.5 | N/A | N/A | N/A | N/A | N/A |

# Supplemental Document Author Index

## Bold page numbers indicate presenter

# Supplemental Document Author Index

# Supplemental Document Author Index